

DYNAMICS OF  
GRANULAR SEGREGATION  
IN DRIVEN BINARY MONOLAYERS

A THESIS SUBMITTED TO THE UNIVERSITY OF MANCHESTER  
FOR THE DEGREE OF DOCTOR OF PHILOSOPHY  
IN THE FACULTY OF SCIENCE AND ENGINEERING

2004

By  
Pedro Miguel Reis  
Department of Physics and Astronomy

# Contents

<b>Abstract</b>	<b>22</b>
<b>Legal Notices</b>	<b>23</b>
<b>The Author</b>	<b>25</b>
<b>Acknowledgements</b>	<b>28</b>
<b>1 Introduction</b>	<b>29</b>
1.1 Granular media: motivation . . . . .	29
1.2 Definition of dry granular materials . . . . .	31
1.3 Early developments . . . . .	32
1.4 Modern investigations . . . . .	33
1.4.1 Rapid granular flows . . . . .	34
1.4.2 Quasi-static packings . . . . .	35
1.4.3 Dense granular flows . . . . .	36
1.5 Particle segregation . . . . .	37
1.5.1 Vertical vibration . . . . .	39
1.5.2 Horizontal vibration . . . . .	43
1.5.3 Segregation in continuous surface flows . . . . .	45
1.5.4 Rotating drums . . . . .	47
1.6 Phase separation in colloidal systems . . . . .	48

<i>CONTENTS</i>	3
1.7 Thesis outline . . . . .	52
<b>2 The experiment</b>	<b>54</b>
2.1 Electro-mechanical system . . . . .	54
2.2 Driving and vibration monitoring . . . . .	59
2.3 Materials used . . . . .	61
2.4 Layer compacity . . . . .	63
2.5 The aspect ratio . . . . .	65
2.6 Setting the initial conditions . . . . .	65
2.7 Visualization and image acquisition . . . . .	66
2.8 Image processing . . . . .	69
2.8.1 Segregation patterns . . . . .	69
2.8.2 Microscopic particle tracking . . . . .	71
<b>3 Granular segregation patterns</b>	<b>75</b>
3.1 Segregation Patterns . . . . .	75
3.2 Space-time diagram construction . . . . .	79
3.3 The average width and number of domains . . . . .	80
3.4 Pattern reproducibility . . . . .	83
<b>4 Domain-level ‘macroscopic’ measures</b>	<b>87</b>
4.1 Compacity dependence studies . . . . .	87
4.2 Space-time diagrams . . . . .	88
4.3 The average domain width: an order parameter . . . . .	90
4.4 Continuous phase transition for segregation . . . . .	92
4.5 The Number of domains . . . . .	94
4.6 Segregation timescales . . . . .	95
4.7 Macroscopic fluctuations of domains . . . . .	98
4.8 Summary: the three phases scenario . . . . .	101

<b>5</b>	<b>'Microscopic' measures</b>	<b>104</b>
5.1	Granular segregation: a 'microscopic' view . . . . .	104
5.2	Local Voronoi area density . . . . .	107
5.2.1	Dynamic evolution . . . . .	109
5.2.2	Compacity studies . . . . .	114
5.2.3	Tracking of the Area density for an individual sphere . . .	118
5.3	Nearest neighbours angular distribution . . . . .	119
5.4	Radial distribution function . . . . .	122
5.5	Summary . . . . .	126
<b>6</b>	<b>Exploration of parameter space</b>	<b>127</b>
6.1	Aspect ratio . . . . .	127
6.2	Compacity phase diagram . . . . .	131
6.3	Forcing parameter-space . . . . .	139
6.4	Summary . . . . .	145
<b>7</b>	<b>Conclusions</b>	<b>148</b>
7.1	General Remarks . . . . .	148
7.2	Possible segregation mechanism . . . . .	150
7.3	Analogies with binary colloids . . . . .	151
7.4	Future work . . . . .	152
<b>A</b>	<b>The radial distribution function</b>	<b>155</b>
<b>B</b>	<b>Nonlinear behaviour</b>	<b>158</b>
B.1	Induction of streaming motion . . . . .	158
B.2	Oscillatory states . . . . .	167
<b>C</b>	<b>Simulations of 2D driven binary mixtures</b>	<b>173</b>

*CONTENTS*

5

**D Public presentation of this work**

**185**

# List of Figures

1.1	The Brazil-nut effect. A large heavy intruder is immersed in a medium of small particles. As the system is vertically vibrated the large particle raises to the surface. Vertical vibration of the container is initiated in (a). The 4 frames correspond to sequential stages until the intruder reaches the surface of the granular column. A layer of black small particles has been introduced in the pack to aid visualisation of the convection current that can be set up through the vibration. Diagram courtesy of S. R. Nagel (Knight, Jaeger & Nagel, 1993) . . . . .	41
1.2	(a) Stratification patterns of binary mixture formed after pouring. (b) Radial segregation in a thin rotating drum. The large sugar particles are shown in white and the small iron spheres in grey. Photographs courtesy of N. Gray (Gray & Hutter, 1997). . . . .	46
1.3	Axial segregation bands in a long rotating drum for a mixture of white salt and black sand. Photograph courtesy of S. Morris (Choo, Molteno & Morris, 1997). . . . .	47

1.4	Schematic diagram for the excluded volume depletion process. (a) Binary hard-sphere system with large and small spheres (two dimensional representation). (b) Volume available to the small particles, $V'$ . Region in grey correspond to excluded volume where the centres of the small particles cannot penetrate. (c) When two large particles come together, there is an increase in the free volume available. The region of excluded volume depletion is shown in blue. . . . .	49
1.5	(a) Micrograph of a colloidal crystal configuration in two dimensions for a mixture of polystyrene spheres of diameter $1.9\mu m$ and $213nm$ . The filling fraction of the small spheres is $\phi = 0.20$ . Only the large spheres are visible. (b) Confocal microscopic photograph of a three dimensional FCC colloidal crystal in a mixture of colloidal spheres ( $0.7 - 1.2\mu m$ diameter) and polystyrene polymer (radius of gyration $\sim 12nm$ ). (a) courtesy of E. Hobbie (1998). (b) courtesy of A. G. Yodh (2001). . . . .	50
2.1	Three dimensional schematic diagram of the experimental apparatus.	55
2.2	Schematic diagram of the experimental apparatus. (a) top view. (b) side view. . . . .	57
2.3	Power spectrum obtained from a Fast Fourier Transform of the accelerometer signal for $f = 12Hz$ and $A = \pm 1.74mm$ with characteristic peaks at the fundamental frequency ( $12Hz$ ), first harmonic ( $24Hz$ ) and second harmonic ( $36Hz$ ). . . . .	59
2.4	Photographs of the various non-spherical particles used. (a) poppy seed. (b) mustard seed. (c) sugar particle. (d) Typical frame of a poppy seed, imaged through a microscope with a $2\times$ objective, which was used in the polydispersity measurements. . . . .	62

2.5	Histogram of the two-dimensional projected areas of 2500 poppy seeds. The solid curve is a gaussian fit with a mean of $0.90mm^2$ and a standard deviation of $0.15mm^2$ . . . . .	63
2.6	Schematic diagram for the definition of the layer compacity. Species $a$ and $b$ have two-dimensional projected areas of $A_a$ and $A_b$ , respectively. $x$ and $y$ are the spacial dimensions of the full tray. . . . .	64
2.7	a) Schematic diagram of the procedure for setting the initial conditions of the binary granular layer. (a) A homogeneous layer of poppy seeds is initially created by vibration at large amplitudes. (b) an independent frame is then superposed on the tray and a perforated plate with $m \times n$ holes is loaded with phosphor-bronze spheres using a funnel. (c) A shutter is then opened and the spheres fall onto the homogeneous layer of poppy seeds in the tray underneath. . . . .	67
2.8	Photograph for the typical initial conditions of the homogeneous mixture of poppy seeds and phosphor-bronze spheres. . . . .	68
2.9	Image processing sequence of the images of the segregation patterns used for the macroscopic measurements in Chapter 3 and 4. (a) Original colour frame. (b) Processed frame after hue and saturation adjustments. (c) Processed frame after extraction of the <i>blue</i> channel. (d) Processed frame after inversion. (e) Processed frame after gaussian blurring. (f) Final processed frame after inversion. . . . .	70
2.10	Image processing of the images of granular segregation used for the microscopic measurements in Chapter 5 and 6. (a) Original experimental frame. (b) Processed frame after gaussian blurring. (c) Final processed frame after inversion. . . . .	71

2.11 Final processed frame. (a) Three-dimensional surface of the grey-scale level images. Red peaks represent the position of individual spheres. (b) Zoomed surface of the processed frame around a single particle showing a gaussian profiled peak. Note that the vertical axes of both (a) and (b) have been inverted to aid visualization such that minima appear as peaks. . . . . 72

2.12 Original experimental frame with the superposed field of particle positions (shown in red) for a mixture with  $C = 0.921$ . . . . . 74

3.1 Typical segregation patterns of two binary granular mixtures: (a) poppy seeds (grey regions) + phosphor-bronze spheres (yellow regions); (b) polystyrene spheres (white regions) + *100's and 1000's* sugar particles (coloured regions). The frames were captured after 15min of vibration of an initially homogeneous mixture,  $C = 1.028$ ,  $\Gamma = 2$ . . . . . 76

3.2 Temporal evolution of segregation patterns of a mixture of poppy seeds and phosphor-bronze spheres ( $C(N_1 = 1596) = 1.028$ ): (a) Initial homogeneous mixture (b)  $t = 6sec$  (c)  $t = 12sec$  (d)  $t = 54sec$  (e)  $t = 594sec$  (f)  $t = 1182sec$ . The white dashed line,  $AB$ , in (a) is the sampling line used in the construction of the space-time diagrams discussed in Section 3.2. The double arrows indicate the direction of the forcing. . . . . 77

3.3 Space-time diagram for the evolution of the patterns which was constructed over a period of  $20min$ , by stacking, in time, the sampling mid cut line  $AB$  of the granular layer (dashed white line in Fig. 3.2a). Regions of poppy seeds are shown in black and regions of phosphor-bronze spheres in white. . . . . 79

3.4 Definition of the average domains width. a) Typical image processed frame with two superposed sampling lines (in red):  $h(x)$  along x-direction ( $y_h = 150pixels$ ). b) Spatial profile for the sampling line  $h(x)$ . The width of each top-hat steps,  $i$ , along  $h(x)$  is  $L_i^x$ . . . . . 81

3.5 Typical time series of pattern evolution at  $C(N_1 = 1596) = 1.028$ . (a) Time series over 20min of average domains width  $\phi$  ( $\bullet$ ), and average number of domains,  $\eta$  ( $\blacksquare$ ), having started from a homogeneous mixture. Frames showing long time evolution of domains in the coarsening regime: (b) pattern with 6 stripes ( $t = 500sec$ ) and (c) pattern with 5 stripes ( $t = 1200sec$ ). . . . . 82

3.6 Schematic diagram for the construction of the Probability Distribution Image (PDI). In the obtained PDI, with  $N = 2$ , black regions have  $PDI(x_i, y_j) = 0$ , white regions have  $PDI(x_i, y_j) = 1$  and grey regions have  $PDI(x_i, y_j) = 0.5$ . . . . . 84

3.7 Probability Distribution Image. a) PDI for 50 realisation of identical experimental runs with  $C(N_1 = 1596) = 1.135$ . b) PDI averaged along the y-direction. . . . . 85

4.1 Series of space-time diagrams as a function of the layer compacity which were constructed as explained in Section 3.2. Each of them is a stack in time, over 10min, of the mid-cut line of the granular layer (white dashed line in Fig. 3.2). At low compacities a mixed state is observed and no segregation occurs. At high compacities segregated structures form within the first minute of forcing. All runs were started from homogeneously mixed initial conditions. . . 89

4.2 Time-series of average domain width,  $\phi$ , for four different compacities: (■)  $C = 0.900$ , (□)  $C = 0.751$ , (●)  $C = 0.729$ , (○)  $C = 0.623$ . Lines are exponential fits to Eqn. (4.1). All runs were started from a homogeneously mixed layer. . . . . 91

4.3 Segregation phase transition. (a) Compacity dependence of average domain width saturation level,  $\Sigma^\phi$ . The solid red line is a square-root given by Eqn. (4.4). (b) Compacity dependence of  $l^\phi(C) = (\Sigma^\phi - \Lambda^\phi)^2$ . The critical point  $C_c^\phi$  is determined from the intercept between the horizontal dashed line and the solid line which is the best least squares fit to  $l^\phi(C) = -(A^\phi)^2 C_c^\phi + (A^\phi)^2 C$  with  $A^\phi = 8.16 \pm 0.29$  and  $C_c^\phi = 0.644 \pm 0.065$ . . . . . 93

4.4 Time-series of average number of domains,  $\eta$ , for four different compacities: (■)  $C = 0.900$ , (□)  $C = 0.751$ , (●)  $C = 0.729$ , (○)  $C = 0.623$ . Lines are exponential fits to Eqn. (4.5). All runs were started from a homogeneously mixed layer. . . . . 95

4.5 Segregation phase transition. (a) Compacity dependence of the saturation level of the average number of domains,  $\Sigma^\eta$ . The solid red line is the square-root given  $\Sigma_\eta^{fit} = A^\eta \sqrt{C - C_c^\eta} + \Lambda^\eta$  obtained from the least square fits of  $l^\eta(C) = -(A^\eta)^2 C_c^\eta + (A^\eta)^2 C$ , within the range  $0.687 < C < 0.921$ . (b) Compacity dependence of  $l^\eta(C) = (\Sigma^\eta - \Lambda^\eta)^2$ . The critical point  $C_c^\eta$  is determined from the intercept between the horizontal dashed line and the solid line which is the best least squares fit to Eqn. (4.7) with  $A^\eta = 18.98 \pm 0.68$  and  $C_c^\eta = 0.687 \pm 0.087$ . . . . . 96

4.6 (a) Segregation time,  $t_s^\phi$ , for the average domain width, obtained from the fits of the initial segregation growth to Eqn. (4.1). (b) Zoom of  $t_s^\phi$  around  $C = 0.9$ . The vertical dashed line, at  $C_m = 0.921$ , represents the location at which the minimum of  $t_s^\phi$  occurs ( $t_s^\phi(C_m) = 9.53sec$ ). (c) Segregation time,  $t_s^\eta$ , for the average number of domains, obtained from the fits of the initial segregation growth to Eqn. (4.5). (d) Zoom of  $t_s^\eta$  around  $C = 0.9$ . The vertical dashed line, at  $C_m = 0.921$ , represents the location at which the minimum of  $t_s^\eta$  occurs ( $t_s^\eta(C_m) = 11.41sec$ ). . . . . 97

4.7 a) Time-series of,  $\phi(t)$ : ( $\nabla$ ) for  $C = 1.028$  ( $\square$ ) for  $C = 0.751$  and ( $\circ$ ) for  $C = 0.580$ . The solid red curves are the digital low-passed experimental signals,  $\phi_{filtered}(t)$ , for the respective compacity values. (b) Time series of the macroscopic fluctuations,  $f(t) = \phi(t) - \phi_{filtered}(t)$  for  $C = 0.751$ . . . . . 99

4.8 Root-mean-square of the fluctuations,  $R$ , plotted as a function of  $C$ . The solid vertical line corresponds to the location of the critical point,  $C_c = 0.665$ , discussed in Section 4.5. The dashed vertical line at  $C_m = 0.921$  corresponds to the location at which the minimum in the segregation time,  $t_s$ , is observed. The solid grey line is a guide to the eye. . . . . 100

4.9 Zoomed photographs of the granular layer in each of the segregation phases. (a) Binary gas at  $C = 0.516$  ( $t = 600sec$ ). (b) Segregation liquid at  $C = 0.772$  ( $t = 660sec$ ). (c) Segregation crystal at  $C = 1.071$  ( $t = 624sec$ ). . . . . 101

- 5.1 Experimental frames of the evolution of segregation domains in a granular mixture of poppy seeds and phosphor-bronze spheres with  $C=0.996$ : (a)  $t = 0sec$  – vibration of the granular layer was initiated from a homogeneous mixture, (b)  $t = 4.36sec$ , (c)  $t = 9.36sec$ , (d)  $t = 16.28sec$ , (e)  $t = 23.2sec$ , (f)  $t = 40.68sec$ . . . . . 106
- 5.2 Definition of the local Voronoi area density of particle positioned at  $\mathbf{C}_1$  (shown in green) with six neighbours (shown in grey with indices  $i = 2 \rightarrow 7$ ). The polygon in red is the Voronoi cell associated with the particle in green and is enclosed by the vertices  $\mathbf{V}_{ij}$ . The boundaries of the Voronoi cell are the segments of the lines  $h_i$ . Each of the points  $\mathbf{H}_{1i}$  is the mid point between  $\mathbf{C}_1$  and the respective particle  $i$ . . . . . 107
- 5.3 Voronoi diagrams obtained from the positions of the phosphor-bronze spheres, for binary mixtures with various values for the compacity: (a)  $C = 0.495$ , (b)  $C = 0.687$ , (c)  $C = 0.793$  and (d)  $C = 1.007$ . The frames correspond to configurations obtained 40sec after vibrating an initially homogeneous mixture. . . . . 109
- 5.4 Temporal evolution of  $PDF(\overline{\rho_v}, t_n)$  for a mixture with  $C = 1.049$ . (yellow)  $t = 6.02sec$ , (blue)  $t = 14.02sec$ , (red)  $t = 22.02sec$ , (green)  $t = 30.02sec$ , (magenta)  $t = 38.02sec$ , (cyan)  $t = 158.02sec$ . The time window used to obtain temporal averages was  $\Delta\tau = 4sec$ . 110
- 5.5 Initial evolution of mean local Voronoi area density, having started from initially homogeneous mixtures: ( $\blacklozenge$ )  $C = 0.495$ , ( $\bullet$ )  $C = 0.729$ , ( $\blacksquare$ )  $C = 1.135$ . . . . . 111

5.6 (a) Segregation rate,  $b(C)$  (b) segregation timescale,  $t_D = 1/b(C)$  of the phosphor-bronze spheres as a function of the layer compacity. The solid vertical line, in both plots, is positioned at the critical point for segregation,  $C_c$  obtained in Chapter 4. The vertical dashed line is the segregation liquid to segregation crystal transition point,  $C_m$ , obtained in Chapter 4. . . . . 113

5.7 Time dependence of mean local Voronoi area density for ( $177 < t < 233$ )*sec*: ( $\blacklozenge$ )  $C = 0.495$ , ( $\bullet$ )  $C = 0.729$ , ( $\blacksquare$ )  $C = 1.135$ . . . . 114

5.8 Probability distribution functions for the local Voronoi area density of the phosphor-bronze spheres,  $PDF(\rho_v)$ , for a series of compacities. The value for the respective compacity is located above each plot. . . . . 116

5.9 Measures extracted from the  $PDF(\rho_v)$  distributions. (a) Typical experimental  $PDF(\rho_v)$  in the binary gas phase, for  $C = 0.537$ , from which the characteristic Voronoi area density,  $\rho_v^{max}$ , and the width of the distribution at  $3/4$  max,  $w_\rho$  are extracted. (b) Dependence of  $\rho_v^{max}$  (left axis) and  $w_\rho$  (right axis) on the layer compacity. The blue and red curves are drawn to guide the eye. The solid vertical line is the critical point for segregation,  $C_c$ , which was obtained in Chapter 4. The vertical dashed line is the segregation liquid to segregation crystal transition point,  $C_m$ , obtained in Chapter 4. . . . . 117

5.10 Particle tracking of the local Voronoi area density for a single sphere: trace I (blue curve) for  $C = 0.580$ , trace II (green curve) for  $C = 0.687$ , trace III (red curve) for  $C = 1.071$ . Note that trace II corresponds to a sphere in a binary mixture with a compacity value near the critical point for segregation,  $C_c$ . . . . . 119

5.11 Schematic diagram for the definition of angles between nearest neighbours,  $\delta$ .  $\mathbf{A}$ ,  $\mathbf{B}$  and  $\mathbf{C}_i$  are the positional coordinates of three neighbouring particles. The angle defined by the three particles, about  $\mathbf{C}_i$ , is  $\delta_i = \alpha_i + \beta_i$ . The solid lines are a section of the Voronoi polygon, belonging to the particle  $\mathbf{C}_i$ , which is defined by the vertices  $\mathbf{V}_1$ ,  $\mathbf{V}_2$  and  $\mathbf{V}_3$ . . . . . 120

5.12 Typical probability distribution functions for the angle between nearest neighbours,  $PDF(\delta)$ : for  $(\bullet)$   $C = 0.516$ ,  $(\blacklozenge)$   $C = 0.687$ ,  $(\blacktriangle)$   $C = 0.815$ ,  $(\blacksquare)$   $C = 1.028$ . . . . . 121

5.13 (a) Position of the peak of the  $PDF(\delta)$  distribution,  $\delta_{max}$ , as a function of layer compacity. The solid and dashed vertical lines are the critical point for segregation,  $C_c$  and segregation liquid to segregation crystal transition point,  $C_m$ , respectively, which were obtained in Chapter 4. . . . . 122

5.14 (a) Radial distribution functions,  $g(r)$ , for spheres' configurations at three compacity values:  $(\blacktriangle)$  binary gas for  $C = 0.495$ ,  $(\blacksquare)$  segregation liquid for  $C = 0.729$  and  $(\bullet)$  segregation crystal for  $C = 1.135$ . Corresponding experimental frames for (b)  $C = 0.495$ , (c)  $C = 0.729$  and (d)  $C = 1.135$ . The insets are schematics of the typical sphere's configurations that gives rise to the characteristic peaks in the  $g(r)$  curves. . . . . 124

5.15 Surface plot for  $g(r)$  as a function of compacity. The value of the  $g(r)$  at the point with a particular compacity and inter-particle diameter is given by the colour level in the adjacent colour bar. . . . . 125

- 6.1 Experimental frames for the granular mixture of poppy seeds and phosphor-bronze spheres for various values of  $\Gamma$ . The images correspond to the layer configuration,  $2min$  after vibrating an initially homogeneous mixture. (a)  $\Gamma = 0.222$  (b)  $\Gamma = 0.667$  (c)  $\Gamma = 1.556$  (d)  $\Gamma = 2.571$  (e)  $\Gamma = 4.500$  (f)  $\Gamma = 9.000$ . The vertical boundaries are observable in (a) and (e). The horizontal boundaries are observable in (e) and (f). . . . . 129
- 6.2 Characteristic local Voronoi area density,  $\rho_v^{max}$ , as a function of aspect ratio  $\Gamma$ . The mean value is  $\langle \rho_v^{max} \rangle_\Gamma = 0.696 \pm 0.040$ , represented by the horizontal solid line. The vertical dashed line is located at  $\Gamma = 2$ , corresponding to the value of the aspect ratio used for the detailed studies in Chapters 3 – 5. . . . . 130
- 6.3 Experimental frames representative of the three segregation phases, at various points in the compacity parameter space: binary gas (*left column*), segregation liquid (*centre column*) and segregation crystal (*right column*). The respective values of  $\varphi_{ps}$   $\varphi_{pb}$  are presented in the frames. . . . . 133
- 6.4 Characteristic Voronoi area density,  $\rho_v^{max}$ , for the granular mixture. The compacity values correspond to data sets with (a)  $\varphi_{pb} = 0.054$ , (b)  $\varphi_{pb} = 0.083$ , (c)  $\varphi_{pb} = 0.118$  and (d)  $\varphi_{pb} = 0.174$ . . . . . 135
- 6.5 Characteristic angle between nearest neighbours,  $\delta^{max}$ , for the granular mixture. The compacity values correspond to data sets with (a)  $\varphi_{pb} = 0.054$ , (b)  $\varphi_{pb} = 0.083$ , (c)  $\varphi_{pb} = 0.118$  and (d)  $\varphi_{pb} = 0.174$ . . . . . 136

6.6 Phase diagram for the  $(\varphi_{pb}, \varphi_{ps})$  parameter space for the mixture of spheres and poppy seeds. (o) binary gas. ( $\square$ ) segregation liquid. (+) segregation crystal. The dashed lines,  $L1$  and  $L3$  are the experimental phase boundaries. The solid lines  $L2$  and  $L4$  are given by Eqns. (6.1) and (6.2), respectively, with  $C_c = 0.665$  and  $C_m = 0.921$ . No data was acquired in the top right hand region since, there, the mixture was not longer in a monolayer regime. . . . . 138

6.7 Experimental frames of the binary mixture at various values of  $f$  and  $A$ . (a) Binary gas for  $(f, A) = (28Hz, \pm 1.18mm)$ . (b) Segregation liquid for  $(f, A) = (16Hz, \pm 1.50mm)$ . (c) Segregation crystal for  $(f, A) = (12Hz, \pm 0.58mm)$ .  $\Gamma = 2$  ( $\Delta y = 180mm$ ) and  $C = 0.900$  with  $N_{pb} = 1596$ . . . . . 140

6.8 Phase diagram for  $(f, A)$  parameter space showing regions of existence for the three phases. (o) Binary gas. ( $\square$ ) Segregation liquid. (+) Segregation crystal. The points  $A$ ,  $B$  and  $C$ , along the parameter ray  $r$ , correspond to the experimental frames shown in Fig. 6.7 (a), (b) and (c), respectively. The phase boundary between the segregation liquid and the binary gas phases is represented by the solid black curve and is given by Eqn. (6.4) with  $\gamma_c = 2.95$ . . . . . 142

6.9 Probability distribution functions for the local Voronoi area density of the phosphor-bronze spheres for various forcing conditions. ( $\blacktriangle$ )  $(f, A) = (8Hz, \pm 1.50mm)$ , ( $\bullet$ )  $(f, A) = (16Hz, \pm 1.50mm)$ , ( $\blacksquare$ )  $(f, A) = (16Hz, \pm 3.35mm)$ . . . . . 143

- 6.10 Transition diagram between a segregated phase and a mixed state, quantified by the characteristic local Voronoi area density of individual spheres, as the non-dimensional maximum acceleration,  $\gamma$ , is varied. The dashed lines are the best least squares fits in the two regimes. The point with lowest  $\gamma$  correspond to a layer for which the forcing was insufficient to agitate the granular mixture. . . . . 144
- A.1 (a) Schematic diagram for the calculation of the radial distribution function,  $g(r)$ . The  $i^{th}$  particle is shown in red and particles are counted within a shell of radius  $r$  and thickness  $dr$ . (b) Nearest neighbour configurations for an hexagonally packed lattice of disks in two dimensions. The  $i^{th}$  particle is shown in red. Neighbours in the 1st shell ( $r = d$ ) are shown in green, in the 2nd shell in blue ( $r = \sqrt{3}d$ ), in the 3rd shell in yellow ( $r = 2d$ ), in the 4th shell in cyan ( $r = \sqrt{7}d$ ) and in the 5th shell in magenta ( $r = 3d$ ). . . . . 156
- B.1 Experimental frames of an example of the coarsening regime patterns for a mixture of phosphor-bronze spheres (bright regions) and poppy seeds (grey regions) acquired at (a)  $t = 218sec$ , (b)  $t = 576sec$ , (c)  $t = 730sec$ , (d)  $t = 1203sec$ , (e)  $t = 1357sec$  and (f)  $t = 1536sec$  after vibration of an homogeneously mixed layer. The experimental parameters were  $\Gamma = 2$ ,  $(f, A) = (12Hz, \pm 1.74mm)$  and  $C = 1.114$ . The white arrows near  $S4$  and  $S5$  represent the motion of the poppy seeds in the regions near the tips of the respective stripes of phosphor-bronze spheres. . . . . 160
- B.2 Schematic diagram of the geometry of the boundaries used in the streaming motion experiments. The aluminium frame is shown in black. The layer of poppy seeds is shown in grey. The whole tray was oscillated sinusoidally along the direction shown by the arrows. 162

B.3	Granular streaming motion. (a) Typical original frame. (b) image processed frame enhancing the visualization of the brightest poppy seeds. (c) Superposition of 50 frames, with a time step of $0.6sec$ , using the <code>Iflighter</code> condition described in the text. . . . .	164
B.4	Steady streaming for a oscillatory sphere emersed in a Stokes flow. Photograph reprinted from “ <i>An album of fluid motion</i> ” by (van Dyke, M. 1982). . . . .	166
B.5	Photographs of the granular layer showing the oscillatory bending of the phosphor-bronze stripes (regions in white), at different times: (a) beginning of cycle, (b) half-cycle, (c) end of cycle. The sample line $L$ located at $1/3$ of the width of the tray was used to construct the space time diagram in Fig. B.6. The yellow arrows indicate the direction of the vortex motion in the regions of poppy seeds. . . . .	169
B.6	(a) Space time diagram constructed from stacks of the cut line, $L$ in Fig. B.5(c), over $5000sec$ . The stripes are labelled on the right hand side of the diagram. (b) Time series of $x_{S3}(t)$ for the centre position of the location of $S3$ , along $L$ . . . . .	170
B.7	Experimental frames after being cropped around $S3$ and image processed following the method introduced in Section 2.8.1. Black for regions of poppy seeds and white for regions of phosphor-bronze spheres. (a) At beginning of cycle ( $t = t_1sec$ ). (b) At quarter-cycle ( $t = (t_1 + 72)sec$ ). (c) At half-cycle ( $t = (t_1 + 143)sec$ ). The centre line of the $S3$ stripe, $x_l(y, t)$ , has been superposed on each frame as a solid blue line. . . . .	171

B.8 Three dimensional spatio-temporal diagram for the centre line of the  $S3$  stripe,  $x_l(y, t)$ . The value of  $x_l(y, t)$  is given by the colour in the adjacent colour bar. . . . . 172

# List of Tables

2.1	Material properties for the particles used. . . . .	61
2.2	Imaging systems used for each of the classes of experiments. . . . .	68
6.1	Values of $\Gamma$ used in the aspect ratio parametric study. $\Delta x$ and $\Delta y$ are the dimensions of the tray in the directions along and orthogonal to the forcing, respectively. . . . .	128

# Abstract

We present results from an experimental investigation of segregation in a binary monolayer of phosphor-bronze spheres and poppy seeds. The particles are driven by the frictional interactions with the surface of a horizontal tray which is forced sinusoidally. Three distinct phases are observed which we classify as *binary gas*, *segregation liquid* and *segregation crystal*. A series of macroscopic and microscopic measures is developed to characterise the phase behaviour of the mixture and analyse its structural configurations. We present evidence for the existence of a continuous phase transition at a critical value of the total filling fraction of the mixture,  $C_c = 0.67 \pm 0.06$ . Below  $C_c$  the layer remains mixed and for  $C > C_c$  segregation domains form. The segregation transition has the typical characteristics of square-root growth of a macroscopic order parameter, critical slowing down and amplification of the microscopic fluctuations. Exploration of the forcing parameter space has also helped uncover a parameter range where segregation is suppressed. The critical value for the dimensionless acceleration of the tray is measured to be  $\gamma_c = 2.95 \pm 0.16$ , above which segregation is not observed. We compare our results to an event driven numerical simulation of a 2D phenomenological model of our experimental system and suggest that the segregation is caused by a competition between the differential driving of the two particle species, which induces separation, and random motion, which acts to prevent it.

# Declaration

No portion of the work referred to in this thesis has been submitted in support of an application for another degree or qualification of this or any other university or other institution of learning.

# Copyright

Copyright in text of this thesis rests with the Author. Copies (by any process) either in full, or of extracts, may be made **only** in accordance with instructions given by the Author and lodged in the John Rylands University Library of Manchester. Details may be obtained from the Librarian. This page must form part of any such copies made. Further copies (by any process) of copies made in accordance with such instructions may not be made without the permission (in writing) of the Author.

The ownership of any intellectual property rights which may be described in this thesis is vested in the University of Manchester, subject to any prior agreement to the contrary, and may not be made available for use by third parties without the written permission of the University, which will prescribe the terms and conditions of any such agreement.

Further information on the conditions under which disclosures and exploitation may take place is available from the Head of the Department of Physics and Astronomy.

# The Author

Pedro Miguel Reis was born in Viseu, Portugal in 1978 and attended Alves Martins Secondary School in Viseu. He studied for his undergraduate degree at the University of Manchester, where he was awarded a First Class B.Sc.(Hons) in Physics. He then joined St. John's College, University of Cambridge, where he was awarded the Certificate for Advanced Studies in Mathematics from the Department of Applied Mathematics and Theoretical Physics.

# Acknowledgments

My first word of gratitude goes to my supervisor Professor Tom Mullin for showing me, with an always encouraging, inspiring and supporting guidance, through the fascinating new world of nonlinear dynamics and complex systems. Cheers Tom, you're the best supervisor that any student could ever ask for.

The work presented in this thesis would not have been possible without the highest standards of the technical support staff in the Physics Department. I am deeply indebted to John Rowcroft and Andy Smith (drawing office), Jim Allen and Mike Needham (electronics workshop), John O'Hara, Mark Sellers, Graham Tudor, Steve May, Stan Gillott and Paul Tipler (mechanical workshop) and Sheila Downes.

I have been extremely fortunate to have been surrounded by a very active and enthusiastic bunch of people at the Manchester Centre for Nonlinear Dynamics who greatly helped keeping some sanity in the everyday work in the lab. The collaboration and long discussions with George Ehrhardt and Andrew Stephenson, who performed the numerical simulations presented in Appendix C, were essential for the development of many of the ideas and results in this Thesis. George has also helped me in the calculations of  $g(r)$  presented in Section 5.4. I would also like to thank Mark Shattuck for hosting me at the Levich Institute, City College of New York, during the last eight months of my Ph.D.

All the people I have met throughout the years in Manchester ensured that I had a truly unique experience. In particular, I would like to stress the great

friendship with some of the best people on this planet: David Buttler for his always most refreshing non-sense, Selin Hekimoglu for all her support and good chats as well as for help printing this thesis, Daniel Hanlon for the caravan weekends, Nathalie Cachet-Gaujard for cheese, wine and good food, Luke Taylor and Simon de Villiers for the many sometimes no-so-sane-adventures we have had together in the mountains, Andrea Mina for great company to the art's world and to everyone with whom I was ever able to share a laugh.

I would like to finish with a very special word of affection to Ines for her Basque sense of humor, enthusiasm and joy of life without whom my days could not be the same and to my family to whom I own everything.

PARA OS MEUS PAIS.

# Chapter 1

## Introduction

### 1.1 Granular media: motivation

Aggregates of grains, i.e. ensembles of macroscopic discrete particles, are ubiquitous in our every day life, nature and of crucial importance in industrial processes (Jaeger & Nagel 1992, Jaeger, Nagel & Behringer 1996). The physical laws governing granular media apply to objects whose dimensions cover several orders of magnitude. They range from particles a few hundred microns such as the powders used in the pharmaceutical industry, to ice floes drifting across the polar sea. Other examples include rice, seeds, sugar and sand, amongst many others.

Understanding the governing laws of granular materials is of huge technological and industrial importance. A wide variety of substances used in industry are routinely handled in the form of granules (Bridgewater 1995), for example cement, pills and cereals. The most common method of moving industrial granular materials is gravity feed. Grain elevators, silos, hopper cars, and coal chutes, all rely on the force of gravity to move materials. A related variant is the rotating drum, which is used to crush, mix, segregate and agglomerate material. Finally, vibrational forcing is used to convey, mix, segregate and pack materials. Understanding the static, dynamic and flow properties of these materials is crucial

for their, storage and processing. It is interesting to note that the total yearly production of granular aggregates is enormous, reaching approximately ten million metric tons and consuming roughly 10% of all the energy produced in the planet (Duran 2000). Hence, any advance in understanding the physics of such materials is bound to have a major economic impact.

Granular processes consisting of large-scale flows of particulate solids are also widespread in geology (Iverson 1997). These are central to the fluidisation of soil by the shaking of violent earthquakes, debris flows and landslides, rock and snow avalanches in mountain slopes, pyroclastic flows and motion of sand dunes. All of these can provoke immense damage and there is a need not only to understand the underlying triggering mechanisms but also to be able to predict the actual size and evolution of such events.

The study of granular materials has a long tradition amongst engineers and geologists who have tended to approach problems in an *ad hoc* way with practical experience playing a greater role than understanding. Over the last decade, significant interest has arisen in the physics community and modern ideas from nonequilibrium statistical mechanics and pattern formation are being used with some success in the description of some aspects of granular phenomena. Nevertheless, a firm mathematical formulation of granular media remains aloof and may well require new theoretical ideas beyond those of standard statistical mechanics, hydrodynamics or traditional solid mechanics (Jaeger & Nagel 1996, Kadanoff 1999). Also, recent developments of well controlled precision experiments have yielded a variety of new and intriguing phenomena and motivated a wealth of further research.

## 1.2 Definition of dry granular materials

The constituent particles of a granular media directly interact with each other and with any boundaries via dissipative contacts and collisional forces. After each collision, a fraction of the particle's energy is dissipated and the coefficient of restitution,  $\varepsilon$  is usually introduced to describe the collisions,

$$\varepsilon = \frac{u_{Af} - u_{Bf}}{u_{Bi} - u_{Ai}}, \quad (1.1)$$

where  $u_{ji}$  and  $u_{jf}$  are the initial and final normal velocity components for the  $j$ th particle, respectively. A collision is elastic if  $\varepsilon = 1$  and totally inelastic if  $\varepsilon = 0$ , i.e. the two particles involved stick together. Energy can also be lost by rubbing, characterized by a coefficient of friction,  $\mu$ . The dissipation of energy through inelasticity and friction raises the temperature of the atoms that constitute the grains but the associated thermal energy is approximately 18 orders of magnitude smaller than the potential energy needed to lift one typical grain over another, in a gravitational field. Therefore, Brownian motion is irrelevant in the collective behaviour and grains remain locked in place once they come to rest. Hence, this dissipation of energy in inter-particle contacts and collisions requires that energy be continuously input into the system to induce or maintain motion.

When the cohesion forces between grains are unimportant the granular media is said to be *dry*. A requirement for this is that the grains are large enough (typically  $\gtrsim 250\mu\text{m}$ ) and that the viscosity of the surrounding fluid is small. Under this constraint, capillary forces, van der Waals forces or viscous interactions can be neglected and, as discussed above, the mechanical properties of the material are controlled only by the momentum transfer during collisions or frictional contacts between grains. In contrast, aggregates of particles of size within  $1\mu\text{m}$  and  $100\mu\text{m}$  are known as *powders* for which cohesive effects can no longer be neglected. For most of this Thesis, we focus our attention on the case of *dry granular materials*.

## 1.3 Early developments

Scientific investigations of granular materials date back to Coulomb (1773) who studied inter-particle friction and its effect on granular piles. The first published studies on shaken granular media are due to Chladni (1787) who observed that sand sprinkled on the surface of a horizontal vibrating plate migrated to displacement nodes inducing a wide range of patterns on the layer's surface. Faraday (1831) showed that these patterns were due to induced motions of the air surrounding the vibrating plate.

In 1885, Reynolds noted that a deformation of an ensemble of particles, for example through shearing, can induce an increase in volume of the packing. This is associated with rearrangements of individual particles which, due to their rigidity, must ride over others for motion to be possible. He denoted this concept by *dilatancy* and used it to explain a variety of phenomena (Reynolds 1885). For example, while walking over wet sand near the water line in a beach one can notice that the sand surrounding a footprint appears to be drier. Reynolds suggested that, due to the imposed deformation, the sand dilates and the water level decreases below the sand's surface, which therefore appears drier.

Static configurations of granular media were first studied by Janssen (1895) who investigated the dependence of the pressure,  $P$ , at the bottom of a container of granular material on the filling level. For a container full of water,  $P$  is proportional to the height of the filling level. If sand is used instead,  $P$  increases with height but eventually saturates above a critical value of the filling height. In addressing the question of the mechanism behind this reduced mass, Janssen realised that the weight of the granular ensemble is partially redirected towards the container's walls thereby supporting the material through frictional contacts.

## 1.4 Modern investigations

The legacy of the early work by Coulomb, Faraday, Reynolds and Janssen was then overlooked by the majority of physicists for most of the 20th century. Research into granular media became an important engineering topic, in particular solid mechanics (Terzaghi 1943). An exception worth noting was the publishing of “*The physics of blown sand and desert dunes*” by Bagnold (1954). He gave a detailed presentation of the behaviour of wind driven sand and put forward an explanation for the formation of small and large scale structures such as surface ripples and dunes, respectively. Renewed interest within the physics community on granular materials began in 1987 with the publication of a controversial paper by Bak, Tang & Wiesenfeld (1987) on *self-organised criticality* where a sand pile was used as the canonical model system. They argued that as the angle of the free surface of the pile was increased, the pile would maintain an average slope by generating avalanches characterised by a  $1/f$  power spectra. Despite this result having been refuted by a number of experiments (Jaeger, Liu & Nagel 1989), this contribution vigorously renewed interest in the behaviour of granular materials.

Since 1987, a large number of detailed experimental developments have revealed a plethora of fascinating phenomena which, along with challenging attempts to formulate appropriate theoretical descriptions, have conferred a active and dynamic sense to the study of granular media. An extensive discussion of recent investigations can be found in the review articles by Jaeger & Nagel (1992, 1996), Jaeger et al. (1996) and Shinbrot & Muzzio (2000, 2001).

Depending on the flow velocity, granular media can be classified into three regimes: rapid flows, dense flows and quasi-static packings. Each of these is discussed next.

### 1.4.1 Rapid granular flows

In rapid granular flows, the system is said to be in a gas-like state such that the constituent grains are highly agitated and sufficiently apart from each other. In this regime, some success has been achieved by applying ideas from kinetic theory of inelastic granular gases. Following the kinetic theory approach, the study of interactions in a large aggregate of particles can be carried out in a statistical mechanical sense to characterise its macroscopic dynamical behaviour. This work was led by Jenkins & Richman (1984) who built up on the classic work on non-uniform gases by Chapman & Cowling (1952). Within the kinetic theory framework, a granular system is regarded as an ensemble of smooth, hard inelastic spheres. The primary assumptions are that collisions between the particles provide the principal mechanism for the transport properties such as momentum and energy and that they occur instantaneously between pairs of spheres, i.e. the collisions are said to be *binary*. As in standard kinetic theory of gases, the motion of particle ensembles that are described by Newton's laws is modelled with Boltzmann equation from which a Navier-Stokes-like continuum set of equations can be derived (Jenkins & Savage 1983). In the case of granular materials, these continuum equations contain an additional term that describes the overall energy loss due to inelastic collisions. For example, Jenkins' theory has been successfully applied to experiments of vertically oscillated granular layers (Bizon, Shattuck & Swift 1999) and to the quantitative description of shocks in a supersonic granular flow past a fixed object (Rericha, Bizon, Shattuck & Swinney 2002). Realistic molecular dynamics simulations of both of these experiments yielded an agreement with kinetic theory to within 10% but typically of the order of 1%.

### 1.4.2 Quasi-static packings

In the quasi-static regime, of which a static sand pile is a canonical example, the inertia of the grains is negligible and each grain interacts with its neighbours through enduring contacts. Investigations of this regime have focused primarily on the study of stress distribution along force chains, as initiated by Janssen (1895). These were first directly observed by Dantu (1967) using an ensemble of birefringent cylinders, visualised through crossed polarisers. More recently Geng, Howell, Longhi, Behringer, Reydellet, Vanel, Clément & Luding (2001) have pursued this experimental approach and presented detailed investigations of the network of force chains and its fluctuations on a granular pile. Amongst many other intriguing aspects, a conical pile exhibits a pressure dip at its centre, as reported by Brockbank, Huntley & Ball (1997) who also noted that this dip could be suppressed, however, on increasing the particle diameter by a factor of 3. Another striking feature of this system is that the properties of granular piles exhibit a strong dependence on the mode of preparation. Depending on whether the pile is constructed by avalanching (*pouring* procedure) or by stacking sequential horizontal layers (*raining* procedure), the local pressure at the container's bottom surface can have a dip or a maxima at the centre of the pile, respectively (Vanel, Howell, Clark, Behringer & Clément 1999). A variety of theoretical approaches have been developed to describe the processes of stress transmission through the pile based on elasto-plastic models (Terzaghi 1943), cellular automata stochastic models (Liu, Nagel, Schecter, Coppersmith, Majumdar, Narayan & Witten 1995) and phenomenological hybrid models (Bouchaud, Cates & Claudin 1995) but a general consensus for the underlying physical mechanisms is still lacking.

Another scenario that has been receiving considerable attention is the case of granular material confined in a tube that is subjected to vertical tapping. This forces the ensemble to undergo consecutive rearrangements. The first experi-

ments of this system were undertaken by the Chicago group (Knight, Fandrich, Lau, Jaeger & Nagel 1995, Nowak, Knight, Ben-Naim, Jaeger & Nagel 1998). In their experiments, Knight et al. (1995) showed that an initially loose packed granular column which is gently tapped will undergo a progressive and very slow compaction. This evolution is well fitted by the inverse of the logarithm of the number of taps and, after more than 10000 taps, the hypothetical steady state is not reached. These results have stimulated numerous theoretical and numerical investigations with a focus on the notions of free volume and geometrical constraints (Barker & Mehta 1993, Krapivsky & Ben-Naim 1994, Barrat & Loreto 2000). In some of these studies an emphasis is placed on the possible connection between the experimentally observed compaction and the structural aging effects commonly observed in glassy systems (Bouchaud 2002).

### 1.4.3 Dense granular flows

In between of the two cases discussed above, there is a dense liquid-like regime in which grain's inertia is important but where a contact network still exists. In these dense granular flows the motion of the grains is constrained because of the high volume fractions involved; forces are transmitted through a percolating network of persisting contacts and the two basic assumptions of kinetic theory, i.e. instantaneous binary collisions and molecular chaos, fail. Despite numerous experimental, numerical and theoretical investigations (Pouliquen & Chevoir 2002, GDR 2004), no well established constitutive equations exist for these dense flows and our understanding of their dynamics and rheology is still incomplete. Different flow configurations have been studied including flow on inclined planes (Gray, Tai & Noelle 2003), annular shear cells (Miller, O'Hern & Behringer 1996), vertical chutes (Nedderman & Laohakul 1980), heaps (Liu, Jaeger & Nagel 1991) and rotating drums (Gray 2001).

An hydraulic-like theory has been proposed by Savage & Hutter (1989) and Gray (2001) for these types of flow. This continuum construction accurately reproduces many features observed in experiments; for example shock waves, dead zones and particle-free regions that form when a thin surface avalanche of granular material flows around a fixed obstacle (Tai, Gray, Hutter & Noelle 2001, Gray et al. 2003).

## 1.5 Particle segregation

An interesting and counter-intuitive feature of granular materials is segregation of binary assemblies, where an initially uniform mixture of particles can spontaneously de-mix into its constituent components under flow (Mullin 2002). Typically, the constituent particles are not identical and may differ in size, density, rigidity or surface properties. Such differences can often lead to separation (Williams 1976, Bridgewater 1993). Intriguingly, segregation does not always happen and the conditions for its occurrence are difficult to predict. A systematic account of the issues involved can be found in the extensive reviews by Shinbrot & Muzzio (2000), Ottino & Khakhar (2000) and Kudrolli (2004).

The phenomena has been recognised for a considerable period of time but, despite more than half a century of research, the underlying nature of the mechanisms involved are not yet well understood. Apart from posing numerous fundamental and difficult questions from a theoretical point of view, knowledge of segregation is needed for many applications. The segregation of particles with different properties is an ubiquitous process of major importance in areas such as agriculture, geophysics, material science, and almost all branches of engineering, i.e. involving preparation of food, drugs, detergents, cosmetics, and ceramics (Fan, Chen & Lai 1990). Processing and transport of mixtures can, thereby, lead to undesirable separation. For example, manufacturing of pharmaceutical

pills usually involves the mixing of a number of components and a mere 1% mal-blending of the constituent substances may have drastic consequences.

Segregation can be brought about by many processes including pouring, shaking, vibration, shear and fluidisation and is observed even in processes designed for particle mixing (Bridgewater 1976, Williams 1976). Since there is no unified framework for understanding segregation, the topic remains controversial in all of these environments. Developing predictive models is therefore essential if we are to understand segregation and thus avoid some of the problems that are important for modern industry.

Size segregation seems to contradict our intuitive knowledge from equilibrium statistical mechanics since the density of the overall packing decreases with the amount of segregation and entropy, in the mere sense of *disorder*, is reduced in the process (Shinbrot & Muzzio 2001). Segregation can occur whenever a mixture of particles of different sizes is disturbed in such a way that a rearrangement of the constituents is possible; i.e. the mixture is fluidised or dilated. Then, gaps between particles will occur, allowing small particles to traverse through, whereas for large particles the gaps are too narrow (Savage & Lun 1988).

The spatial distribution and dynamics of segregation of large and small particles appears to depend on a number of factors besides size difference including density ratio, friction between particles, shape of boundaries, particle velocity and pressure of the interstitial air. Since the parameter space of such a system is large and seemingly unimportant details turn out to have important effects in the segregation of mixtures, much work is still required.

Before we review in detail a variety of geometries commonly used for the study of granular segregation, we would like to highlight the work of Mullin (2000), which formed the basis of our investigation. Mullin observed the formation of striped patterns out of an initially mixed binary shallow layer of particles, under

unidirectional and sinusoidal excitation. The segregation domains formed in a direction which was perpendicular to the drive. Moreover, the width of the domains were found to coarsen with time following a  $t^{1/4}$  power-law and this scaling was independent of the mixture used. Mullin's description for the segregation process in his experiment, for a mixture of copper balls and poppy seeds, is as follows (Mullin 2000). The granular layer was initially prepared by stirring the mixture by hand until it appeared uniform. Upon vibration, the individual copper balls were moved by random impulses from the poppy seeds. The copper balls moved preferentially along the direction of forcing. Hence, when they met other balls they remained together since they were forced from the outside, as the poppy seeds were excluded from the interstitial space. The individual pairs of balls then met others and soon larger clusters formed at random locations. Within timescales of the order of hours, these would progressively merge to form increasingly robust stripes. The final state was found to be non-unique. Mullin suggested this novel segregation mechanism to be relevant to the geological phenomena of *stone striping* (Werner & Hallet 1993). In this, larger stones are observed to form stripes aligned downhill on mountainsides where there is soft soil which cyclically freezes and melts.

Segregation processes have been studied primarily in the following scenarios: vertically and horizontally vibrated beds, filling and emptying of vessels and rotating cylindrical drums. Below we discuss a number of examples of different geometries which have been used to study the driving mechanisms involved in granular segregation.

### 1.5.1 Vertical vibration

One way to achieve segregation is by vertical vibration, where one can observe the so called *Brazil-nut problem* (BNP) (Williams 1963). This phenomena can

be readily observed at the breakfast table where, by shaking a box of muesli one sees the largest pieces rise to the top of the smaller oats.

In classic binary mixtures of immiscible fluids (oil and water, for example) the lighter liquid is found on the top because of Archimedes' principle. The opposite can be observed in vibrated granular materials. In a typical experiment to study this phenomena, a schematic diagram of which is presented in Fig. 1.1, a large heavy particle – the *intruder* – is placed at the bottom of a granular bed of finer grains. When the granular column is subject to vertical vibration, the intruder will, in general rise to the surface, where it remains thereafter (Rosato, Stranburg, Prinz & Swendsen 1987, Jullien, Meakin & Pavlovitch 1992, Duran, Rajchenbach & Clément 1993, Dippel & Luding 1995). Intriguingly, an equally large particle that has a lower density than the bed of fine grains can also sink to the bottom when vibrated (Shinbrot & Muzzio 1998). This second version of the phenomena has been referred to as *reverse buoyancy*. An extension of the problem with a single large intruder is the case of segregation of an initially homogeneously mixture, when the volume fraction of the large and small particles are comparable (Hsiau & Yu 1997).

Despite its apparent simplicity, this phenomena has triggered many discussions in the literature over the past decade (Shinbrot 2004). There is still much controversy as to what particle properties are primarily important in this mode of segregation. An extensive discussion of the intricacies of segregation in vertically vibrated granular mixtures can be found in a recent review by Kudrolli (2004). We now outline some of this debate.

In the experiments of Knight, Jaeger, & Nagel (1993) and Cooke, Warr, Huntley & Ball (1996) the boundaries were found to have a significant impact on segregation. This is because global convective motion can be induced by the frictional interaction of the grains with the side walls. This in turn can force the large heavy

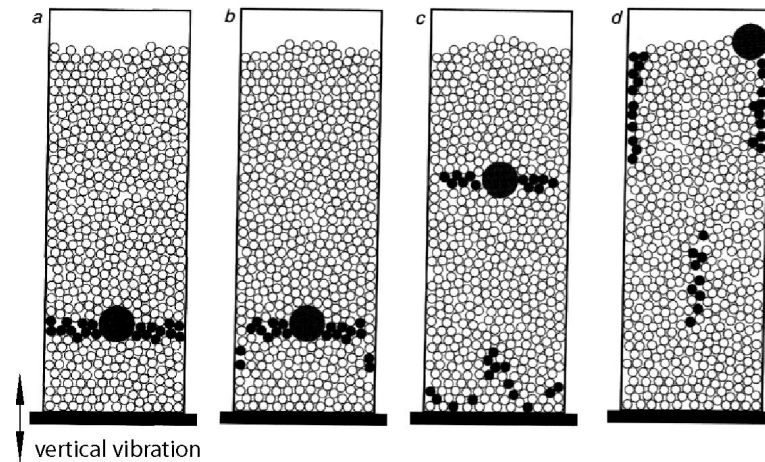


Figure 1.1: The Brazil-nut effect. A large heavy intruder is immersed in a medium of small particles. As the system is vertically vibrated the large particle raises to the surface. Vertical vibration of the container is initiated in (a). The 4 frames correspond to sequential stages until the intruder reaches the surface of the granular column. A layer of black small particles has been introduced in the pack to aid visualisation of the convection current that can be set up through the vibration. Diagram courtesy of S. R. Nagel (Knight, Jaeger & Nagel, 1993)

intruder to either move to the surface or the bottom, depending on the shape of the container. An example of a convection current inducing upwards motion of the intruder is shown in the schematic diagram of Fig. 1.1 where a layer of small particles has been coloured black to aid visualisation. Using numerical simulations and statistical physics arguments, Hong, Quinn & Luding (2001) noted that the large particle could sink to the bottom provided that it was sufficiently heavy denoting this the *Reverse Brazil-nut Problem* (RBNP). They presented a simple relation between the size and density ratios that predicts the crossover from BNP to the RBNP problem, based on a competition between the percolation effect and the condensation of hard spheres. This theory was further supported by

Jenkins & Yoon (2002) who established a similar criterion using kinetic theory for a uniformly heated granular gas under gravity. Even though the predicted borderline in the phase diagram between both effects appears to be confirmed by experiments (Breu, Ensner, Kruehle & Rehberg 2003), some of the assumptions in both of the above theories were found not to be satisfied. For example, spatial gradients in the temperature and density, which are thought to be important in realistic granular systems, have been ignored in both of the above theories.

Moreover, interstitial fluid including ambient air has been found to play an important role in determining the dynamics and spacial distributions of the final segregated state by Möbius, Lauderdale & S. R. Nagel (2001). They observed that the time required for a large particle to rise to the surface depends non-monotonically on both the background air pressure and the density difference between the two particle types. Related experiments were performed by Burtally, King & Swift (2002) who have vertically vibrated a mixture of fine bronze and glass spheres of similar diameters. They observed a variety of regimes depending on the amplitude and frequency of vibration. At low frequencies and moderate amplitudes a sharp separation forms between a lower region of glass and an upper region of heavier bronze. At high frequencies, the bronze separates to a mid-height layer, in a *sandwich* configuration, with a glass layer above and below it. A variety of other oscillatory regimes of periodic tilting were also found. Neither segregation was found below a certain value of the air pressure nor if the bottom plate of the container was made porous such that air could flow through it. Burtally et al. (2002) claim that the mechanism responsible for segregation in their system is based on the differential viscous drag experienced by the two types of particles

More recently, Huerta & Ruiz-Suárez (2004) has provided much insight into the problem by clarifying that there are actually two distinct regimes of segre-

gation. The first is found at higher frequencies of vibration ( $\sim 50Hz$ ), in which the bed becomes fluidized and ordinary buoyancy prevails (heavy intruders sink but light ones float). The other occurs at low frequencies ( $\sim 5Hz$ ), in which intruder inertia and bed convection compete to produce either the BNP or the RBNP, depending on the intruder size and density. If convection is suppressed, the rise of the large particle can be explained in terms of a geometric void-filling mechanism where the probability of a smaller particle filling a void is greater than a large particle (Jullien et al. 1992). It is interesting to note that the point at which the transition between these two regimes occurs ( $\sim 20Hz$ ) coincides with the frequency at which the surface first forms heaps driven by air flow suggesting that the transition between ordinary buoyancy and the RBNP is tied to air flow (Yan, Shi, Hou & Lu 2003).

### 1.5.2 Horizontal vibration

The behaviour of particle mixtures driven by horizontal vibration has been a particularly unexplored question (Betat, Dury, Rehberg, Ristow, Cherer, Scroter & Straßgurger 1998, Kudrolli 2004). A few studies of shaken deep layers have been performed in which complex convective motion, both on the surface and the bulk, was observed (Painter & Behringer 2000, Metcalf, Tennakoon, Kondic, Schaeffer & Behringer 2002). This can give rise to a RBNP (Liffman, Metcalfe & Cleary 1997), of the type mentioned above, by which large particles on a *sea* of small ones can sink to the bottom of a horizontally vibrated container.

The limiting case of a horizontally shaken monolayer of particles has also been addressed. A review of the results on granular patterned segregation observed by (Mullin 2000) when a binary monolayer is horizontally vibrated was presented at the beginning of Section 1.5. Aumaitre, Kruelle & Rehberg (2001) vibrated, in the two horizontal directions, a binary monolayer of different sized particles.

Under this *swirling* excitation, they observed the formation of clusters of the larger ones. By measuring the spacial velocity distribution of the particles they estimated the pressure of the system as a function of position and showed that the pressure between two nearby large disks was lower on average than the mean. Hence, the large particles get pushed together and cluster. Moreover, they have confirmed the results we present in this thesis as to the existence of a critical filling fraction of the mixture below which segregation is suppressed (Reis & Mullin 2002, Aumaitre, Kruelle & Rehberg 2003). In the experiments of Aumaitre *et. al.*, a monodisperse layer of spheres exhibited a *liquid-solid-like* phase transition at a slightly lower critical density than that for segregation. From this they claim that a structural phase transition in the *sea* of small particles is required as a precondition for segregation.

A particularly interesting theoretical and numerical study on granular segregation has recently been performed by Fierro, Nicodemi & Coniglio (2003). They have studied a binary mixture of hard-spheres, with different sizes, on a three-dimensional lattice using Monte Carlo simulations. The two types of spheres were disposed on a cubic lattice and initially prepared in a random loose stable pack. The configurations of the system are explored using tap dynamics, where each tap consists of raising the Monte Carlo bath temperature from zero to a value  $T_\Gamma$  (the tap amplitude) and, after a lapse time (the tap duration), quenching it back to zero. By cyclically repeating the process the system explores the space of inherent states (Coniglio & Nicodemi 2001). Under vertical vibration their simple model replicates both the BNP and RBNP. In the case of horizontal vibrations, Fierro *et. al.* observed the formation of segregation structures reminiscent of those found by Mullin (2000). By measuring the first moment of the structure factor for the large particles, they have found evidence for the existence of a critical point, as the *tapping* amplitude is varied, at a particular value of  $T_\Gamma^*$ .

### 1.5.3 Segregation in continuous surface flows

Another example of segregation occurs when binary mixture of particles of two different sizes is made to flow down an inclined chute and the larger particles are found to preferentially migrate to the surface shear layer of the flow. A typical example of this phenomena occurs in volcanology; pyroclastic flows usually contain particles with a wide range of sizes from blocks of rocks to ashes, i.e. from a few meters to a few microns. Due to this disparity in particle sizes, segregation patterns can be commonly observed in the slopes of volcanos (Cas & Wright 1987).

Savage & Lun (1988) have proposed a theory for this segregation process which is based on the interplay between two mechanisms which compete for the transfer of particles between layers in relative motion. The first, denoted by '*dynamic sieving*', is based on similar geometrical arguments used in the inertial regime of the BNP, discussed above. In this dense gravity driven flows, the probability of creation of a void in the medium decreases with increasing void size, i.e. large voids are less probable than smaller ones. Hence, the small particles have a tendency to fall through small voids towards lower layers. The second process is called '*squeeze expulsion*'; which is the result of an unbalance between the instantaneous forces acting on the grains, and so leads to transverse motion in either direction. The combination of these two mechanisms leads to a net percolation velocity of each species which induces an overall segregation of the mixture.

Savage & Lun also presented experimental results obtained using polystyrene particles of different sizes. This mixture exhibited segregation in agreement with the scenario they suggested, for both the concentration profile and the down stream distance required for complete separation of particles to be achieved.

A related problem to the case of segregation in chute flow is also found in

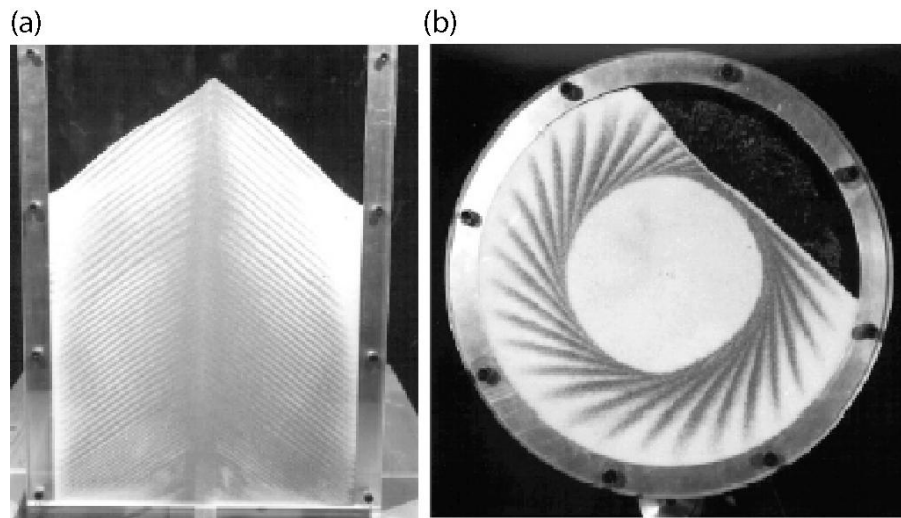


Figure 1.2: (a) Stratification patterns of binary mixture formed after pouring. (b) Radial segregation in a thin rotating drum. The large sugar particles are shown in white and the small iron spheres in grey. Photographs courtesy of N. Gray (Gray & Hutter, 1997).

the formation of a heap when a binary mixture of particles is poured onto a horizontal plate (Drahn & Bridgewater 1983, Gray & Hutter 1997). An example of a segregation pattern observed in this geometry is presented in Fig. 1.2(a). A spontaneous stratification appears, with alternating layers of small and large particles, parallel to the surface of the sand pile. Quantitative experimental results for this version of the phenomenon have been presented by Koeppe, Ens & Kakalios (1998) for the case of a quasi-two-dimensional Hele-Shaw cell and Julien, Lan & Raslan (1997) for three dimensional heaps. Makse, Cizeau & Stanley (1997) have suggested a possible mechanism for this mode of segregation based on the difference in the angles of repose for the two particle species.

### 1.5.4 Rotating drums

Another common geometry for the study of particulate de-mixing is radial segregation in a thin horizontal rotating drum (Donald & Roseman 1962). A typical segregation pattern of this configuration is shown in Fig. 1.2(b), after one period of rotation of a mixture of large sugar particles and small iron spheres. In most studies the drum is approximately half full and rotated about the cylinder axis at low rotational speeds. When the drum rotates the majority of the particles are in solid body rotation moving upwards with the wall and a thin fluidised layer is formed on the surface with downward flow in the form of an avalanche. Segregation is observed within a particular range of the angular velocity of the cylinder with intermittent avalanches and takes place on very short time scales in the shear flow along the surface. The small particles percolate between the larger ones in the flow, getting trapped by the solid body rotation, and a core of small particles at the center of the drum below the surface flow is formed (Clément, Rajchencach & Duran 1995). Recent attempts to develop theoretical models of the problem have suggested that the avalanche properties of the different types of particles has a major role on the segregation (Gray & Hutter 1997).

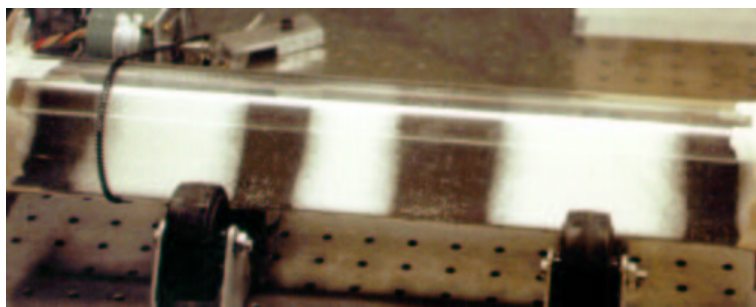


Figure 1.3: Axial segregation bands in a long rotating drum for a mixture of white salt and black sand. Photograph courtesy of S. Morris (Choo, Molteno & Morris, 1997).

On the other hand, axial segregation in long rotating drums happens on much longer time scales than the radial segregation for the thin drums discussed above. Experiments show that if the speed of rotation of the cylinder is large, an initially homogeneous binary mixture segregates into axial bands, whereas at lower speeds the same two materials may mix (Hill & Kakalios 1995). An example of such an axial segregation pattern is given in Fig. 1.3. Here the mechanism for different-sized particles is believed to originate from differences in angles of repose of the two materials which produce small differential axial flows. (Gupta, Bhatia & Khakar 1991, Hill & Kakalios 1994). The phenomena of axial segregation has been long known (Donald & Roseman 1962) but the origin of the bands (Nakagawa 1994) and the nature of its stability (Choo, Molteno & Morris 1997) are topics still actively debated.

## 1.6 Phase separation in colloidal systems

Size separation is not unique to granular materials. Binary colloidal suspensions with spheres of different sizes, of the order of a few microns, also exhibit phase separation (Pusey & van Megen 1986). In contrast to granular media, these are microscopic systems in equilibrium where agitation of the constituent particles is provided by Brownian motion. Hard-sphere models (Wood & Jacobsen 1957, Asakura & Oosawa 1958) have been used to explain the phase behaviour of colloidal mixtures. Despite the simplicity of these binary systems, they contain a wealth of counter-intuitive behaviour. For example, in the case of hard-sphere mixtures with two different sizes, where no attractive forces exist, an effective short-range potential between the larger particles can be induced by the presence of the smaller ones (Asakura & Oosawa 1958).

Consider a system of total volume  $V$  with spheres of two different sizes – Fig. 1.4(a). The free energy in a hard-sphere system of  $N$  particles is entirely entropic

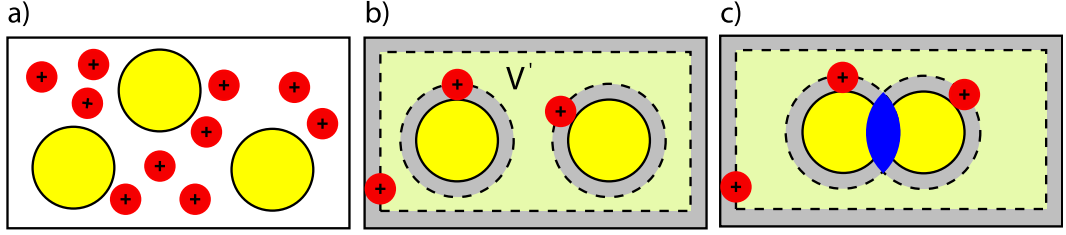


Figure 1.4: Schematic diagram for the excluded volume depletion process. (a) Binary hard-sphere system with large and small spheres (two dimensional representation). (b) Volume available to the small particles,  $V'$ . Region in grey correspond to excluded volume where the centres of the small particles cannot penetrate. (c) When two large particles come together, there is an increase in the free volume available. The region of excluded volume depletion is shown in blue.

and depends on the volume  $V'$  available to each particle,

$$F = -TS \sim -k_B T N \ln \left( \frac{V'}{V} \right), \quad (1.2)$$

where  $k_B$  is Boltzmann's constant and  $T$  is the system's temperature. Adding a small volume  $\Delta V'$  to a gas of  $N$  particles will reduce  $F$  by,

$$\Delta F \sim -k_B T N \frac{\Delta V'}{V}. \quad (1.3)$$

Now, consider a binary mixture of small and large spheres with radius  $r_s$  and  $r_l$ , respectively, with size ratio such that  $r_s/r_l \ll 1$ . Let us assume that there are considerably more small particles,  $s$ , than large particles,  $l$ . This way, the small particles will provide the dominant contribution to the free energy (and entropy) of the system. Because the hard-spheres are impenetrable,  $V'$  excludes a region with volume  $4/3\pi(r_l + r_s)^3$  around each large particle which is therefore referred to as *excluded volume* (yellow and grey regions in Fig. 1.4(b)). If two large spheres come together while exploring phase space, the excluded volume for each sphere can overlap in a region denoted by *depletion zone* (blue region

in Fig. 1.4(c). This overlap increases the volume accessible to the small spheres, thereby decreasing the free energy of the mixture – Eqn. (1.3) – and consequently increasing the entropy of the system (Barrat & Hansen 2003). Thus, entropically, it turns out to be favourable for the large particles to cluster together leading to phase separation.

This entropic argument is equivalent to the mechanistic view that if two particles are close enough so that no other particle may fit between them, they will be subjected to an asymmetric osmotic pressure that leads to a effective inter-particle attractive force. Sufficiently high densities of the small particles can thereby induce phase transitions in the ordering of the two particle species (Dijkstra, van Roij & Evans 1999).

Entropic excluded-volume effects of this type have been widely studied in bi-

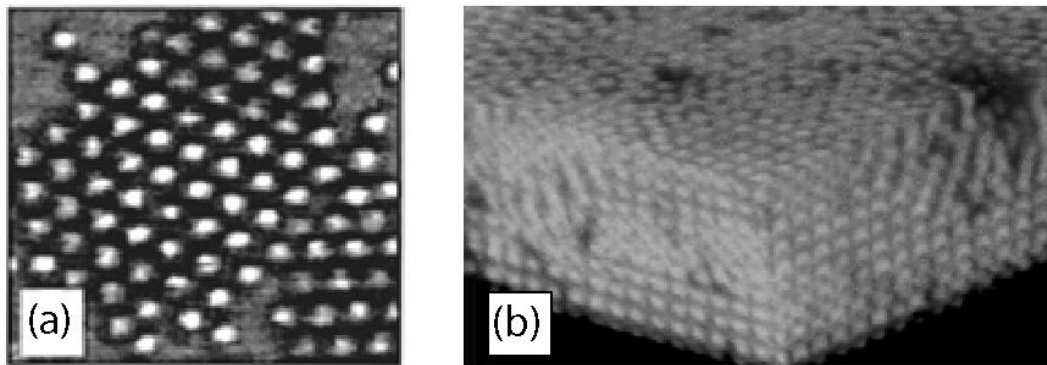


Figure 1.5: (a) Micrograph of a colloidal crystal configuration in two dimensions for a mixture of polystyrene spheres of diameter  $1.9\mu m$  and  $213nm$ . The filling fraction of the small spheres is  $\phi = 0.20$ . Only the large spheres are visible. (b) Confocal microscopic photograph of a three dimensional FCC colloidal crystal in a mixture of colloidal spheres ( $0.7 - 1.2\mu m$  diameter) and polystyrene polymer (radius of gyration  $\sim 12nm$ ). (a) courtesy of E. Hobbie (1998). (b) courtesy of A. G. Yodh (2001).

nary colloids (Dinsmore, Yodh & Pine 1995) and emulsions (Bibette, Roux & Nallet 1990). These ideas have found widespread application at length scales of  $10^{-8}$  to  $10^{-5}$ m in systems which are in or near thermodynamic equilibrium. Colloid-polymer mixtures have been particularly studied as an experimental realization of this scenario. In this case, the polymer coils are considered to be interpenetrable spheres of radius  $r_s$ , corresponding to the radius of gyration. The strength of the entropic attractive interaction can be tuned by changing the volume fraction, i.e. concentration, of the polymer in solution (Crocker, Matteo, Dinsmore & Yodh 1999). Provided that the polymer-to-colloid size ratio  $\xi$  is not too small (typically  $\xi \gtrsim 0.3$ ) this can induce phase separation (Poon 2002), reminiscent of the gas-liquid transition of simple molecular liquids. Moreover, liquid-solid phase separation has been widely reported (Anderson & Lekkerkerker 2002). Examples of experimental realizations of colloidal crystals obtained through this process are presented in Fig. 1.5(a) and (b), for crystals in two and three dimensional geometries, respectively. Note that the production of colloidal crystals results from self-organised assembly of an initially disordered dispersion.

There have been some preliminary attempts of applying concepts of separation in binary colloids to explain phenomena observed in some granular segregation experiments. The role of excluded volume depletion in segregation was first suggested by Duran & Jullien (1999) for a numerical study in two dimensions and by Aumaitre et al. (2001) in the quasi-2D experiment discussed in Section 1.5.2. Nonetheless, few investigations have addressed the extents of validity of such analogies and much work is still required before we understand the impact of non-equilibrium effects, such as the irrelevance of the thermodynamic energy scale  $k_B T$ , inelasticity and non-Brownian driving, on trying to import these concepts from equilibrium systems. A discussion of the application of these ideas to granular systems can be found in the review articles by Shinbrot & Muzzio

(2001) and Kudrolli (2004).

## 1.7 Thesis outline

A description of the apparatus is given in Chapter 2. The precise control aspects such as the vibration, the filling fraction of the granular mixture and the setting of the initial conditions are emphasized. These quantities are then used to define the governing parameters of the system namely, the amplitude and frequency of vibration, the layer filling fraction, the relative number density of the two particle types and the aspect ratio of the tray. The visualization procedures and image processing techniques are then discussed for both the pattern analysis and the tracking of individual particle trajectories.

The segregation patterns of binary mixtures are introduced in Chapter 3. The time evolution of the patterns which arise from an initially homogeneous mixture is discussed. Attention is given to the development of *macroscopic* measures to quantify the segregation process. In particular, the average width and number of domains are analysed. Issues on the reproducibility of the segregation patterns are then discussed.

In Chapter 4, results of the macroscopic measures of the patterns are presented for an investigation into the dependence of granular segregation on filling fraction. Evidence for a continuous phase transition is given based on measurements for both the average width and number of domains. The timescales associated with the segregation process are analysed. A measure for the macroscopic fluctuations of the domains is then presented and this provides evidence for the existence of three qualitatively distinct regimes of the binary mixture.

The idea of three distinct granular phases is developed further in Chapter 5. A variety of microscopic measures, calculated from the individual positions of the phosphor-bronze spheres, are introduced: the local Voronoi area density, the

angle between nearest neighbours and the radial distribution function.

In Chapter 6 we perform an exploration of the parameter space of the system. We investigate the dependence of the aspect ratio, the individual filling fractions of the two particle species on the segregation process and amplitude and frequency of forcing.

Results on some additional experiments, which we have performed to address some nonlinear aspects of our granular system, are presented in Appendix B. In particular, we establish an analogy between large scale motion observed in the granular layer and acoustic streaming in classical fluid dynamics. Furthermore, we present some intriguing results on oscillatory collective dynamics of the patterns with timescales three orders or magnitude larger than that of the sinusoidal driving.

In Appendix C we reprint a paper written in collaboration with G. Ehrhardt and A. Stephenson from the Theoretical Physics Group at the University of Manchester, in which we report results on a numerical event driven simulation of our binary granular system (Ehrhardt, Stephenson & Reis 2004). The numerical simulations are found to reproduce much of the experimentally observed phenomena and the study is extended to an exploration of the parameter space in a way which was inaccessible in the experiments. This study enables us to identify the mechanisms involved in the segregation of our binary mixture.

Finally, conclusions arising from the findings of this study are made in Chapter 7. We compare our experimental results to the numerical simulations presented in Appendix C and suggest what we believe is the principal segregation mechanism present in our experiments. Moreover, we comment on some possible analogies with binary colloidal systems as well as their limitations. Suggestions are then given for possible directions of extension of this work.

# Chapter 2

## The experiment

This chapter contains a description of the apparatus and provides details of the experimental procedures employed in the course of the present study. The experimental set up consisted of a rectangular container connected to an electro-mechanical shaker. A shallow layer of granular materials was placed in the surface of a horizontal tray and oscillated horizontally. The main parameters which govern the state of the system are the amplitude,  $A$ , and frequency,  $f$ , of vibration, the layer compaction,  $C$ , and the aspect ratio of the container,  $\Gamma$ . Particle dynamics and segregation patterns of binary mixtures were illuminated from above and images were acquired by a CCD camera mounted directly above the oscillating tray.

### 2.1 Electro-mechanical system

A schematic diagram of the top view of the apparatus is presented in Fig. 2.2. It consisted of a horizontal smooth rectangular tray, of dimensions  $(x, y) = 180 \times 90mm$  with a flatness of less than  $\pm 5\mu m$ , on which particles were vibrated longitudinally. The tray was machined from aluminum tool plate for increased rigidity and mounted on a horizontal platform which was connected to a Ling

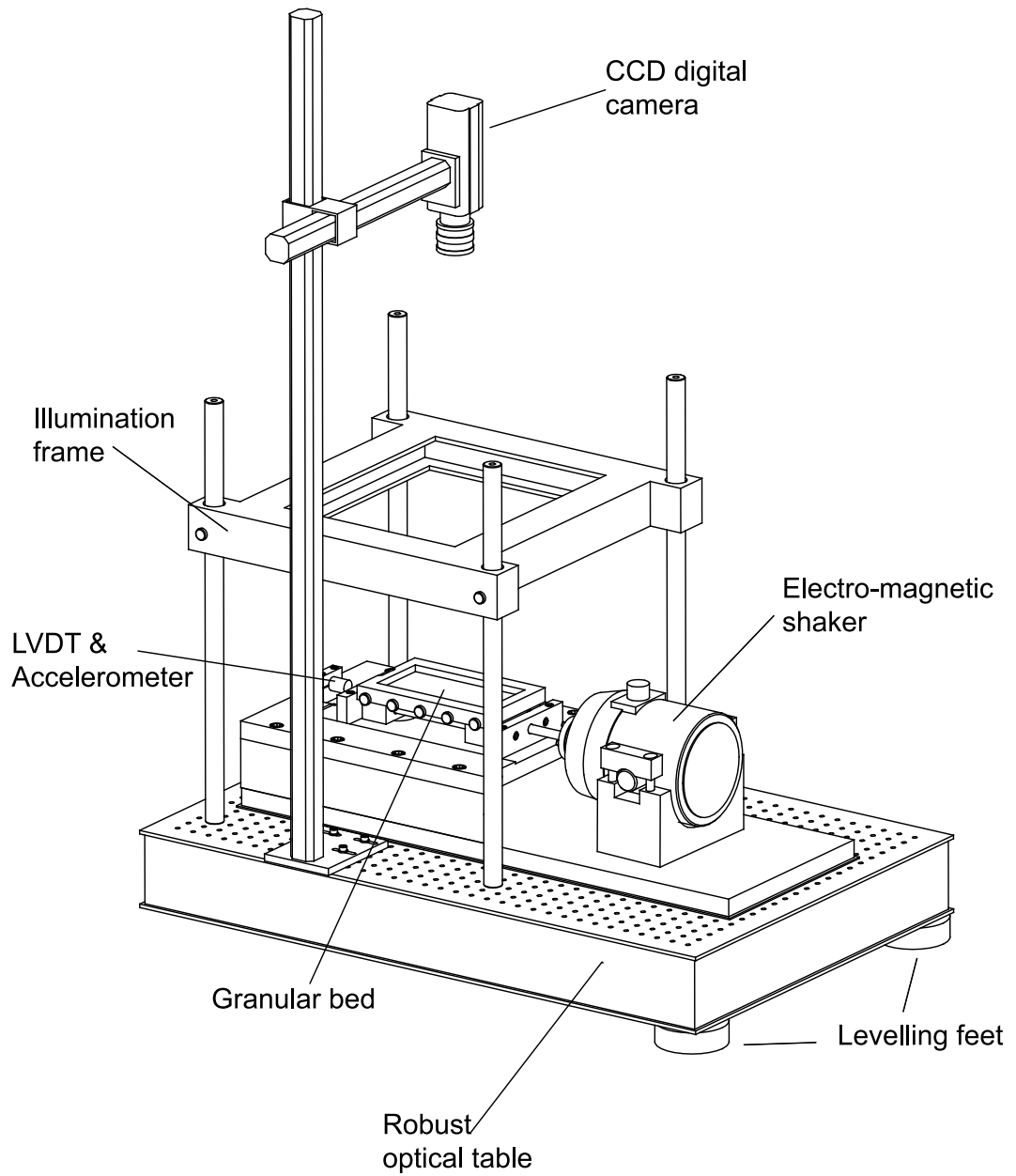


Figure 2.1: Three dimensional schematic diagram of the experimental apparatus.

LDS V409 electro-mechanical shaker<sup>1</sup>. Its motion was constrained to be one dimensional by four lateral high precision linear bush bearings<sup>2</sup>. The stainless steel shafts in which the bearings ran were hardened and precision ground therefore reducing fatigue. To increase smoothness of motion the bearings were lubricated with a fine diffusion pump oil. A coupling, adjustable in two directions, allowed for off-centre misalignment between the independent arm shafts fixed to the shaker and the moving platform, respectively. This minimised out-of-plane stresses on the bearings and therefore increased the quality of the linear motion.

Both the container and the shaker were mounted on a stainless steel base which in turn was securely positioned on an optical table. To avoid the propagation of unwanted vibrations in the system, a  $3mm$  sheet of lead was used at the contact points between the shaker and the stainless steel base. Moreover,  $5mm$  neoprene sheet was sandwiched between the steel base and the optical table. The optical table was raised from the floor by three triangulated anti-vibration machine mounts<sup>3</sup> with a fine-pitch screw which allowed the apparatus to be accurately levelled.

Individual particles or the granular layer were forced via stick-and-slip frictional contacts with the oscillating surface of the container, which we denote by *shaking bed*. Different removable frames could be attached to the tray to allow for changes in size, shape and aspect ratio to be achieved. The side and end walls of the bounding frame were  $5mm$  high. The aluminium surface of the shaking bed was first precision polished and then given a smooth anodising treatment. The black anodised metal of the bed aided the detection and tracking of particles and patterns since there was a significant enhancement in contrast and reflections were effectively eliminated. It should be noted that the anodised surface is a layer

---

<sup>1</sup>LDS Ltd., Royston Herts., UK.

<sup>2</sup>ST12 Bush Bearings from Bearing Services, BSL Manchester

<sup>3</sup>Model 442-662: RS Components Ltd, Corby, UK

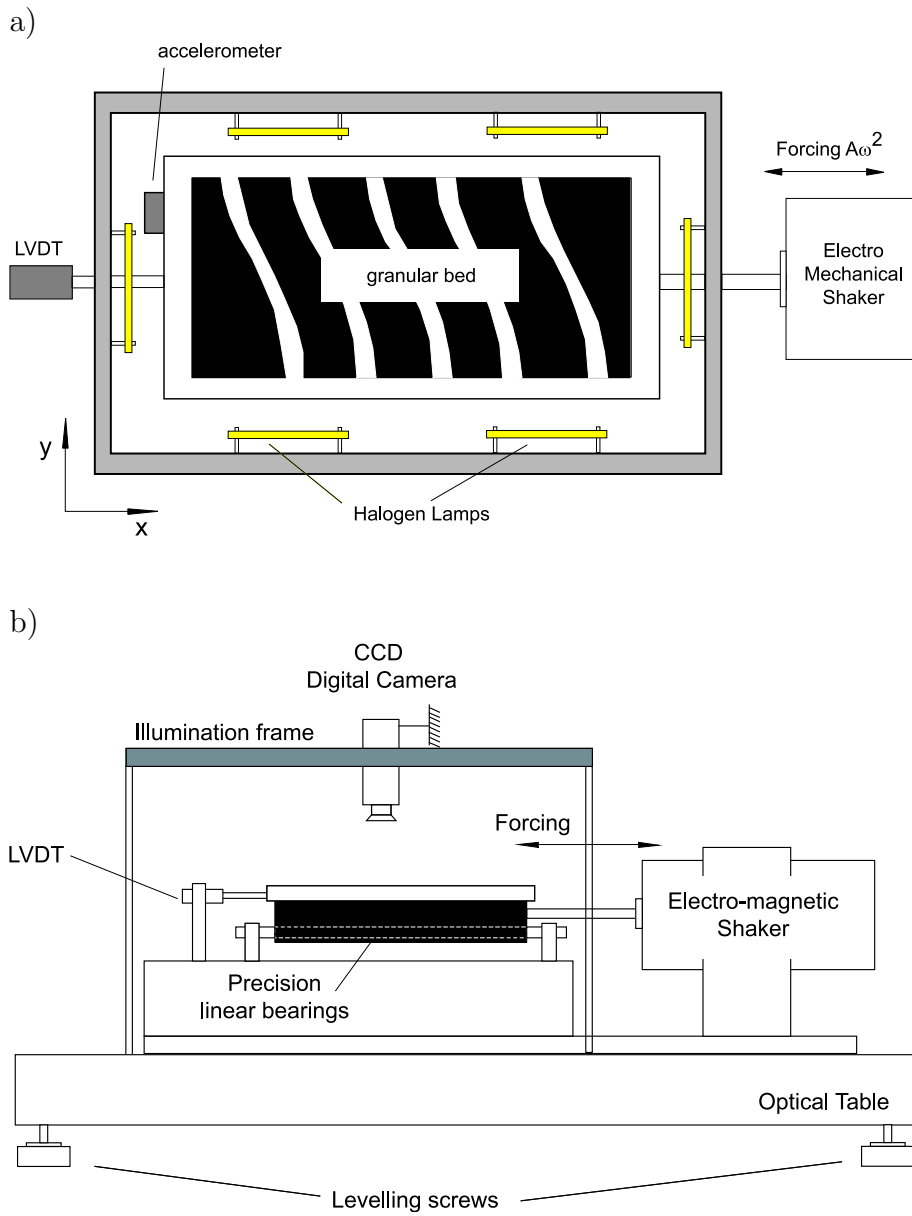


Figure 2.2: Schematic diagram of the experimental apparatus. (a) top view. (b) side view.

of aluminium oxide and, hence, is essentially electrically insulating. This raises the possibility of the build up of surface charges from the continuous rubbing by particles. Electrostatic effects were checked to be unimportant by spraying the surface with an electrically conducting coating of colloidal graphite. This had no qualitative effect on the observations of segregation.

We have also checked for the influence of interstitial air on the particle and segregation dynamics. For this, the container was vacuum sealed with o-rings at the junctions between the frame, the shaking bed and a top glass lid. The vacuum sealed cell was connected to a rotary mechanical vacuum pump. The achieved reduced pressure eliminated air resistance and air-flow effects but no qualitative changes were noticed when the cell was evacuated. In particular, segregation of a binary mixture, as discussed in Chapter 3, persisted in vacuum. Hence, throughout this report, all quantitative results correspond to experiments done at atmospheric pressure. Further research will be necessary to determine to what extent the evacuation of the container has a quantitative effect on the dynamics of segregation.

Levelling of the apparatus is crucial to ensure homogeneous forcing, as slight inclinations of the shaking surface could strongly bias the motion of particles and induce clustering. In particular, the phosphor-bronze spheres were extremely sensitive to any tilt. Firstly, the tray, while stationary, was levelled using a high precision engineering spirit level with an accuracy up to  $\pm 0.01^\circ$  using the three triangulated fine-pitch adjustable screws which supported the optical table. However, due to the weight of the level, this initial levelling of the system applied involved an applied load on the tray with the possibility of bias. Further levelling precision was achieved dynamically by vibrating 100 phosphor-bronze spheres, by shaking the tray at  $f = 12Hz$  and  $A = \pm 1.74mm$ . Optimal levelling was thereby obtained when the spacial distribution of the agitated particles was isotropic

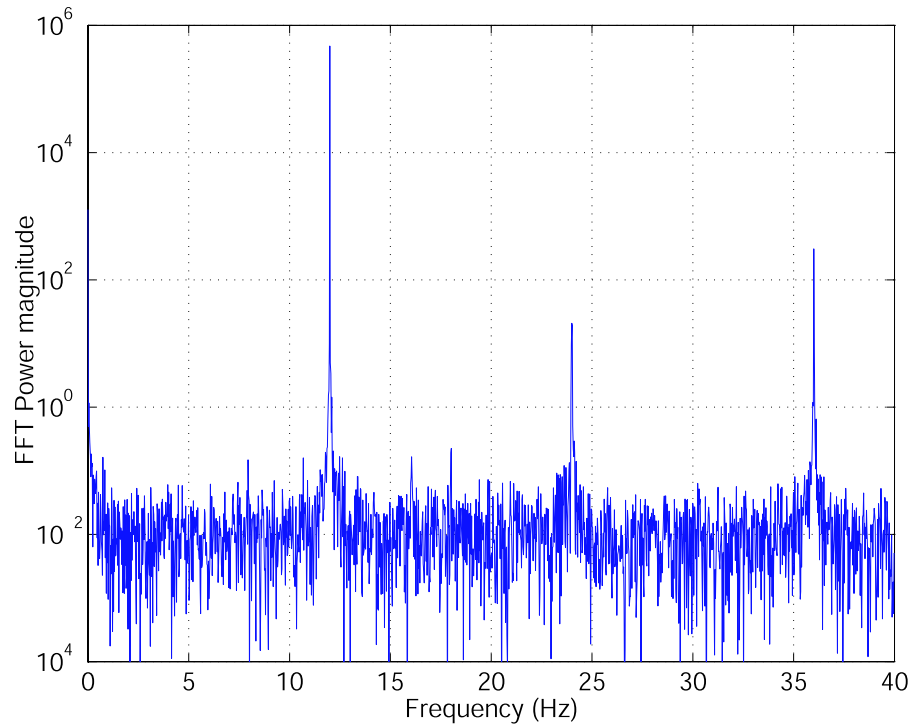


Figure 2.3: Power spectrum obtained from a Fast Fourier Transform of the accelerometer signal for  $f = 12Hz$  and  $A = \pm 1.74mm$  with characteristic peaks at the fundamental frequency ( $12Hz$ ), first harmonic ( $24Hz$ ) and second harmonic ( $36Hz$ ).

and homogeneous across the whole tray. This second procedure was particularly sensitive as any small deviations from the horizontal caused clustering as the spheres easily roll *down hill*.

## 2.2 Driving and vibration monitoring

The shaker was driven sinusoidally using a stable HP 33120A function generator whose output was first amplified by a high quality DC coupled power amplifier.

The dynamic displacement and acceleration of the shaking bed were monitored

by a Sangano Dfg 2.5 Linear Displacement Variable Transformer (LVDT)<sup>4</sup> and a PCB quartz shear piezoelectric accelerometer<sup>5</sup>. The LVDT provided a DC output signal proportional to the displacement of the platform, with a linear calibration of  $820 \pm 10mVmm^{-1}$ . This calibration was performed by aligning the LVDT energised coil and the nickel iron pick up coil on a linear optical stage. The position of the latter was then incrementally increased using a micrometer, over a range of  $\pm 9mm$ . The linear calibration given above was found to be valid on this range. The LVDT output signal was fed back into the DC amplifier. This established a feed-back control loop which ensured that both the LVDT output and shaker input signals matched which helped reduce drifts and therefore accurately stabilised the vibration. The servo feedback control was eventually removed and considered to be unnecessary as the drifts, over the duration of our longest experiments (up to  $20min$ ) were found to be minimal. All experiments were performed within the range of frequencies ( $8 < f < 28$ ) $Hz$  and peak-to-peak amplitudes ( $\pm 0.58 < A < \pm 5.22$ ) $mm$ .

A plot of the power spectrum of the accelerometer signal for typical driving parameters  $f = 12Hz$  and  $A = \pm 1.74mm$ , obtained from Fast Fourier Transform, is shown in Fig. 2.3. In addition to the fundamental peak at  $f = 12Hz$ , two harmonics are evident at  $f_1 = 24Hz$  and  $f_2 = 36Hz$ . The ratio between the power of the first and second harmonic with reference to the fundamental is  $P_1/P_{fundamental} = 4.40 \times 10^{-5}$  and  $P_2/P_{fundamental} = 6.49 \times 10^{-4}$ . The value of the second harmonic is of particular importance as it is the first order measurement of the asymmetry of the signal. This indicates that the oscillatory motion of the tray is accurately sinusoidal to better than 0.1% in power.

---

<sup>4</sup>Model 646-460 Sangano Dfg 2.5 LVDT, RS Components Ltd, Corby, UK

<sup>5</sup>Model 353B43 Quartz Shear Accelerometer, PCB Piezotronics, Techni Measure, Studley, UK

## 2.3 Materials used

A variety of particles were used and these may be classified as spherical and non-spherical particles. Examples in the first class are polystyrene and phosphor-bronze (high precision with 0.012mm sphericity). In the second class, sugar particles (also known as "100's and 1000's"), mustard seeds and poppy seeds were used. In addition to being non-spherical they had a considerably higher surface roughness than the spheres. This is mainly because of their complex surface topology as may be seen in the photographs of Fig. 2.4 (a), (b) and (c). The details of average diameter, density and shape are summarised in Table 2.1.

Material	Average Diameter ( <i>mm</i> )	Density ( <i>gcm</i> <sup>-3</sup> )	Shape
poppy seeds	1.07	0.2	flat 'kidney' shaped
sugar particles	1.71	1.6	roughly spherical
phosphor-bronze	1.50	8.8	precision spherical
polystyrene	0.5	1.1	precision spherical

Table 2.1: Material properties for the particles used.

The majority of the experiments reported in this theses were carried out with the following mixtures:

**Mixture 1:** phosphor-bronze spheres + poppy seeds;

**Mixture 2:** polystyrene spheres + sugar particles;

Mixtures 2 was used to illustrate the robustness of the phenomena under study but Mixture 1 was used extensively for the quantitative analysis. This particular mixture was chosen for the significant differences in contrast which facilitated pattern analysis and individual particle tracking. It was therefore considered

important to quantify the level of polydispersity of the poppy seeds which we consider next.

In measuring the polydispersity of the poppy seeds, we were essentially interested in the distribution of the 2D projected areas. These were obtained by imaging 2500 randomly picked poppy seeds on a microscope with a  $2\times$  objective, as shown in Fig. 2.4(d). The areas of the particles were then determined using the software package `Scion Image 4.02`. This is a publicly available image processing package with extensive image analysis and enhancement capabilities. The projected areas of the poppy seeds were calibrated against a high precision sapphire sphere with radius  $r_{sapphire} = 0.3970 \pm 0.0025mm$ .

The histogram for the areas of the 2500 imaged poppy seeds is presented in Fig. 2.5. The distribution of areas is closely approximated by a gaussian fit with mean area  $\langle A_{ps} \rangle = 0.90mm^2$  and a standard deviation of  $\sigma(A) = 0.15mm^2$ , corresponding to a 17% level of polydispersity.

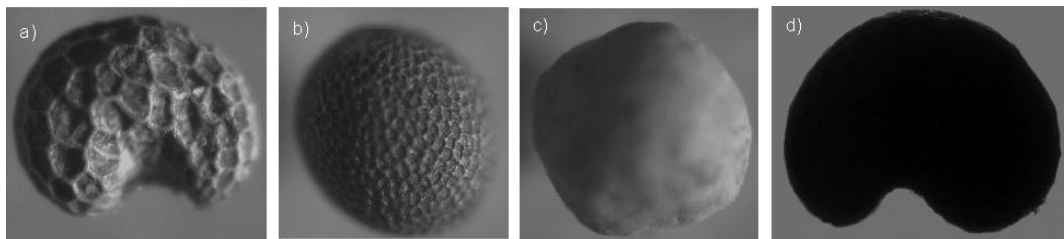


Figure 2.4: Photographs of the various non-spherical particles used. (a) poppy seed. (b) mustard seed. (c) sugar particle. (d) Typical frame of a poppy seed, imaged through a microscope with a  $2\times$  objective, which was used in the polydispersity measurements.

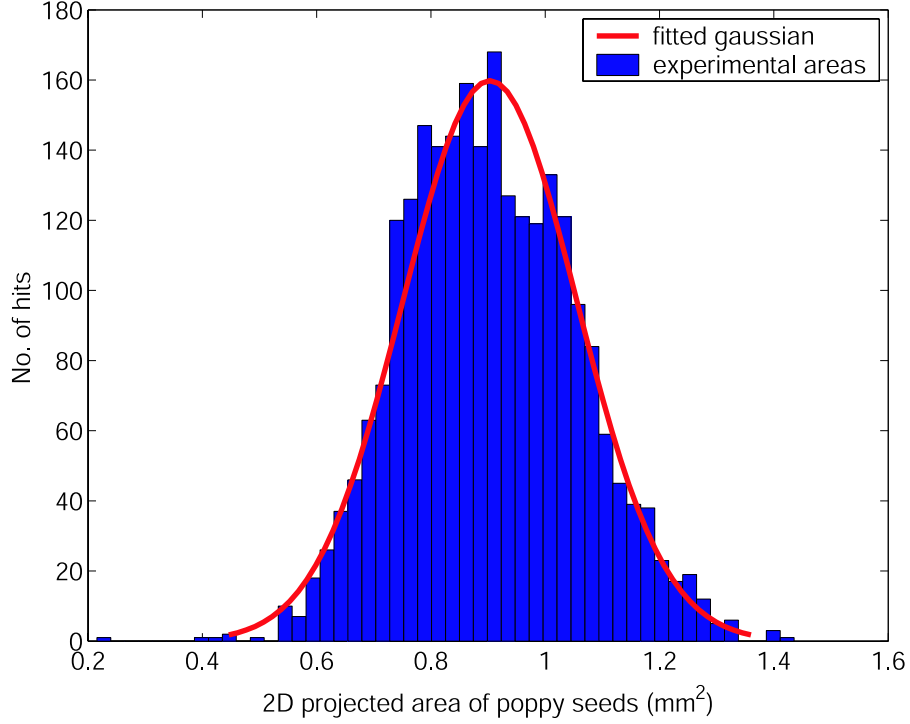


Figure 2.5: Histogram of the two-dimensional projected areas of 2500 poppy seeds. The solid curve is a gaussian fit with a mean of  $0.90\text{mm}^2$  and a standard deviation of  $0.15\text{mm}^2$ .

## 2.4 Layer compacity

Throughout this study, experiments were performed in an *approximately monolayer regime* as discussed below. In the binary mixture studies some overlapping of particles occurred. This was small for the mixtures of poppy seeds and phosphor bronze spheres, with which most of the segregation studies were done, since the size ratio for these two types of particle is  $q \sim 0.71$ .

At this point we define the *layer compacity* to be the total filling fraction of the system. For the case of a mixtures of two types of particles, species  $a$  and species  $b$ , as shown in the schematic diagram of Fig. 2.6 this dimensionless

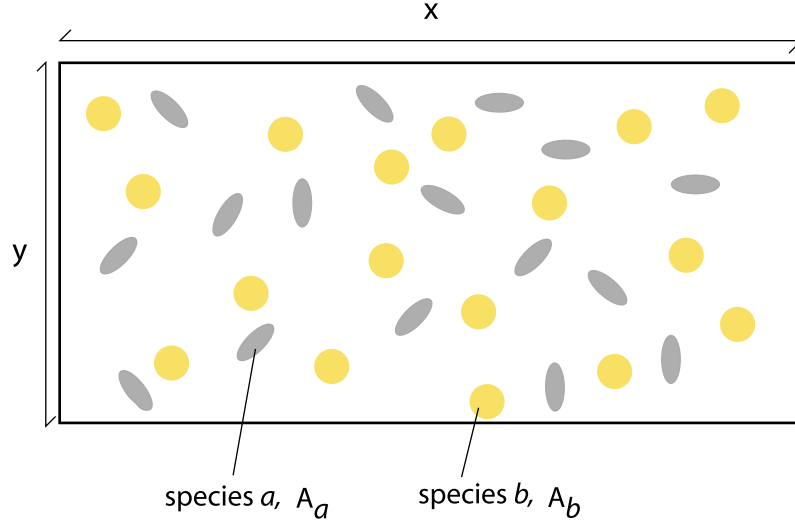


Figure 2.6: Schematic diagram for the definition of the layer compacity. Species  $a$  and  $b$  have two-dimensional projected areas of  $A_a$  and  $A_b$ , respectively.  $x$  and  $y$  are the spacial dimensions of the full tray.

parameter is defined as,

$$C(N_a, N_b) = \frac{N_a A_a + N_b A_b}{xy}, \quad (2.1)$$

where  $N_a$  and  $N_b$  are the numbers of species  $a$  and  $b$  in the layer,  $A_a$  and  $A_b$  are the two dimensional projected areas of the respective individual particles and  $x$  and  $y$  are the longitudinal and transverse dimensions of the rectangular tray. The uncertainty associated with the measurements of  $C$  is approximately 8%.

The larger heavy phosphor-bronze spheres are always a monolayer but the lighter and flatter poppy seeds can overlap. The layer is said to be in the a *monolayer regime* if the extent of overlap of the poppy seeds is never such that its layers' height exceeds the height corresponding to a diameter of the larger spheres. The failure of this criterion is readily noticed as smaller particles can then hop over domains of the larger particles. Hence, for the highest values of the compacity,  $C$  can assume values higher than those corresponding to maximum packing in two dimensions, which, for the case of monodisperse disks is  $\pi/\sqrt{12}$ .

This choice of performing the experiments in this approximately monolayer regime has two advantages. Firstly, particles are always in contact with the oscillatory surface of the tray. In Chapter 6 we study the effect of changing the aspect ratio of the tray on the dynamics of segregation and present evidence that the action of the boundary walls was localized. Therefore, the forcing was provided homogeneously throughout the layer through frictional contacts. Secondly, these approximately two dimensional experiments allow the dynamics of the granular layer to be fully visualised by imaging the system from above.

## 2.5 The aspect ratio

In addition to the driving parameters and the layer compacity a geometrical dimensionless parameter, *aspect ratio*, may be defined as

$$\Gamma = \frac{\Delta x}{\Delta y} \quad (2.2)$$

where  $\Delta x$  is the longitudinal length of the tray and  $\Delta y$  is the transverse width of the tray, perpendicularly to the direction of forcing. The values of  $\Delta x$  and  $\Delta y$  were changed using a variable frame which was positioned on all 4 side walls. Both  $\Delta x$  and  $\Delta y$  could be independently adjusted to the required value of  $\Gamma$ . A parametric study of  $\Gamma$  in the segregation dynamics is performed in Chapter 6. All other experiments were performed in a tray width aspect ratio  $\Gamma = 2$  with dimensions  $((180 \times 90)mm^2)$ .

## 2.6 Setting the initial conditions

Particular care was taken in the setting of the system's initial conditions. The desired initial state of the system is a perfectly mixed state since any small clusters in the initial layer may bias the segregation results. This issue is particularly

difficult to address in three dimensional geometries. However, for our two dimensional system we have devised a reliable and systematic method which we discuss next.

The initial conditions of the binary mixture of poppy seeds and phosphor-bronze spheres was consistently set using a procedure which is schematically presented in Fig. 2.7. Firstly, for a particular compacity,  $N_{ps}$  poppy seeds were vibrated at large amplitudes,  $A \sim \pm 5mm$ , creating an homogeneous and isotropic layer, Fig. 2.7(a). The phosphor-bronze spheres were then suspended above the layer, on a horizontal perforated plate with  $(m \times n)$   $2mm$  diameter holes arranged in a triangular lattice and held by a shutter on an independent superposed frame, Fig. 2.7(b). The shutter was then opened and the  $N_{pb} = m \times n$  phosphor-bronze spheres fell onto the layer of poppy seeds, creating a near homogeneous mixture of the two types of particles, Fig. 2.7(c). A typical example for the homogeneous mixture obtained using this procedure is shown in Fig. 2.8.

## 2.7 Visualization and image acquisition

The dynamics of the granular layer on the shaking bed was visualized, in a light reflection arrangement and the behaviour of the layer was monitored using a CCD (Charge Couple Device) camera mounted directly above the oscillating tray, as shown in Fig. 2.1. Illumination of the granular layer was provided, from above, by a series of six 250W halogen lamps set on a rectangular frame as shown in Fig. 2.2, parallel to the surface of the oscillating tray. This was designed to provide homogeneous illumination. The illumination system was connected to a Variac enabling control of intensity and contrast adjustments. It was found that the optimal working conditions were around 45% of the total power.

As outlined in Section 1.7, two classes of experiments were performed — pattern analysis (Chapter 3 and 4) and multiple particle tracking (Chapters 5

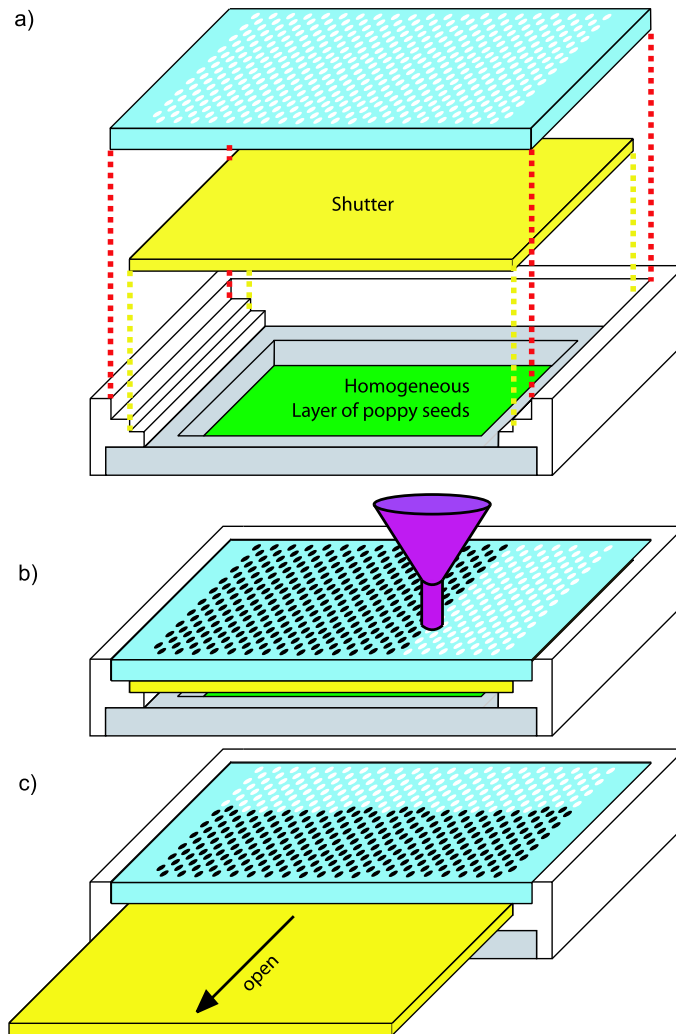


Figure 2.7: a) Schematic diagram of the procedure for setting the initial conditions of the binary granular layer. (a) A homogeneous layer of poppy seeds is initially created by vibration at large amplitudes. (b) an independent frame is then superposed on the tray and a perforated plate with  $m \times n$  holes is loaded with phosphor-bronze spheres using a funnel. (c) A shutter is then opened and the spheres fall onto the homogeneous layer of poppy seeds in the tray underneath.

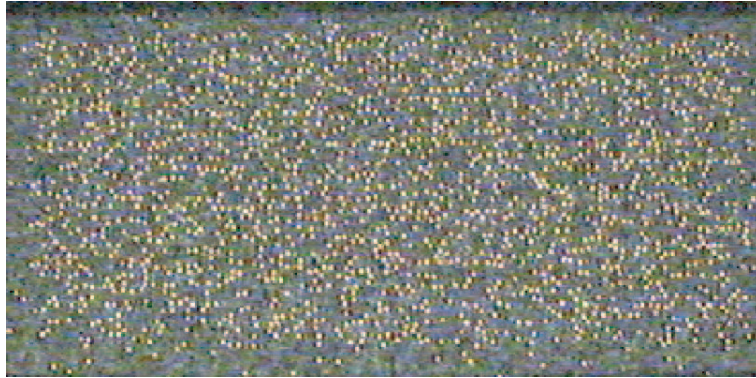


Figure 2.8: Photograph for the typical initial conditions of the homogeneous mixture of poppy seeds and phosphor-bronze spheres.

and 6) — for which different image acquisition systems were used. The details of the camera and acquisition card for each of these are presented in Table 2.2. A colour system was used for the pattern analysis experiments as the hue and saturation between regions poppy seeds and phosphor-bronze spheres enabled identification of the segregation domains.

Type of Experiment	Chapter	Camera Model	Image acquisition card
Pattern Analysis	3 and 4	Colour Sony SSC-C158P	Data Translation DT 3120
Particle tracking	5 and 6	Monochrome Cohu 4910 RS-170	Pinnacle AV/DV E4 overlay video card

Table 2.2: Imaging systems used for each of the classes of experiments.

Both imaging systems were used to acquire a series of frames at a fixed time interval. For the pattern analysis experiments, single frames were digitised using a PC by a colour 24-bit frame grabber, Data Translation DT3120 with maximum acquisition rate of 10  $frames.s^{-1}$ . For the case of particle tracking, 8-bit grey-scale videos at 25  $frames.s^{-1}$  were saved directly into the computer and the

individual frames were then extracted.

Note that the operating frequencies of both of the analogue cameras ( $25Hz$ ) is a precisely half of that of the AC lighting system of  $50Hz$ . This helped prevent complications from beating effects between the camera and the lighting.

For the the pattern analysis experiments the full area of the tray ( $190 \times 80mm$ ) was imaged whereas in the particle tracking experiments the camera field of view was focused to a ( $76 \times 62mm$ ) central area. This was done in order to achieve greater accuracy in the determination of the centres of the individual particles.

## 2.8 Image processing

### 2.8.1 Segregation patterns

Colour frames acquired for the segregation experiments reported in Chapter 3 and 4 were processed using the command line tool `convert` within the image processing library, ImageMagick 5.5.7.<sup>6</sup> This image processing tool was used in conjunction with the scripting language ActivePerl 5.8.0.806.<sup>7</sup> to automatically process large sequences of images.

The general procedure of the processing of the  $600 \times 300pixels$  images of the full tray with a mixture of phosphor-bronze spheres and poppy seeds consisted in converting the original full colour images (Fig. 2.9a) into black and white frames (Fig. 2.9f)). To accomplish this, a sequence of transformations were applied to the original colour frame as described below.

Initially, the hue and saturation values of the images were adjusted to enhance colours. This resulted in regions of bronze spheres which were coloured blue, against black regions containing poppy seeds (Fig. 2.9b)). At this point, the blue

---

<sup>6</sup>The collection of image processing tools and libraries ImageMagick 5.5.7. is freely available, for a variety of platforms, from <http://www.imagemagick.org/>

<sup>7</sup>The language ActivePerl 5.8.0.806 is freely available from <http://www.activestate.com/>

channel was extracted delivering a gray scale image (Fig. 2.9c). After inversion (Fig. 2.9d) the image was passed through a gaussian blurring filter (with a 5 pixels mean and 5 pixels standard deviation) to smooth out background noise and unwanted sharp edges (Fig. 2.9e). Finally, the image was thresholded, i.e. any pixel below a certain threshold was assigned a value of 0 and above this threshold value, a value of 1. This yielded the binary image (Fig. 2.9f)) where a pixel value of 0 (black) corresponds to a region of poppy seeds and a value of 1 (white) to a region of phosphor-bronze spheres. Transformations of the original images into

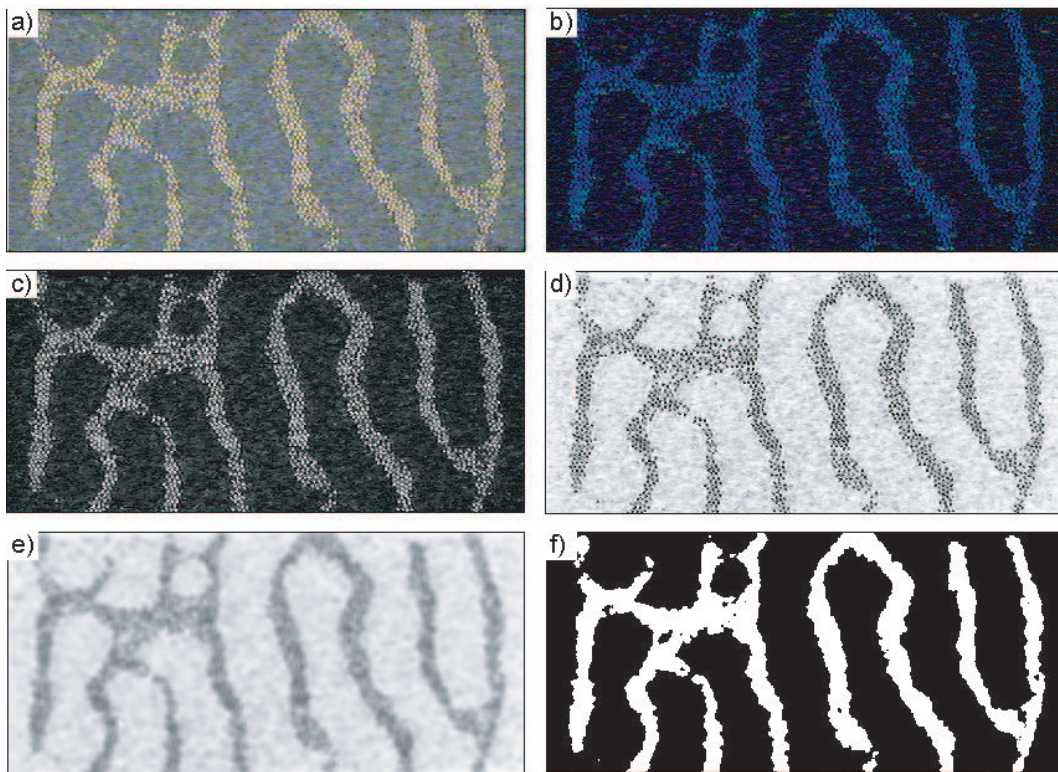


Figure 2.9: Image processing sequence of the images of the segregation patterns used for the macroscopic measurements in Chapter 3 and 4. (a) Original colour frame. (b) Processed frame after hue and saturation adjustments. (c) Processed frame after extraction of the *blue* channel. (d) Processed frame after inversion. (e) Processed frame after gaussian blurring. (f) Final processed frame after inversion.

binary format enabled further quantitative measures of the patterns as will be discussed in Chapter 3 and 4.

### 2.8.2 Microscopic particle tracking

The individual positions of phosphor-bronze spheres were obtained in a visualization window of the layer for the microscopic particle tracking experiments. Higher image resolution than those for the macroscopic analysis of the segregation domains were required for this microscopic analysis and so we focused the camera visualization window on a central  $(708 \times 576) \text{pixels}^2 = (73.14 \times 59.50) \text{mm}^2$  area of the granular layer. The projected 2D area of each phosphor-bronze sphere contained approximately 166 pixels in this case and a typical frame for a mixture is presented in Fig. 2.10(a). Since we performed reflection imaging (the light source was positioned above the layer) and because phosphor-bronze has a high reflection coefficient compared to the poppy seeds, the spheres appeared as sharp bright regions.

The original grey-scale experimental frames were first passed through a gaus-

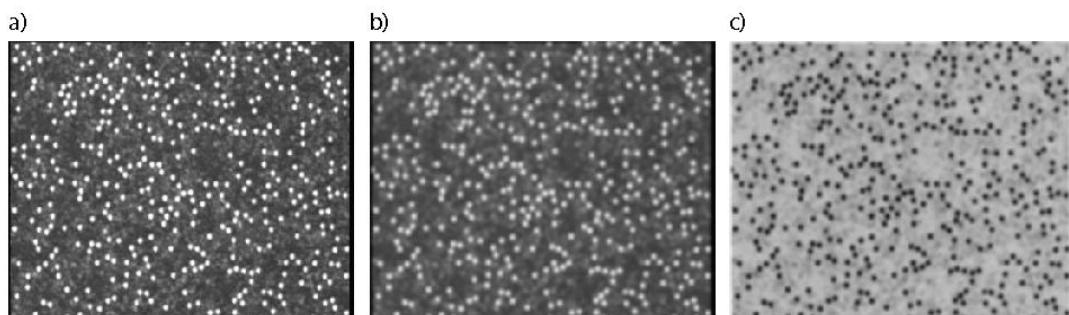


Figure 2.10: Image processing of the images of granular segregation used for the microscopic measurements in Chapter 5 and 6. (a) Original experimental frame. (b) Processed frame after gaussian blurring. (c) Final processed frame after inversion.

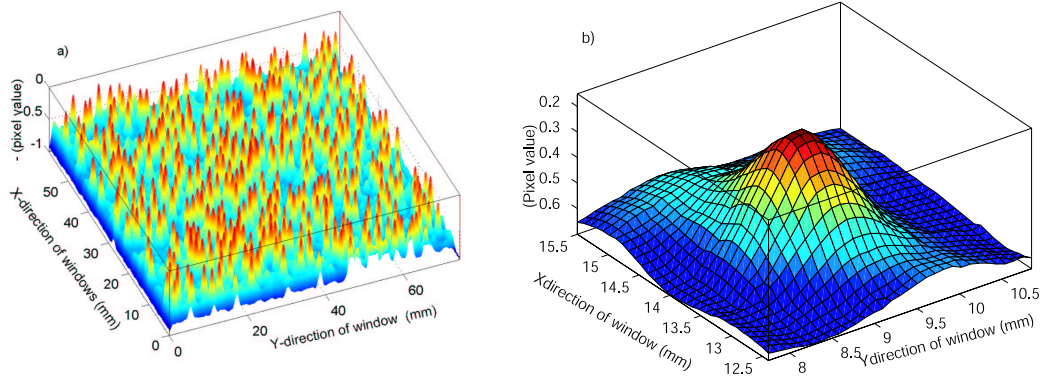


Figure 2.11: Final processed frame. (a) Three-dimensional surface of the grey-scale level images. Red peaks represent the position of individual spheres. (b) Zoomed surface of the processed frame around a single particle showing a gaussian profiled peak. Note that the vertical axes of both (a) and (b) have been inverted to aid visualization such that minima appear as peaks.

sian filter with 5 pixels radius and 5 pixels standard deviation in order to smooth out the images and remove sharp edges (Fig. 2.10b)). The images were then inverted so that the phosphor-bronze spheres appeared as well defined dark regions and the layer of poppy seeds or the trays background as a homogeneous bright background (Fig. 2.10(c)). These image processing operations were performed with ImageMagick by using Perl scripts as discussed above.

Note that the images were grey-scale, *i.e.* individual pixels,  $p$  could have a value within the range  $0 \leq p \leq 1$  (where a value of 0 corresponds to black and a value of 1 to white). with discretised steps of  $\Delta p = 1/256$  for different shades of grey. Hence, the final processed frames (Fig. 2.10c)) may be regarded as a three-dimensional surface, as shown in Fig. 2.11a), where each pixel  $(x_i, y_j)$  in the x-y plane (the spacial dimensions of the imaging window) is assigned a value  $0 \leq p(x_i, y_j) \leq 1$ . We have inverted the z axis of the graph so that minima in the original image now appear as a maxima to aid visualization, *i.e.* *peaks* refer

refer to a minima of  $p$ . A series of well defined peaks is clearly observed at the location corresponding to the centre of each individual sphere.

A zoomed image of the image surface is presented in Fig. 2.11(b). Single peaks have a gaussian-like profile from which the extreme point can be identified. Hence, the positions of all the phosphor-bronze spheres captured in the imaging window can be identified by determining the location of all these local minima, yielding a spacial distribution of points,

$$\Pi(\underline{\mathbf{r}}, t) = \sum_{i=1}^{N(t)} \delta(\underline{\mathbf{r}} - \underline{\mathbf{r}}_i(t)), \quad (2.3)$$

where  $\underline{\mathbf{r}}_i(t) = (x_i, y_i)$  is the location of the  $i$ -th particle in a field of  $N$  particles, at time  $t$ . In Fig. 2.12 we present a superposition of the acquired positions of the particle centres on a typical experimental frame. The distribution  $\Pi(\underline{\mathbf{r}}, t)$  was then used to calculate a variety of microscopic measures which will be discussed in Chapters 4 and 6.

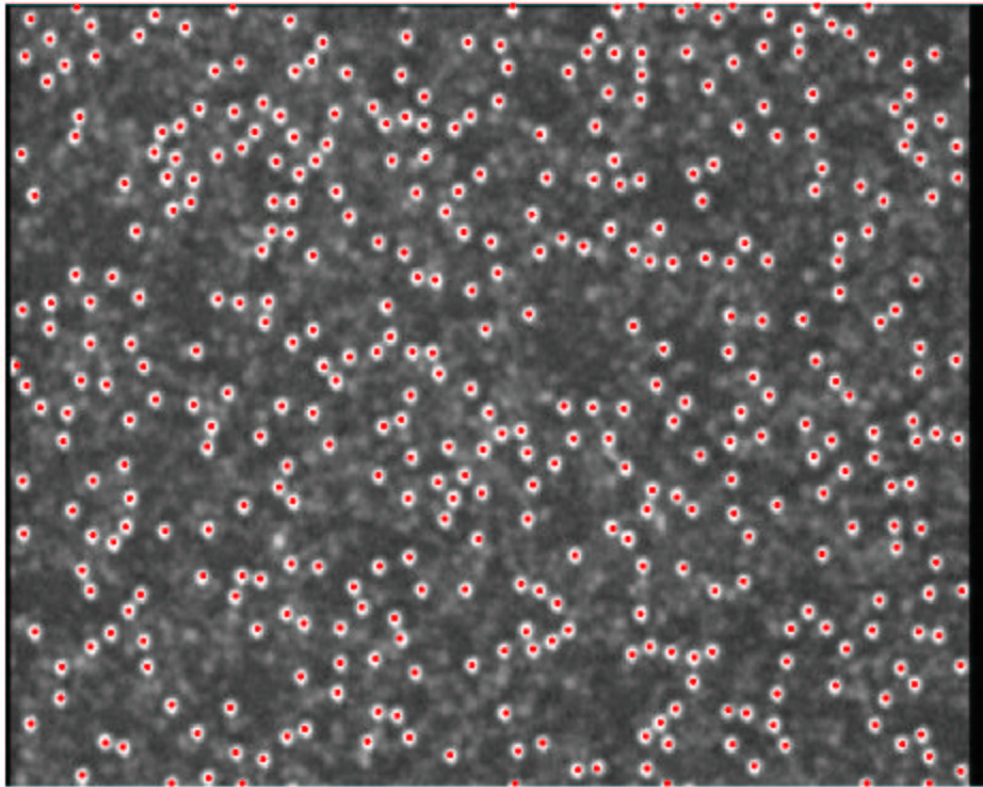


Figure 2.12: Original experimental frame with the superposed field of particle positions (shown in red) for a mixture with  $C = 0.921$ .

# Chapter 3

## Granular segregation patterns

In this chapter the granular segregation patterns for a binary mixture of particles are introduced. The robustness of the phenomena is discussed and the emergence of the patterns from an initially homogeneous mixture is analysed. This is done by introducing a space-time diagram construction for the pattern evolution and the observed behaviour is then quantified by the average width of the domains, along the direction of driving. Two regimes of the segregation process are identified with its own distinct associated timescales. These are the initial segregation growth and the late time coarsening. Finally, the pattern reproducibility is discussed.

### 3.1 Segregation Patterns

In Fig. 3.1 we present typical examples of segregation patterns for two particular granular mixtures: poppy seeds (grey regions) + phosphor-bronze particles in Fig. 3.1(a) and polystyrene spheres (white regions) + sugar particles in Fig. 3.1(b). Qualitatively similar patterns were also found in a mixture of phosphor-bronze spheres and glass beads. The physical properties of the constituent individual particles were discussed in detail in Section 2.3. The snapshots correspond to the segregated states which self-organized after the mixtures were vibrated for a

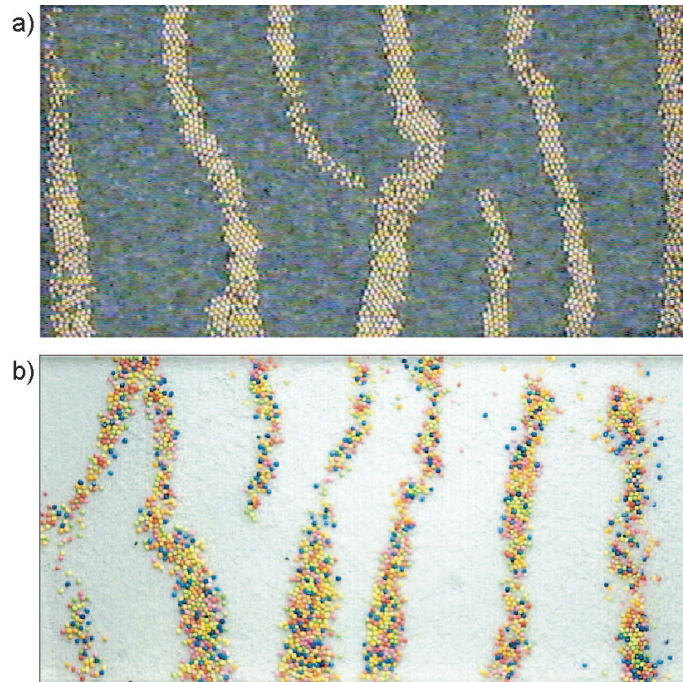


Figure 3.1: Typical segregation patterns of two binary granular mixtures: (a) poppy seeds (grey regions) + phosphor-bronze spheres (yellow regions); (b) polystyrene spheres (white regions) + *100's and 1000's* sugar particles (coloured regions). The frames were captured after 15min of vibration of an initially homogeneous mixture,  $C = 1.028$ ,  $\Gamma = 2$ .

period of 15 minutes, with forcing parameters  $A = \pm 1.74mm$  and  $f = 12Hz$  and aspect ratio  $\Gamma = 2$  with the initial conditions of a homogeneous mixed layer. The method used to produce mixed initial conditions was described in Section 2.6.

The segregation patterns consisted of domains of the larger particles surrounded by a 'sea' of the smaller ones. The domains were elongated, in the form of stripes aligned perpendicularly to the direction of forcing. It is noteworthy that very similar pattern morphology were obtained for both mixtures even though the constituent particles had significantly different physical properties. Moreover, we have performed experiments at reduced pressures by evacuating the mixture in a vacuum cell and the qualitative features of the patterns remained unchanged,

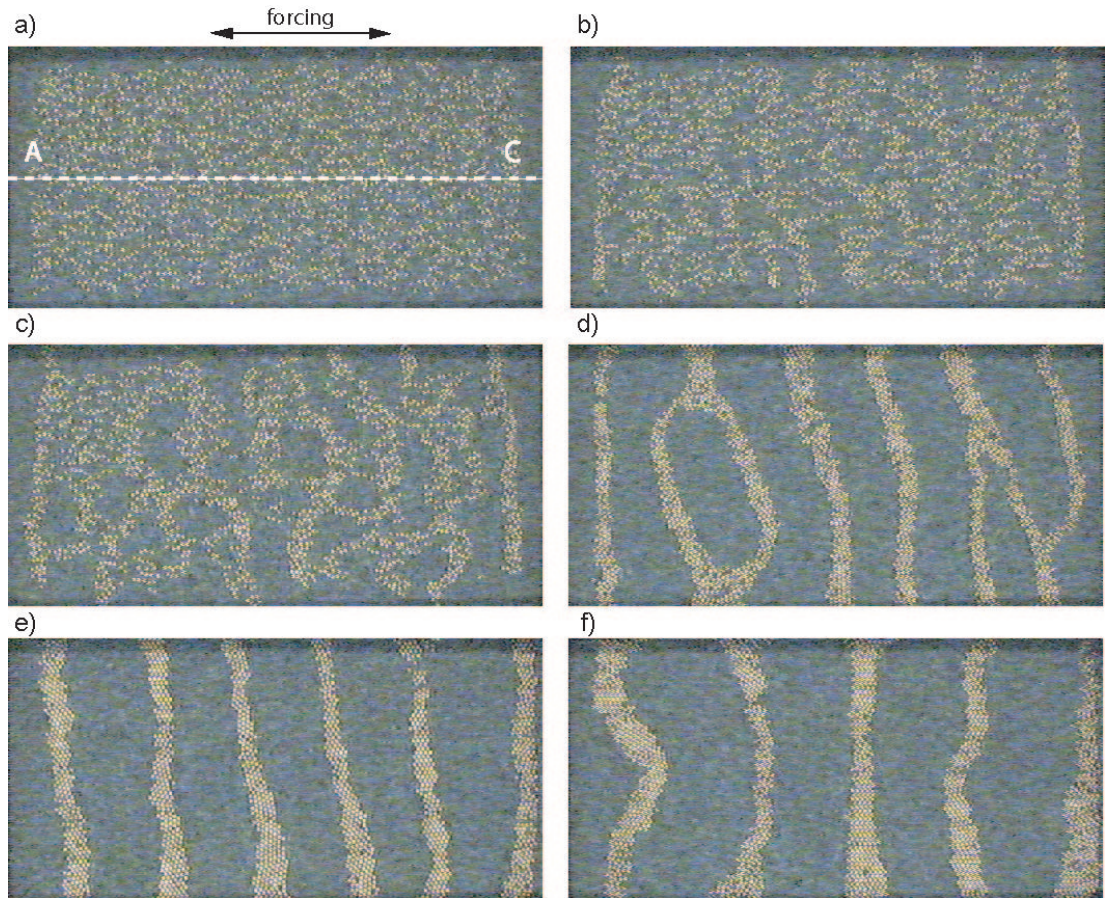


Figure 3.2: Temporal evolution of segregation patterns of a mixture of poppy seeds and phosphor-bronze spheres ( $C(N_1 = 1596) = 1.028$ ): (a) Initial homogeneous mixture (b)  $t = 6\text{sec}$  (c)  $t = 12\text{sec}$  (d)  $t = 54\text{sec}$  (e)  $t = 594\text{sec}$  (f)  $t = 1182\text{sec}$ . The white dashed line,  $AB$ , in (a) is the sampling line used in the construction of the space-time diagrams discussed in Section 3.2. The double arrows indicate the direction of the forcing.

*i.e.* the surrounding air does not appear to play a significant role in the segregation process. This suggests that the segregation mechanism is robust. For the remainder of the study we focus on the particular mixture of poppy seeds and phosphor-bronze spheres since this gave several practical advantages.

In order to introduce both the phenomena under study and the concepts that

will be used in the analysis in the next chapters we will focus on the behaviour at high compacities where stable and robust segregation stripes were observed. In Chapter 4 we will present the dependence of the segregation phenomena on the compacity of the layer in detail.

A typical time evolution for segregation of an initially homogeneous mixture with compacity  $C(N_1 = 1596) = 1.028$  is shown sequentially in the series of frames presented in Fig. 3.2(a-f). These snapshots were taken at the times indicated over an entire segregation sequence which lasted  $20min$ . The time instants in the figure are not equal and were chosen to highlight the fast initial segregation growth. During this period the mechanism of the segregation process is as follows. Initially, single large particles diffuse in a sea of the smaller ones, exploring different local configurations. When two large particles happen to come close together, the smaller particles cannot fit between them, and hence the pair is subjected to an asymmetric pressure that keeps it together. Subsequently, pairs may encounter others so that progressively larger clusters form. The unidirectionality of the driving induces an asymmetry in the segregated domains such that elongated domains of the larger phosphor-bronze spheres develop in a direction which is orthogonal to the direction of the drive. During this initial period, the rapid formation of clusters suggests an effective attractive force between the phosphor-bronze spheres, that leads to aggregation. Eventually, the domains are long enough, in the y-direction, so that, at high compacities, well defined stripes cross the full width of the tray (Fig. 3.2d). The behaviour at low and intermediate compacities is discussed in Chapter 4.

This initial segregation growth, occurring during timescales of the order of  $\sim 1min$ , then ceases and further coarsening of the segregation patterns takes place in much longer time scales. For example, the evolution from a six stripes pattern in Fig. 3.2(e) to the five stripes pattern in Fig. 3.2(f) took 10 min.

## 3.2 Space-time diagram construction

One way of analysing the time evolution of the segregation is via the construction of a space-time diagram. Such a diagram, for the experimental run we have just discussed in the previous Section, with  $C(N_1 = 1596) = 1.028$ , is presented in Fig. 3.3. This was formed by sampling the experimental frames along a single line in the  $x$ -dimension, and progressively stacking them over a period of  $20min$ . The sampling line was positioned at  $1/2$  of the  $y$ -length of the tray as indicated by the white dashed line,  $AB$ , superposed in Fig. 3.2(a). The experimental frames used to construct this space-time diagram were image processed following the procedure described in Section 2.8.1 such that regions of poppy seeds were given a value of 0 (black) and regions of phosphor-bronze spheres a value of 1 (white).

After the fast initial domain growth a pattern with 7 well defined stripes forms which progressively coarsens to 6 stripes (at  $t \sim 4min$ ) and eventually to 5 stripes (at  $t \sim 16min$ ). The late time coarsening of the pattern is driven by a process distinct from the one described above, by which segregation domains initially

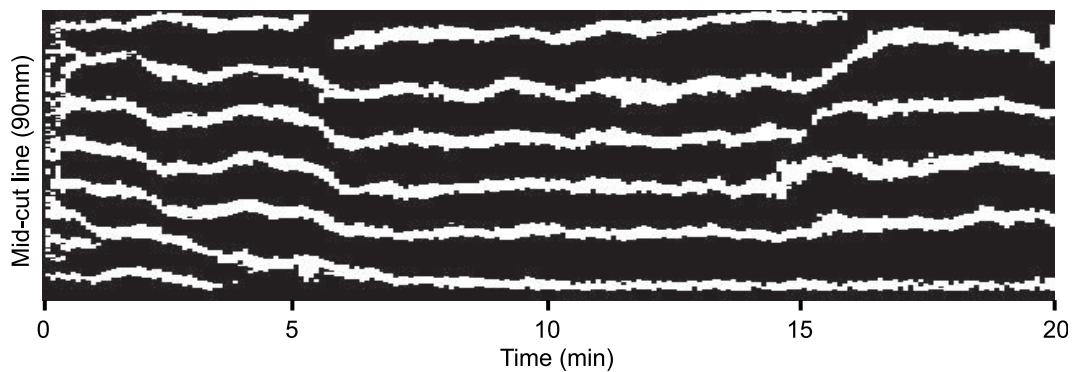


Figure 3.3: Space-time diagram for the evolution of the patterns which was constructed over a period of  $20min$ , by stacking, in time, the sampling mid cut line  $AB$  of the granular layer (dashed white line in Fig. 3.2a). Regions of poppy seeds are shown in black and regions of phosphor-bronze spheres in white.

form. The slow evolution of the patterns indicates the collective motion in the layer of poppy seeds, in the form of large scale vortices. Individual stripes can therefore be deformed through bending which can, in turn, influence collective motion in the layer. If these deformations are large enough, individual stripes can break up and each of the remains can then merge into its neighbouring stripes thereby inducing a coarsening of the pattern. A possible mechanism for the origin of these large scale dynamics will be discussed in Chapter B.

### 3.3 The average width and number of domains

At this point, we introduce a simple measure for the size of the domains that allows for a quantitative analysis of the emergence of the segregation domains and the subsequent evolution of the patterns. We focus on the average size of the clusters of phosphor-bronze spheres. We present a typical image processed pattern of the granular layer in Fig. 3.4(a) which we will use to illustrate the procedure. The image contains  $300 \times 600$  pixels with superposed horizontal,  $h$  sample line. As this line is sampled along  $x$ , a series of discrete jumps from  $0 \rightarrow 1$  and  $1 \rightarrow 0$  are observed. The location of each of these jumps corresponds to a single point in the domain boundary between regions of poppy seeds and regions of phosphor-bronze spheres. An example of a single profile along  $h$  is given in Fig. 3.4(b). Due to the geometry of the patterns, measures along  $h$  exhibited a series of well defined heaviside steps with a characteristic width  $L^x$ . The average domain width for an individual frame, i.e. at a particular time instant, is then calculated by scanning through each of the 300 horizontal lines and the widths,  $L_i^x$ , of each heaviside step are measured yielding a distribution of values. We therefore define the *average domains width* to be,

$$\phi = \langle L_i^x \rangle \quad (3.1)$$

where the brackets  $\langle \cdot \rangle$  denote averaging over all  $i$  steps found, along the 300 lines for a single frame. The number of such steps found, *per pixel line*, averaged over all 300 lines, is defined to be the *average number of domains*,  $\eta$ .

Typical 20min time-series for both  $\phi(t)$  and  $\eta(t)$ , for a layer with  $C(N_1 = 1596) = 1.028$ , are presented in Fig. 3.5(a). As before, the initial conditions

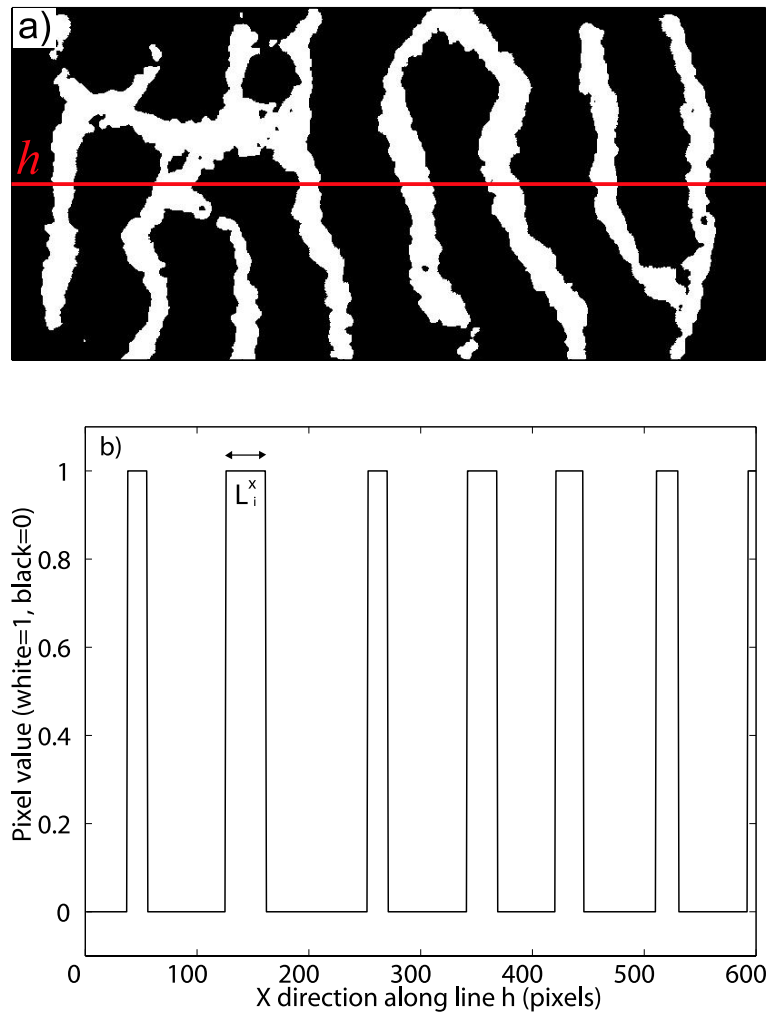


Figure 3.4: Definition of the average domains width. a) Typical image processed frame with two superposed sampling lines (in red):  $h(x)$  along x-direction ( $y_h = 150pixels$ ). b) Spatial profile for the sampling line  $h(x)$ . The width of each top-hat steps,  $i$ , along  $h(x)$  is  $L_i^x$ .

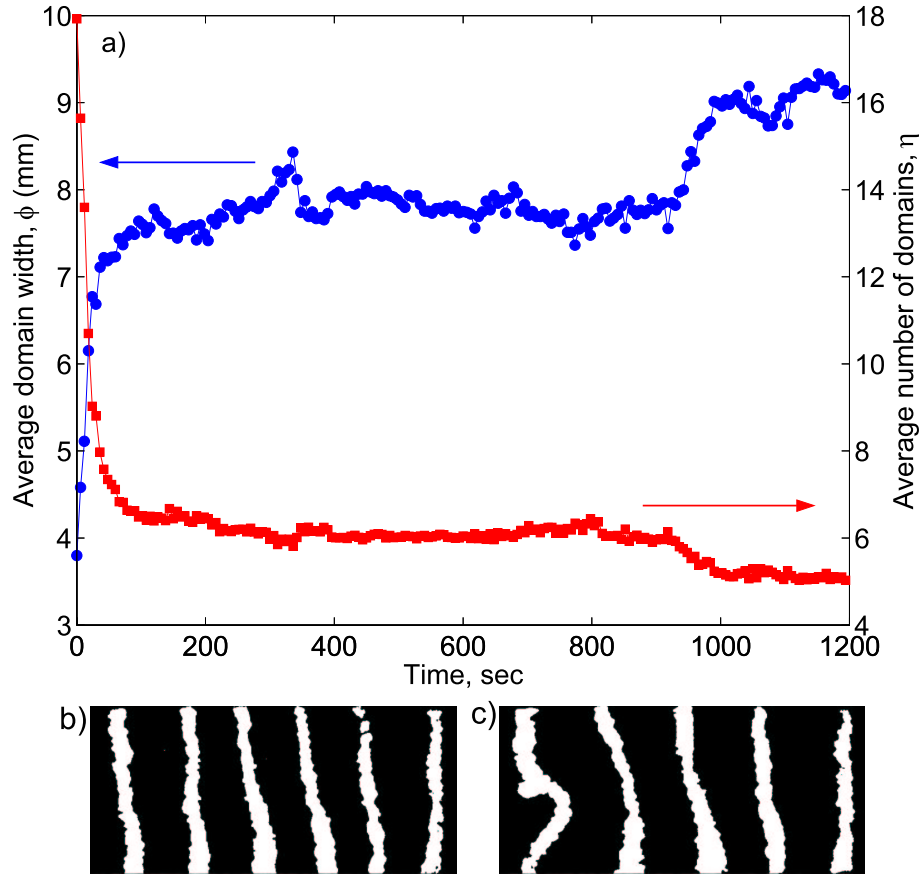


Figure 3.5: Typical time series of pattern evolution at  $C(N_1 = 1596) = 1.028$ . (a) Time series over 20min of average domains width  $\phi$  ( $\bullet$ ), and average number of domains,  $\eta$  ( $\blacksquare$ ), having started from a homogeneous mixture. Frames showing long time evolution of domains in the coarsening regime: (b) pattern with 6 stripes ( $t = 500$ sec) and (c) pattern with 5 stripes ( $t = 1200$ sec).

were a homogeneous mixture. The qualitative features of the pattern evolution discussed above can now be clearly seen. The initially homogeneous mixture has a domain width of  $\phi(t = 0) \sim 3.8$ mm which corresponds to clusters of  $\sim 2$  particles. These occur naturally in the initial conditions and hence set the minimum length of any cluster. As the driving is initiated,  $\phi$  rapidly increases, with a complementary decrease in  $\eta$ , as segregation domains initially form until

a level of  $\phi \sim 7.5mm$  is reached, *i.e.* clusters are, on average, five particles wide. After this point,  $t \gtrsim 1min$  of forcing, the average domain width exhibits a saturation plateau. As this plateau is reached, phosphor-bronze spheres are now part of first 7 (up to  $t \sim 4min$ ) and then 6 well defined stripes which are kept together by the pressure exerted by the surrounding poppy seeds. We denote this initial period, characterised by a fast growth of the domains, by *initial segregation growth regime*.

We refer to the period that follows, after the saturation level has been reached, by *coarsening regime*. As explained earlier, once the well defined domains of phosphor-bronze spheres form, further coarsening occurs via the collective motion in the layer of poppy seeds such that domains can be driven to split and merge. This slow coarsening process can be seen from the evolution of the pattern at  $t = 500sec$  with six stripes, shown in Fig. 3.5(b), which at  $t \sim 950sec$  evolves to the 5 stripes pattern shown in Fig. 3.5(c). We stress that there is a clear separation of the timescales of the initial segregation growth regime and those of the coarsening regime.

A result which may be inferred from both sets of time sequences in Fig. 3.5 is that, when the domains form, there is a progressive coalescence of clusters with an increase of the average width,  $\phi$ , and corresponding decrease in the number of domains,  $\eta$ , in the granular layer.

### 3.4 Pattern reproducibility

Another issue of interest is the reproducibility of the segregated patterns. We have investigated this for the particular mixture with  $C(N_1 = 1596) = 1.135$ . The reproducibility of the pattern was studied by carrying out 50 experimental runs, under identical conditions. Experiments were started from a homogeneous configuration and were run for 10min, after which a photograph of the granular

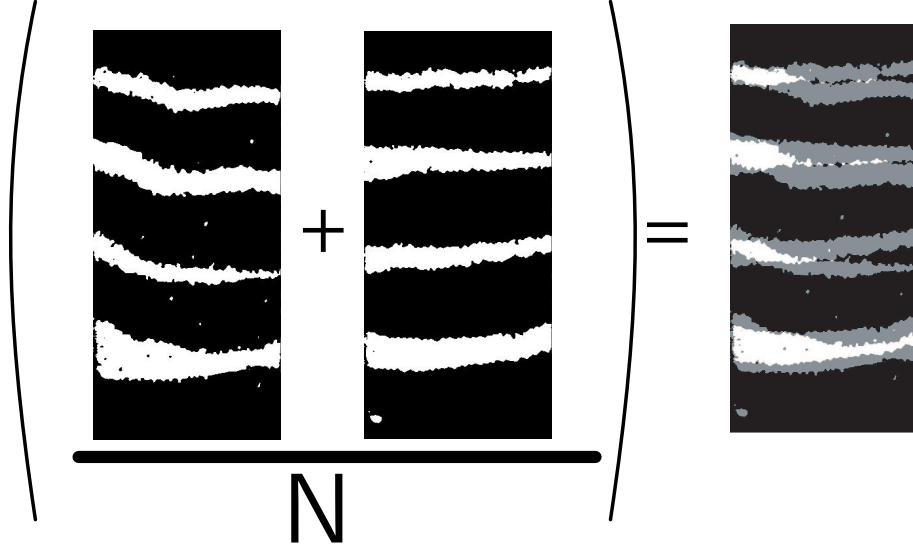


Figure 3.6: Schematic diagram for the construction of the Probability Distribution Image (PDI). In the obtained PDI, with  $N = 2$ , black regions have  $PDI(x_i, y_j) = 0$ , white regions have  $PDI(x_i, y_j) = 1$  and grey regions have  $PDI(x_i, y_j) = 0.5$ .

layer was taken. Each of the  $n$  frames (image processed using the method presented in Section 2.8.1), was thereafter treated as  $(300 \times 600)$  matrices,  $I_n$ , with each element,  $I_n(x_i, y_j)$ , being the pixel value: 0 if pixel corresponds to a region of poppy seeds or 1 if it signifies a region of phosphor-bronze spheres. From these we then constructed a Probability Distribution Image ( $PDI$ ) as shown by the schematic diagram in Fig. 3.6. The matrices were added together and normalized by the number of realization ( $N = 50$ ),

$$PDI(x_i, y_j) = \sum_{n=1}^N \frac{I_n(x_i, y_j)}{N}, \quad (3.2)$$

for  $x_i = 1 \rightarrow 600$  and  $y_j = 1 \rightarrow 300$ . Hence,  $PDI(x_i, y_j) = 1$  if a phosphor-bronze was always found at  $(x_i, y_j)$  or  $PDI(x_i, y_j) = 0$  if a poppy seed was always observed at that location.

In Figure 3.7(a) we show the  $PDI$  for a mixture with  $C(N_1 = 1596) = 1.135$ ,

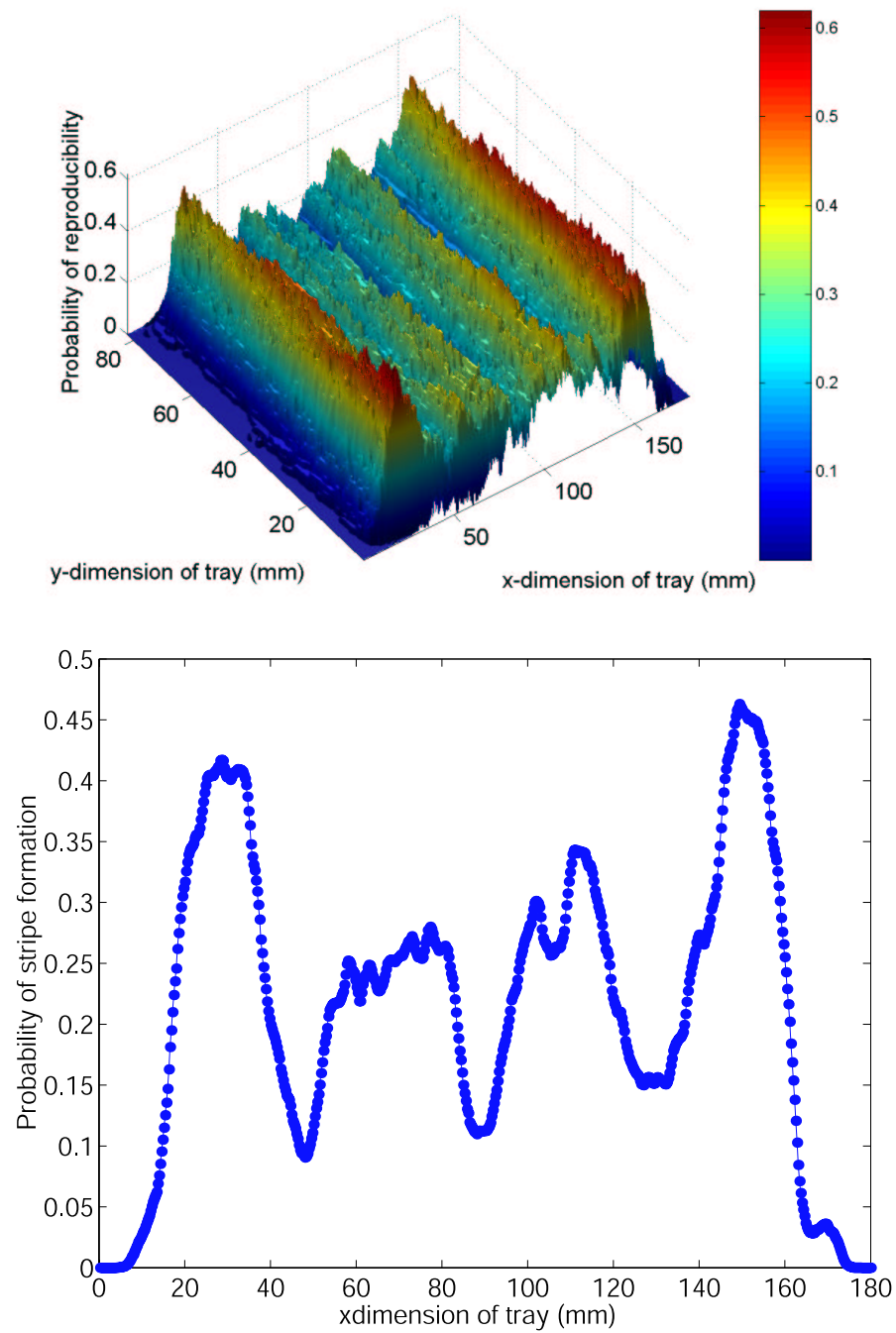


Figure 3.7: Probability Distribution Image. a) PDI for 50 realisation of identical experimental runs with  $C(N_1 = 1596) = 1.135$ . b) PDI averaged along the y-direction.

where 4 distinct peaks can be observed. This indicates that a four stripe pattern emerges on average where the stripes formed preferentially at the same locations and were systematically perpendicular to the direction of the drive. This pattern reproducibility can be seen more clearly in Figure 3.7(b) where the *PDI* has been averaged along the  $y$  direction of the tray. The four stripes form preferentially with their centres at the locations  $x_1 \sim 30mm$ ,  $x_2 \sim 70mm$ ,  $x_3 \sim 117$  and  $x_4 \sim 149mm$ . Also note that the probability of formation for the two outermost stripes, near  $x_1$  and  $x_4$ , is higher than that for the inner stripes, near  $x_2$  and  $x_3$ . This probably results from the presence of the nearby end-walls

# Chapter 4

## Domain-level ‘macroscopic’ measures

In the present Chapter a discussion is presented of the emergence of the segregation domains, as a function of the layer compacity. In particular, the average width and number of domains, as well as their associated evolution timescales, are analysed. Moreover, we report measurements of the macroscopic fluctuations of the domains. The results are interpreted in terms of three distinct segregation phases and these are classified as *binary gas*, *segregation liquid* and *segregation crystal*. Each phase is identified to lie within a distinct range of compacity.

### 4.1 Compacity dependence studies

In Chapter 3 it was shown that there is a distinct separation of timescales in the two regimes which were identified as the *initial segregation growth* and the *slow coarsening* regimes. We now concentrate on the segregation process at early times and study the ‘*macroscopic*’ properties of the domains which form during these period.

Throughout this Chapter the driving parameters are fixed at a single frequency

$f = 12Hz$  and amplitude  $A = \pm 1.74mm$  and the aspect ratio is  $\Gamma = 2$  and all experiments were performed with the mixture of poppy seeds and phosphor-bronze spheres. The principle objective of this part of the study was to investigate the dependence of the segregation process on the total filling fraction of the layer. This was done by incrementally increasing the number of poppy seeds,  $N_{ps}$ , in the layer, in measured steps, while the number of phosphor-bronze spheres,  $N_{pb} = 1596$ , was held constant, i.e.  $C = C(N_{ps})$ . All experimental runs were started from a homogeneous mixture using the procedure described in Section 2.6. For the experimental results presented in this Chapter we chose to perform the experiments by changing the numbers of poppy seeds. The qualitative behaviour presented here was found to be robust over a range of  $N_{pb}$  but in Chapter 6 we discuss, in more detail, the phase diagram behaviour for  $C(N_{ps}, N_{pb})$ .

A digital video of the granular layer was recorded, using the colour system presented in Section 2.7, and the experimental frames were acquired at a frame-rate of  $1/6Hz$  which were further image processed as described in Section 2.8.1. This way, the video frames were processed and transformed into binary images with black regions (pixel value equals 0) for regions of poppy seeds and white regions (pixel value equals 1) for regions of phosphor-bronze spheres.

## 4.2 Space-time diagrams

In Fig. 4.1 we present a series of space-time diagrams for runs of 10min, for increasing  $C$ , which were constructed using the procedure described in Section 3.2. At the lowest compactities, it can be seen that the binary layer remained mixed for the duration of the experiment. The space-time for  $C = 0.516$  is representative of this regime. The behaviour of the system can be considered as similar to that of a low density granular gas with two species. Experimental runs with the highest compactities, of which  $C = 0.985$  is a typical example,

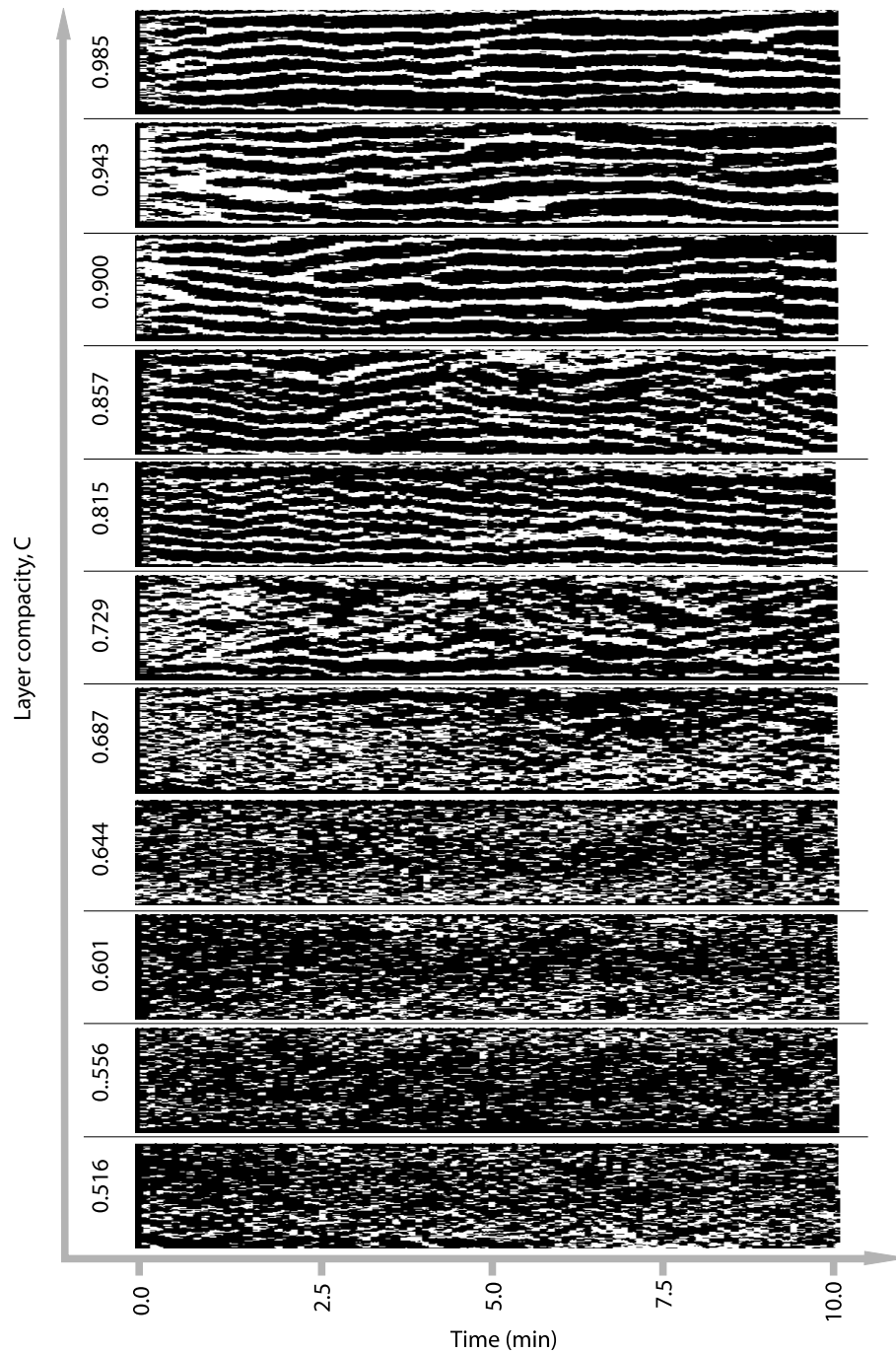


Figure 4.1: Series of space-time diagrams as a function of the layer compacity which were constructed as explained in Section 3.2. Each of them is a stack in time, over 10min, of the mid-cut line of the granular layer (white dashed line in Fig. 3.2). At low compacities a mixed state is observed and no segregation occurs. At high compacities segregated structures form within the first minute of forcing. All runs were started from homogeneously mixed initial conditions.

display qualitatively different behaviour. At early times, small localized clusters of phosphor-bronze spheres (white regions) form and progressively coalesce with neighbouring ones, as described in the Chapter 3. Thereby coarsening occurs, so that well defined crystalline stripes are eventually formed, aligned perpendicularly to the direction of forcing, separated by dense regions of poppy seeds.

At intermediate values of  $C$ , partially segregated states emerge.

### 4.3 The average domain width: an order parameter

The sequence of space-time diagrams presented in Fig. 4.1 suggests the possibility that a critical compacity is required for segregation to occur, as  $C$  is gradually incremented.

In order to proceed, we regard the average domain width of the phosphor-bronze spheres,  $\phi$ , along the x-direction, as an order parameter. The average width of the domains was measured as explained in Section 3.3. We focus on the initial segregation growth regime and study the dynamics of  $\phi(t)$  and its dependence on  $C$ .

In Fig. 4.2, we present typical time-series of  $\phi(t)$  for four different values of  $C$ , over the first 4min of vibration, where each run has been started from a mixed state. At large compacities there is a fast initial growth which saturates after  $\sim 1min$  (see the representative curve with  $C = 0.900$  in Fig. 4.2). As  $C$  is decreased,  $\phi(t)$  exhibits a similar behaviour with a fast initial growth followed by a saturation level, for which  $C = 0.751$  and  $0.729$  are typical examples. However, this saturation level in Fig. 4.2 was systematically lowered and there was a gradual increase of the overall motion of segregation domains so that they became more mobile. At low values of the compacity there is little evolution of  $\phi(t)$  and

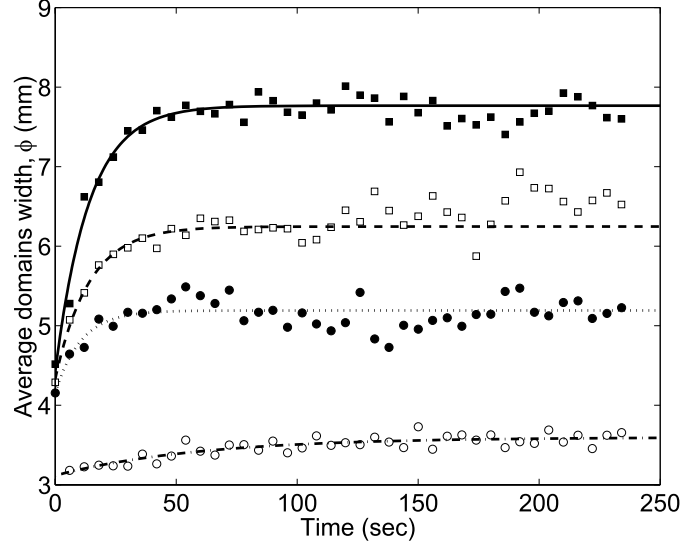


Figure 4.2: Time-series of average domain width,  $\phi$ , for four different compactities: ( $\blacksquare$ )  $C = 0.900$ , ( $\square$ )  $C = 0.751$ , ( $\bullet$ )  $C = 0.729$ , ( $\circ$ )  $C = 0.623$ . Lines are exponential fits to Eqn. (4.1). All runs were started from a homogeneously mixed layer.

no clear segregation domains are observed as shown by the representative curve in Fig. 4.2 for this regime with  $C = 0.623$ .

The superimposed lines, on the experimental time series in Fig. 4.2, are fits of,

$$\phi(C, t) = \Sigma^\phi - b^\phi \cdot \exp\left(-\frac{t}{t_s^\phi}\right), \quad (4.1)$$

to the experimental time series of  $\phi$ , where  $\Sigma^\phi$  is the value at which  $\phi(t)$  saturates,  $\Sigma^\phi - b^\phi$  is the initial value  $\phi(t = 0)$  and  $t_s^\phi$  is the *segregation time*; a timescale associated with the saturation of the domain growth. We denote  $\Sigma^\phi$  by the *segregation level*.

## 4.4 Continuous phase transition for segregation

A plot of the dependence of the segregation level,  $\Sigma^\phi$ , on the compacity of the layer is presented in Fig. 4.3(a). For low compacities, up to a value,  $C_c^\phi \sim 0.665$ , the value of the segregation level is approximately constant at  $\Lambda^\phi = (3.25 \pm 0.24)mm$ . This corresponds to configurations of pairs of spheres and we do not classify these structures as domains; the system is deemed to be in a mixed or unsegregated state. This is essentially a collisional regime since there is enough free volume in the system so that particles collide and randomly diffuse. We denote this regime by a *binary gas*.

As  $C$  is increased, past  $C_c^\phi$ , clusters of the larger particles form and mobile segregation domains, of increasing  $\phi$ , emerge in a nonlinear way. To check this functional dependence of the segregation level, in Fig. 4.3(b) we have plotted the quantity,

$$l^\phi(C) = (\Sigma^\phi - \Lambda^\phi)^2, \quad (4.2)$$

where  $\Lambda^\phi$  is the segregation level for  $C \lesssim C_c^\phi$ . It can be seen that the constant level corresponding to the mixed binary gas state with  $\Lambda^\phi = (3.25 \pm 0.24)mm$ , for  $C \lesssim 0.665$ , is followed by a square root growth in the average domain width of the form,

$$l^\phi(C) = -(A^\phi)^2 C_c^\phi + (A^\phi)^2 C, \quad (4.3)$$

where  $A^\phi = (8.16 \pm 0.29)mm$  is a scaling factor which was determined from a least squared linear fit. The intersect between  $l^\phi(C)$  and  $l^\phi = 0$  provides an estimate for the critical compacity value for granular segregation of  $C_c^\phi = 0.644 \pm 0.065$ . In Fig. 4.3(a), we have superposed the solid curve used for least squares fit of the form,

$$\Sigma_\phi^{fit} = A^\phi \sqrt{C - C_c^\phi} + \Lambda^\phi, \quad (4.4)$$

where  $\{C_c^\phi, \Lambda^\phi\}$  is the critical point for segregation at which the transition oc-

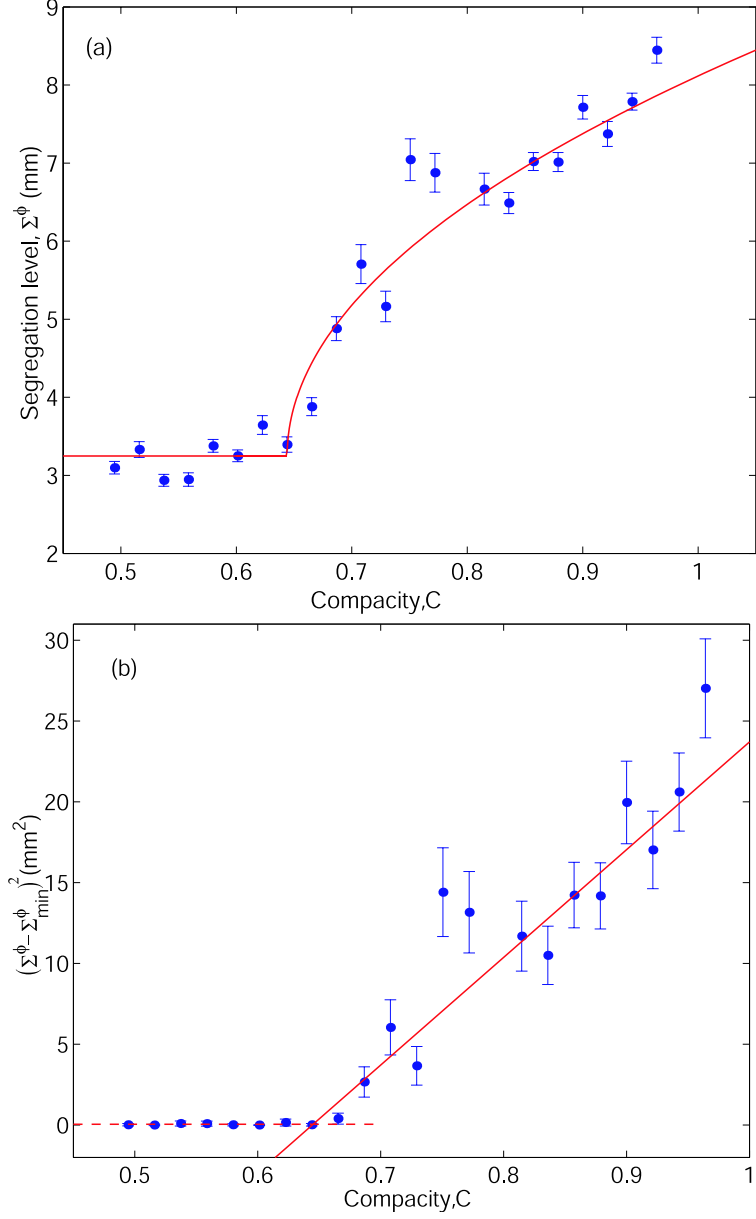


Figure 4.3: Segregation phase transition. (a) Compacity dependence of average domain width saturation level,  $\Sigma^\phi$ . The solid red line is a square-root given by Eqn. (4.4). (b) Compacity dependence of  $l^\phi(C) = (\Sigma^\phi - \Lambda^\phi)^2$ . The critical point  $C_c^\phi$  is determined from the intercept between the horizontal dashed line and the solid line which is the best least squares fit to  $l^\phi(C) = -(A^\phi)^2 C_c^\phi + (A^\phi)^2 C$  with  $A^\phi = 8.16 \pm 0.29$  and  $C_c^\phi = 0.644 \pm 0.065$ .

curs, which is valid within the range  $0.644 < C < 0.964$ . We conclude that this scenario is consistent with the existence of a continuous phase transition for granular segregation of the binary mixture, as the layer compacity is incrementally increased, with a critical point for segregation at  $C_c^\phi = 0.644 \pm 0.065$ .

## 4.5 The Number of domains

We analyse the data for the average number of domains,  $\eta$ , (defined in Section 3.3) in the same way to that followed for the average domain width,  $\phi$ . The corresponding time series for  $\eta$  at four different compacities are shown in Fig. 4.4. One expects, the behaviour of  $\eta$  to be complementary to that of  $\phi$  since the number of phosphor-bronze spheres in the system is constant. Indeed, for large values of  $C$  (*e.g.*  $C = 0.900$ ),  $\eta$  decreases rapidly as increasingly wider domains form, up to a level  $\Sigma^\eta$  at which saturation occurs. The saturation level decreases systematically as the  $C$  is decreased. At the lower values of  $C$  (*e.g.*  $C = 0.623$ ),  $\eta$  shows little evolution since no formation of well defined segregation occurs. Once again, the time series are well fitted by exponentials of the form,

$$\eta(C, t) = \Sigma^\eta + b^\eta \cdot \exp\left(-\frac{t}{t_s^\eta}\right), \quad (4.5)$$

but, now, note the negative coefficient of the  $\exp(\cdot)$  term.

As before, we now extract  $\Sigma^\eta$  as a function of  $C$ . The saturation level of the average number of domains, plotted in Fig. 4.5(a), remains at an approximately constant level ( $\Lambda^\eta = 14.58 \pm 0.29$ ) over a range of  $C$ . However, above  $C \gtrsim 0.623$  it rapidly decreases with  $C$ . In Fig. 4.5(b) we plot the quantity,

$$l^\eta(C) = (\Sigma^\eta - \Lambda^\eta)^2, \quad (4.6)$$

which shows linear behaviour of the form

$$l^\eta(C) = -(A^\eta)^2 C_c + (A^\eta)^2 C, \quad (4.7)$$

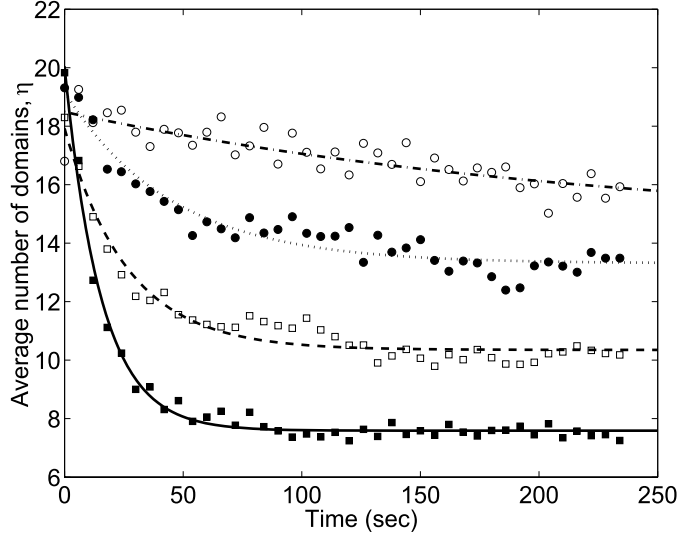


Figure 4.4: Time-series of average number of domains,  $\eta$ , for four different compacities: (■)  $C = 0.900$ , (□)  $C = 0.751$ , (●)  $C = 0.729$ , (○)  $C = 0.623$ . Lines are exponential fits to Eqn. (4.5). All runs were started from a homogeneously mixed layer.

with a scaling factor  $A^\eta = 18.98 \pm 0.68$  and critical point  $C_c^\eta = 0.687 \pm 0.087$ . This reinforces the square root behaviour of  $\Sigma^\eta$  within the range  $0.687 < C < 0.921$ . Note that the critical values for the compacity obtained from both  $\eta$  and  $\phi$  ( $C_c^\phi = 0.644 \pm 0.065$  and  $C_c^\eta = 0.687 \pm 0.087$ , respectively) are self-consistent. From now on, when we refer to the critical point for segregation we use the average of  $C_c^\phi$  and  $C_c^\eta$ , i.e.  $C_c = 0.67 \pm 0.06$ .

## 4.6 Segregation timescales

In Fig. 4.6(a) and (b) we present the segregation times,  $t_s^\phi$  and  $t_s^\eta$ , as a function of  $C$ , obtained from the fits of  $\phi(t)$  to Eq. (4.1) and  $\eta(t)$  to Eq. (4.5). Note that we only define  $t_s$  for  $C > C_c$ , since this is the parameter range over which segregation occurs. As expected for a continuous phase transition,  $t_s$  appears

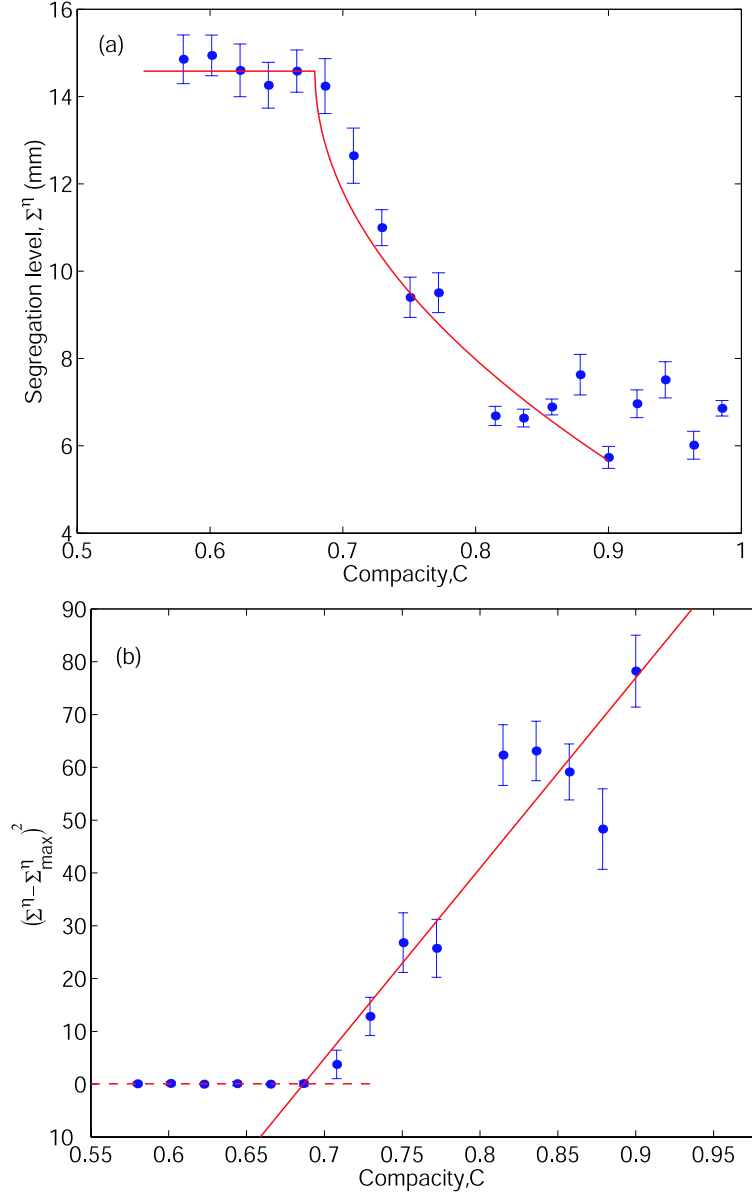


Figure 4.5: Segregation phase transition. (a) Compacity dependence of the saturation level of the average number of domains,  $\Sigma^\eta$ . The solid red line is the square-root given  $\Sigma_\eta^{fit} = A^\eta \sqrt{C - C_c^\eta} + \Lambda^\eta$  obtained from the least square fits of  $l^\eta(C) = -(A^\eta)^2 C_c + (A^\eta)^2 C$ , within the range  $0.687 < C < 0.921$ . (b) Compacity dependence of  $l^\eta(C) = (\Sigma^\eta - \Lambda^\eta)^2$ . The critical point  $C_c^\phi$  is determined from the intercept between the horizontal dashed line and the solid line which is the best least squares fit to Eqn. (4.7) with  $A^\eta = 18.98 \pm 0.68$  and  $C_c^\eta = 0.687 \pm 0.087$ .

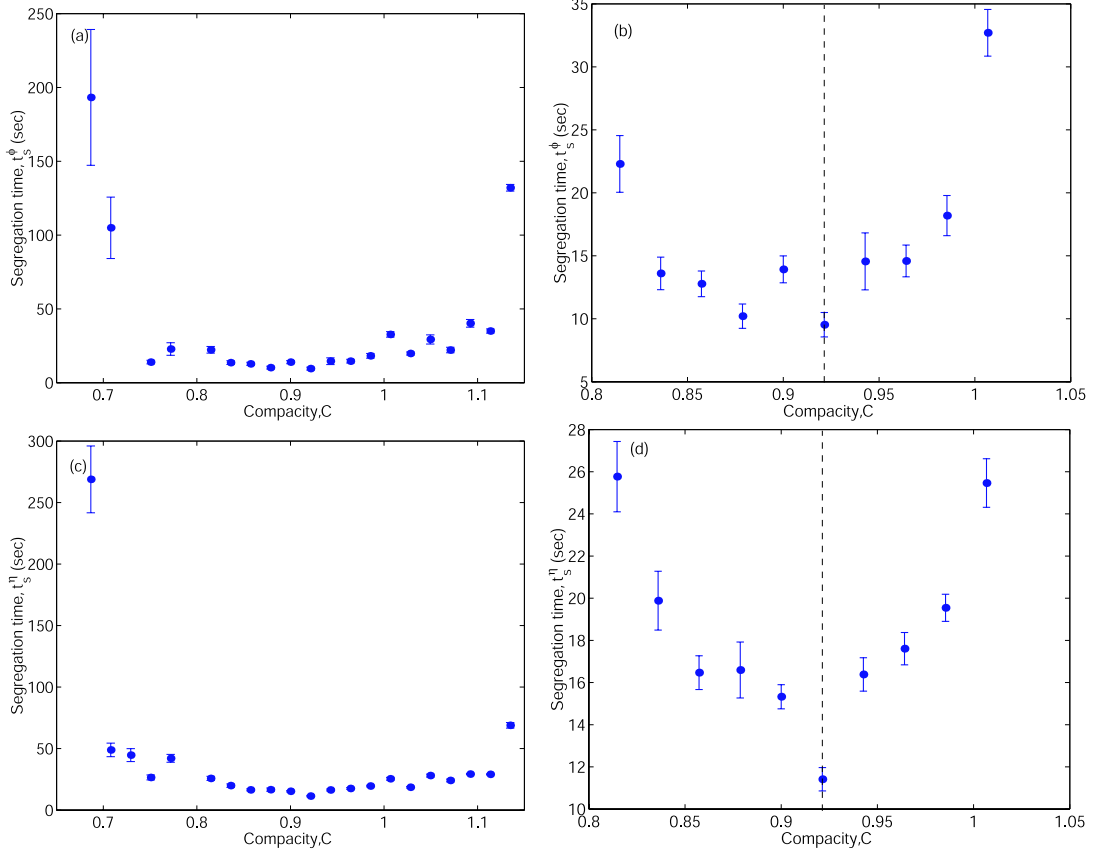


Figure 4.6: (a) Segregation time,  $t_s^\phi$ , for the average domain width, obtained from the fits of the initial segregation growth to Eqn. (4.1). (b) Zoom of  $t_s^\phi$  around  $C = 0.9$ . The vertical dashed line, at  $C_m = 0.921$ , represents the location at which the minimum of  $t_s^\phi$  occurs ( $t_s^\phi(C_m) = 9.53\text{sec}$ ). (c) Segregation time,  $t_s^\eta$ , for the average number of domains, obtained from the fits of the initial segregation growth to Eqn. (4.5). (d) Zoom of  $t_s^\eta$  around  $C = 0.9$ . The vertical dashed line, at  $C_m = 0.921$ , represents the location at which the minimum of  $t_s^\eta$  occurs ( $t_s^\eta(C_m) = 11.41\text{sec}$ ).

to diverges, as  $C$  is decreased from above to values near  $C_c$ . This phenomena is usually referred to as *critical slowing down* (Chaikin 1995) and adds further evidence that supports the existence of a phase transition.

The segregation time decreases with increasing  $C$  up to a point  $C_m$  after which there is a qualitative change in the behaviour. For  $C > C_m$  the granular mixture takes increasingly longer to segregate for increasing  $C$ , *i.e.*  $t_s$  exhibits a minimum at  $C_m$ . In Fig. 4.6(b) and (d) we have zoomed the segregation times around this minimum point at intermediate compacities. The location of these minima (vertical dashed lines in the figure) for both  $\phi$  and  $\eta$  is identical and occurs at  $C_m = 0.921$  with  $t_s^\phi(C_m) = 9.53\text{sec}$  and  $t_s^\eta(C_m) = 11.41\text{sec}$ , respectively. It is interesting to note that the compacity value at which this qualitative change in the segregation dynamics occurs is close to the point of maximum packing of disks in two dimensions:  $C_{max}^{2D} = \pi/\sqrt{12} \sim 0.906$ . Hence, this change in behaviour could have its origin in the fact that for the highest values of the compacity the mixture packs the surface of the tray and the three-dimensionality direction of the layer starts being explored.

## 4.7 Macroscopic fluctuations of domains

We explore the segregation behaviour further by measuring the fluctuations,  $f(t)$ , of  $\phi(t)$ . These fluctuations provide a macroscopic measure of the collective noise of the domains' dynamics.

To obtain  $f(t)$ , we filter  $\phi(t)$  to separate the relatively fast fluctuation dynamics from the slower growth behaviour by high-pass filtering. The time-series for the average domain width,  $\phi(t)$ , were first digitally low-passed filtered, through a low-pass finite impulse response (FIR) digital filter algorithm<sup>1</sup> (Press, Teukolsky,

---

<sup>1</sup>This algorithm is implemented in the Signal Processing Toolbox in the package MATLAB 6.0 (R12).

Vetterling & Flannery 1992) with brickwall at  $\omega = 2.29 \times 10^{-2} Hz$  and  $-3dB$  point at  $\omega = 9.77 \times 10^{-3} Hz$  to obtain  $\phi_{filtered}(t)$ . A typical time series of  $\phi(t)$  and its filtered version  $\phi_{filtered}(t)$ , for  $C = 0.751$ , are presented in Fig. 4.7(a). The macroscopic fluctuations are then given by the difference

$$f(t) = \phi(t) - \phi_{filtered}(t), \quad (4.8)$$

an example of which, for  $C = 0.729$ , is plotted in 4.7(b).

The root mean square (RMS) of these fluctuations,

$$R = \sqrt{\langle f(t)^2 \rangle}, \quad (4.9)$$

is then calculated as a function of  $C$ , where the brackets  $\langle \cdot \rangle$  denote a time average. The top-hat behaviour of  $R(C)$ , shown in Fig. 4.8, indicates that three qualita-

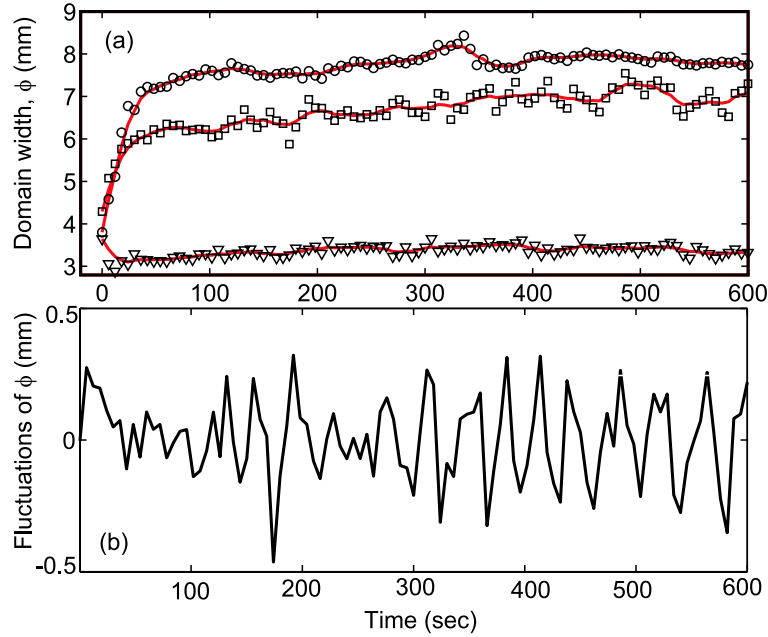


Figure 4.7: a) Time-series of,  $\phi(t)$ : ( $\nabla$ ) for  $C = 1.028$  ( $\square$ ) for  $C = 0.751$  and ( $\circ$ ) for  $C = 0.580$ . The solid red curves are the digital low-passed experimental signals,  $\phi_{filtered}(t)$ , for the respective compacity values. (b) Time series of the macroscopic fluctuations,  $f(t) = \phi(t) - \phi_{filtered}(t)$  for  $C = 0.751$ .

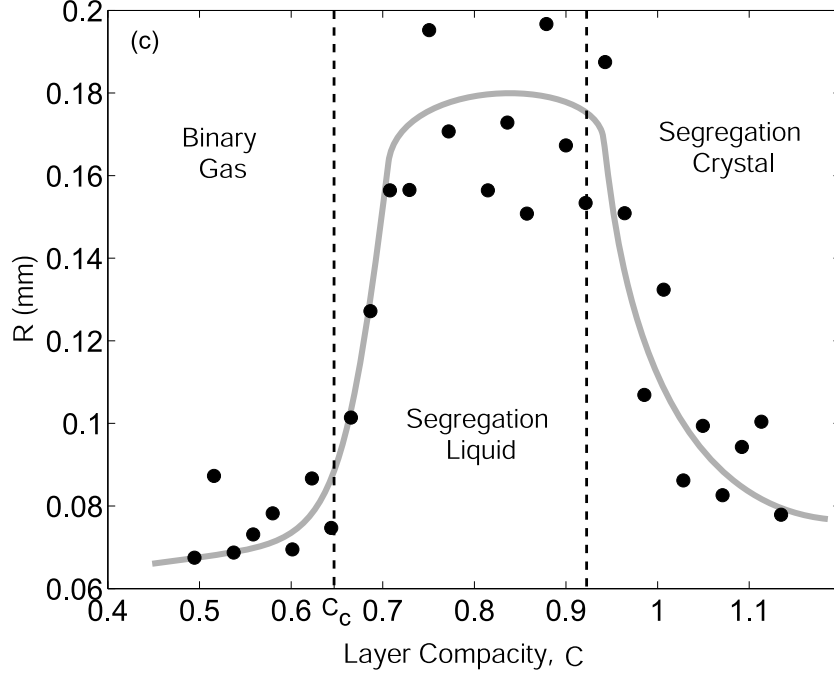


Figure 4.8: Root-mean-square of the fluctuations,  $R$ , plotted as a function of  $C$ . The solid vertical line corresponds to the location of the critical point,  $C_c = 0.665$ , discussed in Section 4.5. The dashed vertical line at  $C_m = 0.921$  corresponds to the location at which the minimum in the segregation time,  $t_s$ , is observed. The solid grey line is a guide to the eye.

tively different regimes exists. At low values of  $C \lesssim 0.665$  no segregation clusters form and  $R$  is low. However, as the critical point,  $C_c \sim 0.665$ , is approached at intermediate compacities ( $0.665 \lesssim C \lesssim 0.921$ ), the macroscopic fluctuations of the domains grows substantially as transient mobile clusters form. As  $C$  is increased further, past  $C \gtrsim 0.921$ ,  $R$  decreases. Note that the compacity point,  $C \sim 0.665$ , at which the rapid increase of the macroscopic fluctuations occurs is consistent with the location of the critical point obtained from  $\Sigma^\phi$  and  $\Sigma^\eta$ , at  $C_c = 0.665 \pm 0.068$  (vertical solid line in Fig. 4.8). Moreover, the fluctuations decrease at the point which coincides with  $C_m = 0.921$  (vertical dashed line in Fig. 4.8) where there is a qualitative change in the behaviour of the segregation

times, as discussed in the Section 4.6.

## 4.8 Summary: the three phases scenario

In this Chapter we have analysed macroscopic measures for granular segregation in a binary mixture of poppy seeds and phosphor-bronze spheres. In particular we have discussed the saturation levels of the average width of the domains and their average numbers. An essential feature of the processes involved was shown to be associated with their segregation timescales including the macroscopic fluctuations. All these quantities exhibit significant changes at two compacity points:  $C_c = 0.665$  and  $C_m = 0.921$ .

All of the above data is consistent with a scenario of three qualitatively distinct regimes: Regime I for  $C < C_c$ , Regime II for  $C_c < C < C_m$  and Regime III for  $C > C_m$ . A useful way of classifying the behaviour is in terms of three phases which we identify as *binary gas*, *segregation liquid* and *segregation crystal*. Typical zoomed photographs of the granular layer in each of these phases are shown in

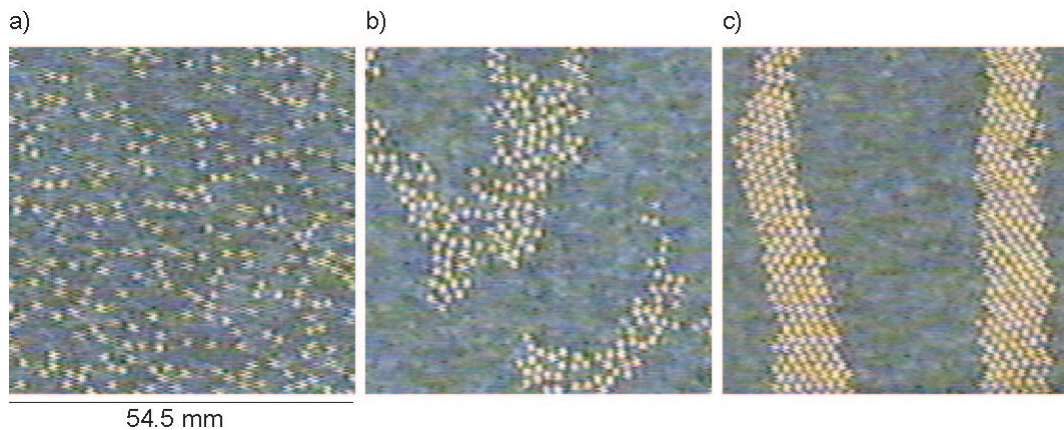


Figure 4.9: Zoomed photographs of the granular layer in each of the segregation phases. (a) Binary gas at  $C = 0.516$  ( $t = 600\text{sec}$ ). (b) Segregation liquid at  $C = 0.772$  ( $t = 660\text{sec}$ ). (c) Segregation crystal at  $C = 1.071$  ( $t = 624\text{sec}$ ).

Fig. 4.9 at (a)  $C = 0.516$ , (b)  $C = 0.772$  and at (c)  $C = 1.071$ .

In the *binary gas* phase, at low compacities, there was enough free volume in the system and individual particles were sufficiently agitated so that particles randomly diffused, without aggregation (Fig. 4.9a). This is essentially a collisional regime.

In the *segregation liquid* phase, above  $C_c$ , aggregation of the phosphor-bronze spheres occurred such that clusters formed (Fig. 4.9b). Near  $C_c$ , the clusters of larger particles were mobile and their movement was reminiscent of oil drops on water as they flowed, merged and split. This motion is evident in the measure of the fluctuations which has a sharp increase at  $C_c$ . As  $C$  was increased further there was a gradual decrease of the overall motion of segregation domains so that they become less mobile. The transition from the *binary gas* to *segregation liquid* phase has the characteristics of a continuous phase transition with square-root dependence of the saturation levels of  $\phi$  and  $\eta$ . Moreover, critical slowing down of the segregation times scales was found near  $C_c$ .

At high compacity values, past  $C_m$ , a second qualitative change of the structure and dynamics of the domains occurs. At this high  $C$  stable crystalline domains form, suggesting a segregation liquid to crystal transition and so we denote this third regime by *segregation crystal* (Fig. 4.9c). At  $C_m$  there is a minimum in the segregation times scales and the domains, for increasing  $C$ , took increasingly longer to develop. This was accompanied by a sharp decrease in the macroscopic fluctuations as individual spheres were *arrested* by the surrounding neighbouring particles. Due to the monodispersity of the phosphor-bronze spheres the segregation domains in this phase consisted of particles disposed in a hexagonally packed lattice.

It is interesting to point out that the value at which the transition between binary gas and segregation liquid phase occurs,  $C_c = 0.67 \pm 0.06$ , is close to the

order-disorder transition in a two dimensional hard sphere system, which occurs at a filling fraction of 0.65, for equally sized particles (Luding 2001).

# Chapter 5

## ‘Microscopic’ measures

In Chapter 4, the dynamics of segregation were discussed from a ‘*macroscopic*’ perspective at the domain level and three distinct phases of the binary mixture were identified: *binary gas*, *segregation liquid* and *segregation crystal*. In this Chapter we report the properties of the mixture found when using a variety of *microscopic* quantities as measured by the positions of the individual phosphor-bronze spheres. These provide further evidence for the proposed phase behaviour scenario. The main aim is not only to quantitatively describe the properties of each of the three granular segregation phases but also to analyse the associated transitions. For this, a variety of quantities commonly used in condensed matter and soft condensed matter physics are employed. In particular, we recur to the local Voronoi area density (Section 5.2), the nearest neighbours angular probability distribution function (Section 5.3), the radial distribution function (Section 5.4) which we use to obtain both dynamical and structural information on the segregation behaviour.

### 5.1 Granular segregation: a ‘microscopic’ view

In this Chapter the focus is on the results of a study of the *microscopic* characteristics of the mixture of poppy seeds and phosphor-bronze spheres. By microscopic,

it is meant that both structural and dynamical quantities are analysed using the positions of the individual phosphor-bronze spheres. Accurate estimation of these measures required high resolution digital images, so we have restricted the view to a central window of the layer with area  $(73.14 \times 59.50) \text{mm}^2$ . The procedure for the extraction of the particle coordinates from the digitised experimental frames was presented in Section 2.8.2. Throughout this Chapter, experiments were performed with the driving parameters set at  $A = \pm 1.74 \text{mm}$  and  $f = 12 \text{Hz}$ , respectively, on a tray of width  $\Delta y = 90 \text{mm}$  and aspect ratio  $\Gamma = 2$ . All experimental runs were consistently started from a homogeneous mixture for the initial conditions.

Since the granular layer was not imaged in full, it should be noted that it was possible for particles to move in and out of the imaging window. However, this should have little effect in the quantities addressed later in this Chapter, namely the Voronoi characteristic area density and associated fluctuations (Section 5.2), the angle between nearest neighbours (Section 5.3) and the radial distribution function (Section 5.4). This is due to the fact that these quantities are local in nature. The calculation of the Voronoi measures and the angle between nearest neighbours depends only on the first shell of nearest neighbours and the radial distribution function is only considered within a neighbourhood of 3.5 sphere diameters.

The temporal evolution of the layer, analogous to the segregation patterns discussed in Section 3.1 is shown in Fig. 5.1(1-f) in the zoomed image geometry, for a mixture with  $C = 0.996$ . When the oscillatory driving was initiated, the initially homogeneous mixture rapidly segregated. Initially, individual large spheres came together to form clusters which coalesced with nearby clusters, thereby inducing segregation. At this compacity value, well structured stripes eventually formed, which were aligned perpendicular to the direction of the driving. The qualitative segregation description of the formation of domains was discussed in

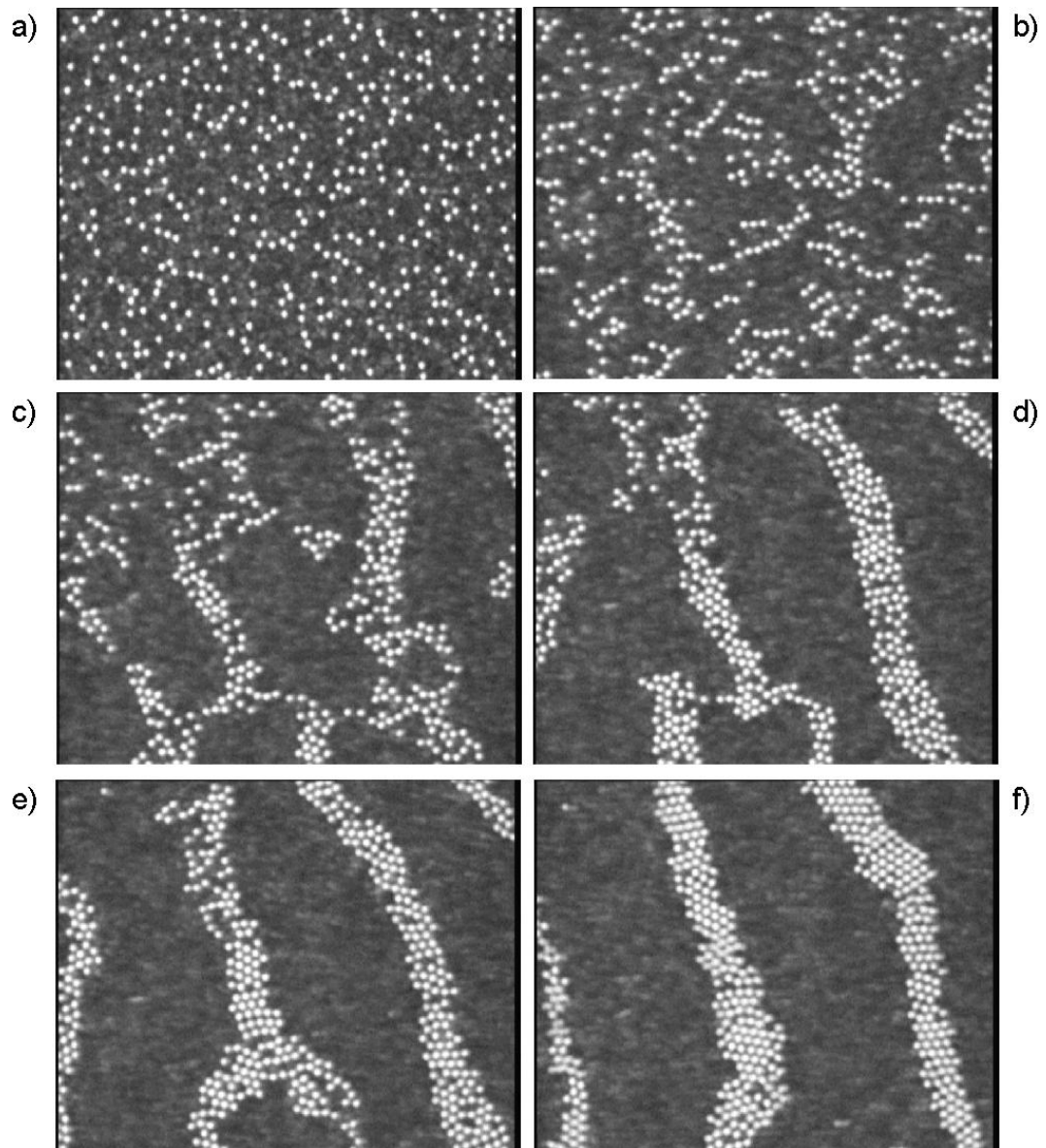


Figure 5.1: Experimental frames of the evolution of segregation domains in a granular mixture of poppy seeds and phosphor-bronze spheres with  $C=0.996$ : (a)  $t = 0\text{sec}$  – vibration of the granular layer was initiated from a homogeneous mixture, (b)  $t = 4.36\text{sec}$ , (c)  $t = 9.36\text{sec}$ , (d)  $t = 16.28\text{sec}$ , (e)  $t = 23.2\text{sec}$ , (f)  $t = 40.68\text{sec}$ .

detail in Section 3.2.

## 5.2 Local Voronoi area density

The first microscopic quantity considered is a measure of the *local area density* associated with each phosphor-bronze sphere. This was calculated from the polygons in a Voronoi construction, also known as Wigner-Seitz cells, which are a standard tool for the study of spacial configurations of particle ensembles and is widely used in condensed matter physics (Okabe, Boots & Sugihara 1992).

The Voronoi construction or tessellation for a given set of points is a numerical method which enables estimates of the area density associated with individual

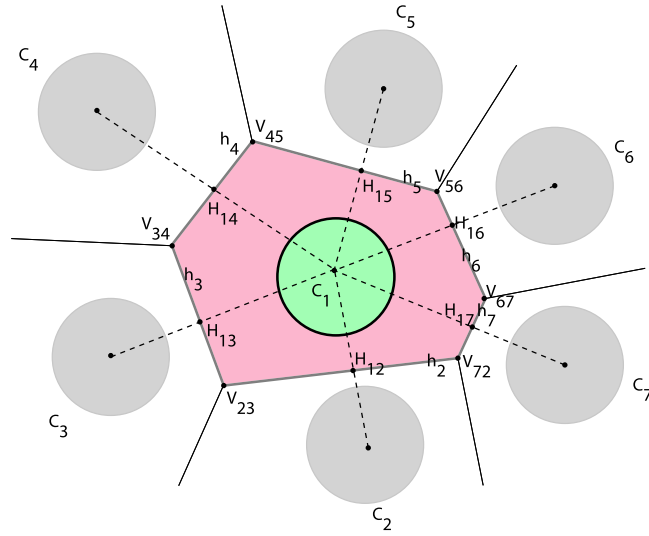


Figure 5.2: Definition of the local Voronoi area density of particle positioned at  $C_1$  (shown in green) with six neighbours (shown in grey with indices  $i = 2 \rightarrow 7$ ). The polygon in red is the Voronoi cell associated with the particle in green and is enclosed by the vertices  $V_{ij}$ . The boundaries of the Voronoi cell are the segments of the lines  $h_i$ . Each of the points  $H_{1i}$  is the mid point between  $C_1$  and the respective particle  $i$ .

spheres to be made. The method may be defined as follows and is illustrated in the schematic diagram of Fig. 5.2, for the case of a central particle labelled  $\mathbf{C}_1$ , surrounded by six neighbours. Consider a set  $\mathbf{P}$  of coplanar particles ( $\mathbf{P} = \{\mathbf{C}_1, \mathbf{C}_2, \mathbf{C}_3, \mathbf{C}_4, \mathbf{C}_5, \mathbf{C}_6, \mathbf{C}_7\}$ ) for the example in Fig. 5.2. Lines are drawn from the centre of a particle to each of its nearest neighbours (lines  $\overline{\mathbf{C}_1\mathbf{C}_i}$  for each pair of particles 1 and  $i = 2 \rightarrow 7$ ) and halved to yield the mid points,  $\mathbf{H}_{1i}$ . The lines  $h_i$  are then defined to be perpendicular to the joining vectors  $\overline{\mathbf{C}_1\mathbf{C}_i}$  and passing through  $\mathbf{H}_{1i}$ . The intersect between each pair of the lines  $h_i$  gives the vertices  $\mathbf{V}_{lm}$  (with  $m = l + 1$ ) which define a polygonal cell, centered at  $\mathbf{C}_1$ . This cell encloses a region (shown in red in Fig. 5.2) in which any point is closer to  $\mathbf{C}_1$  than to any other particle – this is the *Voronoi cell of particle 1*. We have used the `voronoi(x,y)` routine in the numerical package MATLAB 6.0 (R12) to implement this procedure.

The *local Voronoi area density* of the  $i^{\text{th}}$  particle can then be defined as the ratio,

$$\rho_v^i = \frac{A_{particle}}{A_{cell}^i}, \quad (5.1)$$

where  $A_{particle} = \pi(d/2)^2$  is the two-dimensional projected area of the imaged spheres with diameter  $d$  and  $A_{cell}^i$  is the area of its Voronoi polygon.

In Fig. 5.3 we present examples of typical Voronoi constructions, at four different values of  $C$ , constructed using the positions of experimental configurations of the phosphor-bronze spheres. At compactities within the binary gas regime, of which  $C = 0.495$  is a typical example, no segregation occurs and snapshots of the network of Voronoi polygons, as shown in Fig. 5.3(a), appear random. By way of contrast, at  $C = 1.007$  where definite segregation develops, structure appears in the domains as can be seen in Fig. 5.3(d). Two snapshots of the network of Voronoi cells for intermediate values of  $C$  are presented in Fig. 5.3(b) and (c). Note that the particles at the edges of the segregation clusters have an associated

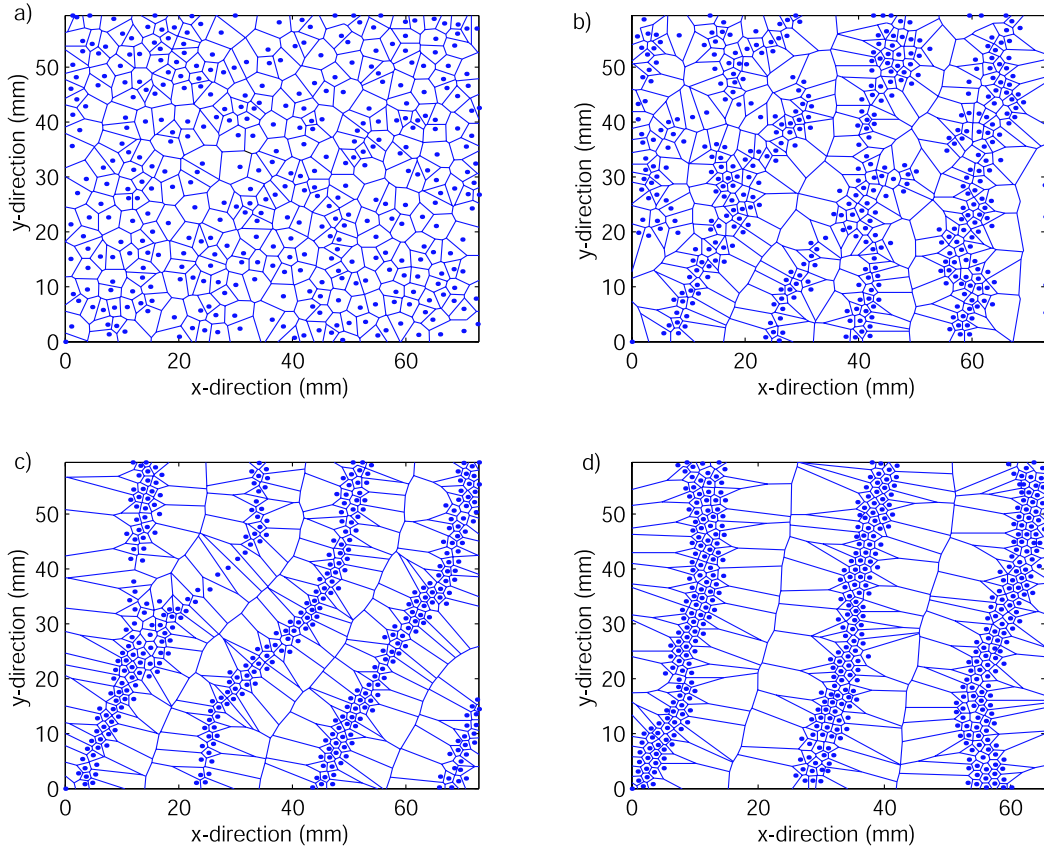


Figure 5.3: Voronoi diagrams obtained from the positions of the phosphor-bronze spheres, for binary mixtures with various values for the compacity: (a)  $C = 0.495$ , (b)  $C = 0.687$ , (c)  $C = 0.793$  and (d)  $C = 1.007$ . The frames correspond to configurations obtained 40sec after vibrating an initially homogeneous mixture.

area density significantly lower than those in the bulk of the domains.

### 5.2.1 Dynamic evolution

We first discuss the time evolution of the local Voronoi area density. For this purpose, a time window of  $\Delta\tau = 4\text{sec}$  is defined, which corresponds to 100 experimental frames, i.e.  $\sim 48$  drive cycles. This is used to obtain dynamic

averages for the area density of individual spheres,  $\rho_v^i$ , as,

$$\overline{\rho}_v \left( t_n = \frac{n\Delta\tau}{2} \right) = \langle \rho_v^i \rangle_n, \quad (5.2)$$

where the brackets  $\langle \cdot \rangle_n$  denote averaging over all the particles,  $i$ , found within the  $n^{\text{th}}$  time window,  $n\Delta\tau < t_n < (n+1)\Delta\tau$  with  $n \in [0, 1, 2, 3, \dots, 59]$ . A time dependent Probability Distribution Function for the local Voronoi area density,  $PDF(\overline{\rho}_v, t_n)$ , was obtained by constructing normalized histograms of  $\overline{\rho}_v$  as a function of the discretised time,  $t_n$ . Each  $PDF(\overline{\rho}_v, t_n)$ , for a certain time window  $n$ , typically contained local area density statistical ensembles with 35,000 to 40,000 particles.

In Fig. 5.4 we present the time evolution of  $PDF(\overline{\rho}_v, t_n)$  for a mixture with  $C = 1.049$ . Initially, the PDF exhibits a low area density principal peak at

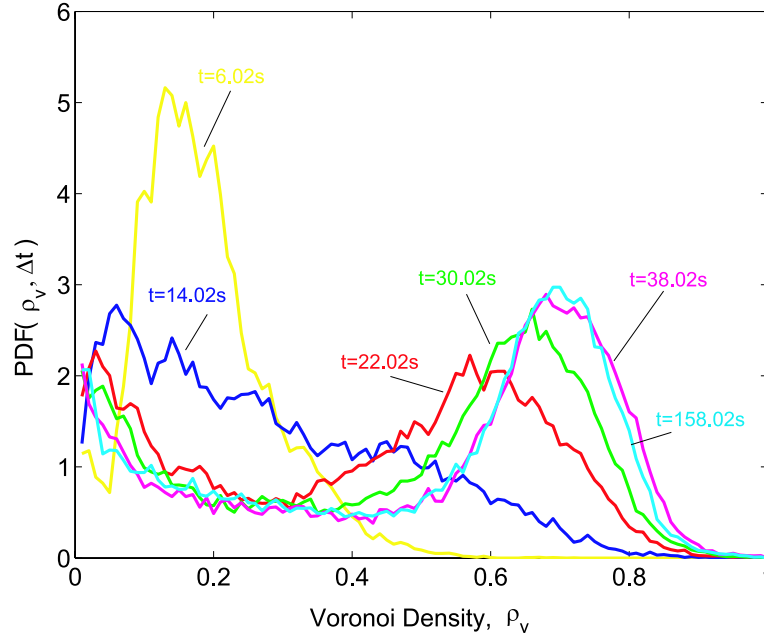


Figure 5.4: Temporal evolution of  $PDF(\overline{\rho}_v, t_n)$  for a mixture with  $C = 1.049$ . (yellow)  $t = 6.02\text{sec}$ , (blue)  $t = 14.02\text{sec}$ , (red)  $t = 22.02\text{sec}$ , (green)  $t = 30.02\text{sec}$ , (magenta)  $t = 38.02\text{sec}$ , (cyan)  $t = 158.02\text{sec}$ . The time window used to obtain temporal averages was  $\Delta\tau = 4\text{sec}$ .

$\rho_v = 0.13$ ; the phosphor-bronze spheres are relatively separated from one another since the layer is in a pre-prepared mixed configuration. This peak progressively shifts to the right which corresponds to segregation of the mixture with formation of clusters and a compaction of the phosphor-bronze spheres within the stripes. After the initial segregation growth, *e.g.*  $t_n = 158.02\text{sec}$ , a striped pattern forms and the  $PDF(\rho_v, t)$  exhibits a high area density peak at  $\rho_v = 0.70$ . In addition, the PDF has a non-zero value at low  $\rho_v$  which results from the contribution of the spheres located at the edges of the segregation clusters. These spheres have an associated low local Voronoi area density, *i.e.* their Voronoi cells are considerable larger than those for the spheres located inside the clusters. This can be clearly seen in the Voronoi construction shown in Fig. 5.3(d).

In Fig. 5.5 we plot the mean value of the distribution  $PDF(\overline{\rho}_v, t_n)$ ,  $D_v(t_n)$ , for three compacity values within the period  $0 < t < 142\text{sec}$ . At  $C = 0.495$ ,  $D_v(t_n)$

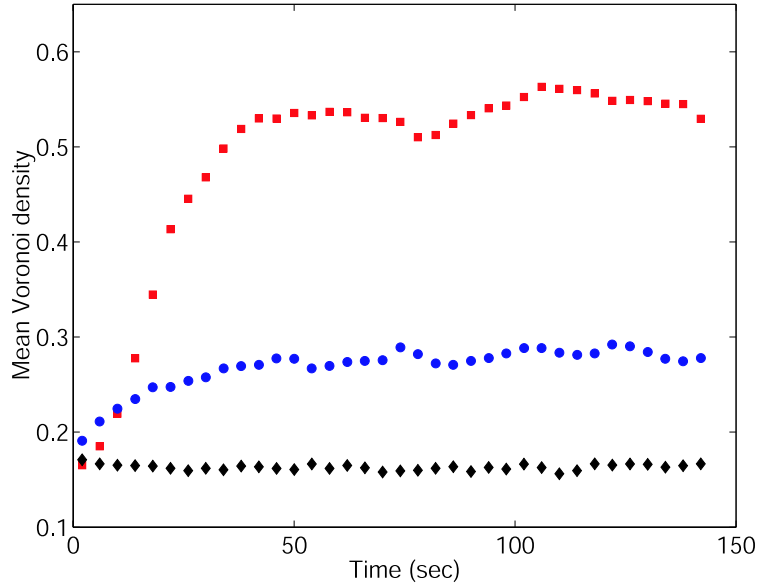


Figure 5.5: Initial evolution of mean local Voronoi area density, having started from initially homogeneous mixtures: (◆)  $C = 0.495$ , (●)  $C = 0.729$ , (■)  $C = 1.135$ .

remains flat as the layer is mixed for all time. At intermediate compacities, of which  $C = 0.729$  is a typical example,  $D_v(t_n)$  exhibits a slow increase up to a value of  $D_v(t_n) \sim 0.3$  as segregation clusters form. At high values of the compacity, of which  $C = 1.135$  is representative, there is a rapid initial evolution, since increasingly dense clusters form, up to a value of  $D_v(t_n) \sim 0.525$  after which the mean area density levels off. This behaviour is consistent with the observation of saturation in the two macroscopic quantities  $\phi$  and  $\eta$  which were discussed in Chapter 4.

The dynamical behaviour of the segregation process can now be analysed as a function of the compacity using the local Voronoi measure. We focus on the initial stages of the formations of domains. During this regime of fast initial segregation growth,  $D_v$  exhibits an approximately linear behaviour of the form,

$$D_v(C, t) = D_v(t = 0) + b(C).t \quad (5.3)$$

where  $D_v(t = 0)$  is the mean area density of the initial homogeneous mixture and  $b(C)$  is the corresponding *rate of segregation*. A value of  $D_v(t = 0) = 0.158 \pm 0.004$  provides a good fit to all experimental runs since the layer is consistently started from an homogeneous mixture. The inverse of the rate of segregation yields a measure of the segregation timescale,  $t_D(C) = 1/b(C)$ . The quantities  $b(C)$  and  $t_D(C)$  are plotted in Fig. 5.6 (a) and (b), respectively. As expected, the growth rate of the segregation remains close to zero up to  $C = 0.644 \pm 0.045$ , after which it steadily increases. This is in agreement with the segregation critical point  $C_c = 0.666 \pm 0.055$  obtained from the macroscopic measures described in Chapter 4. Perhaps, a more significant quantity to consider is the segregation timescale,  $t_D(C)$ , which rapidly increases as  $C_c$  is approached from above, indicating a slowing down of the dynamics which is consistent with the critical slowing down associated with the macroscopic measures discussed in Section 4.6.

The behaviour of  $D_v$  after the initial segregation growth, for  $177 < t < 223 \text{sec}$ ,

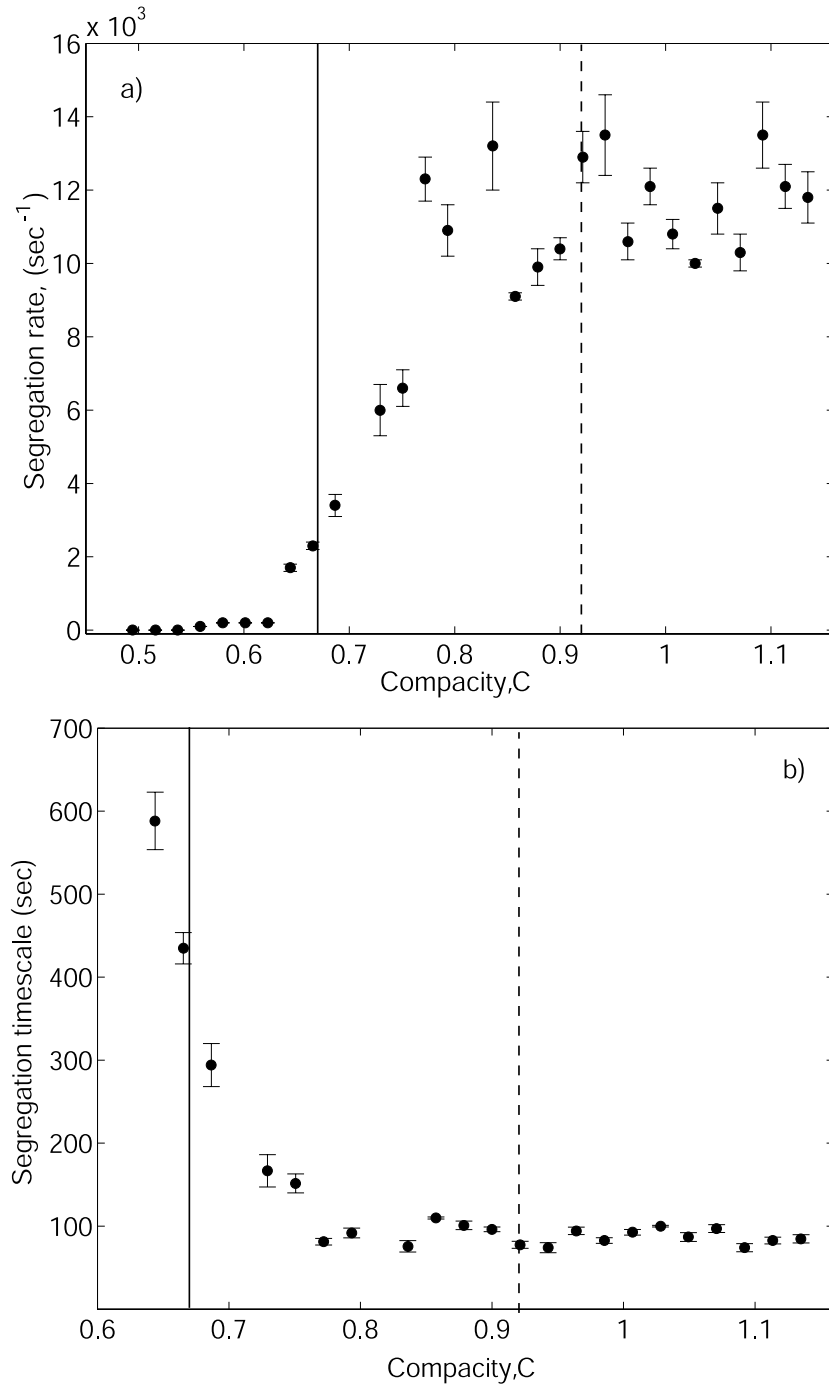


Figure 5.6: (a) Segregation rate,  $b(C)$  (b) segregation timescale,  $t_D = 1/b(C)$  of the phosphor-bronze spheres as a function of the layer compacity. The solid vertical line, in both plots, is positioned at the critical point for segregation,  $C_c$  obtained in Chapter 4. The vertical dashed line is the segregation liquid to segregation crystal transition point,  $C_m$ , obtained in Chapter 4.

is presented in Fig. 5.7, for three values of the compacity. Within this period, the mean Voronoi area density shows little or no evolution, i.e. the system has reached a steady state with a characteristic Voronoi area density for each of these compacity values. An error estimate of the closeness to a steady state can be obtained from the ratio of the standard deviation to the mean of  $D_v(177 < t < 233\text{sec})$ , which was below 6.5% for all values of the compacity considered.

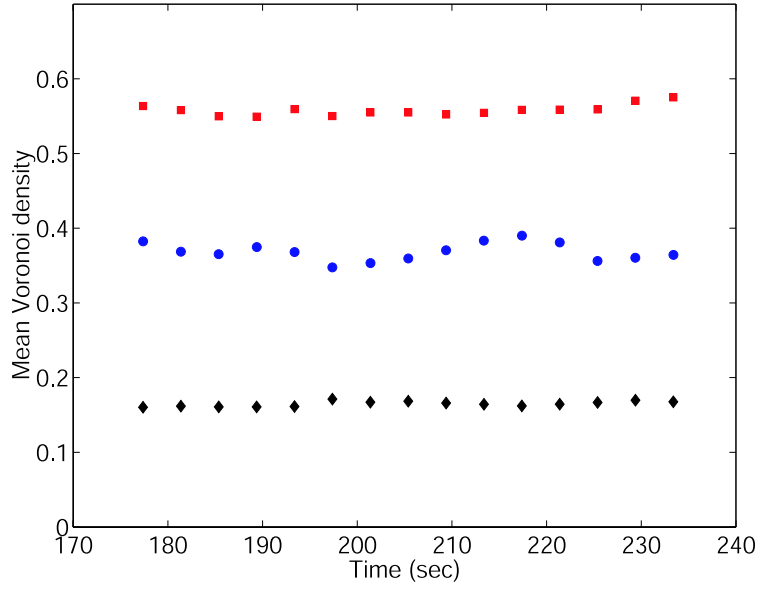


Figure 5.7: Time dependence of mean local Voronoi area density for  $(177 < t < 233)\text{sec}$ : ( $\blacklozenge$ )  $C = 0.495$ , ( $\bullet$ )  $C = 0.729$ , ( $\blacksquare$ )  $C = 1.135$ .

### 5.2.2 Compacity studies

Since the mixture shows little dependence of the mean Voronoi area density for  $t > 3\text{min}$ , we perform time averages within the period  $3 < t < 4\text{min}$  as follows. For each experimental run with a particular compacity value, the binary layer was initiated from a mixed configuration and vibrated for  $3\text{min}$ . At this point 1500 frames were acquired for  $1\text{min}$  at an imaging rate of  $25\text{Hz}$ . A Probability

Distribution Function of the local Voronoi area density,  $PDF(\rho_v)$ , was then constructed from the histograms of  $\rho_v$  for all the particles tracked in the acquired frames. This corresponds to statistical ensembles of approximately 600,000 particles for each experimental run.

A series of  $PDF(\rho_v)$ 's, which were calculated for a variety of compacities, is presented in Fig. 5.8. At low compacities, the PDFs are peaked at low  $\rho_v$ . As the compacity is increased a qualitative change in the shape of the PDFs can be seen and at compacities near  $C \sim 0.65$  they flatten out indicating that there is a greater probability of finding particles with an area density across the entire range. As the compacity is increased, further a new peak develops at high area densities corresponding to particles within the segregation clusters. This peak at high  $\rho_v$  becomes increasingly sharper for high  $C$ , with a drop at values of  $\rho_v \sim 0.9$  which is consistent with maximum packing in 2D of  $\pi/\sqrt{12}$ , for a perfect hexagonal arrangement of disks.

We proceed by providing estimates which quantify the qualitative behaviour of the  $PDF(\rho_v)$  distributions, described above. To illustrate this procedure we first focus on a typical example of such a  $PDF(\rho_v)$  which is shown in Fig. 5.9(a). At a particular  $C$  we extracted a characteristic local area density,  $\rho_v^{max}$ , from the area density value at which the peak of the  $PDF(\rho_v)$  occurred. A measure of the fluctuations of the area density is obtained from the width of the peak of the  $PDF(\rho_v)$ ,  $w_\rho$ . The peak width used was the full width at 3/4 maximum.

Estimations of these quantities  $\rho_v^{max}$  and  $w_\rho$  are both presented in Fig. 5.9(b). When the transition from binary gas to segregation liquid took place by increasing  $C$ ,  $\rho_v^{max}$  grew rapidly as segregation domains formed. Moreover there was a significant amplification of the microscopic area density fluctuations,  $w_\rho$ , which peaked at the particular value of  $C_c = 0.687 \pm 0.051$ . Close to the segregation transition, neighbouring configurational states coexisted and single large spheres

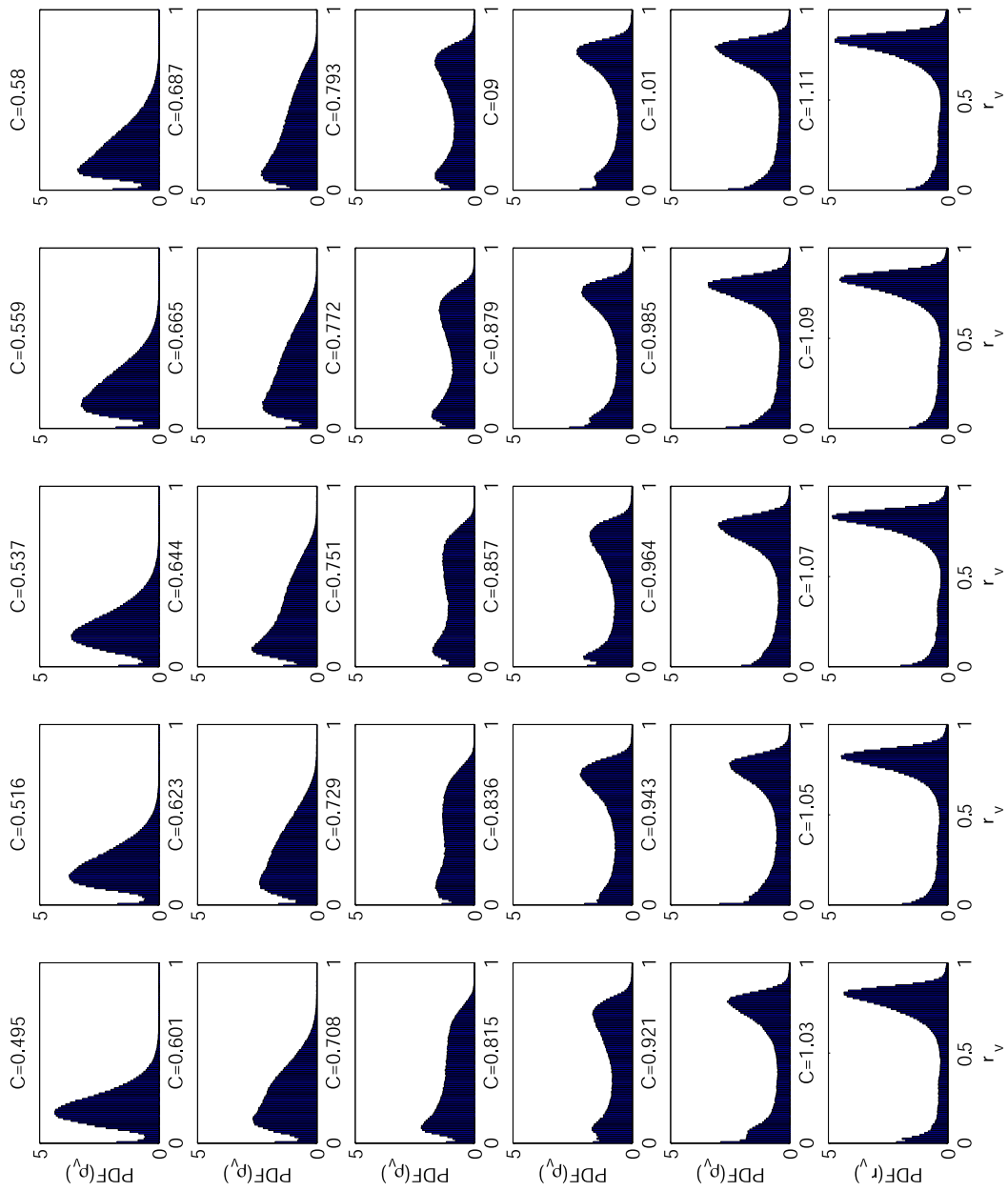


Figure 5.8: Probability distribution functions for the local Voronoi area density of the phosphor-bronze spheres,  $PDF(\rho_v)$ , for a series of compactities. The value for the respective compacticity is located above each plot.

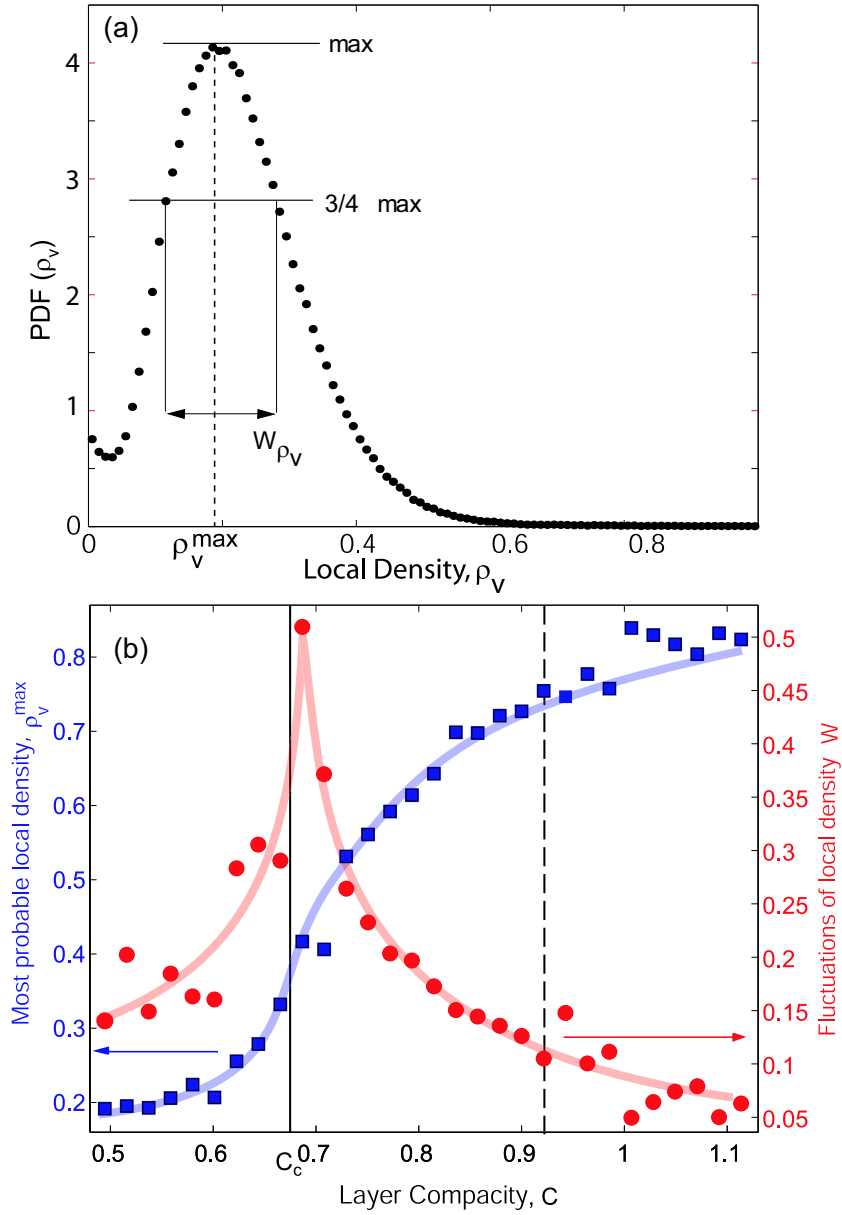


Figure 5.9: Measures extracted from the  $PDF(\rho_v)$  distributions. (a) Typical experimental  $PDF(\rho_v)$  in the binary gas phase, for  $C = 0.537$ , from which the characteristic Voronoi area density,  $\rho_v^{\max}$ , and the width of the distribution at 3/4 max,  $w_\rho$  are extracted. (b) Dependence of  $\rho_v^{\max}$  (left axis) and  $w_\rho$  (right axis) on the layer compacity. The blue and red curves are drawn to guide the eye. The solid vertical line is the critical point for segregation,  $C_c$ , which was obtained in Chapter 4. The vertical dashed line is the segregation liquid to segregation crystal transition point,  $C_m$ , obtained in Chapter 4.

were observed to migrate between segregation domains. This rapid growth of an order parameter combined with amplification of fluctuations is one of the characteristics of equilibrium continuous phase transitions (Binney, Dowrick, Fisher & Newman 1992) which provides further microscopic support for the existence of a critical point for segregation.

### 5.2.3 Tracking of the Area density for an individual sphere

Another indication for critical behavior is provided by the time-series of the local area density associated with a typical single sphere by tracking its Voronoi cell. Close to the transition point  $C_c$ , almost the entire range of possible local area densities ( $0 < \rho_v \leq \pi/\sqrt{12}$  for disks in 2D) is explored, as seen in trace II of Fig. 5.10. On the other hand, a typical time-series in the segregation crystal regime (trace III in Fig. 5.10) illustrates that the particles within the segregation domains are arrested by their hexagonally packed neighbours, yielding small fluctuations about a characteristic high local area density which is indicative of a thermalized crystal. The local area density time-series for a particle in a typical binary gas configuration, shown in trace I of Fig. 5.10, exhibits large fluctuations at low densities as would be expected for gaseous behaviour. Each of the two examples for the time-series of the area density for a single sphere in the binary gas and the segregation liquid phases (traces I and II in Fig. 5.10) was chosen at random out of all the spheres in the layer. The example for the sphere in the segregation crystal was chosen so that it lay inside a segregation cluster rather than at its edge.

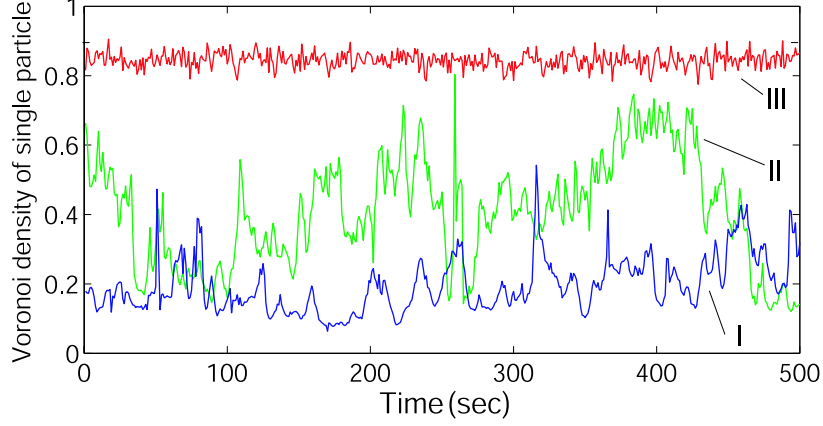


Figure 5.10: Particle tracking of the local Voronoi area density for a single sphere: trace I (blue curve) for  $C = 0.580$ , trace II (green curve) for  $C = 0.687$ , trace III (red curve) for  $C = 1.071$ . Note that trace II corresponds to a sphere in a binary mixture with a compacity value near the critical point for segregation,  $C_c$ .

### 5.3 Nearest neighbours angular distribution

Another quantity that can be calculated from the Voronoi tessellation procedure presented in the previous Section is the angular distribution between nearest neighbours of each individual sphere. The configuration of a section of a schematic Voronoi polygon for a particle with coordinates  $\mathbf{C}_i$  and two of its nearest neighbours,  $\mathbf{A}$  and  $\mathbf{B}$ , is given in Fig. 5.12. We define  $\delta_i$  to be the angle between nearest neighbours set by  $\mathbf{A}$ ,  $\mathbf{B}$  and  $\mathbf{C}_i$ . This can be obtained from the Voronoi tessellation procedure which yields the position of the coordinates of the vertices of the Voronoi polygon  $\mathbf{V}_1$ ,  $\mathbf{V}_2$  and  $\mathbf{V}_3$ . Hence, it follows from the geometric construction around the  $i^{\text{th}}$  particle that,

$$\delta_i = \alpha_i + \beta_i = 180 - (\phi_i + \theta_i) \quad (5.4)$$

where,

$$\theta_i = \cos^{-1} \left( \frac{(\mathbf{V}_1 - \mathbf{V}_2) \cdot (\mathbf{C}_i - \mathbf{V}_2)}{|\mathbf{V}_1 - \mathbf{V}_2| |\mathbf{C}_i - \mathbf{V}_2|} \right), \quad (5.5)$$

and

$$\phi_i = \cos^{-1} \left( \frac{(\mathbf{V}_3 - \mathbf{V}_2) \cdot (\mathbf{C}_i - \mathbf{V}_2)}{|\mathbf{V}_3 - \mathbf{V}_2| |\mathbf{C}_i - \mathbf{V}_2|} \right). \quad (5.6)$$

Probability distribution functions for the angle between nearest neighbours,  $PDF(\delta)$ , can now be calculated in the same way as for the local Voronoi area density discussed in Section 5.2.2. Representative  $PDF(\delta)$ 's for four different compacities are presented in Fig. 5.12. For example, at low compacities the distribution is broad which indicates that the spheres in the granular layer do not exhibit a preferred orientation as expected for a mixture. However, as the compacity is increased the main peak of the distribution shifts towards  $60^\circ$  and the width of the peak decreases significantly.

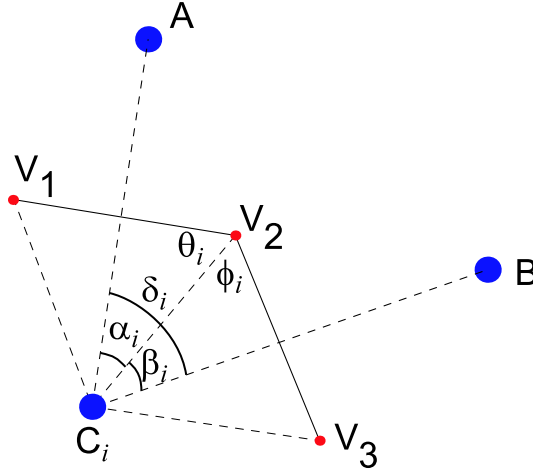


Figure 5.11: Schematic diagram for the definition of angles between nearest neighbours,  $\delta$ .  $\mathbf{A}$ ,  $\mathbf{B}$  and  $\mathbf{C}_i$  are the positional coordinates of three neighbouring particles. The angle defined by the three particles, about  $\mathbf{C}_i$ , is  $\delta_i = \alpha_i + \beta_i$ . The solid lines are a section of the Voronoi polygon, belonging to the particle  $\mathbf{C}_i$ , which is defined by the vertices  $\mathbf{V}_1$ ,  $\mathbf{V}_2$  and  $\mathbf{V}_3$ .

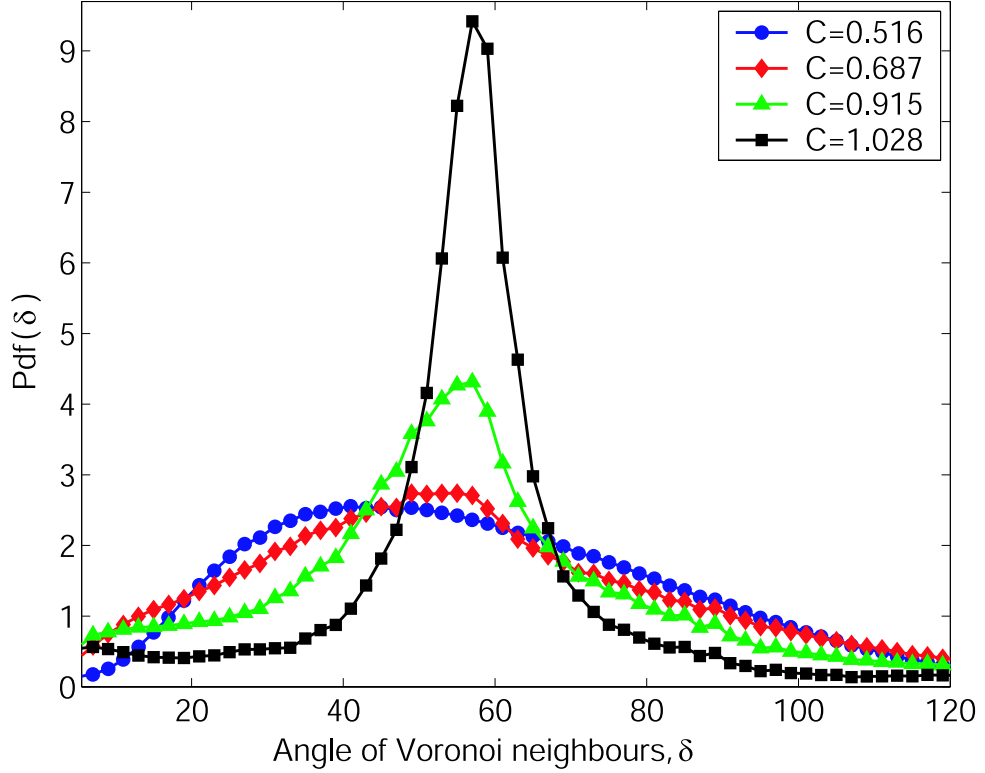


Figure 5.12: Typical probability distribution functions for the angle between nearest neighbours,  $PDF(\delta)$ : for ( $\bullet$ )  $C = 0.516$ , ( $\blacklozenge$ )  $C = 0.687$ , ( $\blacktriangle$ )  $C = 0.815$ , ( $\blacksquare$ )  $C = 1.028$ .

By way of analogy with the local Voronoi area density distributions, we now quantify the evolution of the  $PDF(\delta)$ 's by monitoring the position of the peak. Once again, the discussion is presented in relation to the two characteristic compacity points  $C_c = 0.67$  (vertical solid line in Fig. 5.13) and  $C_m = 0.921$  (vertical dashed line in Fig. 5.13) for the location of the binary gas to segregation liquid and segregation liquid to segregation crystal transitions, respectively. We recall that these were obtained from the macroscopic measures described in Chapter 4.

As shown in Fig. 5.13, the location of the peak of the  $PDF(\delta)$  distribution is approximately flat at  $\delta = (44.7 \pm 0.4)^\circ$  for low compacities up to  $C_\delta = 0.601 \pm 0.043$ , after which it rapidly grows. Note that the location of  $C_\delta$  appears to occur

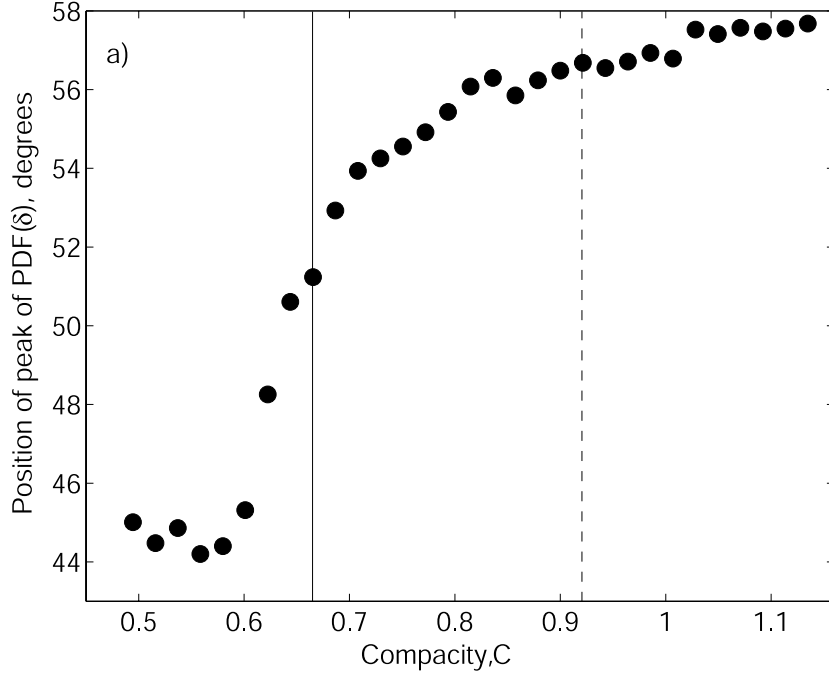


Figure 5.13: (a) Position of the peak of the PDF( $\delta$ ) distribution,  $\delta_{max}$ , as a function of layer compacity. The solid and dashed vertical lines are the critical point for segregation,  $C_c$  and segregation liquid to segregation crystal transition point,  $C_m$ , respectively, which were obtained in Chapter 4.

earlier than the segregation critical point but it is consistent with  $C_c$ , to within experimental resolution, since  $C_\delta - C_c = 0.065 \pm 0.070$ . At high compacities there is a levelling off in the position of the peak at  $\delta_{peak} \sim (57.5 \pm 2.0)^\circ$ . This is a signature of approximately crystalline ordering of the spheres within the domains. A perfect hexagonal packing of particles would correspond to a delta-function located at  $60^\circ$ .

## 5.4 Radial distribution function

We now discuss the use of the radial distribution function,  $g(r)$ , to obtain information on the structural configurations of the phosphor-bronze spheres during

segregation.  $g(r)$  is the normalized probability, statistically averaged over the system, of finding a particle as a function of distance from the centre of another particle. Hence,  $g(r)dr$  yields the number of particles to be found in the shell bound by  $r$  and  $r + dr$ , normalized by the number of particles that would be expected for a uniform distribution of particle positions. Details of the definition and calculation of  $g(r)$  are given in Appendix A.

In Fig. 5.14 we show curves of  $g(r)$  obtained for the phosphor-bronze spheres at three values of the compacity which each correspond to one of three phases of granular segregation. In the binary gas phase at  $C = 0.495$ ,  $g(r)$  has a peak at  $r/d = 1$  which quickly decays at large distances, as expected for a disordered gas. At the intermediate value of  $C = 0.729$ , *liquid-like* behavior is observed and  $g(r)$  is peaked at 1, 2 and 3 particle diameters. The positions of neighbouring spheres are correlated and the maxima may be associated with concentric shells of neighbours and the oscillations are rapidly damped, showing the decay of short-range order. This behaviour is commonly seen in hard sphere liquids and was first observed experimentally by Bernal (1964). In the segregation crystal phase, at high  $C$ , (typical curve for  $C = 1.135$ ) two further peaks emerge near  $r/d = \sqrt{3}$  and  $r/d = \sqrt{7}$ , which are characteristic of a hexagonally packed crystal, in two dimensions.

Representative snapshots of the granular mixture corresponding to each of the three curves discussed above are shown in Fig. 5.14(b,c,d) for the binary gas, segregation liquid and segregation crystal, respectively. Also shown are schematic diagrams of possible particle configurations which would give rise to the characteristic peaks in  $g(r)$ . Specifically, in the binary gas phase a single peak arises from sphere dimers at a distance  $d$  apart (Fig. 5.14(b1)). In the segregation liquid, in addition to the dimer configuration, chains of three and four particles will be present (Fig. 5.14(c1,c2)). While in the segregation crystal, two additional

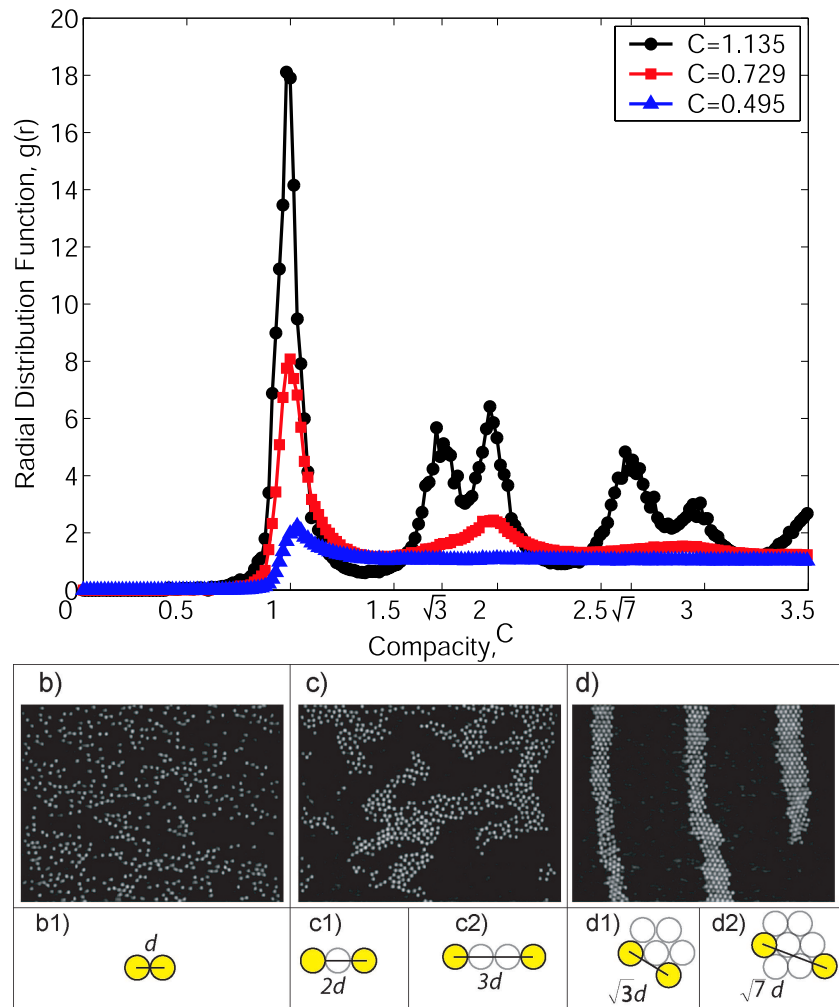


Figure 5.14: (a) Radial distribution functions,  $g(r)$ , for spheres' configurations at three compacity values: ( $\blacktriangle$ ) binary gas for  $C = 0.495$ , ( $\blacksquare$ ) segregation liquid for  $C = 0.729$  and ( $\bullet$ ) segregation crystal for  $C = 1.135$ . Corresponding experimental frames for (b)  $C = 0.495$ , (c)  $C = 0.729$  and (d)  $C = 1.135$ . The insets are schematics of the typical sphere's configurations that gives rise to the characteristic peaks in the  $g(r)$  curves.

characteristic inter-particle distances of  $\sqrt{3}d$  and  $\sqrt{7}d$  emerge as expected for an hexagonal packing (Fig. 5.14(d1,d2)).

In Fig. 5.15,  $g(r)$  is plotted as a function of both the inter-particle distance and layer compacity. The value of the  $g(r)$  is given by the adjacent colour bar. The emergence of the characteristic peaks of  $g(r)$  can be clearly seen as the compacity is increased. Up to  $C \sim 0.6$ , in the binary gas phase, a single peak is observed at  $r/d = 1$ , which gradually grows as the compacity is increased. In the intermediate compacity range,  $0.6 \lesssim C \lesssim 0.95$ , a second and third peak become prominent at  $r/d = 2$  and  $r/d = 3$ . At  $C \sim 0.95$  the two further peaks at  $r/d = \sqrt{3}d$  and  $r/d = \sqrt{7}d$  appear, corresponding to the crystallization configurations.

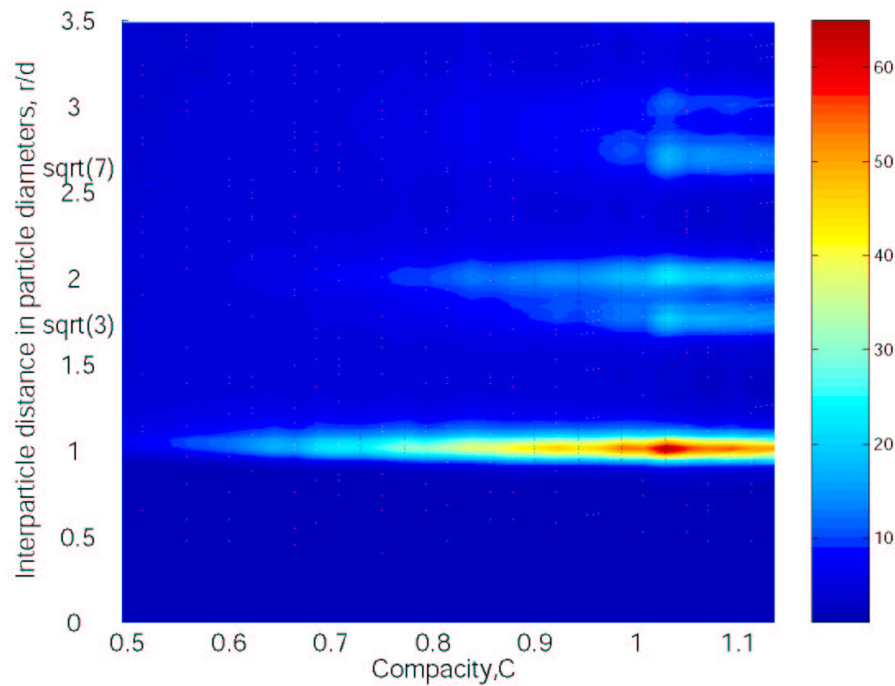


Figure 5.15: Surface plot for  $g(r)$  as a function of compacity. The value of the  $g(r)$  at the point with a particular compacity and inter-particle diameter is given by the colour level in the adjacent colour bar.

Hence, the radial distribution function provides additional support for the idea of the three distinct phases – binary gas, segregation liquid and segregation crystal – observed in the segregation process, for different values of the layer compacity.

## 5.5 Summary

In this Chapter, further analysis of the segregation behaviour of the granular mixture has been performed as a function of the layer compacity using a variety of microscopic measures. These quantities were constructed from the coordinates of a species in the mixture; the phosphor-bronze spheres. The idea was to determine how the features observed during the macroscopic studies presented in Chapter 4 are captured at the microscopic level of the individual spheres.

A number of dynamical and structural quantities was investigated, namely: the local Voronoi area density, the angle between nearest neighbours and the radial distribution function. The main conclusion is that these microscopic quantities present further evidence for the segregation transition and support the existence of each of the previously suggested phases of the granular mixture: *binary gas*, *segregation liquid* and *segregation crystal*.

It should be noted that the analysis thus far has been performed uniquely as a function of  $C$  (by changing uniquely the number of poppy seeds in the layer), all other parameters being fixed. In the next Chapter, a wider section of the parameter space will be explored with the aim of showing that the behaviour of the granular mixture we have presented is robust over a range of parameters.

# Chapter 6

## Exploration of parameter space

In this Chapter we present the results of an extended study of the parameter space of the binary mixture of poppy seeds and phosphor-bronze spheres. In Section 6.1, we report an exploration of the effect of varying the system size and find that the segregation behaviour is approximately independent on the aspect ratio of the system. In Section 6.2 we then turn to the compacity parameter space  $C(N_{ps}, N_{pb})$  and determine the regions of existence of the three phases of segregation for various relative numbers of the two types of particles. Finally, in Section 6.3, the dependence of the segregation behaviour on the external excitation is investigated. In particular we observe that a segregation pattern can be destroyed by increasing the maximum value of the tray's acceleration. A sharp transition is uncovered between a mixed and a segregated phase as the maximum acceleration of the tray is decreased.

### 6.1 Aspect ratio

In the previous Chapters, the study of granular segregation in the binary mixture was centered on its dependence on the layer compacity. Since  $C$  is a dimensionless ratio between the combined two-dimensional projected area occupied by the two types of particles and the total area, it is now of interest to explore the effect of

varying the total area and aspect ratio of the tray. A frame with movable walls in both  $x$  and  $y$  was used to accomplish this. The side walls were mounted in precision machined parallel grooves and the respective dimensions adjusted using a Vernier scale which was accurate to within  $\pm 0.05\text{mm}$ . The range of the aspect ratio,  $\Gamma$  (as defined in Section 2.5), used in this investigation is presented in Table 6.1.

$\Delta x$ (mm)	$\Delta y$ (mm)	Total area (mm <sup>2</sup> )	$\Gamma$
20	90	1800	0.222
40	90	3600	0.444
60	90	5400	0.667
80	90	7200	0.889
100	90	9000	1.111
120	90	10800	1.333
140	90	12600	1.556
160	90	14400	1.778
180	90	16200	2.000
180	70	12600	2.571
180	60	10800	3.000
180	50	9000	3.600
180	40	7200	4.500
180	30	5400	6.000
180	20	3600	9.000

Table 6.1: Values of  $\Gamma$  used in the aspect ratio parametric study.  $\Delta x$  and  $\Delta y$  are the dimensions of the tray in the directions along and orthogonal to the forcing, respectively.

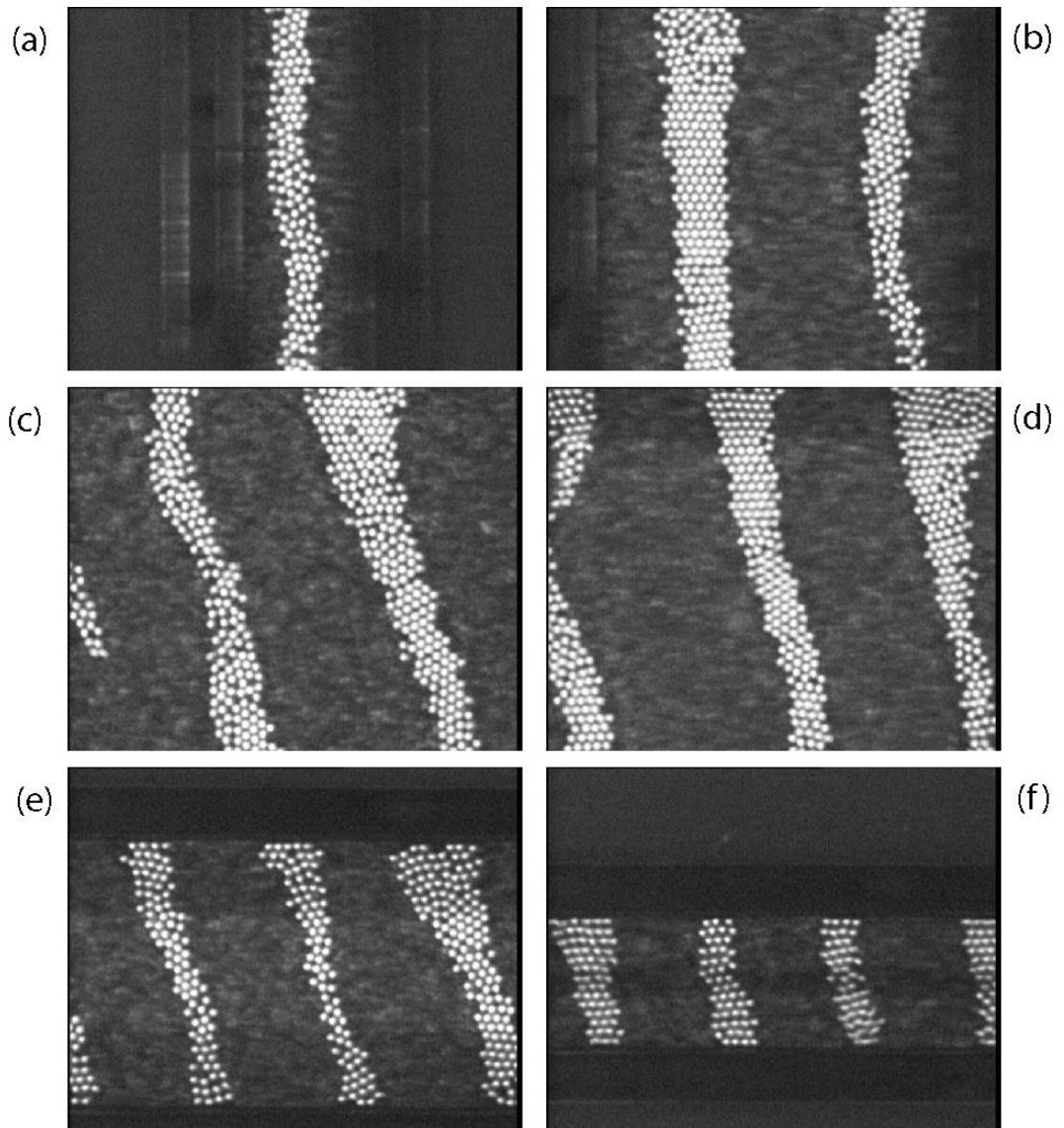


Figure 6.1: Experimental frames for the granular mixture of poppy seeds and phosphor-bronze spheres for various values of  $\Gamma$ . The images correspond to the layer configuration,  $2min$  after vibrating an initially homogeneous mixture. (a)  $\Gamma = 0.222$  (b)  $\Gamma = 0.667$  (c)  $\Gamma = 1.556$  (d)  $\Gamma = 2.571$  (e)  $\Gamma = 4.500$  (f)  $\Gamma = 9.000$ . The vertical boundaries are observable in (a) and (e). The horizontal boundaries are observable in (e) and (f).

The layer compacity was fixed at  $C = 0.900$  with  $N_{pb} = 1596$  phosphor-bronze spheres. The forcing parameters, as in the previous Chapters, were set at  $f = 12Hz$  and  $A = \pm 1.74mm$ . Example snapshots of the granular layer taken after  $2min$  of vibration of an initially homogeneous mixture are presented in Fig. 6.1, for various values of  $\Gamma$ . The imaging window is the same as that used for the microscopic studies in Chapter 5. For  $\Gamma \ll 1$ , of which the frame in Fig. 6.1(a) is a representative example, a single stripe formed which was aligned perpendicularly to the direction of forcing. For larger values of  $\Gamma$ , a number of well defined stripes rapidly developed in a similar way to the particular case of  $\Gamma = 2$  which was studied in detail in Chapters 3–5.

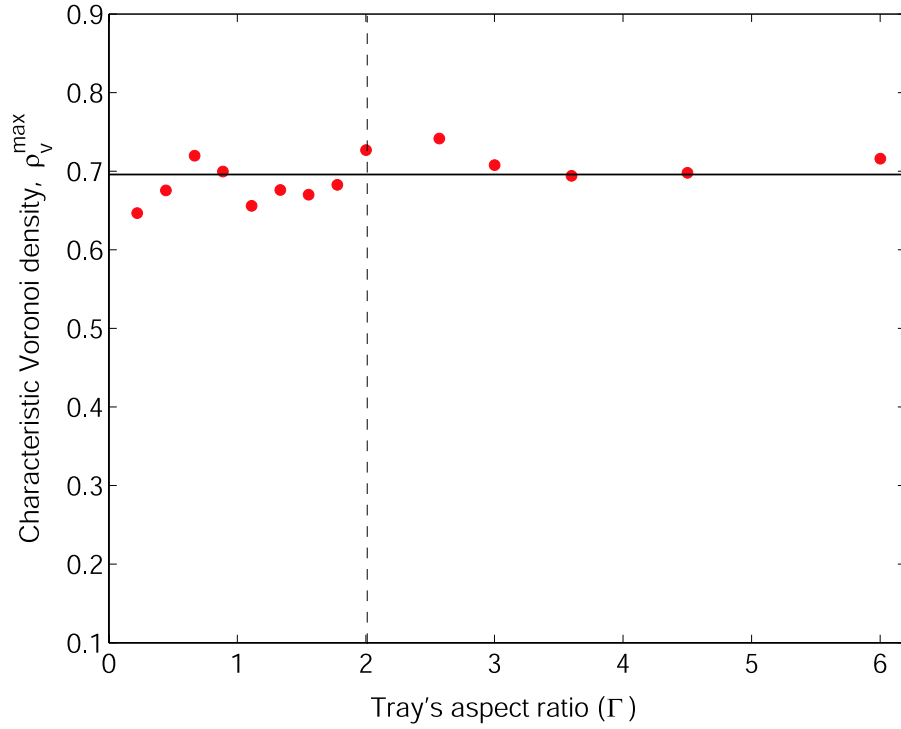


Figure 6.2: Characteristic local Voronoi area density,  $\rho_v^{max}$ , as a function of aspect ratio  $\Gamma$ . The mean value is  $\langle \rho_v^{max} \rangle_{\Gamma} = 0.696 \pm 0.040$ , represented by the horizontal solid line. The vertical dashed line is located at  $\Gamma = 2$ , corresponding to the value of the aspect ratio used for the detailed studies in Chapters 3 – 5.

We measured the characteristic local Voronoi area density of the spheres,  $\rho_v^{max}$  (introduced in Section 5.2.2) to monitor the segregation behaviour as  $\Gamma$  was varied. This quantity is shown in Fig. 6.2 as a function of aspect ratio. The statistics were performed for 1500 frames (at an acquisition rate of  $25Hz$ ) which were acquired  $1min$  after vibration was initiated from an initially homogeneous mixture. As the aspect ratio of the tray was changed, the local area density of the phosphor-bronze spheres remained approximately constant with an average value of  $\langle \rho_v^{max} \rangle_\Gamma = 0.696 \pm 0.040$ , to within 6%. This suggests that the segregation behaviour appears to be independent of the tray's total area and aspect ratio and presents further evidence that  $C$  is, indeed an important parameter of the system. This finding is, in a way, surprising since the smallest dimensions of the trays considered, in the extreme values of  $\Gamma = 0.222$  and  $\Gamma = 9$ , were only one order of magnitude larger than the size of the individual particles. Therefore, one could expect the effect of the boundaries to be of considerable importance in those extreme situations of  $\Gamma$ , which does not appear to be the case.

It should be noted that the study the effect of changing the aspect ratio on the segregation patterns was performed for a single value of the layer compacity ( $C=0.900$ ), where robust stripes formed. Even though we believe that the fact that the segregation behaviour is independent of  $\Gamma$  is robust, in future work this should be checked for other values of  $C$ .

## 6.2 Compacity phase diagram

In the previous Section, we found that the segregation behaviour of the system appears to be primarily dependent on the total filling fraction of the layer and independent on both the tray's area and aspect ratio. We now decouple  $C$  into two of its components, *i.e.*  $C(N_{ps}, N_{pb}) = \varphi_{ps} + \varphi_{pb}$ , where  $\varphi_{ps} = N_{ps}A_{ps}/(xy)$  and  $\varphi_{pb} = N_{pb}A_{pb}/(xy)$  are the filling fractions of each of the particle species: the

poppy seeds and the phosphor-bronze spheres, respectively. The notation used is identical to that of Section 2.4. Regarded this way,  $C$  is a two dimensional parameter determined by the relative amounts of each of the particle types in the layer. We studied the  $C$ -dependence further by exploring the *compacity parameter space*,  $(\varphi_{ps}, \varphi_{pb})$ , with the aim of determining the phase diagram of the mixture. To do this, we scanned along  $\varphi_{ps}$ , by increasing the number of poppy seeds in the layer, for four values of  $\varphi_{pb} = \{0.054, 0.083, 0.118, 0.174\}$ . The value of  $\varphi_{pb} = 0.174$  was the same as that used for the compacity studies in Chapters 4 and 5. The initial conditions and the data acquisition procedures were identical to those considered in Chapter 5.

In Fig. 6.3 we present a series of experimental frames of the binary mixture in various points of the compacity parameter space. Representative examples were chosen showing that each of the three phases introduced in Chapter 4 and investigated in detail in Chapter 5 were observed for different values of  $\varphi_{pb}$ . At low values of  $C$  – Fig. 6.3(*left column*) – a binary gas was observed. At intermediate  $C$  values – Fig. 6.3(*centre column*) – the phosphor-bronze spheres clustered in mobile segregation domains and individual spheres were agitated within the domains; the mixture was in the segregation liquid phase. For high  $C$  – Fig. 6.3(*right column*) – the rigid segregation domains consisted of spheres disposed in hexagonally packed configurations; the segregation crystal phase. Note that at low values of  $\varphi_{pb}$ , of which Figs. 6.3(b,c,e,f) are typical cases, there were not enough spheres in the layer for the domains to span the width of the tray. Instead, small clusters formed. In the particular cases of the segregation liquid phase, typical examples of which are given in Figs. 6.3(b,e), these clusters were reminiscent of mobile *liquid drops*.

We proceed with a quantitative analysis of the segregation behaviour in the  $(\varphi_{ps}, \varphi_{pb})$  parameter space. As in the study of the effect of  $\Gamma$  discussed in the

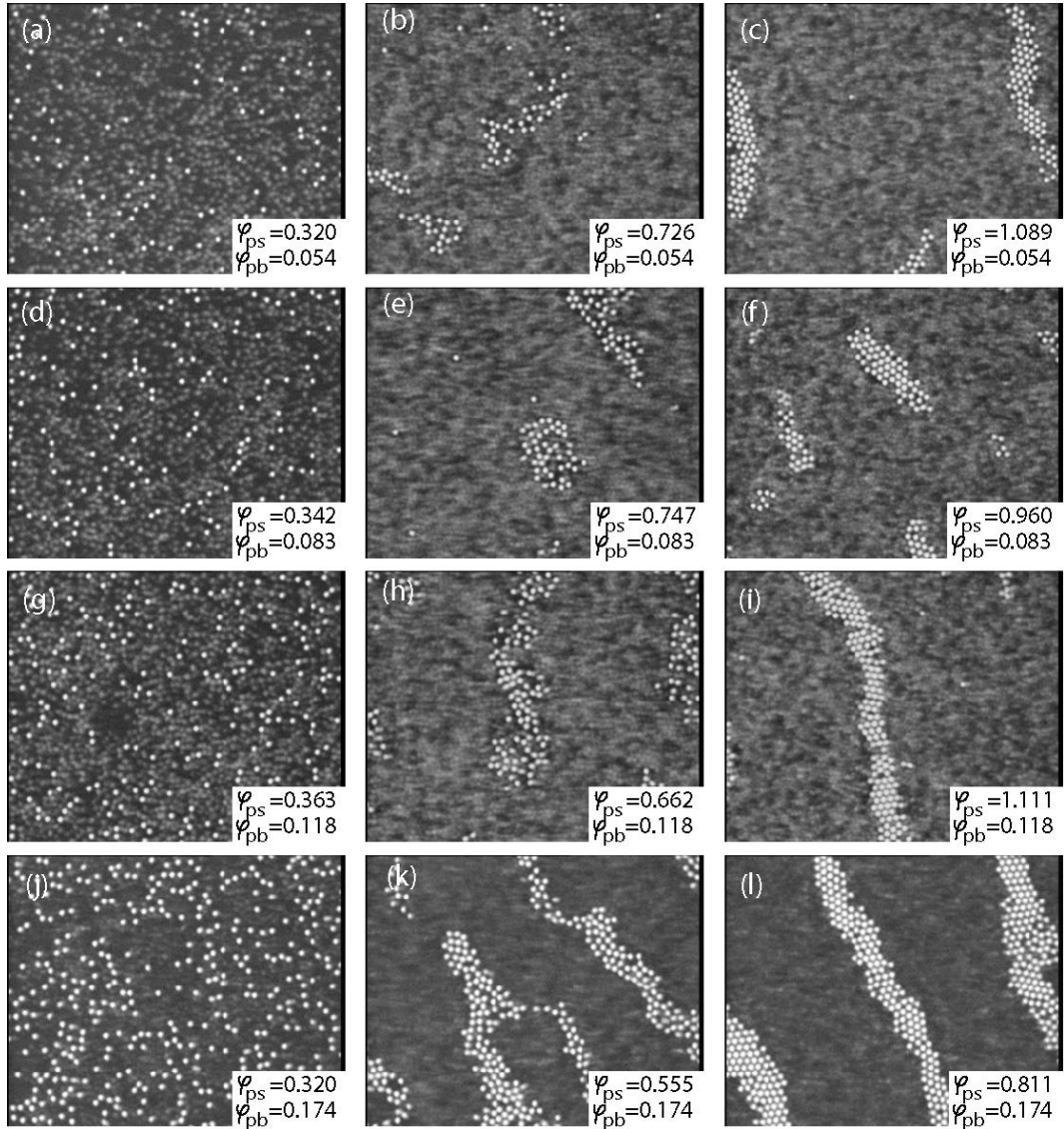


Figure 6.3: Experimental frames representative of the three segregation phases, at various points in the compacity parameter space: binary gas (*left column*), segregation liquid (*centre column*) and segregation crystal (*right column*). The respective values of  $\varphi_{ps}$   $\varphi_{pb}$  are presented in the frames.

previous section, focus is given to the Voronoi measures which were originally developed in Section 5.2. For this, a layer of poppy seeds and phosphor-bronze sphere was initially prepared as an homogeneous mixture, in a  $\Gamma = 2$  geometry, with  $\Delta y = 180mm$ . The mixture was then vibrated at  $f = 12Hz$  and  $A = \pm 1.74mm$  for  $3min$  after which 1500 frames were acquired within  $1min$ . For this acquisition period, PDFs for the local Voronoi area density,  $\rho_v$ , (Section 5.2) and the angle between nearest neighbours,  $\delta$ , (Section 5.3) were constructed. The studies were done as a function of  $C$  for the four data sets with four different values of  $\varphi_{pb}$ .

The results for the characteristic Voronoi area density,  $\rho_v^{max}$ , obtained from the value at which the maximum of  $PDF(\rho_v)$  occurred, are presented in Fig. 6.4. The data in Fig. 6.4(d) is taken from Fig. 5.9(b) and is included for comparison purposes. All four data sets exhibit a clear transition between a mixed state (low area density) and segregated (high area density) state. A particularly interesting feature is that the transition becomes sharper in the mixtures with lower values of  $\varphi_{pb}$  but without any significant variation in the position of the segregation critical point. The branch of the mixed state is consistently lower as  $\varphi_{pb}$  is decreased which is to be expected since the overall area density of the phosphor-bronze spheres in the mixture is this way decreased, i.e. the total number of spheres in the tray is smaller for lower  $\varphi_{pb}$ . However, the branch corresponding to the segregated phase does not show any significant changes, for different  $\varphi_{pb}$ , with local densities of  $\rho_v \sim 0.8$  being attained in all four cases, at the highest values of  $C$ . In future investigations, it would be interesting to assert whether this sharpening of the transition at the lower values of  $\varphi_{pb}$ , is merely a signature of the resolution of the control parameter  $C$  or, on the other hand, the transition goes from being continuous to discontinuous.

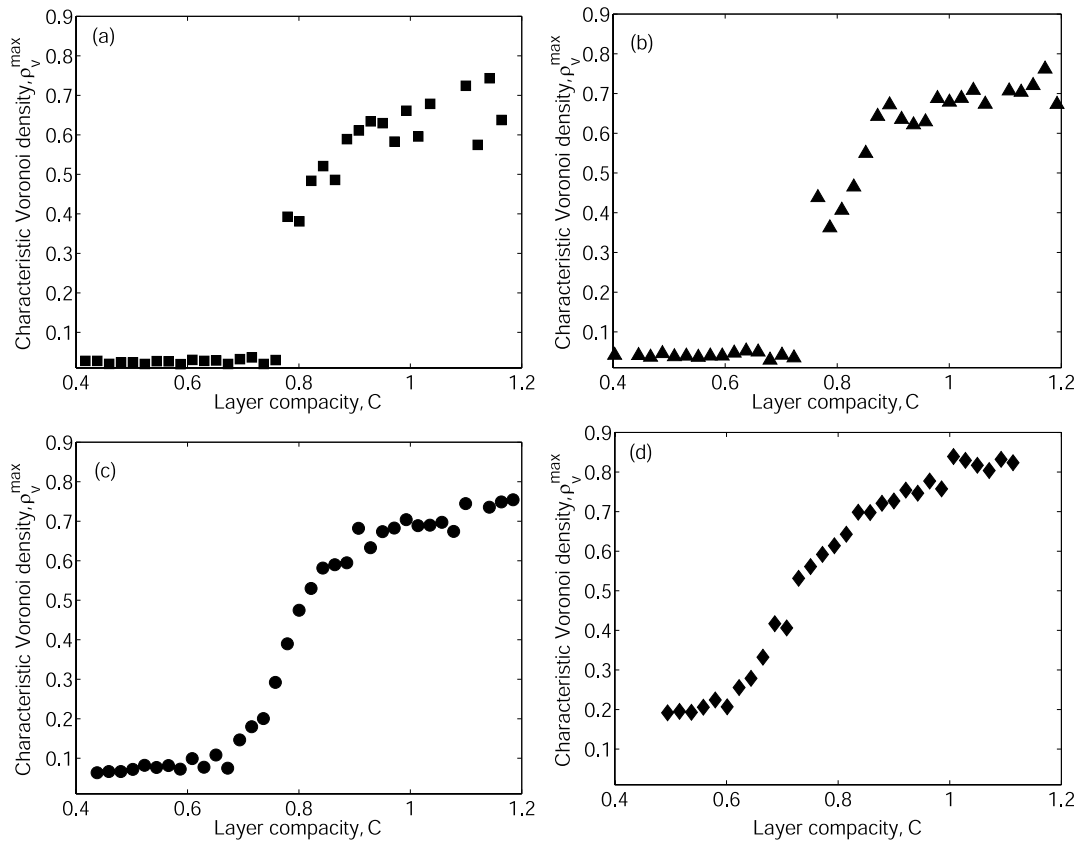


Figure 6.4: Characteristic Voronoi area density,  $\rho_v^{max}$ , for the granular mixture. The compacity values correspond to data sets with (a)  $\varphi_{pb} = 0.054$ , (b)  $\varphi_{pb} = 0.083$ , (c)  $\varphi_{pb} = 0.118$  and (d)  $\varphi_{pb} = 0.174$ .

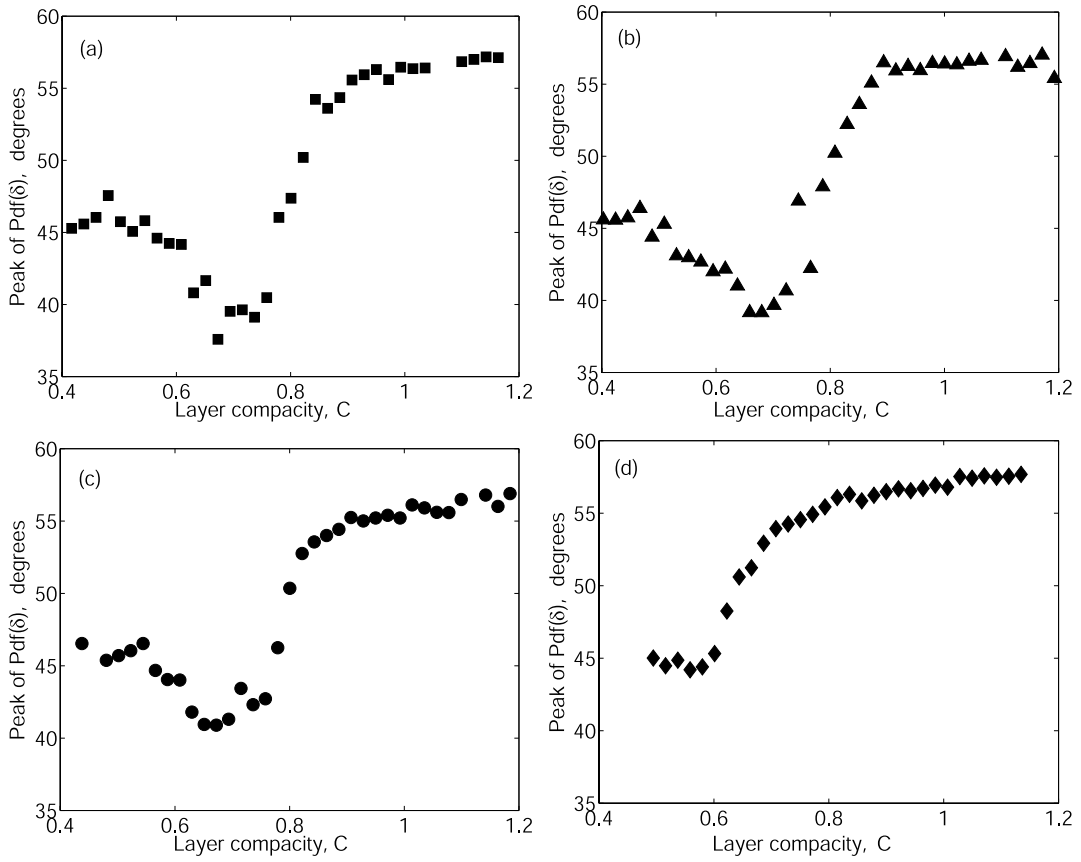


Figure 6.5: Characteristic angle between nearest neighbours,  $\delta^{max}$ , for the granular mixture. The compacity values correspond to data sets with (a)  $\varphi_{pb} = 0.054$ , (b)  $\varphi_{pb} = 0.083$ , (c)  $\varphi_{pb} = 0.118$  and (d)  $\varphi_{pb} = 0.174$ .

As in Section 5.3, the location of the maximum of  $PDF(\delta)$  yields the characteristic angle between nearest neighbours,  $\delta^{max}$ . In Fig. 6.5 we present the results of  $\delta^{max}$  for the four data sets with different  $\varphi_{pb}$ , as a function of  $C$ . Again, the data in Fig. 6.5(d) is identical to that in Fig. 5.13(b) and is redisplayed to aid comparison. Striking behaviour becomes apparent in this measure for lower values of  $\varphi_{pb}$ . Take, for example, the data in Fig. 6.5(a) for  $\varphi_{pb} = 0.054$ . At the lowest values of  $C$ ,  $\delta^{max}$  tended to  $45^\circ$ . However, as  $C$  was increased,  $\delta^{max}$  followed a non-monotonic variation, as the mixture went through the segregation transition. The characteristic angle first decreased down to  $38^\circ$  only to then sharply increase past the segregation transition point. At the highest values of  $C$  the phosphor-bronze spheres were arranged in a nearly hexagonal pack in a similar way to that described in Sections 4.8 and 5.4, for which one would expect  $\delta_{hex}^{max} = 60^\circ$ . This is consistent with the value of  $\delta^{max} = (57.2 \pm 2.0)^\circ$  measured at the highest values of  $C$ . It is interesting to note that the non-monotonic dependence of  $\delta^{max}$  on  $C$  appears to be robust and clearly persists in the other two data sets with  $\varphi_{pb} = 0.083$  and  $\varphi_{pb} = 0.228$  in Figs. 6.5(b) and (c), respectively. However, as  $\varphi_{pb}$  is increased this effect becomes weaker and can hardly be noticed at  $\varphi_{pb} = 0.174$ .

In Fig. 6.6 the four data sets discussed thus far are combined in a  $(\varphi_{ps}, \varphi_{pb})$  phase diagram. The aim is to determine the locus of existence and stability of the three segregation phases. The binary gas is located in the left hand side of the diagram in the regions of low  $\varphi_{ps}$ . The segregation liquid exists in the central region of the diagram. The segregation crystal is observed at large values of  $\varphi_{ps}$ , on the right hand side of the phase diagram. Note also that the phase boundaries  $L1$  and  $L3$  (dashed lines in Fig. 6.6) are approximately parallel for the data sets with  $\varphi_{pb} = \{0.083, 0.118, 0.174\}$ . This points, once again, to the fact that the layer compacity appears to be a primary parameter which determines

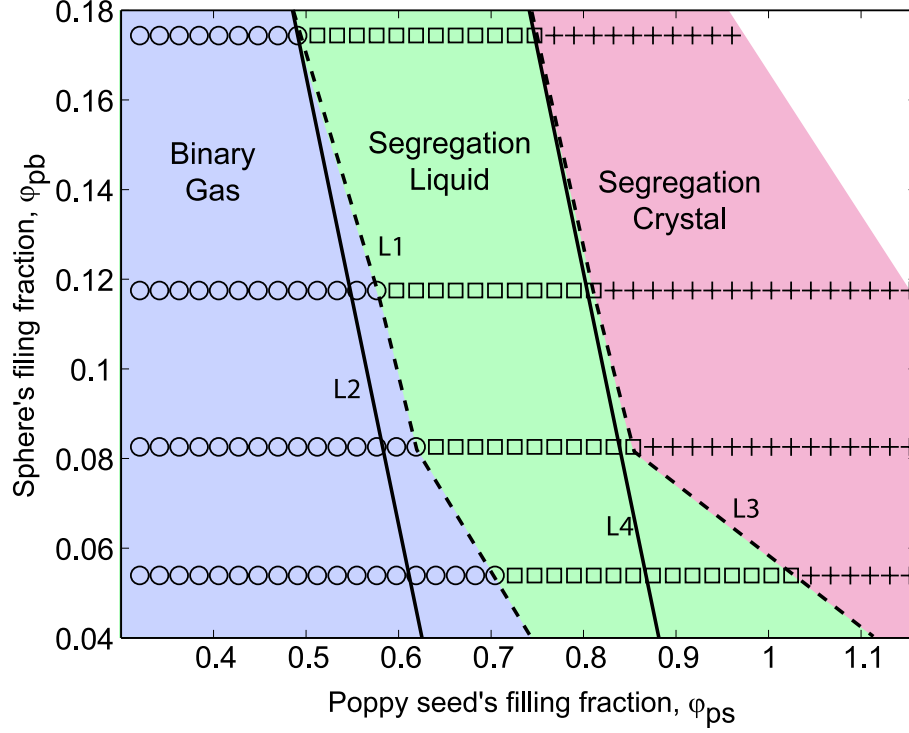


Figure 6.6: Phase diagram for the  $(\varphi_{pb}, \varphi_{ps})$  parameter space for the mixture of spheres and poppy seeds. (o) binary gas. ( $\square$ ) segregation liquid. (+) segregation crystal. The dashed lines,  $L1$  and  $L3$  are the experimental phase boundaries. The solid lines  $L2$  and  $L4$  are given by Eqns. (6.1) and (6.2), respectively, with  $C_c = 0.665$  and  $C_m = 0.921$ . No data was acquired in the top right hand region since, there, the mixture was not longer in a monolayer regime.

the system's behaviour, rather than the absolute amounts of each of the particle types. If this was strictly the case, one would expect the phase boundaries to lie in exactly parallel lines given by

$$\varphi_{pb}^{L2} = C_c - \varphi_{ps} \quad (6.1)$$

and

$$\varphi_{pb}^{L4} = C_m - \varphi_{ps} \quad (6.2)$$

where  $C_c$  is the location of the binary gas to segregation liquid transition and  $C_m$  is

the segregation liquid to segregation crystal transition. The lines corresponding to Eqns. (6.1) and (6.2) are plotted in Fig. 6.6 as the solid lines  $L2$  and  $L4$ , with the values of  $C_c = 0.665$  and  $C_m = 0.921$  for the transition points which were determined in Chapter 4. The variations between the experimental phase boundaries and the lines  $L2$  and  $L4$  are smaller than  $\sim 9\%$  for the three highest values of  $\varphi_{pb}$  and, therefore, of the same order of the error in the determination of  $C$  ( $\sim 8\%$ ). Greater deviations of  $\sim 16 - 17\%$  are observed for  $\varphi_{pb} = 0.054$ .

We stress that strong deviations from the results presented here are to be expected in the limiting cases as the mixture approaches the single component regimes: i)  $\varphi_{pb} \rightarrow 0$  and ii)  $\varphi_{ps} \rightarrow 0$ . Two sub-limits of particular interest are those for the dense cases: iii) ( $\varphi_{pb} \rightarrow \sqrt{12}/\pi, \varphi_{ps} \rightarrow 0$ ) where crystallization of the phosphor-bronze spheres are foreseen to prevail and ( $\varphi_{pb} \rightarrow 0, \varphi_{ps} \rightarrow 1$ ) where the dense liquid-like nature of the poppy seeds are expected to dominate the segregation behaviour. It is worth recalling that the 17% level of polydispersity of the poppy seeds prevents crystallization. In the range of  $\varphi_{pb}$  we have studied, no clear signature was observed for the limits mentioned above, near which we believe segregation may be suppressed. These limiting cases may be of interest to study in future investigations.

## 6.3 Forcing parameter-space

Thus far, our parametric investigation has been centered on the compacity and the aspect ratio which are parameters associated with the total filling fraction of the layer. The forcing parameters, on the other hand, have been kept fixed at  $f = 12Hz$  and  $A = \pm 1.74mm$ . We now explore the forcing parameter space,  $(f, A)$ . The aspect ratio and compacity are fixed at  $\Gamma = 2$  ( $\Delta y = 180mm$ ) and  $C = 0.900$  with  $N_{pb} = 1596$ . All experimental runs in this section, as before, are initiated from a homogeneously mixed configuration.

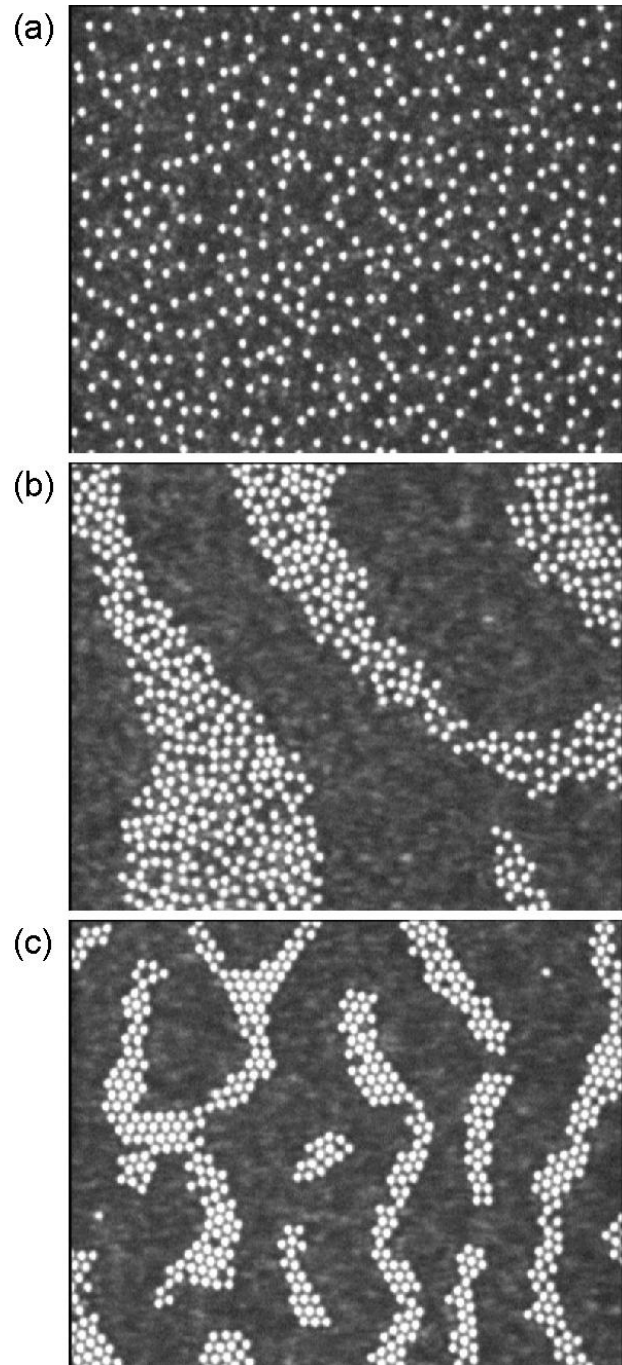


Figure 6.7: Experimental frames of the binary mixture at various values of  $f$  and  $A$ . (a) Binary gas for  $(f, A) = (28Hz, \pm 1.18mm)$ . (b) Segregation liquid for  $(f, A) = (16Hz, \pm 1.50mm)$ . (c) Segregation crystal for  $(f, A) = (12Hz, \pm 0.58mm)$ .  $\Gamma = 2$  ( $\Delta y = 180mm$ ) and  $C = 0.900$  with  $N_{pb} = 1596$ .

With  $(f, A) = (12Hz, \pm 1.74mm)$  the above conditions corresponded to a dense segregation liquid. However, all three phases identified in the previous compacity studies can now be observed in different locations of the  $(f, A)$  space. Examples of each of these phases can be seen in the experimental frames presented in Fig. 6.7. A typical example of a binary gas is shown in Fig. 6.7(a) for  $(f, A) = (28Hz, \pm 1.18mm)$ . The forcing is sufficiently large such that the motion phosphor-bronze spheres is apparently random across the layer and no segregation occurs. This example of the binary gas differs from the cases considered in Section 6.2 and Chapters 4 and 5 in the sense that, at this high compacities ( $C = 0.900$ ), the particles in the layer have persistent contacts with their neighbours and there is little or no free area in the tray. This is, therefore, a highly agitated but non-collisional state. At  $(f, A) = (16Hz, \pm 1.50mm)$ , the segregation liquid shown in Fig. 6.7(b) was observed and segregation occurred. A representative example of a segregation crystal is shown in 6.7(c) for,  $(f, A) = (12Hz, \pm 0.58mm)$ , where spheres within the domains were disposed in hexagonally packed configurations.

The corresponding phase diagram for the  $(f, A)$  parameter space is presented in Fig. 6.8. Two instances of the segregation crystal phase were found in the lower right hand corner of the diagram, for low amplitudes and frequencies. At intermediate values of the forcing a segregation liquid phase was observed. At relatively large values of  $f$  and  $A$  segregation did not occur and a binary gas phase persisted. The points  $A$ ,  $B$  and  $C$  along the parameter ray,  $r$ , correspond to the experimental frames in Figs. 6.7(a), (b) and (c), respectively. The nature of the phase boundary between the segregation liquid and the binary gas phases is discussed below.

We now want to quantify further this behaviour and, for each point in the  $(f, A)$  space, the  $PDF(\rho_v)$  of the distribution of the local Voronoi area density was constructed once again. Three typical PDF's for these distributions are

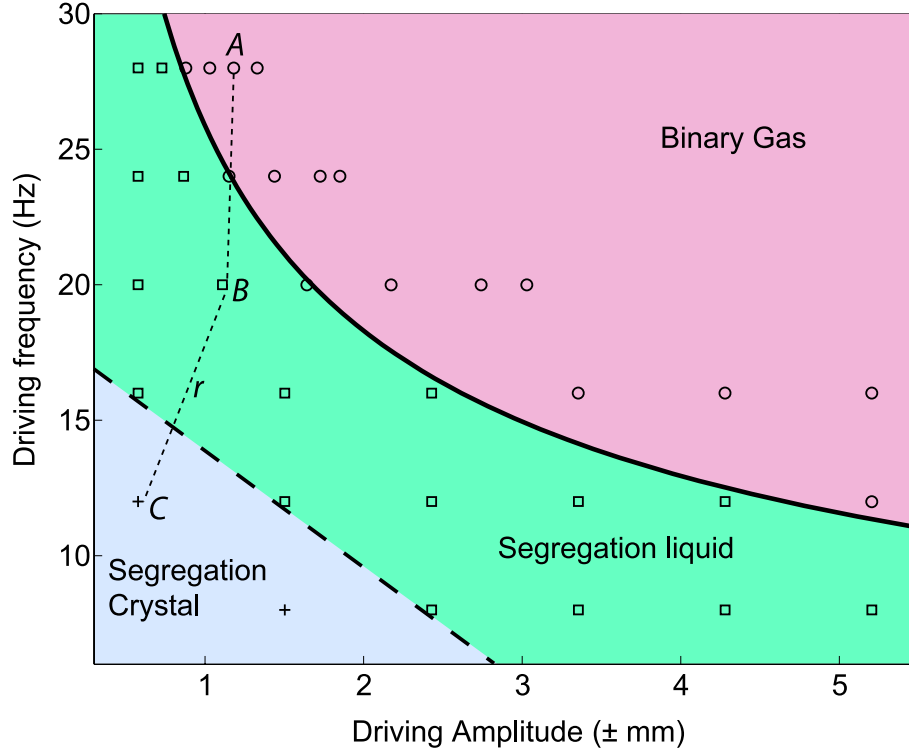


Figure 6.8: Phase diagram for  $(f, A)$  parameter space showing regions of existence for the three phases.  $(\circ)$  Binary gas.  $(\square)$  Segregation liquid.  $(+)$  Segregation crystal. The points  $A$ ,  $B$  and  $C$ , along the parameter ray  $r$ , correspond to the experimental frames shown in Fig. 6.7 (a), (b) and (c), respectively. The phase boundary between the segregation liquid and the binary gas phases is represented by the solid black curve and is given by Eqn. (6.4) with  $\gamma_c = 2.95$ .

presented in Fig. 6.9. The data for these distributions was acquired from 1500 temporal realizations over a period of  $1min$  after the mixture was vibrated for  $3min$ . The characteristic local Voronoi area density,  $\rho_v^{max}$ , was then obtained from the location of the maximum of the distribution in the same way to that followed in Sections 6.2 and 5.2.2.

Now we introduce a non-dimensional parameter for the forcing which is, es-

sentially, the dimensionless maximum acceleration of the tray,

$$\gamma = 4\pi^2 \frac{Af^2}{g} \quad (6.3)$$

where  $g$  is gravity's acceleration. This parameter  $\gamma$  is commonly used in the vertically vibrated granular systems (Melo, Umbanhowar & Swinney 1995) in which gravity plays a dominant role and the granular layer requires  $\gamma > 1$  to leave the vibrating plate. In our horizontal set up, gravity enters the problem indirectly through the frictional forces acted on individual particles,  $F = \mu mg$  where  $m$  is the particle mass and  $\mu$  its friction coefficient. In the ideal scenario of no rolling, the value of the non-dimensional acceleration at which relative motion

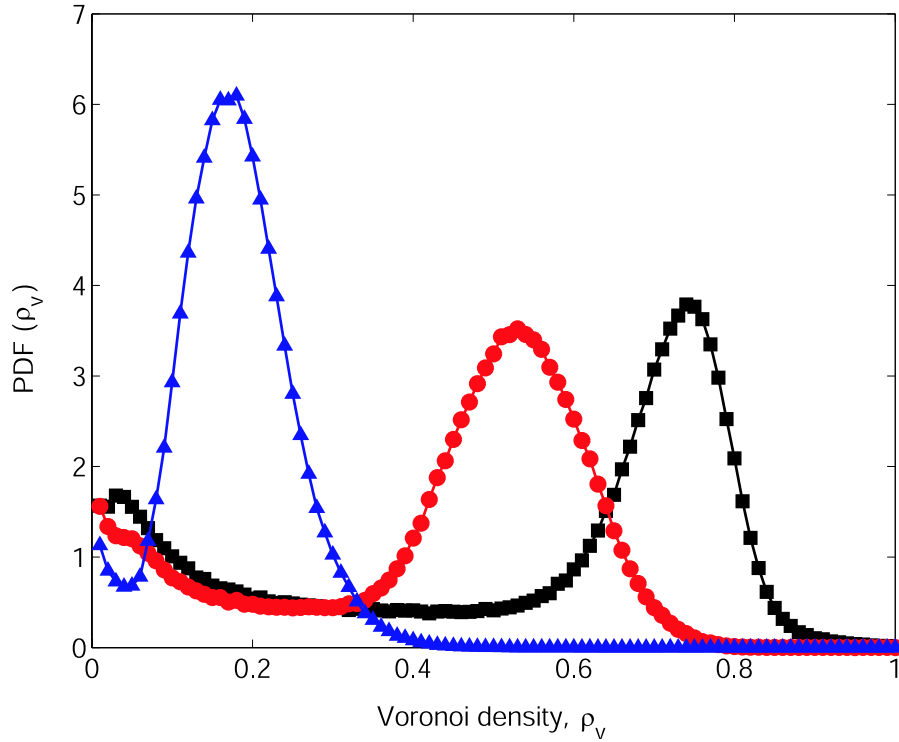


Figure 6.9: Probability distribution functions for the local Voronoi area density of the phosphor-bronze spheres for various forcing conditions. ( $\blacktriangle$ )  $(f, A) = (8Hz, \pm 1.50mm)$ , ( $\bullet$ )  $(f, A) = (16Hz, \pm 1.50mm)$ , ( $\blacksquare$ )  $(f, A) = (16Hz, \pm 3.35mm)$ .

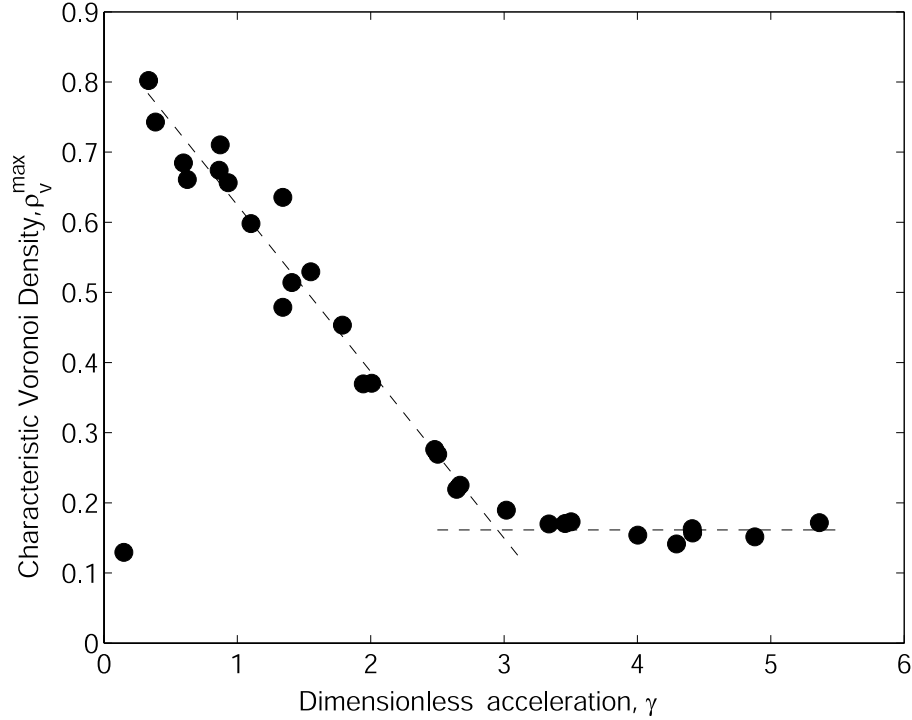


Figure 6.10: Transition diagram between a segregated phase and a mixed state, quantified by the characteristic local Voronoi area density of individual spheres, as the non-dimensional maximum acceleration,  $\gamma$ , is varied. The dashed lines are the best least squares fits in the two regimes. The point with lowest  $\gamma$  correspond to a layer for which the forcing was insufficient to agitate the granular mixture.

between the particle and the oscillatory tray is eminent would occur at  $\gamma = \mu$ .

In Fig. 6.10 the characteristic local Voronoi area density is plotted as a function of  $\gamma$ . All data points from the  $(f, A)$  parameter space shown in Fig. 6.8 collapse in a single curve, indicating that  $\gamma$  is, indeed, an appropriate parameter to describe the forcing of the granular mixture through oscillatory motion of the tray. Note that the point with lowest  $\gamma$  corresponds to an experimental realization in which the granular layer moved with the tray since the forcing was not sufficiently large to cause motion of particles.

Between  $\gamma = 0.15$  and  $\gamma = 0.34$  there is a jump in  $\rho_v^{\max}$  as the layer goes

from the immobile regime, in which there is no relative motion between the granular layer and the tray, and a regime in which segregation occurs. Above  $\gamma = 0.34$ ,  $\rho_c^{max}$  exhibits two clearly different regimes. At high accelerations, for  $\gamma \gtrsim 3$ , the characteristic Voronoi area density remains approximately constant with increasing  $\gamma$ . In this regime, the layer was in the highly agitated binary gas phase discussed above and no segregation occurred. As  $\gamma$  is decreased below  $\gamma \sim 3$  the final state achieved becomes increasingly more dense in an approximately linear fashion. The dashed lines in Fig 6.8 were obtained from the best least squares fits of the form  $\rho_v^{max}(\gamma) = m\gamma + n$ , in the region  $0.34 < \gamma < 2.67$ , in the segregation phase, and  $\rho_v^{max}(\gamma) = p$  in the region  $3.34 < \gamma < 5.37$ , in the binary gas phase. The fitting parameters were  $m = -0.238 \pm 0.012$ ,  $n = 0.862 \pm 0.019$  and  $p = 0.161 \pm 0.004$ . The intercept of the two lines yields the location of the transition point which was measured to be  $\gamma_c = 2.95 \pm 0.16$ .

Having successfully achieved the collapse of  $\rho_v^{max}$  for the points in the  $(f, A)$  parameter space in a single curve, dependent on  $\gamma$ , and having numerically determined  $\gamma_c$ , we now comment on the nature of the phase boundary between the binary gas and segregation liquid phases. This phase boundary,  $f'(A')$ , is well fitted by

$$f' = \frac{1}{2\pi} \sqrt{\frac{\gamma_c g}{A'}}, \quad (6.4)$$

as shown by the solid curve in Fig. 6.8, which once again suggests that  $\gamma$  is the appropriate parameter to describe the forcing of the tray. On the other hand the transition between the segregation liquid to segregation crystal (dashed line in Fig. 6.8) does not show any particular features in the  $\gamma$  dependence of  $\rho_v^{max}$ .

## 6.4 Summary

We have undertaken a detailed exploration of the parameter space of the binary granular mixture in order to further investigate the layer's phase behaviour and

constructed the associated phase diagrams.

Firstly, we investigated the dependence of the characteristic local Voronoi area density of the phosphor-bronze spheres on the dimensions of the tray for a fixed values of  $C$  and of the forcing parameters. This showed the segregation behaviour to be approximately independent of both the tray's total area and aspect ratio, to within 6%. This finding suggests that the layer compacity is an appropriate parameter with which to study the segregation phases of the mixture and that the packing of the layer plays a major role in the segregation behaviour.

Moreover, we explored the compacity parameter space by decoupling the parameter  $C$  into two of its components: the filling fractions of the poppy seeds and of the spheres,  $\varphi_{ps}$  and  $\varphi_{pb}$ , respectively. The resulting phase diagram contained regions of existence and stability for the three segregation phases uncovered in Chapters 4 and 5. The location, in  $C$  for the respective phase transition points,  $C_c$  and  $C_m$ , were unchanged to within 9%, for  $0.083 < \varphi_{pb} < 0.174$ , but deviations of up to 17% were observed for  $\varphi_{pb} = 0.054$ . These results provide evidence that the phase behaviour discussed in Chapters 4 and 5 is robust over a range of the parameter space  $(\varphi_{pb}, \varphi_{ps})$ . Exceptions to this behaviour are to be expected in the limiting cases discussed at the end of Section 6.2.

Finally, the effect of changing the frequency and amplitude of vibration was then studied, thereby changing the amount of momentum transferred to the granular mixture. The compacity of the layer was fixed at the high value of  $C = 0.900$ . Under the previous vibration conditions, a binary mixture at this parameters would evolve to a dense segregation liquid. A phase diagram of the parameter space  $(f, A)$  was constructed which exhibited regions of existence of the three phases observed previously in the compacity studies. In this sense, a variety of final states could be attained all the way from a highly dense segregation crystal through to a dilute and highly agitated binary gas, as a function of the forcing.

Furthermore, the dimensionless maximum acceleration of the tray,  $\gamma$ , was used to collapse the data for the characteristic local Voronoi area density of the spheres into a single curve. This enabled a well defined transition to be uncovered at the value of  $\gamma_c = 2.95 \pm 0.16$  between a mixed regime, for  $\gamma > \gamma_c$ , and a regime where segregation occurred, for  $\gamma < \gamma_c$ .

# Chapter 7

## Conclusions

### 7.1 General Remarks

We have presented a detailed investigation of segregation behaviour in a monolayer of two types of particles driven by an oscillatory horizontal tray. Even though, the segregation patterns could be obtained with a variety of other granular materials, our study focused on mixtures of phosphor-bronze spheres and poppy seeds. When vibrated, an initially homogeneously mixed layer gave rise to robust patterns such that stripes of one particle type formed within the other over a range of parameters.

The two principal parameters of the system were found to be the layer compacity and the dimensionless acceleration of the driving. The segregation process appeared to be independent of both the area and aspect ratio of the tray. We used a number of measures, macroscopic (at the level of segregation domains) and microscopic measures (from the positions of individual spheres), to characterise the system's behaviour.

As the compacity was systematically varied, we uncovered the existence of three segregation phases of the mixture. At low  $C$ , a binary gas was observed where both particle types apparently randomly diffused through the layer without

aggregation. At intermediate  $C$ , in the segregation liquid phase, mobile clusters of the phosphor-bronze spheres formed, reminiscent of drops of oil in water. In the segregation crystal phase, at high  $C$ , robust stripes formed where the spheres ordered into an hexagonal packing within the domains. The respective transition points were measured to be  $C_c = 0.67 \pm 0.06$  for the binary gas to segregation liquid transition and  $C_m = 0.92 \pm 0.08$  for the segregation liquid to crystal transition. In particular, the transition at  $C_c$  had the characteristics of a continuous phase transition with an associated square-root growth of a macroscopic order parameter, critical slowing down and amplification of the microscopic fluctuations. The structural configurations, as measured by the probability distribution function of nearest neighbours and the radial distribution function, provided further evidence for the classification we have proposed. This phase behaviour was found to be robust over a range of the  $C = (\varphi_{ps}, \varphi_{pb})$  parameter space, for the filling fractions of each of the two particle types.

Moreover, all three phases were also observed while fixing the value of the compacity ( $C = 0.90$ ) and exploring the frequency and amplitude of the forcing. The characteristic Voronoi area density was used to quantify the segregation at each point in the  $(f, A)$  parameter space and collapse of the data into a single curve was attained as a function of the dimensionless acceleration of the tray,  $\gamma$ . This revealed an additional segregation transition with the forcing, at  $\gamma_c = 2.95 \pm 0.16$ . For  $\gamma > \gamma_c$  the mixture was in a highly agitated state and no segregation occurred. This high compacity mixed state differed from the binary gas observed in the compacity studies, at low  $C$ , in the sense that there were now enduring contacts between the particles in the layer and there was little or no free area in the tray. As the dimensionless acceleration was decreased below  $\gamma_c$ , the final state of the system was increasingly denser in an approximately linear fashion.

## 7.2 Possible segregation mechanism

In parallel to the experimental work presented in this Thesis, we established a collaboration with George Ehrhardt<sup>1</sup> and Andrew Stephenson<sup>1</sup> who performed an event driven numerical simulation of a two-dimensional phenomenological model of our experimental system (Ehrhardt et al. 2004). The results of this investigation are presented in Appendix C.

In the simulations, the two-dimensional motion of individual particles was modelled by a Langevin equation with the forcing being provided by a sinusoidal term (oscillatory motion of the tray) and by a Gaussian white noise term (to reflect the randomness observed in the motion of individual particles potentially due to a combined effect of non-sphericity and the stick-slip frictional interactions with the surface of the tray). The segregation behaviour of the numerical system is found to be in good qualitative agreement with our experiments. In particular, a segregation transition is also found as  $C$  is increased at a value of  $C_{sim} \sim 0.6$ , which is consistent with our experimentally determined  $C_c$ . Nonetheless, this transition is not found to be as sharp as in the experiments and no critical slowing down was observed in the vicinity of the transition.

By exploring parameter space in a way which was inaccessible in the experiments, the principal mechanism underlying segregation in our system was suggested to be the differential driving between each of the particle species. In the experiments, this is thought to be due to the different surface properties of the phosphor-bronze spheres and the poppy seeds which induce different frictional interactions with the surface of the oscillatory tray. Other effects such as different size, inelasticity, shape, noise strength or noise correlation are also possible candidates to drive the process but the simulations suggest that they appear to

---

<sup>1</sup>Theoretical Physics Group, Department of Physics and Astronomy, University of Manchester.

be secondary. Note that the introduction of a noise forcing term was required to more closely reproduce the experimental behaviour. In conclusion, these numerical results suggest that the transition from the binary gas to the segregation liquid phases is caused by a competition between the differential driving of the two particle types, which induces segregation, and noise, which acts to prevent it.

### 7.3 Analogies with binary colloids

There are some analogies between segregation in our granular system and phase separation in binary colloids (Dinsmore et al. 1995), a discussion of which was given in Section 1.6. Firstly, the protocol in our experimental study, of increasing  $\varphi_{ps}$  while keeping  $\varphi_{pb}$  constant is analogous to changing the concentration of the polymer in solution of colloid-polymer mixtures. In the colloidal case, this procedure results in the deepening of the inter-particle potential  $U$  and in the decrease of the overall temperature  $T$  but has the combined effect of increasing the dimensionless parameter  $U/k_B T$  (Poon 2002). The strength of the interaction can thereby be tuned to induce gas-to-liquid and liquid-to-crystal transitions (Anderson 1993). The scenario of three phases of segregation that we have observed can therefore be linked to the various phases seen in colloidal systems. In particular, visual inspection suggests that our segregation crystals closely resemble 2D colloidal crystals (Hobbie 1998), an example of which was given in the photograph of Fig. 1.5(a). Also the size ratio in our granular mixture  $q = 0.71$  is consistent with that required in colloidal mixtures ( $q \gtrsim 0.3$ ) for gas, liquid and crystal phases to be obtained (Poon, Egelhaaf, Stellbrink, Allgair, Scofield & Pusey 2001, Poon 2002). Another striking similarity is the fact that the increase in free area available to the poppy seeds when a homogeneous mixture segregates at high  $C$ , can be as high as 16% as shown in Fig. 4 of Appendix C. This is consistent with

what is observed in colloid-polymer mixtures undergoing phase separation where the free volume available to the polymer in solution considerably increases when the large colloidal particles aggregate (Dinsmore et al. 1995).

Despite these similarities, a major difference between the two systems is the thermalization of individual particles. In colloidal systems, Brownian motion is an intrinsic part of the equilibrium dynamics. In our system, which is driven, dissipative and far from equilibrium, energy is injected through frictional interactions between the grains in the layer and the oscillatory tray. As mentioned above, the principal mechanism for segregation in our system appears to be the differential driving between the two particle types, an effect not present in equilibrium systems. Hence, our results may open the potential of extending ideas of phase separation in binary colloidal mixtures to granular segregation, but they also highlight the need to account for additional non-equilibrium effects such as inelasticity and differential non-Brownian driving. Hence, a direct connection between the two systems remains speculative.

## 7.4 Future work

The understanding of segregation in the new experimental scenario we have proposed is a long way from a predictive theoretical model. However, we believe that this system is an ideal configuration in which to explore particular features of granular segregation with relevance to a more general knowledge of separation of particulate solids. Below, I discuss possible directions for future work.

1. The first natural extension of our work would be to attempt to bring closer the type of experiments we have presented and the numerical simulations of the type reported in Appendix C. One way to do this experimentally is to use two types of identical discs of the same material and size, the

only difference being the roughness of the surface in contact with the oscillatory tray. This would allow for the effect of differential forcing alone to be studied in detail. In addition, high precision tracking of the position and velocity distributions of the discs for the cases of individual particles and single component layers (at various filling fractions) would enable an accurate measurement of the parameters involved in the numerical model. This would allow for a more accurate comparison between experiments and simulations to be performed in order to more conclusively test the validity of the segregation mechanism we have proposed.

2. Another direction is the exploration of particle shape on the segregation behaviour.
3. It will be important to complement the new experiments proposed in the above points 1. and 2. with an extensive numerical study in order to thoroughly sweep the vast parameter space in the system, in ways not accessibly experimentally.
4. Finally, it would be interesting to further explore the long term collective motion of the mixture, some preliminary results of which are presented in Appendix B. An issue of particular appeal is the analogy between acoustic streaming in classical fluids and vortex-like motion when a oscillatory object is inserted in a fluidised layer of grains (Section B.1). In collaboration with Mark Shattuck<sup>2</sup>, the Author is currently developing a new experiment to study this phenomena. The geometry is based on a modification of a design by Olafsen & Urbach (1999) where the *granular fluid* is generated by vertical vibration of a granular layer of spheres in a gap between two horizontal parallel plates. The gap between the plates is 1.6 sphere diameters, which

---

<sup>2</sup>Levich Institute, City College of New York, New York, USA.

ensures a quasi-2D geometry and an independent oscillatory disk is inserted in the fluidised layer to induce the streaming motion. We are hoping to be able to compare the experimental streaming velocity profiles with the predictions of Kinetic Theory.

# Appendix A

## The radial distribution function

A general tool for the analysis of structural configurations of materials is the *radial distribution function*,  $g(r)$  (Chaikin 1995), which specifies the number of particles (here grains) to be found at any distance  $r$  from an arbitrary chosen particle. Its functional form is given by,

$$g(r) = A(r) \left\langle \sum_i \sum_{j \neq i} \delta(r - r_{ij}) \right\rangle, \quad (\text{A.1})$$

where  $r_{ij}$  is the separation between the  $i$  and  $j^{\text{th}}$  particles and the angled brackets denote a time average.  $A(r)$  is a normalization constant. An illustration of the calculation of  $g(r)$  is shown in the schematic diagram of Fig. A.1(a). The quantity  $g(r)dr$  yields the number of particles to be found in the shell bound by  $r$  and  $r + dr$ , normalized by the number of particles that would be expected for a uniform distribution of particle positions. Note that for a system with finite size, the portions of the shells,  $[r, r + dr]$ , lying outside the boundaries (green regions in Fig. A.1a) must be removed from the normalization procedure. Hence,  $g(r)$  is the normalized probability, averaged over the system, of finding a particle as a function of distance from the centre of another particle,  $i$ .

To better illustrate the information extracted from this structural measure, consider a two dimensional hexagonal crystal of disks at absolute zero where  $g(r)$

can be determined from the geometrical structure of the lattice. A schematic diagram of this configuration is presented in Fig. A.1(b). For a central particle,  $i$ , shown in red in Fig. A.1(b), the shortest possible distance from the centre of particle  $i$  to another particle is one particle diameter and corresponds to six nearest neighbours which are shown in green in Fig. A.1(b). The next nearest neighbours are also six (blue particles in Fig. A.1(b)) and lie at a distance  $\sqrt{3}d$  from the original particle. The following shell of neighbours is located at a distance  $2d$  from  $i$  (yellow particles in Fig. A.1(b)). Thus particles in the lattice are located on a series of consecutive spherical shells, centered on the chosen particle, whose radii bear a simple numerical relationship to  $d$ , determined by the geometry of the lattice:  $d$ ,  $\sqrt{3}d$ ,  $2d$ ,  $\sqrt{7}d$ ,  $3d$  and so on. Therefore, the

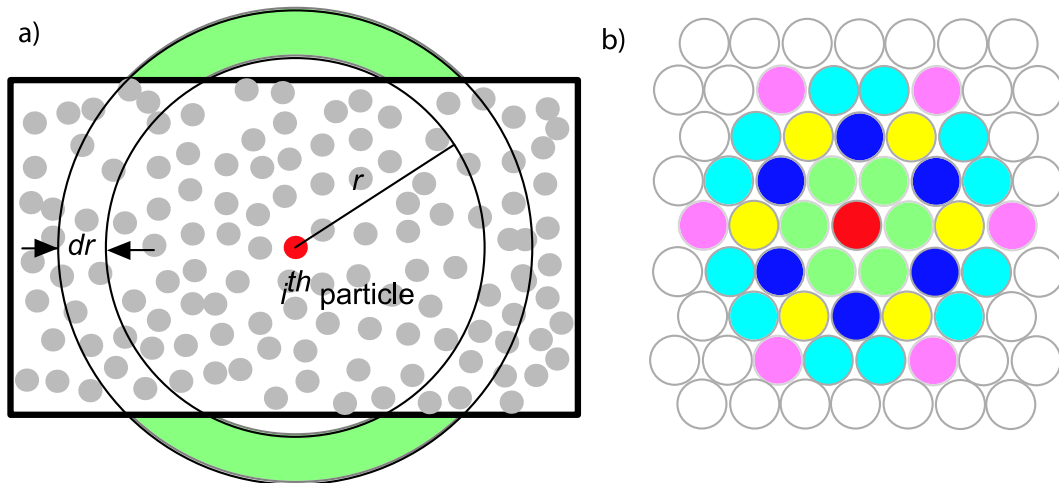


Figure A.1: (a) Schematic diagram for the calculation of the radial distribution function,  $g(r)$ . The  $i^{th}$  particle is shown in red and particles are counted within a shell of radius  $r$  and thickness  $dr$ . (b) Nearest neighbour configurations for an hexagonally packed lattice of disks in two dimensions. The  $i^{th}$  particle is shown in red. Neighbours in the 1st shell ( $r = d$ ) are shown in green, in the 2nd shell in blue ( $r = \sqrt{3}d$ ), in the 3rd shell in yellow ( $r = 2d$ ), in the 4th shell in cyan ( $r = \sqrt{7}d$ ) and in the 5th shell in magenta ( $r = 3d$ ).

radial distribution function for hexagonally packed disks exhibits  $\delta$ -peaks at the characteristic distances corresponding to the particular shell with their height proportional to the number of neighbours in each of those shells. If the crystal is not at absolute zero the  $\delta$ -peaks are smoothed due to the local agitation of the particles in the lattice.

In liquid-like configurations,  $g(r)$  is zero up to a distance corresponding to the particle diameter, exhibits a maximum at this distance and then oscillates with a rapid decay with distance until it asymptotes to unity. Note that for an ideal gas of hard spheres,  $g(r)$  is independent of positions and is equal to unity anywhere, apart from  $r < d$  where  $g(r < d) = 0$ .

# Appendix B

## Nonlinear behaviour

In this Appendix we focus on the nonlinear behaviour of the segregation patterns where interesting effects such as time dependence are observed at high compacities. The dynamics of the merging of stripes is discussed with emphasis on the vortex-like motion observed in the regions of the poppy seeds. We report results of an additional experiment which was performed to investigate the effect of introducing an oscillatory object into a fluidised single component layer of poppy seeds. This is found to induce streaming motion reminiscent of acoustic streaming in fluid flow. We then turn to the description of a long term oscillatory state observed in mixtures with high compacities. Intriguingly, the period of this regular collective motion was estimated to be  $\sim 3500$  times longer than that of the oscillatory driving.

### B.1 Induction of streaming motion

The investigation, thus far, was centered on the phase behaviour of the binary mixture with emphasis on the *initial segregation growth regime*. As defined in Section 3.3 this regime is the first phase of segregation in which clusters form, having started from a homogeneously mixed granular layer (for  $C > C_c$ ). The timescales associated with this initial process are of the order of a few tens of seconds. In

Chapter 3 we mentioned the existence of a considerably slower *coarsening regime* that occurs after the initial segregation growth regime, with timescales of the order of tens of minutes. In this second regime, segregation clusters in the layer can progressively coalesce to form larger clusters. We believe that this *separation of timescales* is characteristic of the different mechanisms associated with each of these regimes. As described in Section 3.1, the initial segregation is essentially a diffusive process as individual spheres encounter others, through random motion across the granular layer, to form clusters. The process for coarsening of the patterns (for  $C > C_c$ ) appeared to be distinct and is considered next.

An example of a coarsening evolution between a pattern with six to five stripes is presented in the series of experimental frames shown in Fig. B.1. They correspond to an experimental run of a binary mixture of phosphor-bronze spheres and poppy seeds for a layer with compacity  $C = 1.114$  and  $N_{pb} = 1596$  in the original tray with  $\Gamma = 2$  ( $\Delta y = 180mm$ ). The frame in Fig. B.1(a) was acquired  $t = 218sec$  after vibration of an initially homogeneous mixture with forcing parameters  $(f, A) = (12Hz, \pm 1.74mm)$ . A label for each of the stripes has been inserted in the figure to aid the description, i.e.  $S1, S2, S3, S6$  and  $S7$  are stripes that span the full width of the system and  $S4$  and  $S5$  are the central discontinuous stripes. The differences in frictional properties between the two particle types and the tray gave rise to differential motion between the regions of poppy seeds and the stripes of phosphor-bronze spheres. Near the tips of  $S4$  and  $S5$  continuous *vortex-like motion* in the region of the poppy seeds was observed. This took the form of two pairs of vortex cells such that poppy seeds were expelled at the left and right hand sides of each of the discontinuous stripes, circulated to the middle of the cell and then returned towards the tips of  $S4$  and  $S5$ , respectively. These vortex structures were clearly observed by eye using time-lapsed video.

A schematic of this motion has been superposed on Fig. B.1(a) as four white

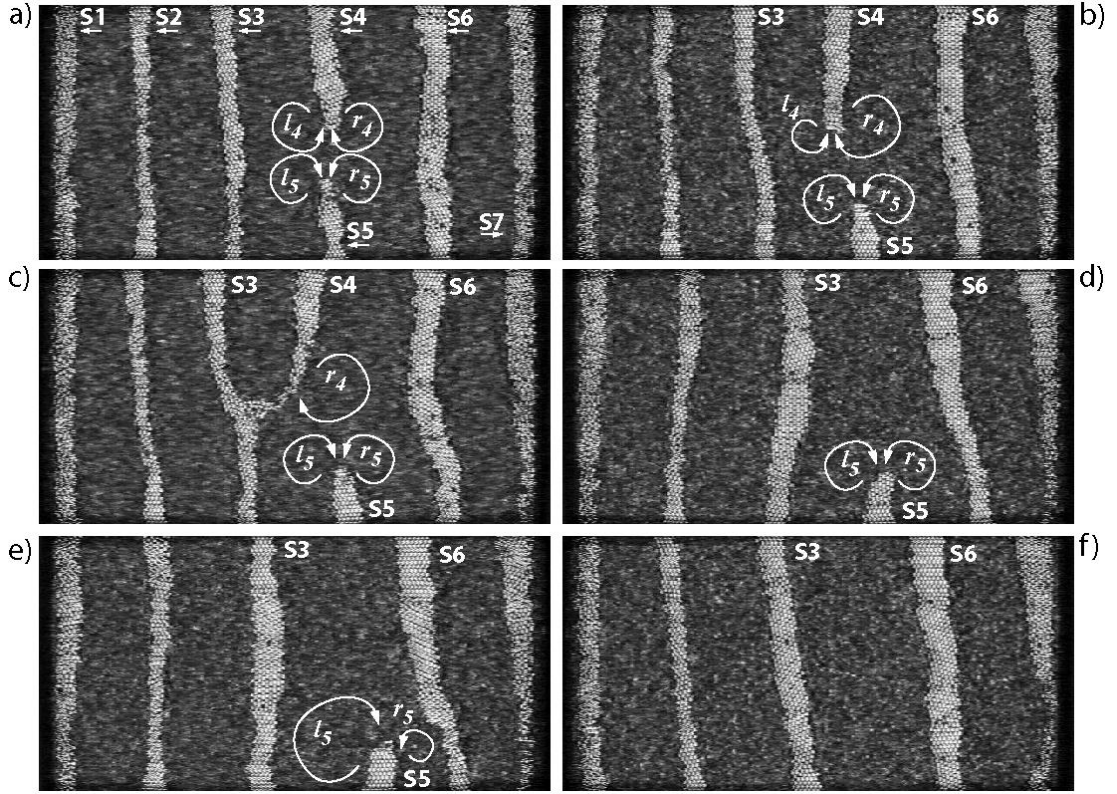


Figure B.1: Experimental frames of an example of the coarsening regime patterns for a mixture of phosphor-bronze spheres (bright regions) and poppy seeds (grey regions) acquired at (a)  $t = 218\text{sec}$ , (b)  $t = 576\text{sec}$ , (c)  $t = 730\text{sec}$ , (d)  $t = 1203\text{sec}$ , (e)  $t = 1357\text{sec}$  and (f)  $t = 1536\text{sec}$  after vibration of an homogeneously mixed layer. The experimental parameters were  $\Gamma = 2$ ,  $(f, A) = (12\text{Hz}, \pm 1.74\text{mm})$  and  $C = 1.114$ . The white arrows near  $S4$  and  $S5$  represent the motion of the poppy seeds in the regions near the tips of the respective stripes of phosphor-bronze spheres.

arrows near  $S4$  and  $S5$  and the direction of the arrows represents the direction of the flow. At  $t = 218\text{sec}$  these four vortices were approximately symmetric. However, in the period ( $218 < t < 576$ ) $\text{sec}$ , the vortex labelled  $l_4$  in Fig. B.1(a) grew over  $r_4$  and consequently the stripe  $S4$  moved towards  $S3$  (Fig. B.1b). Eventually,  $S4$  merged with  $S3$  at  $t = 730\text{sec}$  (Figs. B.1c,d).

During this merging process, the two vortices around  $S5$ ,  $l_5$  and  $r_5$ , remained approximately unchanged. By  $t = 1203\text{sec}$ ,  $S4$  had merged with  $S3$  and  $S5$  remained the only disconnected stripe in the layer (Fig. B.1d). The stripe  $S5$  then underwent the same process to that of  $S4$ . The vortex  $l_5$  grew over  $r_5$  and  $S5$  progressively moved to the right as shown in Fig. B.1(e), to then merge with  $S6$ , yielding the pattern with five stripes presented in Fig. B.1(e).

This coarsening mechanism through vortex-like motion appears to be responsible for the discontinuities in the time series of the macroscopic quantities (average domain width and the average number of domains) discussed in Chapter 3. An example of such a sharp jump can be seen in the time series of both  $\phi$  and  $\eta$ , shown in Fig. 3.5, when the pattern coarsens from six to five stripes at  $t \sim 950\text{sec}$ .

A possible mechanism for the streaming motion around the tip of the stripes is now considered. An experiment was performed with the idea of investigating the effect of an oscillatory object on a fluidised single component layer of poppy seeds. The aim was to reproduce the production of vortices in a simpler geometry than that of the region bound by  $S3$  and  $S6$ , shown in Fig. B.1(d). The schematic diagram of the new rigid boundaries set by a rigid frame attached above the flat tray is shown in Fig. B.2. The central object consisted of a 5mm high aluminium frame with a central  $45 \times 10\text{mm}$  rigid bar attached to the frame as shown in the Fig. B.2. This bound a U-shaped region in the tray (grey in Fig. B.2) which contained a single layer of poppy seeds with  $\varphi_{ps} = 0.90$ . The whole tray was then

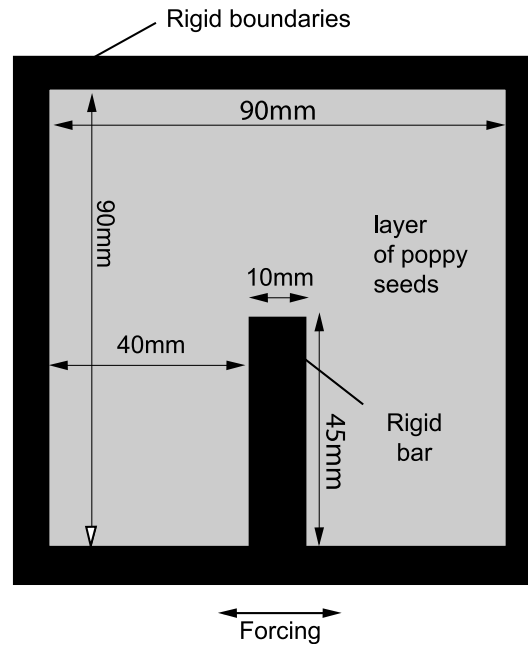


Figure B.2: Schematic diagram of the geometry of the boundaries used in the streaming motion experiments. The aluminium frame is shown in black. The layer of poppy seeds is shown in grey. The whole tray was oscillated sinusoidally along the direction shown by the arrows.

vibrated at  $f = 12Hz$  and  $A = \pm 1.74mm$ .

Upon vibration, the granular layer was fluidised and the action of the end walls, perpendicular to the direction of drive, was observed to be localized within a  $\sim 5mm$  wide band. Slipping occurred between the poppy and the bottom surface of the oscillatory tray. Hence, there was relative motion of the grains with respect to the tray/frame assembly and the layer was forced by the central bar in an oscillatory way.

A typical experimental frame is presented in Fig. B.3(a). The location of the central rigid bar has been highlighted by a red rectangle. The video frames were image processed by adjusting the *tone map* using the package Corel PhotoPaint 6.0 so that only the brightest poppy seeds were made visible as shown in Fig.

B.3(b). These were used as particle tracer to visualise the resulting flow.

In Fig. B.3(c) we present an image created from a superposition of 50 sequential imaged processed experimental frames. The time-step between each frame is 0.6sec and the superposition was performed by adding the grey-scale value of each pixel of the new frame, at  $t$ , to the previous one, at  $t - 1$ , with the condition that the value of the pixel in the new frame be higher than in the previous one, otherwise it was left unchanged. This was accomplished by using the `Iflighter` routine in Corel Photopaint 6.0. Therefore, the white streaks in Fig. B.3(c) correspond to particle trajectories advected by the resulting granular flow. A mean flow in the granular layer was clear as particles were *expelled* at the sides of the central rigid bar, circulated to the top of the cell away from the bar and then returned towards the rigid bar. The yellow arrows in the Fig. B.3 represent the direction of this continuous granular flow. The streaming motion obtained this way closely resembles the vortex-like motion around the tip of discontinuous stripes obtained in the case of the dense binary granular mixture discussed above.

There are similarities between the granular flow we have generated in our experiments and the case of *acoustic* or *secondary streaming* when an oscillatory object is inserted in a fluid. In such oscillatory flows mean quantities can be altered from those in the steady case such that a non-zero net flux of momentum across surfaces in the fluid induces drifting motion. This arises from non-zero averages of the mean quantities in the non-linear terms in the Navier-Stokes equations, due to the oscillatory forcing (Batchelor 1967, pp 358-364). A classic example of an experimental realization of this phenomena is shown in the photograph of Fig. B.1 which was reprinted from “*An album of fluid motion*” (van Dyke 1982). It corresponds to the acoustic streaming motion generated by an oscillatory sphere in a Stokes flow. The fluid has been doped with flow visualization and illuminated with a light sheet in order to enable the observation of

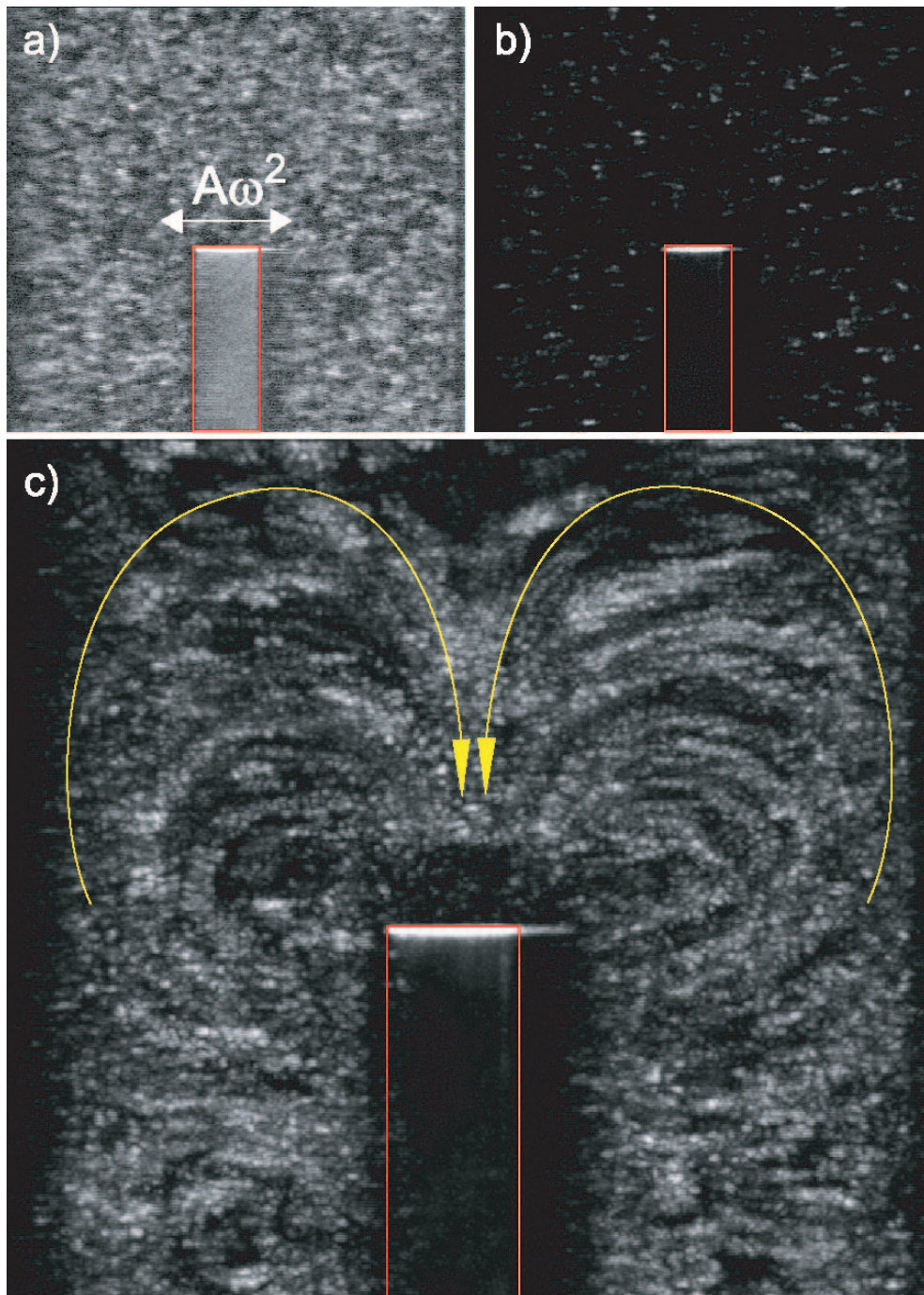


Figure B.3: Granular streaming motion. (a) Typical original frame. (b) image processed frame enhancing the visualization of the brightest poppy seeds. (c) Superposition of 50 frames, with a time step of 0.6sec, using the `Iflighter` condition described in the text.

the streaming cells. The photograph was taken using a long exposure technique so that white streaks are trajectories of individual visualization particles that are advected with the mean flow.

The connection between secondary streaming in classical fluids and streaming motion in granular flows has been reported by Savage (1988). He performed a theoretical analysis of continuum-like equations for a single type of grain and undertook experiments on a vertically vibrated cell and suggested that the obtained streaming cells originate from the momentum transfer from the vibrating bottom plate into the granular media.

Other experimental studies have reported the existence of vortex-like cells but in the context of buoyancy driven granular convection. For example Knight, Ehrides, Kuperman, Flint, Jaeger & Nagel (1996) observed granular convection in a 3D geometry using tracer particle techniques and magnetic resonance imaging. More recently Wildman, Huntley & Parker (2001) have performed an experimental study in a three dimensional vertically vibrated system. They reported the observation of convection-like rolls in the highly fluidised flow regime, using positron emission particle tracking. Lan & Rosato (1997) performed molecular dynamics simulations and noted that the onset of convection reported in the granular literature is not only determined by the acceleration of the vibrating bottom plate but also by the ratio of the particle diameter to system size. In numerical simulations of Navier-Stokes like equations for granular materials, Bourzutschky & Miller (1995) have found that to obtain the same direction of circulation of the convection rolls to that found in experiments of vibrated granular cells, negative-slip boundary conditions had to be introduced. To our knowledge, the case of a streaming flow induced by an oscillatory object emersed in a granular material and analogous to the classical fluid case has not yet been reported in the literature.



Figure B.4: Steady streaming for a oscillatory sphere emersed in a Stokes flow. Photograph reprinted from “*An album of fluid motion*” by (van Dyke, M. 1982).

## B.2 Oscillatory states

Coupling between flow in the regions of poppy seeds and deformations of the segregation domains of spheres was also observed when the stripes oscillated at large values of  $C$ . In Fig. B.5 we show three sequential photographs which correspond to (a) the beginning of the cycle, (b) half-cycle and (c) full cycle points of one oscillation in a pattern with five stripes. These experimental frames were captured  $20min$  (the time required for the pattern to form) after having started from a homogenous mixture of poppy seeds and phosphor-bronze spheres. Once formed, this pattern was found to be stable over a period of  $\sim 1.5hrs$ . The mixture was set with a compacity of  $C = 1.135$  ( $N_{pb} = 1596$ ) and was vibrated at  $f = 12Hz$  and  $A = \pm 1.74mm$  in a  $(180 \times 90)mm$  tray. In these oscillations of the pattern, the phosphor-bronze stripes bent periodically, backwards and forwards, in a reproducible way. For each of the regions of poppy seeds in between two phosphor-bronze stripes, there was a complementary collective motion in the form of a single large vortex. The direction of rotation of the vortex was reversed every half-cycle of the oscillation as represented by yellow arrows in Fig. B.5.

In Fig. B.6(a), we illustrate the periodic nature of the oscillations with a space-time diagram of the process which was obtained following the method described in detail in Section 3.2. This was constructed by sampling along a single line in the  $x$ -dimension and progressively stacking the lines over a period of  $1.5hrs$ . The sampling line was positioned at  $1/3$  of the  $y$ -length of the tray as indicated by the solid red line,  $L$ , superposed in Fig. B.5(c). The oscillations of all five stripes were observed to be in phase. We stress that these oscillations were found to be stable for  $\sim 5400sec$ , i.e. more than four order of magnitude longer than the period of the oscillatory driving.

In Fig. B.6(b), we plot the time-series for the position  $x_{s3}(t)$  of the central stripe along  $L$ . The amplitude of the oscillations appeared to be slightly irregular

but a clear cycle is observed with a well defined period which, using the autocorrelation of  $x_{S3}(t)$  (Press et al. 1992), we have estimated to be  $T_{S3} = (2.9 \times 10^2)_{sec}$ .

In addition to the temporal periodicity at the particular intersection point between the centre of  $S3$  and the sample line  $L$ , the oscillations of the stripes are also spatially regular. To explore this point further we focus, again, on the central stripe  $S3$ . The experimental frames were first cropped around  $S3$  and along  $x$  (i.e. the height of the cropped images was kept at  $\Delta y = 90mm$ ). The frames were then image processed using the method presented in Section 2.8.1. This enabled the original frames to be transformed into binary images assigning white regions (pixel value of 1) for regions of phosphor-bronze spheres and black regions (pixel value of 0) for regions of poppy seeds. For each frame, the location of the centre line of the stripe  $x_l(y, t)$  was then determined from the longitudinal midpoint of the white domains. A series of processed frames with the corresponding superposed  $x_l(y, t)$  lines are presented in Fig. B.7, at three stages of the cycle.

A three dimensional spatio-temporal diagram for the dynamics of the central line of the  $S3$  stripe is presented in Fig. B.8 where it is shown that the stripes bent periodically along  $\pm x$ . The point of the central line of the stripe with lowest amplitude was that with  $y = \Delta y/2$ , i.e. at the centre of the tray. The amplitude of  $x_l(y, t)$  increased for  $y \rightarrow 0$  and  $y \rightarrow \Delta y$  and the extreme points  $x_l(0, t)$  and  $x_l(\Delta y, t)$  had the highest amplitude and oscillate out of phase, with respect to each other.

It is interesting to note that the timescale associated with these oscillations is  $\sim 3500$  times slower than the driving (at  $12Hz$ ) excluding the possibility of a simple resonance in the driving/granular-layer system. The mechanism which gives rise to this oscillatory phenomena remains, as yet, unexplained.

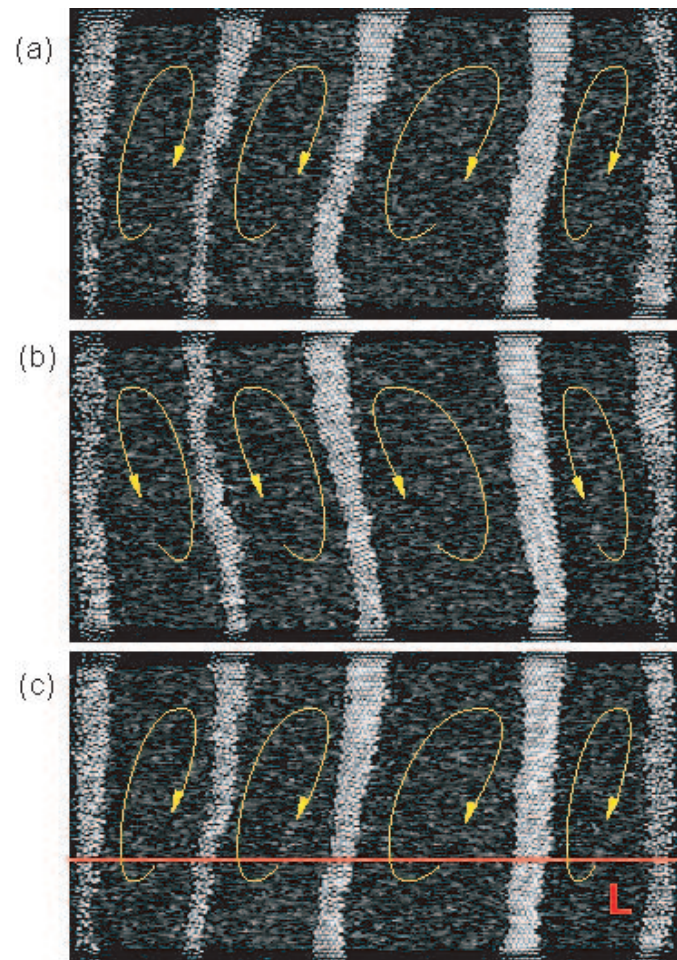


Figure B.5: Photographs of the granular layer showing the oscillatory bending of the phosphor-bronze stripes (regions in white), at different times: (a) beginning of cycle, (b) half-cycle, (c) end of cycle. The sample line  $L$  located at  $1/3$  of the width of the tray was used to construct the space time diagram in Fig. B.6. The yellow arrows indicate the direction of the vortex motion in the regions of poppy seeds.

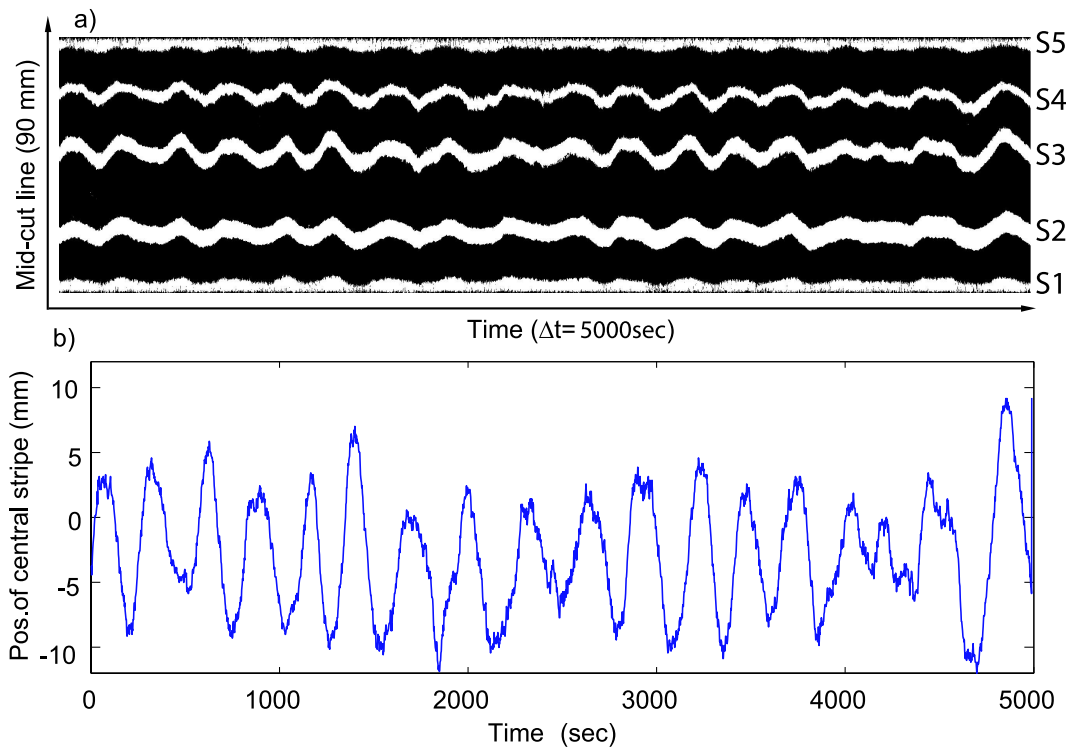


Figure B.6: (a) Space time diagram constructed from stacks of the cut line,  $L$  in Fig. B.5(c), over  $5000 \text{ sec}$ . The stripes are labelled on the right hand side of the diagram. (b) Time series of  $x_{S3}(t)$  for the centre position of the location of  $S3$ , along  $L$ .

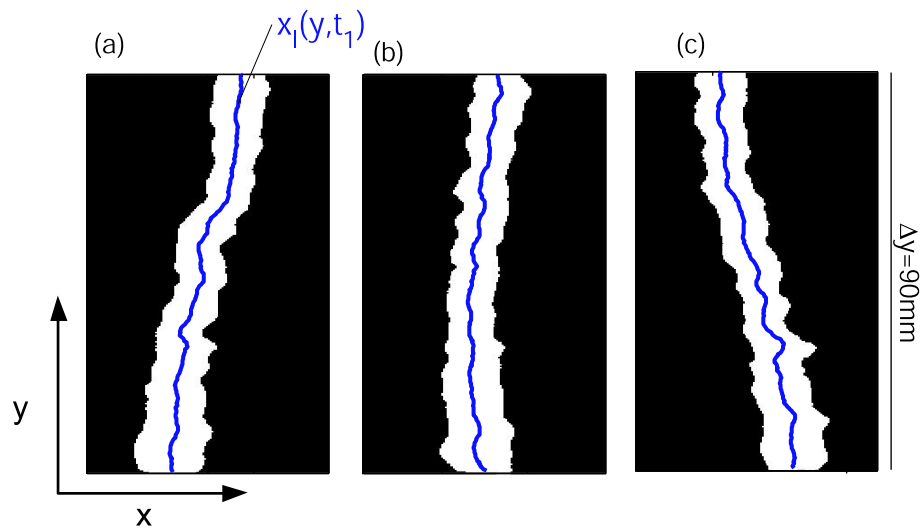


Figure B.7: Experimental frames after being cropped around  $S3$  and image processed following the method introduced in Section 2.8.1. Black for regions of poppy seeds and white for regions of phosphor-bronze spheres. (a) At beginning of cycle ( $t = t_1 \text{ sec}$ ). (b) At quarter-cycle ( $t = (t_1 + 72) \text{ sec}$ ). (c) At half-cycle ( $t = (t_1 + 143) \text{ sec}$ ). The centre line of the  $S3$  stripe,  $x_l(y, t)$ , has been superposed on each frame as a solid blue line.

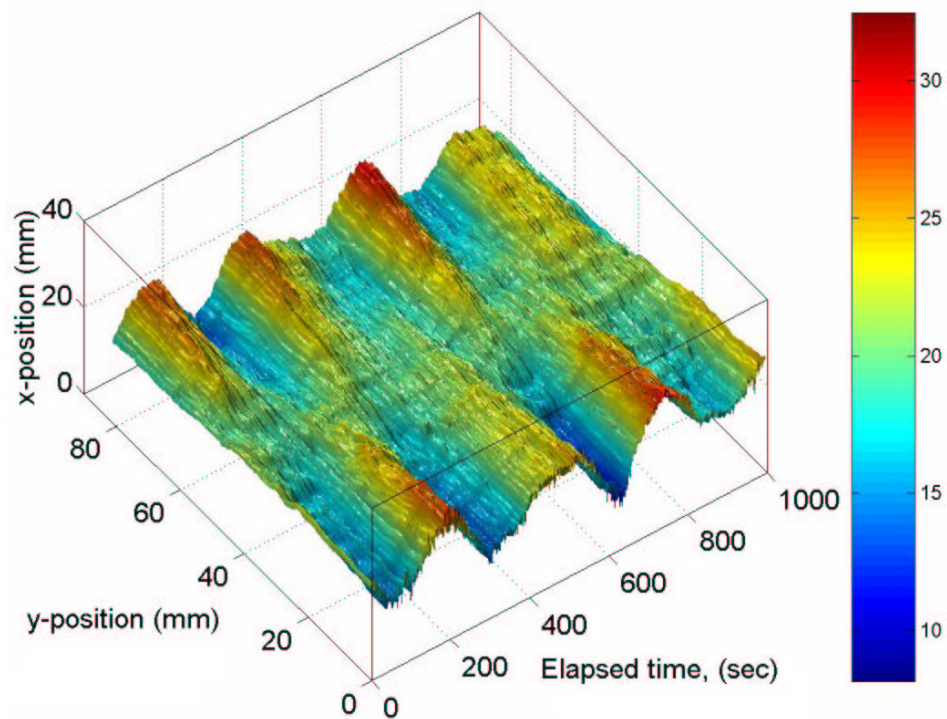


Figure B.8: Three dimensional spatio-temporal diagram for the centre line of the  $S3$  stripe,  $x_l(y, t)$ . The value of  $x_l(y, t)$  is given by the colour in the adjacent colour bar.

# Appendix C

## Simulations of 2D driven binary mixtures

In this Appendix we reprint a paper which resulted from a collaboration with George Ehrhardt<sup>1</sup> and Andrew Stephenson<sup>1</sup> who performed event driven numerical simulation of a two-dimensional phenomenological model for a driven binary mixture of particles (Ehrhardt et al. 2004). The aim of this work was to construct a simplified numerical realization of our experimental system and explore parameter space in away not accessibly experimentally, in order to identify possible segregation mechanisms.

---

<sup>1</sup>Theoretical Physics Group, Department of Physics and Astronomy, University of Manchester

# Segregation Mechanisms in a Model of an Experimental Binary Granular Mixture

George C.M.A. Ehrhardt\* and Andrew Stephenson

*Theoretical Physics Group, Department of Physics and Astronomy, The University of Manchester, M13 9PL, UK.*

Pedro M. Reis

*Manchester Centre for Nonlinear Dynamics, The University of Manchester, M13 9PL, UK.*

(Dated: March 10, 2004)

A simple phenomenological model of a binary granular mixture is developed and investigated numerically. We attempt to model the experimental system of [1, 2] where a horizontally vibrated binary monolayer was found to exhibit a transition from a mixed to a segregated state as the filling fraction of the mixture was increased. This model is found to reproduce much of the experimentally observed behaviour, most importantly the transition from the mixed to the segregated state. We use the model to investigate granular segregation mechanisms and explain the experimentally observed behaviour.

PACS numbers: 02.50.Ey, 45.70.-n, 64.75.+g, 82.70.Dd

## I. INTRODUCTION

Granular systems exhibit a wide range of intriguing and often counterintuitive phenomena. Segregation of two or more species of grains due to vibration or shearing is one such example [3, 4]. Many mechanisms, including buoyancy, temperature gradients, differing angles of repose, and differing roughness of particles, have been proposed [4, 5, 6, 7]. Recently, segregation of a vibrated binary mono-layer has been demonstrated in a series of experiments [1, 2, 3] that imply/suggest the existence of a segregation critical point as the filling fraction is varied, with associated growth of fluctuations and timescales in the vicinity of that point.

In this paper we propose a phenomenological model of the experimental system which captures its essential features. We show that there is qualitative agreement between the model and the experiment and, in particular, that the quantitative measures reported in [1, 2] are of the same form in both cases. We then use the model to study segregation mechanisms, giving one definite mechanism and demonstrating that a second may also play a role.

The experimental system used in [1, 2] consists of a smooth horizontal tray of dimensions  $L_x = 180mm$  by  $L_y = 90mm$  vibrated sinusoidally parallel to its major axis at a frequency of  $f = 12Hz$  and amplitude of  $A = 1.74 \pm 0.01mm$ . The grains are high-precision phosphor-bronze spheres (denoted by  $c$  in the following) of radius  $R_c = 0.75mm$  and mass  $m_c = 16.8\mu g$  and poppy seeds (denoted by  $p$  in the following) of average radius and mass  $R_p = 0.54mm$  and  $m_p = 0.52\mu g$  respectively. The poppy seeds are rough, non-spherical polydisperse [8] particles.

Particles placed on the oscillating tray predominantly move periodically with the driving. They also have some

quasi-random component to their motion, caused in the case of the  $ps$  by their non-sphericity which means that they do not roll smoothly but instead 'slick and slip' and scatter. The  $cs$  are affected less by the driving since they roll as the tray moves beneath them. However they too, when placed individually on the tray, are seen to have some quasi-random component to their motion. The overall impression is of a granular bed of agitated particles with the predominant motion being parallel to the driving.

The control parameter used in the experiments was the 2-dimensional filling fraction, termed the compacity  $C = (N_c\pi R_c^2 + N_p\pi R_p^2)/(L_x L_y)$ , with  $N_c$  fixed. The value of  $N_c$  is also important but for simplicity the experiments focussed on  $N_c = 1600$  and varied  $N_p$ . The system was quasi 2-dimensional in that  $0.49 < C < 1.12$ , high  $C$  being achieved by poppy seeds 'riding up' and overlapping each other to some extent, although never so much that they were above and overlapping the  $cs$ .

Starting from a uniformly mixed initial distribution, the final state reached by the system varies with  $C$ . For  $C \lesssim 0.65$  the system remains mixed whilst above that value small mobile segregated clusters of  $cs$  form. As  $C$  increases, these clusters grow in size and become anisotropic, forming stripes perpendicular to the direction of driving for  $C$  large. For  $C \gtrsim 0.93$  the  $cs$  within these stripes crystallise to form a densely packed hexagonal lattice. These three phases were termed binary gas, segregation liquid, and segregation crystal. The existence of a phase transition from the binary gas to segregation liquid, with an associated critical value of  $C$ , was reported in [2]. The details of these results are given in [1, 2].

The experimental system has several appealing properties from the point of view of studying granular matter: except at high compacities where stripes form, the final state reached is a function only of the compacity, i.e. the initial conditions are not relevant. The particles are always in contact with the tray and hence are always effectively 'thermalised'. This is in contrast to the

---

\*Now at The Abdus Salam ICTP, Strada Costiera 11, 34014 Trieste (Italy); Electronic address: gehrhard@ictp.trieste.it

behaviour of particles in granular systems such as sand-piles where the grains spend most of their time locked in position, or some vertically vibrated systems where much of the time is spent in free flight [9]. The constant ‘thermalisation’ of the particles, their ability to explore many possible states, and the irrelevance of initial conditions suggests that the system might be a good choice for studying the ‘statistical mechanics’ of granular matter. However detailed balance, equipartition of energy and other rigorous features of equilibrium statistical mechanics are of course not obeyed in this system [10].

## II. DESCRIPTION OF MODEL

We here develop a phenomenological model of the experimental system. The aim is to capture the essential features of the experiment in the model, thereby discovering what those features are and in particular what the segregation mechanism(s) is(are).

The following features are, we believe, necessary: there is a tray of dimensions  $L_x \times L_y$  whose base moves with sinusoidal velocity  $A \sin(\omega t)$ . There are two particle species, named  $c$  and  $p$ . The particles moving relative to the tray surface are subject to a frictional force. The particles feel a randomisation of their velocity caused by their stick-slip motion with the oscillating tray and their non-sphericity (thermalisation). The particles collide inelastically.

We therefore model the system as 2-dimensional with the particles behaving as hard disks of mass  $m_\alpha$  and radius  $R_\alpha$ , where  $\alpha$  denotes the species ( $c$  or  $p$ ). Except during collisions the particles obey the Langevin equation

$$m_\alpha \dot{\mathbf{v}}_{\alpha i} = -\gamma_\alpha (\mathbf{v}_{\alpha i} - \mathbf{v}_{tray}) + \boldsymbol{\eta}_{\alpha i}(t) \quad (1)$$

where  $\mathbf{v}_{tray} = \mathbf{i}A \sin(\omega t)$  and  $\gamma$  provides a linear damping.  $\boldsymbol{\eta}_\alpha(t)$  is Gaussian white noise of mean zero and standard deviation  $\langle \boldsymbol{\eta}_\alpha(t) \cdot \boldsymbol{\eta}_\alpha(t') \rangle = 2\sigma_\alpha^2 \delta(t - t')$  and this provides the ‘thermalisation’. The particles interact through smooth hard-disk inelastic collisions with coefficient of restitution  $r_{\alpha,\beta}$ , i.e. in the centre of mass frame,  $\mathbf{v}_{\parallel i} \rightarrow -r_{i,j} \mathbf{v}_{\parallel i}$ ,  $\mathbf{v}_{\perp i} \rightarrow \mathbf{v}_{\perp i}$ , where  $\mathbf{v}_{\parallel}$  and  $\mathbf{v}_{\perp}$  are the velocity components parallel and perpendicular to the line joining the centres of the particles  $i$  and  $j$ . For simplicity, the disks have been taken to be smooth sided so that angular momentum can be ignored. A similar model has been used in [11] to describe colloidal particles driven by an external electrical field. Also [12] have used a similar model without noise to model granular particles driven by a vertically oscillating air column [13].

These are the essentials. We have also kept the walls of the box stationary for simplicity but modelled the motion of the end walls by considering that in collisions they have a velocity  $\max(\mathbf{i}A_1 \sin(\omega t), 0)$  for the left wall and  $\min(\mathbf{i}A_1 \sin(\omega t), 0)$  for the right wall. We felt that this was necessary in order to model the low-density region near each end wall caused by the vigorous collisions with

the end walls. The width of the low-density region is independent of the system size, thus we used  $A_1 = A/10$  rather than  $A_1 = A$  in the results described here in order to reduce the ‘finite size effect’ of this region as the system size is changed.

There are many approximations of the real system made here, the most significant ones are: the friction term  $\gamma \mathbf{v}$  is only an approximation, it is chosen as being the simplest possible form. The noise is in fact due to the stick and slip interactions between the particles and the oscillatory surface, and also their non-sphericity when interacting with each other and with the tray. We do not try to directly model this since it would require detailed specification of the shape of each particle and its actual interaction with the tray, which is not known. Even a single high-precision phosphor-bronze sphere conducts a quasi-random walk when placed on the oscillating tray, indicating that the randomness can depend on very small imperfections of the particles and the tray (and possibly also in the driving). Both because of this immense difficulty and in order to have a reasonably simple model whose behaviour we can understand, we instead choose to include the noise phenomenologically. We assume that the noise the particles receive is independent of their neighbours and of the phase of the tray cycle, both of which are unlikely to be accurately what happens in the experiments. The assumption that the noise is Gaussian and white is an approximation. For simplicity we are using a 2-dimensional model, which ignores the overlapping of  $ps$  and the rolling of particles. The particles and walls are assumed to be smooth and so angular momentum is not considered. We have ignored the polydispersity of the  $ps$ . Polydispersity was included to check its importance and was found to leave the qualitative behaviour unchanged. The final approximation is that the coefficients of restitution are constant which is a commonly made one [14]. Despite these simplifications and approximations, in Section III we show that our phenomenological model captures much of the behaviour observed experimentally.

### A. Parameter Values

Static parameter values such as mass and size can be measured reasonably accurately, for the poppy seeds we have used the mean values of a sample of measurements [15]. Dynamic parameters were less accurately known,  $\gamma_\alpha$  was estimated from the distances travelled by single particles striking the moving end walls. Using the result for the noiseless case,

$$x(\infty) = x(0) + v_x(0)m/\gamma \quad (2)$$

and estimating  $v_x(0)$  to be equal to the maximum velocity of the end wall gives approximate values for  $\gamma_\alpha$ . The value for the noise is the hardest to determine since no velocity or accurate  $\mathbf{r}(t)$  path measurements were available. We merely estimated that the mean square velocity

due to the noise,  $\langle \mathbf{v}_\alpha^2 \rangle = \sigma_\alpha^2 m_\alpha / \gamma_\alpha$  should be equal to  $\approx (A/F)^2$  where the factor  $F = 3$  for the  $p$  case and  $F = 13$  for the  $c$  case.

Clearly these last estimates are rather crude. However, extensive study of a wide range of these parameters has shown that the qualitative features are robust to variation of these estimates.

The coefficients of restitution,  $r_{\alpha,\beta} = r_{\beta,\alpha}$ , are estimated to be:  $r_{c,c} = 0.9$ ,  $r_{c,p} = 0.2$ ,  $r_{p,p} = 0.1$ ,  $r_{c,w} = 0.9$ ,  $r_{p,w} = 0.2$  where  $w$  denotes a side wall. Other values have been studied, but the qualitative behaviour is unchanged. The main effect of increasing(decreasing)  $r_{\alpha,\beta}$  is to increase(decrease) the granular temperature which in general merely moves the onset of segregation to slightly higher(lower) compacity values.

The parameters then are the following.

property	$c$ value	$p$ value
$m_\alpha$ mass	$1.6800 \times 10^{-5}$	$5.2000 \times 10^{-7}$
$R_\alpha$ radius	$7.5000 \times 10^{-4}$	$5.4000 \times 10^{-4}$
$\gamma_\alpha$ damping term	$4.3636 \times 10^{-6}$	$1.0000 \times 10^{-5}$
$\sigma_{x\alpha}$ noise term	$8.1819 \times 10^{-8}$	$1.0000 \times 10^{-7}$
$\sigma_{y\alpha}$ noise term	$8.1819 \times 10^{-8}$	$1.0000 \times 10^{-7}$
$r_{\alpha,\beta}$	$r_{c,c} = r_{c,w} = 0.9$	$r_{c,p} = r_{p,w} = 0.2$
$r_{\alpha,\beta}$	$r_{c,p} = 0.2$	$r_{p,p} = 0.1$

Table II A. The parameters used for the simulation results described below (SI units are used at all times unless stated otherwise).  $\sigma_{x\alpha}$  and  $\sigma_{y\alpha}$  are the  $x$  and  $y$  components of  $\sigma$ .

## B. Simulation Method

We have simulated the model via an event driven code [14]. The process is as follows:

1. For each particle, predict when it will next collide.
2. Identify the first collision to occur.
3. Move the particle(s) involved so that they touch.
4. Update the velocities of the particle(s) involved (change in velocity due to damping and noise since they were last updated).
5. Collide the particle(s) [16].
6. Re-predict the next collision(s) of the particle(s) and their neighbours.
7. Repeat from 2 until time has advanced by  $t_{minupdate}/2$
8. Update all particles that have not been updated in the last  $t_{minupdate}/2$  seconds.
9. Repeat from 1 until time has advanced by  $t_{takedata}$ .
10. Record data.
11. Repeat from 1.

The prediction of collisions assumes that the particle's velocities do not change during their motion. The error caused by this is small provided that  $t_{minupdate} \ll$

$\min(\tau_\alpha)$  where  $\tau_\alpha = m_\alpha / \gamma_\alpha$  is the time constant of the velocity decay. We set  $t_{minupdate} = 0.01 \times \min(\tau_\alpha)$ .

The hard sphere model with inelastic collisions can undergo inelastic collapse [17], where the particles undergo an infinite number of collisions in a finite time. Clearly a simulation that implements each collision will 'stall' in these circumstances. One way around this unphysical singularity is the tc model [18] which prevents the collapse by setting  $r_{\alpha,\beta} = 1$  for any particle which collided within the last  $t_{tcolmin}$  seconds. We found that for  $t_{tcolmin} < 1 \times 10^{-4}$  the results did not change. For the results presented here we chose  $t_{tcolmin} = 5 \times 10^{-5}$ .

The initial conditions were created by running a reduced size system  $N_c/25$ ,  $N_p/25$ , of twice the aspect ratio with particles initially placed randomly on a square lattice. An external force was applied to compress the particles into an area of size  $L_x/5 \times L_y/5$ . The particles were then allowed to move in this box without the external force until equilibrated. The initial condition was then created by tessellating the full system size with 25 replicas of the reduced system. To prevent long-range order the replicas were randomly inverted in both the  $x$  and  $y$  directions (the differing noises received by the particles in conjunction with the chaotic behaviour of the particles would rapidly remove any correlations in any case). During this stage, both particle species had the same properties, including  $r_{\alpha,\beta} = 1$ , except for their radii. This method produced initial conditions which appeared to be as homogeneous as those for the experiment.

The simulations were run on standard PCs. For comparison with the experiments our results are for the same system size ( $18cm \times 9cm$ ), except where stated otherwise. The aspect ratio is here 2 : 1 in all cases.

## III. RESULTS

As with the experiments, we used the number of  $ps$ ,  $N_p$  as our control parameter. The main quantities measured were those found experimentally [1, 2, 3] and related to the  $cs$  only: the mean stripe width (MSW), and the local density,  $\rho_i$ , of the  $i$ th particle. We also visualised the system and watched its behaviour. In addition, we also measured the area available to the  $ps$ , and the kinetic energy or 'granular temperature' of the particles.

The MSW measures the mean width of the stripes in the  $x$  direction by pixellating an image of the system, deciding which pixels  $P_{x,y}$  are within a  $c$  domain, then running along each pixel row  $P_y$  and counting the width and number of domains. All the rows  $P_y$  are summed and the average domain width found. Whether  $P_{x,y}$  is within a domain is decided by blurring the image with a gaussian smoothing function and then setting a threshold. This measure was used in [1, 2] even when the domains had not formed into stripes since it provided a simple measure of the domain sizes in the longitudinal direction.

The normalised local density  $\rho_i$  was found by Voronoi tessellation [19] of the  $cs$ , such that each  $c_i$  has around

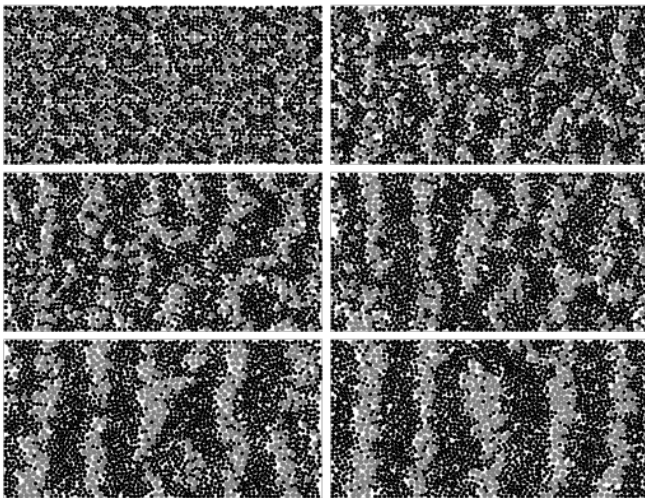


FIG. 1: The time evolution of a simulation showing the coarsening into domains for a system of  $1/4$  the area of the experiment and  $C = 0.6721$ . The times are, top left:  $t=0.04s$ , top right:  $t=4.18s$ , middle left:  $t=8.37s$ , middle right:  $t=16.75s$ , bottom left:  $t=33.51s$ , bottom right:  $t=62.83s$ . The  $ps$  are coloured black.

it a polygonal area all points of which are closer to  $c_i$  than to any other  $c$ .  $\rho_i$  is then the minimum possible area, which is  $2\sqrt{3}R_c^2$ , divided by the polygonal area. Polygonal cells on the edge of the system which are not bounded are discarded.

In addition to the MSW as a measure of the amount of coarsening, we also measured the area available to the  $ps$ . This 'available area' is just the fractional area of the system in which a  $p$  could be placed without overlapping a  $c$ . Each  $c$  has a circular 'excluded area' around it of radius  $Rc + Rp$ , inside which the centre of a  $p$  cannot be placed. If all  $N_c$   $cs$  are widely separated, the available area is  $1 - N_c \pi(Rc + Rp)^2/LxLy$ , whilst if all the  $cs$  are hexagonally packed in one domain the available area will be larger ( $\approx 1 - N_c 2\sqrt{3}Rc^2/LxLy$ ) since the excluded areas now overlap. Thus the available area gives a measure of how segregated the  $cs$  are. In Section IV B we will show that the available area is relevant to noise segregation.

Figure 1 shows 6 images of the evolution of a coarsening system. It can be seen that the initial segregation into relatively small domains is rapid. This is followed by slower coarsening as domains merge and as larger domains grow at the expense of smaller ones that 'evaporate'. This growth rate is also clearly seen in the time-series plots of figures 3 and 4. Figure 2 shows three images of the system at differing compactities for late times, the lowest compacity ( $C=0.446$ ) shows a binary mixture, the second ( $C=0.582$ ) a segregated 'liquid' which has mobile and transient clusters and shows a slight anisotropy, and the third ( $C=0.717$ ) shows a system that has coarsened into stripes. The first two are in a steady state whilst the third is still evolving slowly due to the high

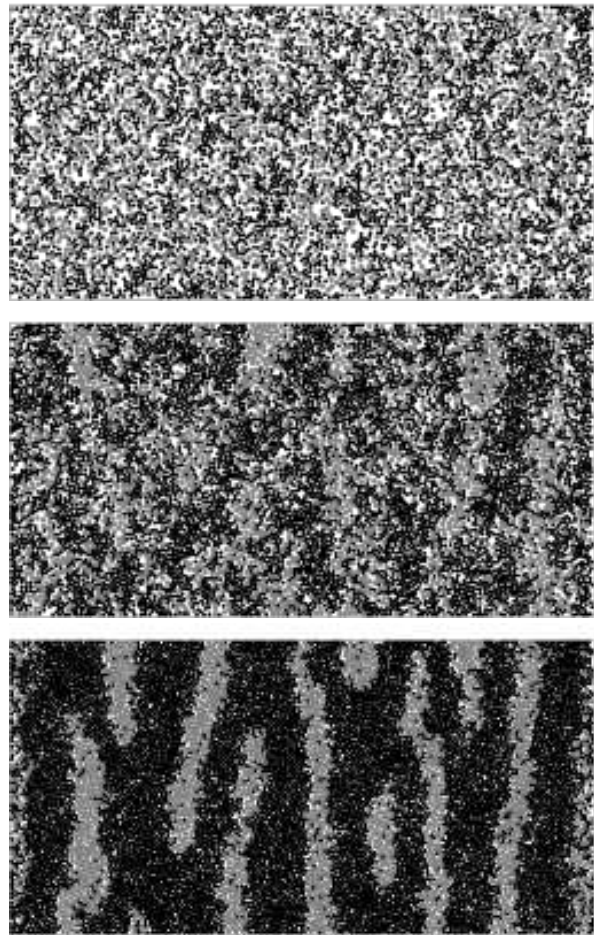


FIG. 2: Examples of a binary mixture, segregated liquid, and segregated stripes. Compactities are 0.446, 0.582, and 0.717, respectively.  $ps$  are coloured black. The pictures were taken after 100 seconds for the gas and 200 seconds for the liquid and crystal, by which time the first two have reached a steady state whilst the third is still slowly evolving.

compacity (for a strictly 2-dimensional system) which causes particles to be 'blocked' by other particles.

Figure 3 shows  $MSW_C(t)$  for several compactities. As  $C$  increases, the  $cs$ , which were initially mixed with the  $ps$ , coarsen into domains whose size increases with  $C$ . The early-time coarsening is rapid, followed by slower coarsening and then saturation at some relatively steady value. For the lowest compactities, there is no coarsening, the system remains in a mixed, disordered state. The highest  $C$  value shown has not reached a final steady state, the stripes are still moving and merging at a very slow rate compared to the initial coarsening. At higher compactities, the system becomes blocked or jammed, the particles being unable to rearrange themselves in 2-dimensions, the slow timescales of the top curve show the onset of this jamming. This jamming does not occur to the same extent in the experimental system since the particles do not always form a monolayer and  $ps$  can

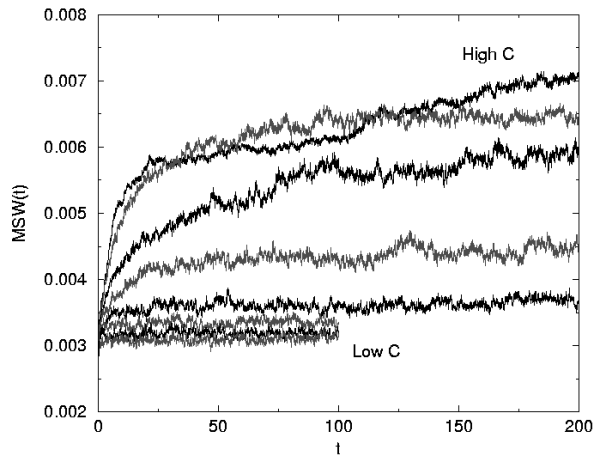


FIG. 3: Plots of MSW against time for various compacities. From the right, top to bottom, the compacities decrease from  $C=0.717$  to  $C=0.401$  in uniform increments. Thus it can be seen that for low  $C$  the system does not coarsen whilst when  $C$  is increased, the system coarsens to a roughly constant value which increases with  $C$ . For the largest value of  $C$ , the system has undergone rapid initial coarsening but then slowed as the large domains move more slowly, especially at this high compacity where the system is becoming somewhat ‘jammed’. The MSW was measured every 0.0209 seconds.

move out of the way of  $cs$  by ‘riding up’ on top of each other.

Figure 4 shows a plot of the value of the area available to the  $ps$  against time, it is similar to that for the MSW. It is a more repeatable measure than the MSW since it is less affected by stripes merging, for example, two runs with the same parameters naturally differ due to the chaotic behaviour of the particles. This means that for high compacities merging of stripes in two realizations at the same parameters may occur at different times, causing the  $MSW_C(t)$  curves to differ between runs at late times (since  $MSW_C(t)$  is inversely proportional to the number of domains). The available volume is less affected by this and thus provides a ‘cleaner’ measure of the coarsening. Thus for later results we will use the available volume, although the MSW provides similar, if more noisy, results. Experimentally, the available volume has not been measured since the experimental system was only imaged in it’s central region, thus the number of  $cs$  changes with time making the measure somewhat arbitrary (the changes due to  $cs$  entering or leaving the system would be more significant than the coarsening). We note that for the highest compacity curve, the area available has increased by  $\approx 0.15$  whilst the maximum range of the available area stated before is  $\approx 0.30$ .

In figures 5 and 6 we plot the late time values of the MSW and available volume as a function of the compacity. This was done by fitting exponentials to the time-series of the type shown in figures 3 and 4 and using the late-time values. We do not claim that the time se-

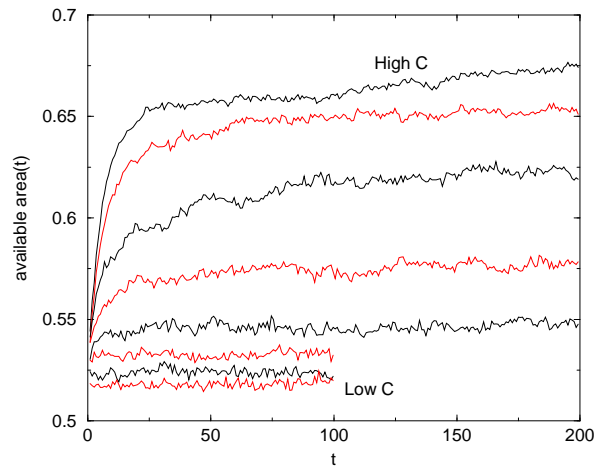


FIG. 4: Plots of the available volume for the  $ps$  against time for various compacities. From the right, top to bottom, the compacities decrease from  $C=0.717$  to  $C=0.401$  in uniform increments. The conclusions are similar to those for figure 3 except that the curves here always remain in the same order. The available volume was measured every 0.838 seconds.

ries are exponential, but the fits provide us with a reasonable measure of the late-time values. The MSW vs  $C$  curve is the same measure as that used experimentally in [2, 20] to claim a mixed state to segregated state phase transition for the experimental system. In [2] a square root curve was fitted to the right hand side of the data, the data to the left of the transition being taken to be roughly constant, i.e.  $MSW_{sat}(C) = B$  for  $C < C_{transition}$  and  $MSW_{sat}(C) = B + D\sqrt{C - C_{transition}}$  for  $C > C_{transition}$ , where  $B$  and  $D$  are constants. From figure 5 we see that this is not the case for the simulation data, which, as  $C$  is increased, initially rises slowly, then increasingly rapidly before slowing again for large  $C$ . There is no indication of a discontinuity in the gradient of the order parameter, merely a rapid increase. In [20] the same experimental data is presented with a sigmoid shaped ‘guide to the eye’ curve rather than a square root. In our opinion the simulation data is similar to the experimental data but not to the square root form suggested in [2]. The main conclusion from both the experimental and simulation  $MSW_{sat}(C)$  curves is that  $MSW_{sat}(C)$  has a roughly sigmoid shape, with  $MSW_{sat}(C)$  increasing rapidly with  $C$  in the central region.

The simulation value of  $C$  at which the rapid increase occurs ( $\approx 0.58$ ) differs somewhat from the experimental value ( $0.647 \pm 0.049$ ) [2]. In the next section we show how this value changes continuously as we vary the noise strength or other parameters. Thus, by increasing the noise strength we can increase the value of  $C$  at which the rapid increase occurs.

Figure 7 shows histograms of the local Voronoi density for various compacities, the results are qualitatively similar to the experimentally reported ones [1]. At the lowest

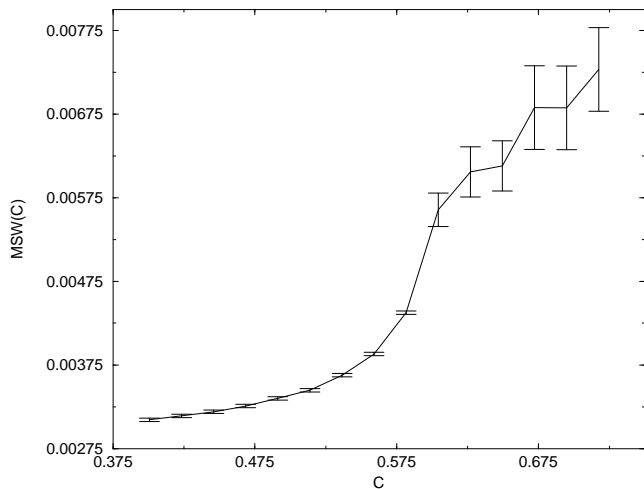


FIG. 5: Plot of the saturated (late time) mean stripe width as a function of compacity. The saturated values were found by fitting exponentials to the  $MSW(t)$  curves. Two runs were done at each compacity, and the results averaged. The error bars are based on the difference between these two runs.

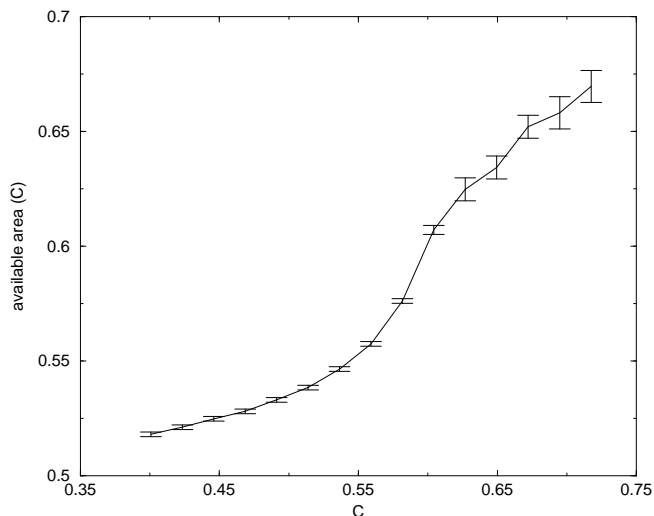


FIG. 6: Plot of the saturated (late time) area available to the  $ps$  as a function of compacity. The saturated values were found by fitting exponentials to the available-area( $t$ ) curves. Two runs were done at each compacity, and the results averaged. The error bars are based on the difference between these two runs. Note that the error bars are smaller than for the  $MSW$  vs  $C$  plot since, as stated in the text, the available area is a 'cleaner' measure.

$C$  values, corresponding to the mixed state, the distribution is peaked at low densities as one would expect for unclustered  $cs$ . At high  $C$  the distribution is peaked at large densities as one would expect for clustered (i.e. segregated)  $cs$ . There is a crossover between these two cases, with figure 7d showing a broad histogram due to almost the full range of densities being present in almost

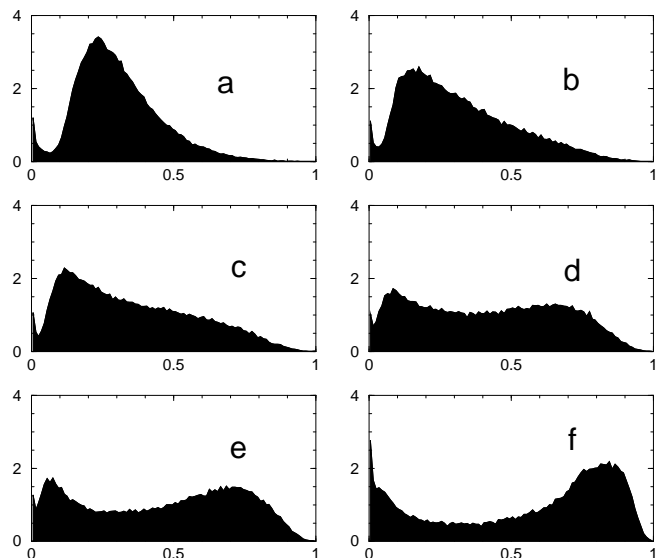


FIG. 7: Normalised histograms of the Voronoi densities plotted against normalised density, for  $C=0.400728$ (a),  $0.559$ (b),  $0.582$ (c),  $0.604$ (d),  $0.627$ (e), and  $0.740$ (f). Note the crossover with increasing  $C$  from a single peak on the left to two peaks, then a larger peak on the right. For each compacity the data was measured in the steady state from 45 frames of 1600  $cs$  each.

equal weights. Unlike the experimental results however, the high  $C$  distribution also has a peak at low density caused by a small fraction of isolated  $cs$  which are not present in the experiment. There is a crossover between these two extremes as  $C$  is increased, the central 4 figures (b-e) show this crossover. Following [1], we plot the location of the peak(s) and their widths as a function of compacity in figure 8. In [1] the peak width used was the full width  $3/4$  maximum since the peak did not extend far enough above the rest of the distribution for a full width  $1/2$  maximum to be meaningful. Here we did the same although a full width  $3/4$  maximum also does not exist in one case. Figure 8 is qualitatively different from its experimental equivalent and we conclude that although the histograms are qualitatively similar, the results derived from them are not.

The results presented here show that our model reproduces the segregation and its qualitative behaviour with  $C$  of binary gas, segregated liquid, and segregated stripes as seen experimentally. This behaviour is not immediately obvious from the model rules - it emerged from the set of rules which we believed contained the important microscopic features of the experiment. We have also shown that the  $MSW$  as a function of time and its saturated value as a function of compacity behave in a qualitatively similar manner to the experiment. These reproductions of experimentally observed behaviour lead us to conclude that the 'necessary features' listed in section II capture the essential behaviour of the system. Nonetheless, our phenomenological model does not quantitatively

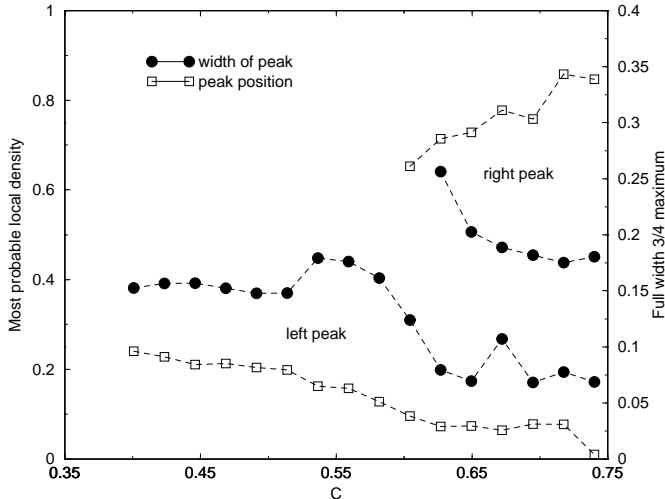


FIG. 8: Plots of data derived from the Voronoi histograms as shown in figure 7. Squares show the position of the peak(s) in the histograms, representing the ‘most probable’ densities, the lower curve is for the leftmost peak and the upper curve is for the rightmost peak. Filled circles show the full width of each peak at 3/4 maximum (where the peak does have a distinct 3/4 maximum). The curves differ from their experimental equivalents where there was only one maximum (thus just two single curves) which moved steadily to the right and where the width was peaked at an intermediate compacity. These differences are due mainly to the presence in the simulation density histograms of a second peak at low density which is always present and is caused by a small number of isolated  $cs$ , something not observed in the experiment.

reproduce the experiment (it was never expected to do so), in particular the Voronoi histograms differ from the experimental ones sufficiently that the data derived from them (figure 8) is qualitatively different.

#### IV. SEGREGATION MECHANISMS

Having shown that our model is relevant to the experiment, we now use it to investigate segregation mechanisms.

##### A. Segregation due to Oscillatory Driving

That the domains are anisotropic and indeed form stripes at high  $C$  indicates that the anisotropy of the driving is significant. Experimentally the stripes form perpendicular to the driving even for aspect ratios greater than 1, e.g.  $L_y/L_x = 2$ .

The side-to-side driving causes the two species to move at different rates due to their differing masses and friction coefficients. A single particle will oscillate with

$\langle x_\alpha(t) \rangle = A/\sqrt{1 + \omega^2(m_\alpha/\gamma_\alpha)^2} \sin(\omega t)$  where the average is over the noise. Thus  $\langle x_c(t) \rangle = 6.00 \times 10^{-6} \sin(\omega t)$  and  $\langle x_p(t) \rangle = 4.30 \times 10^{-4} \sin(\omega t)$ . Thus the  $ps$  would ‘like’ to move a distance of order their radius during a cycle whilst the  $cs$  hardly move. Consider a state of only  $ps$ , if we remove the noise then all the  $ps$  move in the same sinusoidal way, if we transfer to the (non-inertial) reference frame in which they are at rest, we see that this is identical to the state with no sinusoidal driving (apart from edge effects at the walls) for which the dissipation causes the particles to be stationary. The same can be said of a state of only  $cs$ . In a mixed state, however, the  $ps$  will collide with the  $cs$  and the system will ‘scatter’ into a different state. Stable states, i.e. those that do not undergo further scatterings, will be those for which the  $cs$  are separated from the  $ps$  in the  $x$  direction by distances of at least the amplitude of the  $ps$ ’ oscillations. For the packing fractions considered here, this can only happen by the two species segregating into domains. The fact that the area available to the  $ps$  increases with time is consistent with this interpretation. This argument only holds when the driving is not too large compared to the dissipation. For example if the amplitude of oscillation were of order the system size then it would not be valid. An argument similar to this was also given in [12].

We have studied systems with very low noise and the results obtained agree with the heuristic argument given above. The addition of noise, which causes particles to diffuse, will tend to cause mixing. Thus there is a competition between the periodic driving which causes segregation and the noise which prevents it. This is shown in the results presented below.

For the standard parameters but with  $\sigma_\alpha \rightarrow 0.1 \times \sigma_\alpha$ , the system segregates for all the compacities studied in section III (see figure 9), indicating that, as expected, the noise acts to prevent segregation. To confirm this we then gave the two species identical parameters (the  $p$  parameters) and set all  $r_{\alpha,\beta} = 1$ . The only difference was that the  $ps$  experienced the periodic driving term  $\gamma \mathbf{v}_{tray}$  whilst the  $cs$  did not. The results are shown in figure 10 and demonstrate that a difference in the periodic driving alone can cause segregation.

For  $C = 0.498$  with the same parameters except  $\gamma_\alpha \rightarrow 2 \times \gamma_\alpha$  (to reduce the granular ‘temperature’ which is higher than usual due to the  $r = 1$ ) we varied  $\sigma$  and, as shown in figure 11, the system segregates for low  $\sigma$  and remains mixed for high  $\sigma$ .

These results confirm that the state of the system is a result of a competition between the periodic driving which causes segregation and the noise or ‘granular temperature’ which prevents it. Varying our control parameter,  $N_p$ , causes us to go from a mixed to a segregated state because increasing  $N_p$  both reduces the granular temperature (since it increases the number of collisions which are highly inelastic) and also increases the ‘pressure’ that the  $cs$  feel due to collisions with a greater number of oscillating  $ps$ . Figure 12 shows results for all properties set to  $p$  values including all  $r = 0.1$  but with only the  $ps$  feeling

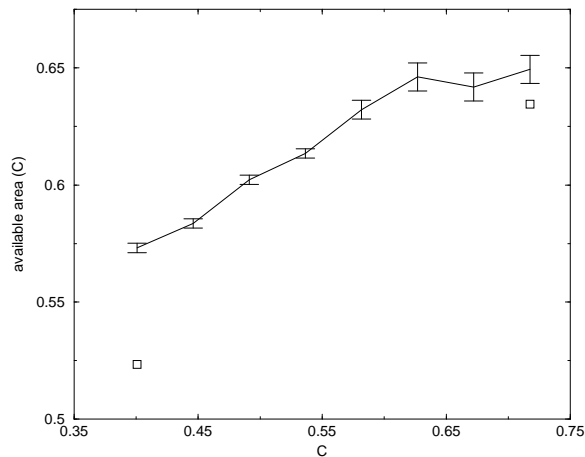


FIG. 9: Plot of the area available to the  $ps$  at late times as a function of compacity. The curve shows standard parameters but with low noise ( $\sigma_\alpha \rightarrow 0.1 * \sigma_\alpha$ ) results, the two box points are the equivalent results for the standard parameters. Thus it can be seen that all compacities have segregated. For high  $C$  a few large domains form whilst at lower compacities there is enough space for a larger number of small domains to be stable. Note that the area of the system is  $1/4$  that of the experimental system. The late-time results were found by fitting an exponential to the available area vs time curves.

the periodic driving, showing that the results remain of the same form for  $r < 1$ .

Finally, we find that the system with standard parameters does not segregate if the oscillatory motion is turned off.

These results show that the differential oscillatory driving can cause segregation and present good evidence that it is the responsible mechanism in the system in conjunction with the noise which acts to prevent segregation. The transition from a mixed to a segregated state as  $C$  is varied is due to the compacity changing the relative strengths of these two competing effects.

### B. Noise Segregation

It was suggested in [1, 2] that the segregation mechanism might be similar to the depletion interaction in equilibrium binary systems [21]. As an example consider a colloidal suspension containing non-adsorbing polymers. In the ideal case where there are no forces present, the free energy depends only on the entropy of the system. Treating the polymers as spheres [22], it is clear that each colloidal particle has an ‘excluded volume’ around it of radius  $R_{colloid} + R_{sphere}$  which the centre of the polymer cannot enter. Thus the volume available to the polymers is the volume of the system less the excluded volumes around the colloidal particles and the system edges. However, the excluded volumes overlap when colloidal particles are closer than  $2(R_{colloid} + R_{sphere})$ , thus the volume available to the polymers, and hence their entropy,

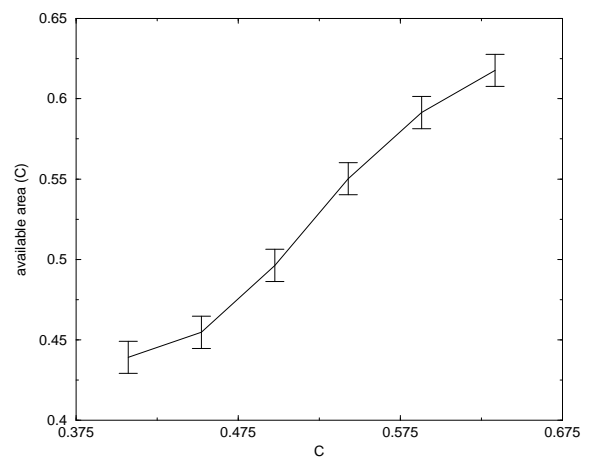


FIG. 10: Plot of the area available to the  $ps$  at late times as a function of compacity. The data is for a system where both particle types are the same (standard  $p$  parameters) except that only the  $ps$  feel the periodic driving. We get a mixed state for low  $C$  and a segregated state for high  $C$ , as we did for the standard parameters. Note that the area of the system is  $1/4$  that of the experimental system. The late-time results were found by fitting an exponential to the available area vs time curves.

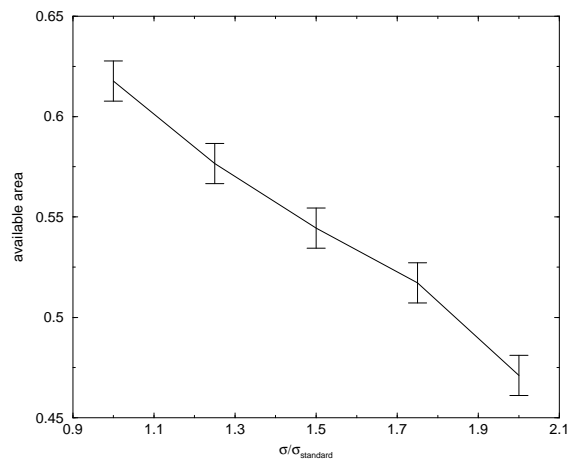


FIG. 11: Plot of the area available to the  $ps$  at late times as a function of the noise strength  $\sigma/\sigma_{standard}$ , for  $C = 0.498$ . Increasing the noise strength brings us from a segregated to a mixed state. Note that the area of the system is  $1/4$  that of the experimental system. The late-time results were found by fitting an exponential to the available area vs time curves.

is larger if the colloidal particles are close to each other. This entropic ‘effective potential’ can be large enough to cause the colloid to coagulate. This mechanism was one reason for measuring the area available to the  $ps$  in our simulations. Segregation has been observed in simulations of hard spheres of two different sizes [23] for large size ratios, e.g.  $R_1/R_2 = 10$ , and also experimentally in binary mixtures of hard sphere colloids [24].

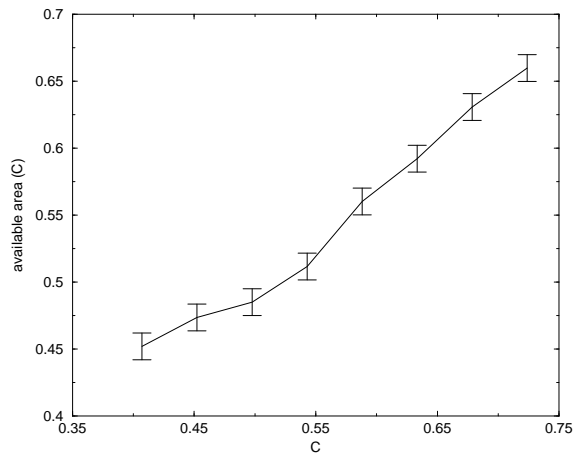


FIG. 12: Plot of the area available to the  $ps$  as a function of compacity, the parameters are as for figure 10 except that here the coefficients of restitution are all 0.1 rather than 1. It can be seen that this does not qualitatively change the results. Note that the area of the system is 1/4 that of the experimental system.

We may equivalently view the entropy argument from the kinetic point of view. Two particles which are close to each other such that no third particle may fit in the space between them will feel a pressure on all sides due to collisions with other particles *except* on their neighbouring sides. Thus the particles feel an effective attractive force. This pressure argument may be extended to systems that are not in equilibrium, for example the granular experiment studied here. The size ratio  $R_c/R_p$  is much closer to unity than for simulated equilibrium segregating systems [23], implying that the difference in size alone does not cause segregation.

In our out-of-equilibrium system there are several possible differences between the two species besides a difference in size. For our system, it seemed possible that the lighter, faster moving  $ps$  might, through the differential pressure mechanism, cause the  $cs$  to coagulate even in the absence of periodic driving. As stated before, this was not observed for the standard parameters. We therefore increased the noise of the  $ps$  and/or reduced the noise of the  $cs$  in order to increase the  $p$  to  $c$  temperature and hence pressure ratio. Noticeable segregation occurred over a wide range of compacity values for  $\sigma_p \rightarrow 10 \times \sigma_p$ , for  $\sigma_p \rightarrow 2 \times \sigma_p$  and  $\sigma_c \rightarrow 0.1 \times \sigma_c$ , and also for  $\sigma_c \rightarrow 0.05 \times \sigma_c$ . Whilst the first of these cases is outside the reasonable parameter range, the second and third are at parameters which might be physical. Figure 13 shows an example for the third case. Notice that many of the  $cs$  have coagulated at the walls as one would expect since the pressure argument for two-particle attraction also applies to the particle-wall case. Although this marked congregation at the walls is observed in experiments with colloids, it is not observed in the experiments of [1, 2]. Re-introducing the periodic driving of

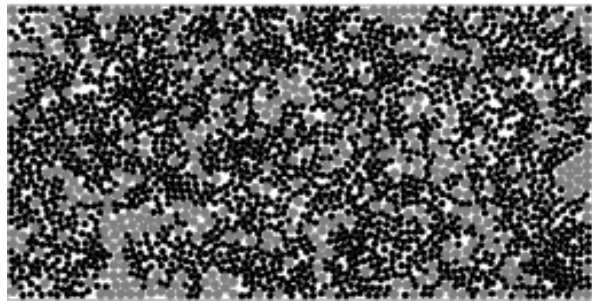


FIG. 13: Segregation of  $cs$  for the standard parameters but with no periodic driving and  $\sigma_c \rightarrow 0.05 \times \sigma_c$ . Notice the domains of  $cs$  at the edges of the system. Note that the area of the system is 1/4 that of the experimental system.  $ps$  are coloured black.

the end walls prevented congregation at the  $x = 0, L_x$  walls whose large momentum transfer to the particles, as stated earlier, gives rise to low-density regions next to them. However, for all parameter values studied that displayed segregation with no driving, the  $cs$  still congregated at the  $y = 0, L_y$  walls when the driving was turned on. Since stripes that touch the top and bottom walls are stable in the experiment, it seems unlikely that agitation due to the motion of the top and bottom walls is what prevents the liquid domains from coagulating there. It is possible to remove this experimentally unobserved effect by giving  $\sigma_x$  and  $\sigma_y$  differing values such that  $\sigma_{xc}$  is lower and  $\sigma_{yc}$  is higher than that needed to produce segregation. Whilst we had previously kept  $\sigma_x = \sigma_y$  for simplicity, it is reasonable that  $\sigma_x > \sigma_y$  since random motion caused by sticking and slipping is likely to be larger in the direction of driving. This extra modification produces segregation without  $cs$  congregating on the walls (provided that the  $x = 0, L_x$  walls are ‘driving’) whether there is periodic driving of the tray base or not. Figure 14 shows an example.

We therefore conclude that this differential pressure segregation mechanism may play a role in the experiment. We had to ‘tune’ the parameters which implies that the mechanism is less robust than the oscillatory driving mechanism. Accurate experimental measurements of the parameters would help to resolve whether this mechanism is indeed present. Directly distinguishing the two mechanisms mentioned would require accurate tracking of all particles and their collisions, coupled with investigations of other binary mixtures in order to get readings for different noise to side-to-side movement ratios. This is likely to prove a difficult task and at present all we can conclude is that differential pressure segregation may play a role in the experiment in addition to the differential driving discussed above.

To demonstrate that different temperatures alone can cause segregation we have studied two species with standard  $p$  parameters but all  $r_{\alpha,\beta} = 1$ . The temperature difference is produced by  $\sigma_p \rightarrow 40 \times \sigma$  and also setting all

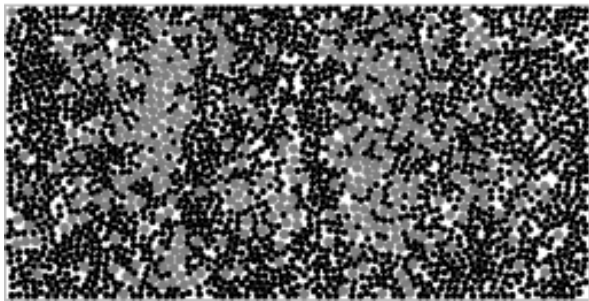


FIG. 14: Segregation of  $cs$  for standard parameters but with  $\sigma_{cx} \rightarrow 0.05 \times \sigma_{cx}$  and  $\sigma_{px} \rightarrow 2 \times \sigma_{px}$  and no driving of the tray base. Thus we get segregation but without coagulation at the top and bottom walls. The left and right walls are oscillating and prevent coagulation there. Note that the area of the system is  $1/4$  that of the experimental system.  $ps$  are coloured black.

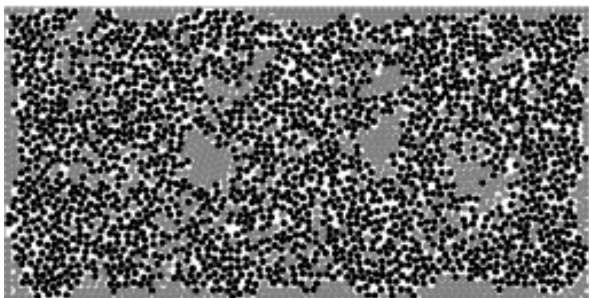


FIG. 15: Coagulation of  $cs$  after 96 seconds due only to temperature difference  $T_p=1600 \cdot T_c$ . The system is still evolving, the groups of  $cs$  in the centre will eventually attach to the sides of the system. Note that the area of the system is  $1/4$  that of the experimental system.  $ps$  are coloured black.

$\gamma \rightarrow 100 \times \gamma$  so that the time constants  $\tau = m/\gamma$  are sufficiently small that particles remember the temperature of their heat baths rather than only the temperature of their previous collision partners. This imposed temperature difference causes coagulation of the lower temperature particles as shown in figure 15. Whilst these parameters are very different from the standard ones, they clearly show another segregation mechanism in a nonequilibrium system and that the heuristic arguments regarding pressure differences out of equilibrium are valid.

### C. Further Mechanisms

One further possible mechanism is that the noise of the particles is correlated among the particles but differently for the  $cs$  and the  $ps$ . This could cause segregation in the same way as the periodic driving since it also would produce different collective motions for the two species. The correlation could be caused by, for example, the  $ps$

all changing from sticking to the tray base to slipping at the same time in the periodic cycle. Whilst this mechanism is at least plausible, the collective motions due to correlated noise and due to periodic driving (which would have caused the correlated noise in the first place) would not be clearly distinguishable. At the level of this phenomenological model which breaks the driving into a periodic and a noise component, any such mechanism is, therefore, not meaningful.

It is possible that there are other segregation mechanisms not discussed here, however we believe that we have considered the ones most likely to be relevant in the experiment.

## V. CONCLUSION

In this paper we have introduced and numerically studied a (relatively) simple phenomenological model of a recently reported granular segregation experiment. We have measured the same quantities as measured experimentally and shown that our model reproduces most of the features of the experiment, the most important being a transition from a mixed to a segregated state as the compacity is increased. This behaviour is not *a priori* built into the model - it emerges from the simple rules governing the motion of the particles. This is significant as it shows that we have a set of basic features necessary for an explanation of the experimentally observed behaviour.

We then used our model to investigate and identify segregation mechanisms and elucidate the experimental behaviour. We showed that the transition from mixed to segregated state in the model is caused by competition between the different driving felt by the  $cs$  and  $ps$ , which acts to cause segregation, and the noise, which acts to prevent segregation. We are led to conclude that this is also the main mechanism present in the experiment. We have also considered and demonstrated segregation due to different pressures and shown that it is possible that this might play a role in the experiment. The differential driving segregation mechanism is applicable to many binary driven systems [11, 13].

This work goes some way to explaining the intriguing experimental results of [1, 2, 3]. Experiments with other particle types in conjunction with more accurate experimental measurements, particularly with regard to particle positions and velocities, should allow more accurate comparisons with our model and also refinements of the model. In particular more accurate values for the parameters used.

Now that we have shown our model to be relevant to the experimental system, it is possible to use it further to investigate the 'granular statistical mechanics' of this type of system. In particular, it may be of use in developing and testing theories for agitated granular mixtures before attempting the more difficult task of accurately comparing with experiments.

### Acknowledgments

G.E. thanks Timo Aspelmeier and Sam Carr for useful discussions. P.M.R. thanks Tom Mullin for many stimu-

lating conversations. P.M.R. was supported by a doctoral scholarship from the Portuguese Foundation of Science and Technology.

- 
- [1] P.M. Reis, G.C.M.A. Ehrhardt, A. Stephenson, T. Mullin, *condmat* 0312331 (2003).
- [2] P.M. Reis, T.Mullin, *Phys. Rev. Lett.* **89**, 244301 (2002).
- [3] T.Mullin, *Phys. Rev. Lett.* **84**, 4741 (2000).
- [4] J. M. Ottino, D. V. Khakhar, *Annu. Rev. Fluid Mech.* **32** 55 (2000).
- [5] H. A. Makse, P. Cizeau, and H. E. Stanley, *Phys. Rev. Lett.* **78**, 3298 (1997).
- [6] P. Cizeau, H. A. Makse, and H. E. Stanley, *Phys. Rev. E* **59**, 4408 (1999).
- [7] S. Shoichi, *Mod. Phys. Lett. B* **12**, 115 (1998).
- [8] The 2-dimensional projected areas of the particles follow to a reasonable approximation a Gaussian distribution with a standard deviation of 17% of the mean.
- [9] H. M. Jaeger, S. R. Nagel, R. P. Behringer, *Rev. Mod. Phys.* **68**, 1259 (1996).
- [10] An interesting example of a macroscopic system described by near-equilibrium statistic mechanics is given in: R.P. Ojha, P.-A. Lemleux, P.K. Dixon, A.J. Liu and D.J. Durian,, *Nature* **427**, 521 (2004)
- [11] J. Dzubiella, G. P. Hoffmann, H. Lowen, *Phys. Rev. E* **65**, 021402 (2002).
- [12] P. Biswas, P. Sanchez, M. R. Swift, P. J. King, *Phys. Rev. E* **68**, 050301(R) (2003).
- [13] N. Burtally, P. King, M. Swift, *Science* **295**, 1877 (2002).
- [14] H. J. Herrmann, S. Luding, *Continuum. Mech. Thermodyn.* **10**, 189 (1998). D. C. Rappaport, *The Art of Molecular Dynamics Simulations* (Cambridge, 1995).
- [15] 2500 ps were measured to calculate the mean radius.
- [16] In the uncommon event that the particles are no longer moving together after the velocity update, they are not collided.
- [17] S. McNamara, W. R. Young, *Phys. Rev. E* **50**, R28 (1994).
- [18] S. Luding, S. McNamara, *Granular Matter*, 1(3):113, (1998), *cond-mat* 9810009.
- [19] A. Okabe, B.Boots, K. Sugihara, *Spacial Tesselations: Concepts and Applications of Voronoi Diagrams*, Wiley (1992).
- [20] P.M. Reis, G.C.M.A. Ehrhardt, T. Mullin, *condmat* 0312330 (2003).
- [21] S. Asakura, F. Oosawa, *J. Chem. Phys.* **22**, 1255 (1954). S. Asakura, F. Oosawa, *J. Polym. Sci.* **33** 183 (1958).
- [22] D. Frenkel, *Physica A* 313 (2003) 1-31.
- [23] L. Lafuente, J. A. Cuesta, *Phys. Rev. Lett.* **89**, 145702 (2002). M. Dijkstra, R. van Roij, R. Evans, *Phys. Rev. Lett.* **82**, 117 (1999).
- [24] D. J. Dinsmore, A. G. Yodh, D. J. Pine, *Phys. Rev. E* **52**, 4045 (1995).

# Appendix D

## Public presentation of this work

### Publications in refereed journal:

1. **P.M. Reis** and T. Mullin, ‘Granular segregation as a critical phenomena’, *Phys. Rev. Lett.* **89**(14), 244301 (2002).
2. **P.M. Reis**, G. Ehrhardt, A. Stephenson and T. Mullin, ‘Gases, liquids and crystals in granular segregation’, *Europhys. Lett.* **66** 357 (2004);
3. G. Ehrhardt, A. Stephenson and **P.M. Reis**, ‘Segregation mechanisms in a model of an experimental binary granular mixture’, *Phys. Rev. E* (2004), (accepted for publication; preprint: arXiv:cond-mat/0403273).

### Conference proceedings:

1. **P.M. Reis**, G. Ehrhardt and T. Mullin, ‘Segregation phases in a vibrated binary granular layer’, *Unifying concepts in the physics of glasses and granular media*, Capri, Italy (2003), (to appear in proceedings; preprint: arXiv:cond-mat/0312330).

**Press review on this work:**

1. A Poor Mix, Research Highlights, *Nature Physics Portal*, 25th November (2002).
2. Granular Games, *Nature Materials*, **2** (1), 6 (2003).

**Conference communications and invited seminars**

1. Poster, “*Gases, liquids and crystals in granular segregation*” at the *Gordon Research Conference on Granular and Granular-Fluid Flows*, Colby College Waterville, ME, USA (June 2004).
2. Invited seminar: “*Gases, liquids and crystals in granular segregation*”, Physical Mathematics Seminars, Department of Mathematics, Massachusetts Institute of Technology, USA (May 2004).
3. Contributed talk: “*Gases, liquids and crystals in granular segregation*”, *Transition and flow regimes in granular media* workshop at the *Granular and particle-laden flows* programme, Isaac Newton Institute, Cambridge, UK. (September 2003).
4. Invited Seminar: “*Gases, liquid and crystals in granular segregation*”, Non-linear Dynamics Group, Department of Physics, Univ. of Toronto, Canada (April 2003).
5. Contributed talk: “*Gases, liquid and crystals in granular segregation*”, APS March meeting, Austin, Texas, USA. (March 2003).
6. Contributed talk: “*Dynamics of segregation in granular monolayers*”, GDR Midi workshop on *Granular compaction and slow dynamics*, ESPCI, Paris. (December 2002).

7. Plenary talk, “*Patterns in the Sand*” at the 2002 Young Physicist Conference, Institute of Physics, University of Manchester, UK. (December 2002).
8. Invited seminar, “*Granular segregation in binary monolayers*” at the Manchester Centre for Nonlinear Dynamics, University of Manchester, UK. (September 2002).
9. Poster, “*Segregation in binary monolayers of dry particles: Entropic ordering in granular media?*” at the Faraday Discussion 123 on *Non-Equilibrium behaviour of colloidal dispersions*, Royal Society of Chemistry, University of Edinburgh, UK. (September 2002).
10. Invited Talk, “*Granular segregation in forced granular monolayers*” at the London Mathematical Society Workshop on *Particle Size Segregation, Mixing and Pattern Formation in Granular Materials*, St. Martin’s College, Lancaster, UK. (August 2002).
11. Poster, “*Granular segregation in binary shallow layers as a critical phenomena*” at the *Gordon Research Conference on Granular and Granular-Fluid Flows*, Holderness School, NH, USA. (July 2002).
12. Contributed talk, “*Coarsening of self-organized clusters due to segregation in a two-component monolayer of particles*”, at Dynamic Days 2001, Dresden, Germany. (June 2001).

# Bibliography

- Anderson, R. (1993), ‘Sorting out natural stone stripes’, *Nature* **361**, 117.
- Anderson, V. J. & Lekkerkerker, H. N. W. (2002), ‘Insights into phase transition kinetics from colloid science’, *Nature* **416**, 811–815.
- Asakura, S. & Oosawa, F. (1958), ‘Interaction between particles suspended in solutions of macromolecules’, *J. Polym. Sci* **33**, 183–192.
- Aumaitre, S., Kruelle, C. A. & Rehberg, I. (2001), ‘Segregation in granular matter under horizontal excitation’, *Phys. Rev. Lett.* **64**, 041305.
- Aumaitre, S., Kruelle, T. S. C. A. & Rehberg, I. (2003), ‘Granular phase transition as a precondition for segregation’, *Phys. Rev. Lett.* **90**, 114302.
- Bagnold, R. A. (1954), *The physics of blown sand and desert dunes*, Methuen and Co. ltd.
- Bak, P., Tang, C. & Wiesenfeld, K. (1987), ‘Self-organised criticality: an explanation of  $1/f$  noise’, *Phys. Rev. Lett.* **59**, 381–384.
- Barker, G. C. & Mehta, A. (1993), ‘Transient phenomena, self-diffusion, and orientational effects in vibrated powders’, *Phys. Rev. E* **47**, 184.
- Barrat, A. & Loreto, V. (2000), ‘Response properties in a model for granular matter’, *J. Phys. A* **33**, 4401.

- Barrat, J.-L. & Hansen, J.-P. (2003), *Basic concepts for simple and complex liquids*, Cambridge University Press.
- Batchelor, G. K. (1967), *An introduction to fluid dynamics*, Cambridge University Press.
- Bernal, B. (1964), ‘The bakerian lecture, 1962. the structure of liquids.’, *Proc. Roy. Soc. A* **280**, 299–322.
- Betat, A., Dury, C., Rehberg, I., Ristow, G., Cherer, M., Scroter, M. & Straßburger, G. (1998), *Formation of Patterns in Granular Materials*, In: F. Busse and S. C. Muller (eds.), *Evolution of spontaneous structures in dissipative continuous systems* Springer.
- Bibette, J., Roux, D. & Nallet, F. (1990), ‘Depletion interactions and fluid-solid equilibrium in emulsions’, *Phys. Rev. Lett.* **65**, 2470–2473.
- Binney, J. J., Dowrick, N. J., Fisher, A. J. & Newman, M. E. J. (1992), *The theory of critical phenomena*, OUP.
- Bizon, C., Shattuck, M. D. & Swift, J. B. (1999), ‘Linear stability analysis of a vertically oscillated granular layer’, *Phys. Rev. E* **60**, 7210–7216.
- Bouchaud, J., Cates, M. E. & Claudin, P. (1995), ‘Stress distribution in granular media and nonlinear wave equations’, *J. Phys. France I* **5**, 639–656.
- Bouchaud, J. P. (2002), *Granular media: some ideas from statistical physics*, In: Barrat, J.-L.; Feigelman, M.V.; Kurchan, J.; Dalibard, J. (Eds.) (eds.), *Slow Relaxations and Nonequilibrium Dynamics in Condensed Matter* Springer.
- Bourzutschky, M. & Miller, J. (1995), ‘Granular convection in a vibrated fluid’, *Phys. Rev. Lett.* **74**, 2216–2219.

- Breu, A. P. J., Ensner, H.-M., Kruelle, C. A. & Rehberg, I. (2003), 'Reversing the brazil-nut effect: Competition between percolation and condensation', *Phys. Rev. Lett.* **90**, 014302.
- Bridgewater, J. (1976), 'Fundamental powder mixing mechanisms', *Powder Technology* **15**, 215–236.
- Bridgewater, J. (1993), *Mixing and segregation mechanisms in particle flow*, In: *Granular Matter* A. Metha (Ed.) 161–195, Springer-Verlag.
- Bridgewater, J. (1995), 'Particle technology', *Chemical Engineering Science* **50**, 4081–4089.
- Brockbank, R., Huntley, J. & Ball, R. (1997), 'Contact force distribution beneath a three-dimensional granular pile', *J. Phys. II France* **7**, 1521–1532.
- Burtally, N., King, P. & Swift, M. (2002), 'Spontaneous air-driven separation in vertically vibrated fine granular mixtures', *Science* **295**, 1877–1879.
- Cas, R. A. F. & Wright, J. V. (1987), *Volcanic Successions, Modern and Ancient*, Allen and Unwin, London.
- Chaikin, P. M. (1995), *Principles of condensed matter physics*, Cambridge University Press.
- Chapman, S. & Cowling, T. G. (1952), *The mathematical theory of non-uniform gases*, Cambridge Mathematical Library, Cambridge University Press.
- Chladni, E. F. (1787), *Entdeckungen uber die Theorie des Klanges*, Weidmanns, Erben und Reich.
- Choo, K., Molteno, T. & Morris, S. (1997), 'Travelling granular segregation patterns in a long drum mixer', *Phys. Rev. Lett.* **79**, 2975–2978.

- Clément, E., Rajchenbach, J. & Duran, J. (1995), ‘Mixing of a granular material in a bidimensional rotating drum’, *Europhys. Lett.* **30**, 7–12.
- Coniglio, A. & Nicodemi, M. (2001), ‘A statistical mechanics approach to the inherent states of granular media’, *Physica A* **296**, 451.
- Cooke, W., Warr, S., Huntley, J. & Ball, R. (1996), ‘Particle size segregation in a two-dimensional bed undergoing vertical vibration’, *Phys. Rev. E* **53**, 2812–2822.
- Coulomb, C. A. (1773), ‘Memoires de mathematiques et de physique presentes a l’academie royal des sciences par divers sacans et lus dans les assemblees’, *L’imprimerie Royale* p. 343.
- Crocker, J., Matteo, J., Dinsmore, A. & Yodh, A. (1999), ‘Entropic attraction and repulsion in binary colloids probed with a line optical tweezer’, *Phys. Rev. Lett.* **82**, 4352.
- Dantu, P. (1967), ‘Etude expérimental d’un milieu pulvérulent’, *Ann. Ponts Chauss.* **IV**, 193–202.
- Dijkstra, M., van Roij, L. & Evans, R. (1999), ‘Direct simulation of the phase behavior of binary hard-sphere mixtures: tests of the depletion potential description’, *Phys. Rev. Lett.* **82**, 117–120.
- Dinsmore, A. D., Yodh, A. G. & Pine, D. J. (1995), ‘Phase-diagrams of nearly hard-sphere binary colloids’, *Phys. Rev. E* **52**, 4045–4057.
- Dippel, S. & Luding, S. (1995), ‘Simulation on size segregation: geometrical effects in the absence of convection’, *Journal de Physique I France* **7**, 1527–1537.

- Donald, M. & Roseman, B. (1962), ‘Mixing and demixing of solid particles’, *Br. Chemical Engineering* **7**, 749–753.
- Drahn, J. A. & Bridgewater, J. (1983), ‘The mechanics of free surface segregation’, *Powder Tech.* **36**, 39–53.
- Duran, J. (2000), *Sands, Powders, and Grains: An Introduction to the Physics of Granular Materials*, Springer-Verlag, New York.
- Duran, J. & Jullien, R. (1999), ‘Attractive forces in a granular cocktail’, *Phys. Rev. Lett* **80**, 3547–3550.
- Duran, J., Rajchenbach, J. & Clément, E. (1993), ‘Arching effect model for particle size segregation’, *Phys. Rev. Lett* **70**, 2431–2434.
- Ehrhardt, G., Stephenson, A. & Reis, P. M. (2004), ‘segregation mechanisms in a model of an experimental binary granular mixture’, in press (cond-mat:0403273).
- Fan, L. T., Chen, Y. & Lai, F. S. (1990), ‘Recent developments in solids mixing’, *Powder Tech.* **61**, 255–287.
- Faraday, M. (1831), ‘On a peculiar class of acoustical figures; and on certain forms assumed by groups of particles upon vibrating elastic surfaces’, *Phil. Trans. R. Soc.* **131**, 299–340.
- Fierro, A., Nicodemi, M. & Coniglio, A. (2003), ‘Edwards’ approach to horizontal and vertical segregation of hard spheres under gravity’, *J. Phys.: Condens. Matter* **15**, S1095–1105.
- GDR, M. D. (2004), ‘on dense granular flows’, *Eur. Phys. Jou. E* (to be published).

- Geng, J., Howell, D., Longhi, E., Behringer, R. P., Reydellet, G., Vanel, L., Clément, E. & Luding, S. (2001), 'Footprints in sand: The response of a granular material to local perturbations', *Phys. Rev. Lett* **87**, 035506.
- Gray, J. M. N. T. (2001), 'Granular flow in partially filled slowly rotating drums', *J. Fluid. Mech.* **441**, 1–29.
- Gray, J. M. N. T. & Hutter, K. (1997), 'Pattern formation in granular avalanches.', *Contin. Mech. & Thermodyn.* **9**, 341–345.
- Gray, J. M. N. T., Tai, Y.-C. & Noelle, S. (2003), 'Shock waves, dead zones and particle-free regions in rapid granular free-surface flows', *J. Fluid. Mech.* **491**, 161–181.
- Gupta, S. D., Bhatia, S. K. & Khakar, D. V. (1991), 'Axial segregation of particles in a horizontal rotating cylinder', *Chem. Eng. Sci.* **46**, 1513–1517.
- Hill, K. M. & Kakalios, J. M. (1994), 'Reversible axial segregation of binary mixtures of granular materials', *Phys. Rev. E* **49**, R3610–R3613.
- Hill, K. M. & Kakalios, J. M. (1995), 'Reversible axial segregation of rotating granular media', *Phys. Rev. E* **52**, 4393–4400.
- Hobbie, E. K. (1998), 'Metastability and depletion-driven aggregation', *Phys. Rev. Lett.* **81**, 3996–3999.
- Hong, D. C., Quinn, P. V. & Luding, S. (2001), 'Reverse brazil nut problem: Competition between percolation and condensation', *Phys. Rev. Lett.* **86**, 3423–3426.
- Hsiau, S. S. & Yu, H. Y. (1997), 'Segregation phenomena in a shaker', *Powder Tech.* **93**, 83–88.

- Huerta, D. A. & Ruiz-Suárez, J. C. (2004), ‘Vibration-induced granular segregation: A phenomenon driven by three mechanisms’, *Phys. Rev. Lett.* **92**, 114301.
- Iverson, R. M. (1997), ‘The physics of debris flows’, *Rev. Geophys.* **35**, 245–296.
- Jaeger, H. & Nagel, S. (1992), ‘Physics of the granular state’, *Science* **255**, 1523–1531.
- Jaeger, H. M. & Nagel, S. (1996), ‘Granular solids, liquids and gases’, *Rev. of Mod. Phys.* **68**(4), 1259–1273.
- Jaeger, H. M., Liu, C. & Nagel, S. R. (1989), ‘Relaxation at the angle of repose’, *Phys. Rev. Lett.* **62**, 40–43.
- Jaeger, H., Nagel, S. & Behringer, R. (1996), ‘The physics of granular material’, *Physics Today* pp. 32–38.
- Janssen, H. (1895), ‘Test on grains pressure in silos’, —*Z. Vereins Deutsch Ing.* **39**, 1045–1049.
- Jenkins, J. T. & Richman, M. W. (1984), ‘Grad’s 13-moment system for a dense gas of inelastic spheres’, *Archive of Rational Mechanics and Analysis* **87**, 355–377.
- Jenkins, J. T. & Savage, S. B. (1983), ‘A theory for the rapid flow of identical, smooth, nearly elastic, spherical particles’, *J. of Fluid Mech.* **130**, 187–202.
- Jenkins, J. T. & Yoon, D. K. (2002), ‘Segregation in binary mixtures under gravity’, *Phys. Rev. Lett.* **88**, 194301.
- Julien, P., Lan, Y. & Raslan, Y. (1997), *Experimental mechanics of sand stratifications*, In: Behringer R. and Jenkins J (eds.), *Powder & Grains 97*, Balkema, Rotterdam.

- Jullien, R., Meakin, P. & Pavlovitch, A. (1992), ‘Three-dimensional model for particle-size segregation by shaking’, *Phys. Rev. Lett* **69**, 640–643.
- Kadanoff, L. (1999), ‘Built upon sand: theoretical ideas inspired by granular flows’, *Rev. of Mod. Phys.* **71**(1), 435–444.
- Knight, J. B., Ehrides, E. E., Kuperman, V. Y., Flint, J. K., Jaeger, H. M. & Nagel, S. R. (1996), ‘Experimental study of granular convection’, *Phys. Rev. E* **54**, 5726–5738.
- Knight, J. B., Fandrich, C. G., Lau, C. N., Jaeger, H. M. & Nagel, S. R. (1995), ‘Density relaxation in a vibrated granular material’, *Phys. Rev. E* **51**, 3957–3962.
- Knight, J. B., Jaeger, H. M., & Nagel, S. R. (1993), ‘Vibration-induced size separation in granular media: The convection connection’, *Phys. Rev. Lett.* **70**, 3728.
- Koepe, J. P., Ens, M. & Kakalios, J. (1998), ‘Phase diagram for avalanche stratification of granular media’, *Phys. Rev. E* **58**, R4104.
- Krapivsky, P. L. & Ben-Naim, E. (1994), ‘Collective properties of adsorption-desorption processes’, *J. Chem. Phys.* **100**, 6778.
- Kudrolli, A. (2004), ‘Size separation in vibrated granular matter’, *Rep. on Prog. in Phys.* **67**, 209.
- Lan, Y. D. & Rosato, A. D. (1997), ‘Convection related phenomena in granular dynamics simulations of vibrated beds’, *Phys. of Fluids* **9**, 3615–3624.
- Liffman, K., Metcalfe, G. & Cleary, P. (1997), *Convection due to horizontal shaking*, In: Behringer R. and Jenkins J (eds.), *Powder & Grains 97*, Balkema, Rotterdam.

- Liu, C. H., Jaeger, H. M. & Nagel, S. R. (1991), 'Finite-size effect in a sandpile', *Phys. Rev. A* **43**, 7091–7092.
- Liu, C. H., Nagel, S. R., Schecter, D. A., Coppersmith, S. N., Majumdar, S., Narayan, O. & Witten, T. A. (1995), 'Force fluctuations in bead packs', *Science* **269**, 513–515.
- Luding, S. (2001), 'Global equation of state of two-dimensional hard sphere systems', *Phys. Rev. E* **63**, 042201.
- Makse, H., Cizeau, P. & Stanley, H. (1997), 'Possible stratification mechanism in granular mixtures', *Phys. Rev. Lett.* **78**, 3298–3301.
- Melo, F., Umbanhowar, P. & Swinney, H. (1995), 'Hexagons, kinks and disorder in oscillated granular layers', *Physical Review Letters* **75**(21), 3838–3841.
- Metcalf, G., Tennakoon, S. G. K., Kondic, L., Schaeffer, D. G. & Behringer, R. P. (2002), 'Granular friction, coulomb failure, and the fluid-solid transition for horizontally shaken granular materials', *Phys. Rev. E* **65**, 031302.
- Miller, B., O'Hern, C. & Behringer, R. P. (1996), 'Stress fluctuations for continuously sheared granular materials', *Phys. Rev. Lett.* **77**, 3110–3113.
- Möbius, M. E., Lauderdale, B. E. & S. R. Nagel, H. M. J. (2001), 'Size separation of granular particles', *Nature* **414**, 270.
- Mullin, T. (2000), 'Coarsening of self-organized clusters in binary mixtures of particles', *Phys. Rev. Lett.* **84**(20), 4741–4744.
- Mullin, T. (2002), 'Mixing and de-mixing', *Science* **295**, 1851.
- Nakagawa, M. (1994), 'Axial segregation of granular flows in a horizontal rotating cylinder', *Chemical Engineering Science, Shorter communications* **49**, 2540–2544.

- Nedderman, R. & Laohakul, C. (1980), ‘The thickness of the shear zone of flowing granular materials’, *Powder Tech.* **25**, 91–100.
- Nowak, E. R., Knight, J. B., Ben-Naim, E., Jaeger, H. M. & Nagel, S. R. (1998), ‘Density fluctuations in vibrated granular materials’, *Phys. Rev. E* **57**, 1971–1982.
- Okabe, A., Boots, B. & Sugihara, K. (1992), *Spacial Tesselations: Concepts and Applications of Voronoi Diagrams*, Wiley.
- Olafsen, J. S. & Urbach, J. S. (1999), ‘Clustering, order, and collapse in a driven granular monolayer’, *Phys. Rev. Lett.* **81**, 4369.
- Ottino, J. M. & Khakhar, D. V. (2000), ‘Mixing and segregation of granular materials’, *Annu. Rev. Fluid Mech.* **32**, 55–91.
- Painter, B. & Behringer, R. P. (2000), ‘Substrate interactions, effects of symmetry breaking, and convection in a 2d horizontally shaken granular system’, *Phys. Rev. Lett.* **85**, 3396–3399.
- Poon, W. C. K. (2002), ‘The physics of a model colloid-polymer mixture’, *J. Phys.: Condens. Matter* **14**, R859–R880.
- Poon, W., Egelhaaf, S., Stellbrink, J., Allgair, J., Scofield, A. & Pusey, P. (2001), ‘Beyond simple depletion: phase behaviour of colloid-star polymer mixtures’, *Phil. Trans. R. Soc. Lond. A* **359**, 897.
- Pouliquen, O. & Chevoir, F. (2002), ‘Dense flows of dry granular material’, *C. R. Physique* **3**, 163–175.
- Press, W., Teukolsky, W., Vetterling, W. & Flannery, B. (1992), *Numerical Recipes in C: The art of scientific computing*, 2nd edn, Cambridge University Press.

- Pusey, P. N. & van Megen, W. (1986), ‘Phase behaviour of concentrated suspensions of nearly hard colloidal spheres’, *Nature* **320**, 340–342.
- Reis, P. M. & Mullin, T. (2002), ‘Granular segregation as a critical phenomena’, *Phys. Rev. Lett* **89**, 244301.
- Rericha, E., Bizon, C., Shattuck, M. & Swinney, H. (2002), ‘Supersonic granular flow of supersonic sand’, *Phys. Rev. Lett.* **88**, 014302.
- Reynolds, O. (1885), ‘On the dilatency of media composed of rigid particles in contact’, *Philosophical Magazine* **20**, 469–481.
- Rosato, A., Stranburg, K. J., Prinz, F. & Swendsen, R. H. (1987), ‘Why the brazil nuts are on top: Size segregation of particulate matter by shaking’, *Phys. Rev. Lett.* **58**, 1038–1040.
- Savage, S. B. (1988), ‘Streaming motions in a bed of vibrationally fluidized dry granular material’, *J. Fluid Mech.* **194**, 457–478.
- Savage, S. B. & Hutter, K. (1989), ‘Finite mass of granular material down a rough incline’, *J. Fluid Mech.* **199**, 177–215.
- Savage, S. B. & Lun, C. K. K. (1988), ‘Particle size segregation in inclined chute flow of cohesionless granular solids’, *J. Fluid Mech.* **189**, 311–335.
- Shinbrot, T. (2004), ‘The brazil nut effect - in reverse’, *Nature* **429**, 352–353.
- Shinbrot, T. & Muzzio, F. (2000), ‘Nonequilibrium patterns in granular mixing and segregation’, *Physics Today* pp. 25–30.
- Shinbrot, T. & Muzzio, F. (2001), ‘Noise to order’, *Nature* **410**, 251–258.
- Shinbrot, T. & Muzzio, F. J. (1998), ‘Reverse buoyancy in shaken granular beds’, *Phys. Rev. Lett.* **381**, 4365–4368.

- Tai, Y., Gray, J., Hutter, K. & Noelle, S. (2001), 'Flow of dense avalanches past obstructions', *Annal. Glac.* **32**, 281–284.
- Terzaghi, K. (1943), *Theoretical soil mechanics*, Wiley: New York.
- van Dyke, M. (1982), *An album of fluid motion*, Stanford: Parabolic Press.
- Vanel, L., Howell, D., Clark, D., Behringer, R. & Clément, R. (1999), 'Memories in sand: Experimental tests of construction history on stress distributions under sandpiles', *Phys. Rev. E* **60**, R5040–R5043.
- Werner, B. & Hallet, B. (1993), 'Numerical simulation of self-organized stone stripes', *Nature* **361**, 142–145.
- Wildman, R. D., Huntley, J. M. & Parker, D. J. (2001), 'Convection in highly fluidized three-dimensional granular beds', *Phys. Rev. Lett.* **86**, 3304–3307.
- Williams, J. C. (1963), 'The segregation of powders and granular materials', *Fuel Soc.* **14**, 29–34.
- Williams, J. C. (1976), 'The segregation of particulate materials. a review.', *Powder Tech.* **15**, 245–251.
- Wood, W. W. & Jacobsen, J. D. (1957), 'Preliminary results from recalculation of the monte carlo equation of state of hard spheres', *J. Chem. Phys.* **26**, 1207–1208.
- Yan, X., Shi, Q., Hou, M. & Lu, K. (2003), 'Effects of air on the segregation of particles in a shaken granular bed', *Phys. Rev. Lett.* **91**, 014302.